From Dust to Planets: Dust Aggregation in the Post-Fractal Growth Regime

Von der Fakultät für Elektrotechnik, Informationstechnik, Physik
der Technischen Universität Carolo-Wilhelmina
zu Braunschweig
zur Erlangung des Grades eines
Doktors der Naturwissenschaften
(Dr.rer.nat.)
genehmigte
Dissertation

von Carsten Güttler
geboren in Bünde, Westfalen

1. Referent:	Prof. Dr. Jürgen Blum, Institut für Geophysik und extraterrestrische Physik, Technische Universität Carolo-Wilhelmina zu Braunschweig
2. Referent:	Prof. Dr. Carsten Dominik, Astronomical Institute 'Anton Pannekoek', Faculty of Science, University of Amsterdam
eingereicht am:	04. September 2009
mündliche Prüfung am:	01. Dezember 2009
Druckjahr:	2009

Vorabveröffentlichung der Dissertation

Teilergebnisse aus dieser Arbeit wurden mit Genehmigung der Fakultät für Elektrotechnik, Informationstechnik, Physik, vertreten durch den Mentor der Arbeit, in folgenden Beiträgen vorab veröffentlicht:

Publikationen:

Geretshauser R.J., Speith, R., Güttler, C., Krause, M., Blum, J. (2009) Numerical Simulations of Highly Porous Dust Aggregates in the Low-Velocity Collision Regime, in Vorbereitung

Zsom, A., Ormel, C.W., Güttler, C., Blum, J., Dullemond, C.P. (2009). The outcome of protoplanetary dust growth: pebbles, boulders, or planetesimals? II. Introducing the bouncing barrier, *Astronomy & Astrophysics*, eingereicht

Güttler, C., Blum, J., Zsom, A., Ormel, C.W., Dullemond, C.P. (2009). The outcome of protoplanetary dust growth: pebbles, boulders, or planetesimals? I. Mapping the zoo of laboratory collision experiments, *Astronomy & Astrophysics*, eingereicht

Güttler, C., Krause, M., Geretshauser, R.J., Speith, R., Blum, J. (2009). The Physics of Protoplanetesimal Dust Agglomerates. IV. Towards a Dynamical Collision Model, *The Astrophysical Journal*, 701:130-141

Güttler, C., Krause, M., Geretshauser, R.J., Speith, R., Blum, J. (2009). Towards a Dynamical Collision Model of Highly Porous Dust Aggregates, *Powders and Grains 2009: Proceedings of the 6th International Conference on Micromechanics of Granular Media*, AIP Conference Proceedings, 1145:941-944

Weidling, R., Güttler, C., Brauer, F., Blum, J. (2009). The Physics of Protoplanetesimal Dust Agglomerates. III. Compaction in Multiple Collisions, *The Astrophysical Journal*, 696:2036-2043

Tagungsbeiträge:

Güttler, C., Krause, M., Geretshauser, R.J., Speith, R., Blum, J. (2009). Towards a Dynamical Collision Model of Highly Porous Dust Aggregates, Powders and Grains 2009: 6th International Conference on Micromechanics of Granular Media, 13. – 17. Juni 2009, Golden, CO, USA

Güttler, C., Blum, J., Zsom, A., Ormel, C.W., Dullemond, C.P. (2009). The first phase of protoplanetary dust growth: the bouncing barrier, Goldschmidt 2009 - "Challenges to Our Volatile Planet", 21. – 26. Juni 2009, Davos, Schweiz

Zsom, A., Güttler, C., Ormel, C.W., Dullemond, C.P., Blum, J. (2009). Circumstellar disks and dust aggregates: the biggest billiard game with the smallest balls, 2. – 6. März 2009, Tübingen

Blum, J., Güttler, C., Krause, M. Geretshauser, R.J., Speith, R. (2008). Collision Mechanics of Protoplanetary Dust Agglomerates, International Summer School "Advanced Problems in Mechanics", 6. – 10. Juli 2008, St. Petersburg, Russland

Contents

Summary

The formation of planets in the first growth phase is not well understood. Theory and experiments agree that it begins with (sub-)micrometer sized dust grains, which gently collide and effectively stick to each other, and, by this, form fractal dust aggregates. However, as these aggregates grow in size, their relative velocities increase and collisions do not necessarily lead to sticking anymore but may result in bouncing and fragmentation which can inhibit further growth. In the last years, many collision experiments were performed to study this post-fractal growth regime, but a conclusive picture on the bottom-up evolution of the aggregates was still lacking. In this thesis, new experiments are presented which give us an insight into the bouncing behavior and the dynamic compaction of protoplanetary dust aggregates. Apart from the direct application, these results are used for the calibration of a physical collision model which yields a deeper understanding of the involved processes as well as making predictions for collisions that are not yet experimentally studied. In a second step, all available dust collision experiments and physical models are utilized to construct a new model that gives a quantified collisional outcome for every set of collision parameters (i.e. collision velocity, aggregate masses, aggregate porosities) that may occur for collisions under realistic solar nebula conditions. This model is used as a 'collision kernel' for a coagulation simulation that computes the evolution of dust aggregates in the solar nebula, and the result of this simulation is that aggregates can effectively grow up to centimeter sizes until further growth is inhibited by bouncing. As soon as this 'bouncing barrier' is reached, the whole system is in a quasi steady-state as the mass of each aggregate is sustained and they are only compacted by the processes previously studied in the experiments. Although the ultimate growth to even larger bodies can actually not be explained, this study presents a conclusive picture for the growth from micrometer-sized dust grains to centimeter-sized, porous dust aggregates.

Zusammenfassung

Die Entstehung von Planeten und im Besonderen deren erste Wachstumsphase ist bisher nur in groben Zügen verstanden. Sowohl Theorie als auch Experimente sagen voraus, dass das Wachstum mit (Sub-)Mikrometer großen Staubkörnern beginnt, die sanft stoßen und effektiv aneinander haften, wodurch sich fraktale Aggregate bilden. Sobald die Größe dieser Aggregate jedoch anwächst, werden auch die Stoßgeschwindigkeiten größer und Stöße führen nicht mehr zwangsweise zum Wachstum sondern gegebenenfalls zum Abprallen oder zur Fragmentation, was das weitere Wachstum hemmt. In den vergangenen Jahren wurden viele Experimente durchgeführt, um diese post-fraktale Wachstumsphase zu untersuchen, jedoch gibt es noch kein schlüssiges Modell, das die Entwicklung dieser Staubaggregate wirklich lückenlos erklären kann. In dieser Arbeit werden neue Experimente präsentiert, die uns einen Einblick in das Abprall-Verhalten und die dynamische Kompaktierung von protoplanetaren Staubaggregaten liefern. Abgesehen von der direkten Anwendung werden diese Ergebnisse zur Kalibrierung eines physikalischen Stoßmodells verwendet, welches sowohl ein tieferes Verständnis der Stoß-Prozesse liefern wird, als auch Vorhersagen für Stöße machen wird, die noch nicht im Labor untersucht wurden. In einem zweiten Schritt werden alle verfügbaren Stoßexperimente wie auch physikalischen Modelle verwendet, um ein neues Modell zu konstruieren, welches für jede mögliche Kombination von Stoßparametern (d.h. Stoßgeschwindigkeit, Aggregatmassen, Aggregatporositäten), die unter protoplanetaren Bedingungen vorkommen können, ein quantitatives Stoßresultat vorhersagt. Dieses Modell wird als 'Stoß-Kernel' für eine Koagulationssimulation verwendet, die die Entwicklung von Staubaggregaten im solaren Nebel errechnet, und das Ergebnis dieser Simulation ist, dass Aggregate effektiv bis zu Zentimeter Größe agglomerieren können, bis das weitere Wachstum durch abprallende Stöße gestoppt wird. Sobald diese Grenze – die 'bouncing barrier' – erreicht ist, befindet sich das gesamte System nahezu in einem Gleichgewicht, da die Masse der einzelnen Aggregate erhalten bleibt und diese nur durch die zuvor experimentell untersuchten Prozesse verdichtet werden. Obwohl das weitere Wachstum zu größeren Körpern letztlich nicht geklärt werden kann, wird in dieser Arbeit erstmals ein schlüssiger Weg für das Wachstum von Mikrometer großen Staubkörnern zu Zentimeter großen, porösen Staubaggregaten dargelegt.

Chapter 1

Introduction: Dust Growth in the Early Solar System

It is in our human nature to ask the fundamental questions concerning our origin. Where do we come from? What holds the world together? How did it form? These questions, general curiosity, and the fascinating view of the dark night sky in the Middle Ages inspired scientists like Nikolaus Kopernikus, Johannes Kepler, and Galileo Galilei to observe and explain the movement of the planets (the "wandering stars") of our solar system with the Sun in the center. After this great achievement, one major question could be specified into how the *solar system* and the planets – especially Earth – formed. Although more in a philosophical way, the first recognized attempt for a naturalistic explanation of the solar system origin was by Descartes (1644). He hypothesized that the planets (and the major satellites) formed in fourteen or more vortices, being globally arranged around the primitive Sun, where Jupiter and Saturn must have formed in the largest of these. However, he could neither specify the origin of these vortices, nor the planet formation inside these. In later influential works, Kant (1755) and Laplace (1796) deduced that the planets formed in a cooling and contracting gas cloud, rotating around a central star. It was their achievement to realize that this cloud had to flatten into a disk around the central star. Until the mid-20th century, this disk – as the birthplace of the planets – was referred to as the Kant-Laplace nebula. Moreover, Kant (1755) speculated that the observed extended astronomical objects, which were also called nebulae, might be planetary systems in their state of formation. Although this was not exactly the case, it was still a long-sighted perception of the existence of extrasolar planets, which was only 240 years later, in 1995, confirmed by Mayor and Queloz, who observed the first extrasolar planet orbiting around a main-sequence star by the radial velocity method. Planetary systems, i.e. stars with more than one orbiting planet, were observed in 1999 by Butler et al. and at the hand-in of this thesis, in September 2009, 373 extrasolar planets were confirmed[1], of which 11 planets were observed by direct imaging. A spectacular

[1] Up-to-date information about extrasolar planet search, i.e. their number, properties, observation technique, etc. can be found on `www.exoplanets.eu`.

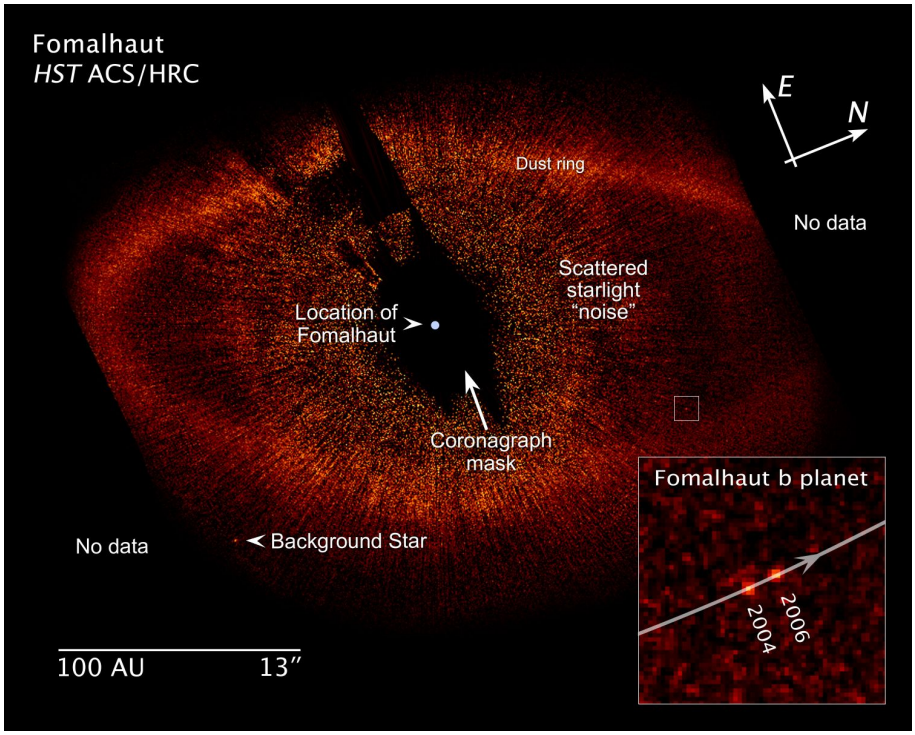

Figure 1.1: A prominent example for an extrasolar planet, which was directly imaged by the Hubble Space Telescope (Kalas et al., 2008). The planet Fomalhaut b with a mass < 3 Jupiter masses orbits its central star at a distance of 115 AU. Credit: NASA, ESA, and Z. Levay (STScI)

observation was the Hubble Space Telescope image of Fomalhaut b as analyzed by Kalas et al. (2008) (see Fig. 1.1). The existence of the solar nebula, as hypothesized by Kant and Laplace, can today also be confirmed. Direct imaging and spectral energy distribution of young solar objects show that these nebulae are very common around young stars (Haisch et al., 2001, Carpenter et al., 2005, Wyatt, 2008). All these facts and theories are a strong motivation to study the formation of planets in more detail and to fill a piece of the puzzle concerning our origin.

1.1 Setting the Stage for the Formation of Planets

From the successful search for extrasolar planets, we know that planet formation must be a quite common process and our solar system is definitely not the only system to host planets. From the large number of stars tested for extrasolar planets, 6 % bear a planet, which is even a lower limit, restricted by the measurement precision[2]. If one planet is

[2]The most common and successful method to search for extrasolar planets is the radial velocity method. The orbiting planet pulls on the star and forces it to rotate around their shared center of mass. The star's velocity component in the direction of the observer (Earth) can be measured by a Doppler shift in the spectrum. Heavy planets with small radial distance to the star are thus easier to detect. The current detection limit is 1 m s^{-1}.

already found orbiting around a star, the probability of finding a second planet around the same star is enhanced by a factor of two (12 %, Udry et al., 2007), so planetary systems are also common. Moreover, this probability increases if the star is metal-rich. For stars with [Fe/H] = 0.5 (i.e. $10^{0.5}$ times more relative metal than the Sun), the probability of detecting an orbiting planet is 26.5 % (Fischer and Valenti, 2005). From these facts, people try to constrain planet-formation models. One interesting idea is that around metal-rich stars (in metal-rich disks) more solid material is available and the probability to form planets is increased. Another interesting finding from the extrasolar planet search is that basically no planets are found in the mass-range from 20 to 60 Jupiter masses (Fig. 2 in Udry et al., 2007). This so called *brown-dwarf desert* separates the number of stars with small masses and the detected extrasolar planets with high masses and is regarded as an indication that the formation process for stars and planets must be different. If both were formed by the same process, it would be unlikely why objects with these masses should be depleted.

However, the formation of planets is still closely connected to the formation of their host star as both form from the same material and within the same period of time. Stars evolve from molecular clouds which can have dense regions (e.g. by local shocks) that collapse under their own gravity. After the first contraction and the formation of a central object, the initially small rotation of the contracting region (e.g. by the differential rotation of the galaxy) speeds up due to the conservation of angular momentum. Centrifugal forces lead to the formation of a flat disk, in which most of the material can not directly accrete from all directions but only in the plane of the disk (for details on the cloud contraction and disk formation see e.g. Tscharnuter, 1987, Tscharnuter et al., 2009). Above, this disk was historically introduced as the *Kant-Laplace nebula*, while in modern terminology, from the perspective of star formation, it is referred to as the *accretion disk* or the *solar nebula* because it provides the material for the star accretion. In terms of planet formation, this disk is also called the *protoplanetary disk* (PPD), as it also provides the primary material for the formation of planets inside this disk.

We can observe these disks due to their small fraction of dust, whereas their structure and evolution is determined by their gas. Various models for the disk at the time when the formation of planets sets in are under discussion, among which the most common model is the so called *minimum mass solar nebular* (MMSN) model as outlined by Weidenschilling (1977b). The basic assumption is that the planets of our present solar system formed at the radial distances where they reside today and that all solid material of the PPD was incorporated into the planets – the minimum mass assumption. The first important parameter describing this disk is the surface density in the midplane of the disk

$$\Sigma(r) = \Sigma_0 \left(\frac{r}{1 \text{ AU}} \right)^{\delta} , \tag{1.1}$$

where r is the radial distance to the central star in astronomical units (AU) and Σ_0 is the surface density at 1 AU being the density which is projected to the midplane of the disk. In case of the MMSN the values are $\Sigma_0 = 1700$ g cm^{-2} and $\delta = -1.5$ (Hayashi et al., 1985). Although this model has commonly been used in the past decades, it has lately

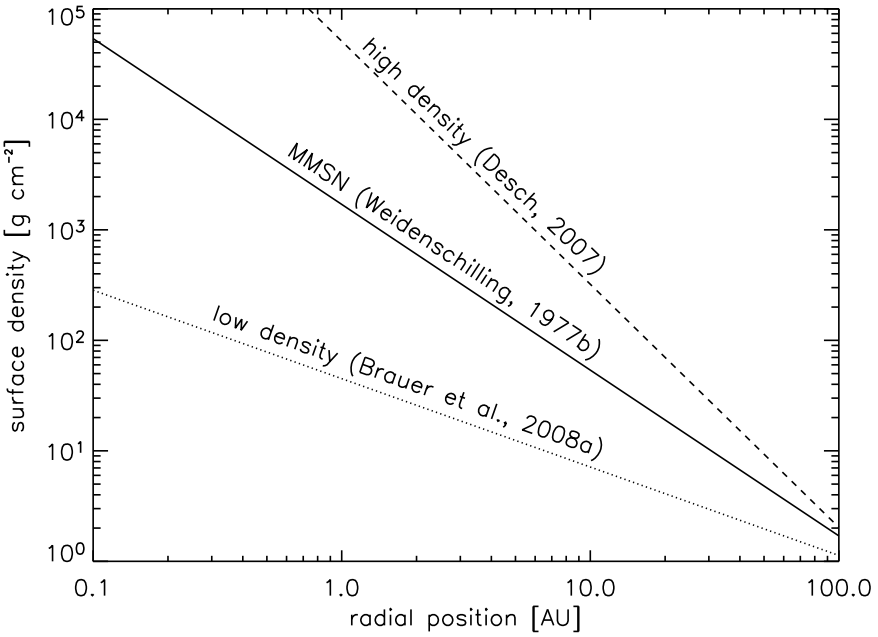

Figure 1.2: The gas surface densities for the three disk models following Eq. 1.1, which are being considered in this work (i.e. in Chapters 2 and 5). The minimum mass solar nebula (MMSN) model is based on the current state of the solar system, while the low density model uses astronomical observations of protoplanetary disks, and the high density model is based on our solar system in which the planets migrate after their formation ('Nice' model).

been challenged: based on resolved millimeter emission maps of PPDs (Andrews and Williams, 2007), Brauer et al. (2008a) suggested a much lower density ($\Sigma_0 = 45$ g cm^{-2}) with a flatter radial decay ($\delta = -0.8$). In contrast to that, Desch (2007) followed the finding from the 'Nice' model (Tsiganis et al., 2005) that the planets do not reside on their formation position but considerably migrate and even swap positions. Constructing another minimum mass model from the predicted positions of the 'Nice' model yields a disk with significantly higher density ($\Sigma_0 = 51\,000$ g cm^{-2}, $\delta = -2.2$). These three disk models (MMSN, low density, high density) stretch a wide range in the material density if we consider the disk at a radial distance of 1 AU (see Fig. 1.2) but all three have their justified eligibility. As the choice of the nebular model considerably influences the material density and the relative velocities of the dust in the disk, we will further on consider all three models and compare the results.

Although the protoplanetary disk is dominated by the gas, about one percent of the mass is in solid material (i.e. oxides, silicates, ices, organics, etc.), which condenses when the disk sufficiently cools down within a few 10^5 years after its formation. The sizes of these dust grains are very important as they determine their sticking properties which result from attractive van der Waals forces among the grains (e.g. Johnson et al., 1971, Heim et al., 1999, Poppe et al., 2000). For these grain sizes, we have some evidence from

our own solar system and observation of interstellar dust, which include interplanetary dust particles (typically 0.3 μm, Jessberger et al., 2001), interstellar particles (also submicrometer, Li and Greenberg, 2003), meteorites (micrometer size, Scott and Krot, 2005, Righter et al., 2006) and Comet Wild 2 (nanometer to above 10 μm, Brownlee et al., 2006, Zolensky et al., 2006). The bottom line is that most experiments (Blum and Wurm, 2008) and computer models (e.g. Paszun and Dominik, 2008) dealing with the aggregation of these dust grains consider micrometer-sized dust grains as the starting material.

One discussed scenario for the accumulation of this dust into planetesimals[3] and planets is the gravitational instability of substructures or rings in the PPD. Like the formation of the star from the molecular cloud, planetetesimals or planets would accumulate only by their own gravitational attraction as soon as the local density is higher than a critical value, i.e. by settling to the midplane. This idea goes back to Safronov (1969) and Goldreich and Ward (1973) and would be a straightforward way to directly form large bodies (i.e. 100 m-sized according to Goldreich and Ward, 1973) within a short time. However, as it was long known that the gas in the disk must be turbulent for many reasons (Weizsäcker, 1944, Safronov, 1969, Völk et al., 1980), this concept was always challenged, and, in 1995, Weidenschilling showed that a gravitational instability of that type would not work in a protoplanetary disk. Turbulence would prevent the disk from getting dense enough by stirring up material from the midplane. However, it should be noted that local gravity assisted growth is still a hot candidate for the growth at a stage where other processes fail to explain the growth (see e.g. Johansen et al., 2007). This issue will be taken up in the concluding Chapter 6.

An alternative, widely accepted growth scenario is the collisional coagulation of the dust. As collisions among dust grains and aggregates are most fundamental for this scenario, the relative velocities and the sources for these become important. These can be named as Brownian motion, differential settling, radial drift, and turbulence. *Brownian motion* is caused by the statistically distributed collisions with gas molecules that lead to a thermal, diffusive motion as first described by Einstein (1905). *Differential settling* is relevant for dust aggregates above the midplane of the disk, which then feel a component of the protostar's gravity acting in the direction of the midplane, preferentially causing larger aggregates to settle towards the midplane while the smaller ones better couple to the gas. *Radial drift* of dust grains and small aggregates is caused by the sub-Keplerian rotation velocity of the gas to which they are coupled. As the gravitational attraction of the central star is thus not fully compensated by the centrifugal force, they drift inwards (Weidenschilling, 1977a). *Turbulence* is an important source for relative velocities where dust feels the acceleration of the turbulent gas with ever changing eddies at different scales. As the dust does not instantaneously couple to the gas but has a certain coupling time due to inertia, aggregates develop a relative velocity with respect to the gas and – due to the aggregate-size dependence of the coupling time – among themselves (Ormel

[3]Planetesimal is an artificial name ("infinitesimal planet") for kilometer-sized bodies, which are regarded as the seeds for the planets. Although there are strong indications for the existence of these planetesimals (in particular the comets), it not fully clear if they really ever existed.

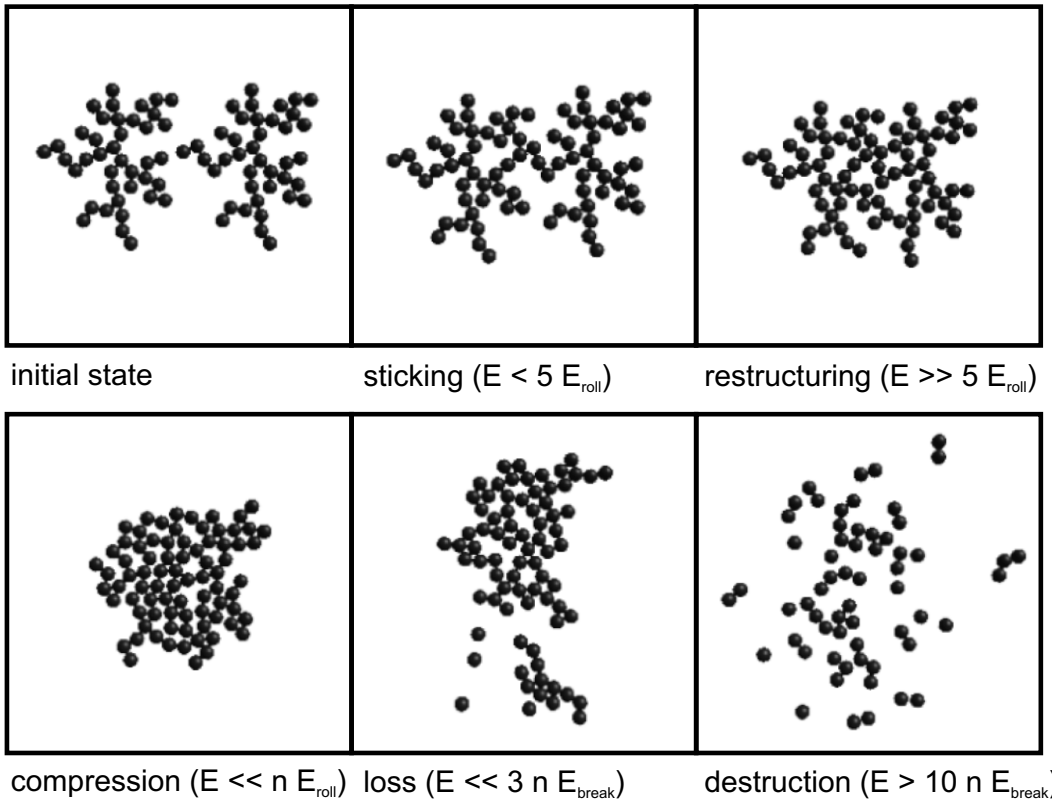

Figure 1.3: Molecular Dynamics simulations of collisions between two fractal aggregates as presented by Dominik et al. (2007) (based on Dominik and Tielens, 1997, Blum and Wurm, 2000). For small kinetic energies, the aggregates grow by hit-and-stick (top middle), while for increasing energy, the aggregates are compacted (top right, bottom left), or destroyed (bottom middle, bottom right). The important quantities which determine the thresholds between these regimes are the breaking energy $E_{\rm break}$ necessary to break a contact between two grains, and the rolling energy $E_{\rm roll}$ which is the energy that is dissipated when rolling one grain over another by a quarter of a circumference.

and Cuzzi, 2007). PPDs must be turbulent to explain the accretion efficiency (i.e. the luminosity) of the protostar, but the reason for this turbulence can be manifold. The most important source of turbulence is believed to be the magneto rotational instability (Balbus and Hawley, 1991).

All these different sources of relative velocities lead to collisions among dust grains and aggregates. For small collision velocities, dust grains stick to each other and they form fractal structures (e.g. Kempf et al., 1999, Blum et al., 2000). Sticking occurs as long as the relative velocity and the kinetic energy are small enough. For micrometer-sized dust grains, it has been experimentally shown that the sticking threshold is around 1 m s^{-1} (Poppe et al., 2000), while for collisions of fractal aggregates Blum and Wurm (2000, experiments) and Dominik and Tielens (1997, MD simulations) found an energy threshold of $3nE_{\rm break}$ (Fig. 1.3). Here, n is the number of the aggregates' dust grains (monomers in their case) and $E_{\rm break}$ is the energy necessary to break up the contact between two

grains. For collision energies exceeding $5E_{\rm roll}$ ($E_{\rm roll}$: energy for rolling over a quarter of the particle circumference), Blum and Wurm (2000) and Dominik and Tielens (1997) found a restructuring of the originally fractal aggregates, and for smaller energies they found sticking on first contact (hit-and-stick growth, Fig. 1.3, top middle). It is generally accepted that these growth processes (hit-and-stick and sticking with restructuring) are efficient for the growth up to 100 μm aggregates and we have a conclusive picture for this growth regime (see Blum, 2006 and references therein). Subsequent processes are not so far evolved and will be in the focus of this work. A brief review on the work done in experiments and computer simulations in this field will be given in the next two sections.

1.2 Experiments on Post-Fractal Dust Aggregation

The utmost objective for today's dust aggregation experiments is quite clear: protoplanetary dust aggregates may grow to approx. 100 μm sizes (previous chapter) but their further evolution is very speculative and needs to be verified in the laboratory. For a long time, people doing theoretical growth simulation in protoplanetary disks, assumed a sticking probability of unity such that the aggregation from micrometer-sized dust up to kilometer-sized planetesimals seemed to be straightforward (see Sect. 1.4). However, this is not the case as the following review on collision experiments will show.

In 1993, Blum and Münch showed that collisions among millimeter-sized, porous dust aggregates do not lead to sticking at all. In their experiments, they collided aggregates of $ZrSiO_4$ dust with a volume filling factor of $\phi = 0.26$ (defined as the volume of solid material divided by the aggregate volume) at velocities from 0.15 to 4 m s^{-1}, and found that the aggregates only bounce off as long as the collision velocity is less than approx. 1 m s^{-1}. By this, they showed that we are facing a wide range of bouncing for collision velocities from 0.15 to 1 m s^{-1}, if the $ZrSiO_4$ material they used can be regarded as representative for protoplanetary dust. Indeed, Langkowski et al. (2008) and Poppe et al. (2000) gave indications that the choice of material in terms of composition, shape and size distribution is not very important for the mechanical properties of the dust samples and that the results qualitatively remain the same. In a parameter range comparable to the bouncing experiments of Blum and Münch (1993), Heißelmann et al. (2007) confirmed the bouncing also for 5 mm-sized $\phi = 0.15$ aggregates at a collision velocity of 0.4 m s^{-1}. The samples used in these experiments were formed from 1.5 μm diameter SiO_2 grains, grown by random ballistic deposition (RBD) as described by Blum and Schräpler (2004).

For velocities above 1 m s^{-1}, Blum and Münch (1993) found that both $ZrSiO_4$ aggregates fragment into many smaller aggregates with a broad size distribution. The strength of fragmentation was found to increase with increasing velocity, which becomes evident by smaller fragments. In detail, they found that the aggregates fragment into a power-law size distribution with a constant slope but a velocity dependent pre-factor. Although Blum and Münch (1993) hypothesized a velocity dependent slope for the power-law slope, we will ignore this fact as it is not directly evident from their results and also not consistent with new results in this work (for details see section 4.2.2). It is to mention, that

there has also been earlier work on the fragmentation of porous aggregates or targets (e.g. Hartmann, 1978, Ryan et al., 1991) which were often used in theoretical models. However, from the perspective of protoplanetary dust aggregate collisions these results – although pioneering and appreciated – are not directly applicable as the constituent grains of the used aggregates were presumably much larger or even glued. This has a large impact on the aggregate strength and cannot be regarded as representative for protoplanetary dust aggregate analogs.

In terms of protoplanetary growth, these results of collisions between mm-sized aggregates are rather frustrating, but there are also few experiments which can in principle lead to the growth of larger bodies. These all have in common that a large aggregates grows by the accretion of considerably smaller bodies. One growth mechanism is the growth of a large target aggregate by small projectile aggregates or even single grains. As Poppe et al. (2000) showed, impacts of micrometer-sized dust grains onto larger targets (solid in their case) lead to sticking if the collision velocity does not exceed 1 m s^{-1}. Blum and Schräpler (2004) and Blum et al. (2006) used this effect to grow centimeter-sized aggregates out of single dust grains, impacting at velocities around 0.1 m s^{-1}, and in principle it would be no problem to grow to considerably larger bodies. However, it is questionable whether this process can lead to the growth of larger bodies in PPDs as the small grains will be depleted at one time such that the large bodies are not 'fed' any more.

Langkowski et al. (2008) and Blum and Wurm (2008) showed that growth is possible if a (sub-)millimeter-sized, porous or compact projectile impacts into a much larger and highly porous ($\phi = 0.07$ .. 0.15) aggregate. For velocities above a certain threshold (slightly mass dependent but roughly around 1 m s^{-1}), the projectile can penetrate into the target and be embedded into it. If the collision energy is too low, they found that the projectile does not penetrate deep enough and bounces off. In that case it will even be mass transferred from the target to the projectile. Both processes change the surface roughness and the porosity of the target. As Langkowski et al. (2008) showed, this surface roughness which is determined by the history of the target can be important. When they used the same highly porous target aggregates but changed the surface curvature such that it locally resembled the size of the projectile aggregates (see their Fig. 1c and 6 bottom), they found that collisions between the projectile and a 'hill' structure resembles that of a collision between similar-sized aggregates (no sticking but bouncing, Heißelmann et al., 2007) whereas an impact into a 'valley' leads to the sticking of the projectile. Conclusively, these effects alone would probably also not lead to ultimate growth as the target porosity in these collisions will decrease and in the next collision the projectile may not penetrate deep enough to be embedded.

Another potential growth mechanism involves the fragmentation of a porous projectile in a collision with a much larger and compact target. In that case, the projectile cannot destroy the target and it has been observed that parts of the projectile (in the order of 10 % in mass) stick to the target. This has first been described by Wurm et al. (2005b) in collisions between centimeter-sized projectiles with a larger, compressed dust target. In their impacts at velocities from 6 to 24 m s^{-1}, they found a growth of the target by up to 50 % of the projectile mass for velocities larger than 13 m s^{-1}. For the smaller velocities

the growth was in the order of 10 %. **?** followed up these experiments and showed that also a second and third impact onto the same spot still leads to the same growth. Exposing solid targets of different shapes to a continuous stream of sub-millimeter sized dust aggregates at 7.7 m s^{-1}, **?** showed, that these targets continue to grow until the particle stream is cut off. It is important to note that all these experiments were not performed under micro-gravity conditions but in all cases the projectile hit the target top-down in the direction of gravity. It is without doubt that this process also works under micro-gravity as S. Kothe, C. Güttler and J. Blum (unpublished data) have shown that partial sticking also occurs in single bottom-up collisions against gravity. However, it is still not clear whether the process is viable for multiple collisions. As Kothe et al. (unpublished data) observed, an upper limit for the total accretion per surface area is achieved because previously accreted dust may chip off the target and fall down. Both attempts are not realistic: top-down collisions yield an optimistic growth rate while bottom-up collisions lead to a pessimistic result. Currently ongoing micro-gravity experiments will hopefully solve this issue. Still, in case that this process works as proposed by **?**, a cyclic fragmentation process as proposed by **?** is necessary to produce small enough projectile aggregates which do not destroy the target aggregate – an underlying requirement for this process to work is a sufficient size ratio between destroyed projectile aggregate and growing target.

In conclusion, it is to say that current experiments on dust aggregation cannot decisively identify a process that inevitably leads to the growth of large, i.e. meter-sized, bodies. Various processes may still lead to growth in the millimeter- to centimeter regime (i.e. Langkowski et al., 2008, **?**) but these processes only work under certain conditions. It will be one of the major objectives of this thesis (Chapters 4 and 5) to decide which processes can ultimately lead to growth and how large these bodies can really grow.

1.3 Computer Simulations on Dust Aggregation

As mentioned before, the aggregation from single dust grains to approx. 100 μm aggregates is in principle understood – also with substantial help of computer simulations – and the problems now start at this point. Besides collision experiments, two methods in computational physics have the most potential to increase our knowledge about the further growth.

One method is based on *Molecular Dynamics* (MD) simulations, which have been applied to dust aggregate collisions in the pioneering work of Dominik and Tielens (1995, 1996, 1997). Using this method, each single dust grain is modeled in terms of motion and interactions with other grains (i.e. contacts), and the underlying contact properties, the energies E_{break} and E_{roll} to break and to roll a contact, were deduced from static and dynamic experiments with micrometer-sized SiO_2 spheres (Heim et al., 1999, Poppe et al., 2000). Although the sizes of aggregates simulated with MD are currently limited to approx. 10^5 particles (i.e. a 250 μm diameter aggregate of 1.5 μm diameter grains and with $\phi = 0.15$), the descriptive and also predictive power of the method is considerable. For collisions of fractal aggregates, Dominik and Tielens (1997) were able to distinguish

between regimes of sticking, restructuring, and fragmentation (see Fig. 1.3), which could quantitatively be confirmed by experiments of Blum and Wurm (2000). In spite of the limited number of computed dust grains, Paszun and Dominik (2008) made the approach to deduce macroscopic material parameters of aggregates and were able to reproduce the laboratory measurements of the compressive strength curve (Blum and Schräpler, 2004) and the sound speed (Blum and Wurm, 2008) of RBD dust aggregates. Wada et al. (2007, 2008, 2009) and Suyama et al. (2008) also performed MD simulations and were able to confirm the results of Dominik and Tielens (1997). Moreover, they pointed out that the porosity of these aggregates is an important parameter for the collisional outcome as it determines the number of bonds and found effective growth in ice-aggregate collisions with velocities up to 50 m s^{-1}. It must be noted that their assumed surface energy for ice aggregates was not measured in the laboratory but extrapolated with theoretical assumptions. Moreover, their simulations predict that growth is not only favored by the assumed stickiness of ice but also by their choice of smaller constituent grains, i.e. spheres with 0.1 μm diameter. Compared to an aggregate with large grains, an aggregate with small, and therefore more, constituent grains has more inner contacts. Although smaller grains have a smaller breaking energy (which scales with grain radius), the energy $3nE_{\mathrm{break}}$, which is the fragmentation threshold as predicted by Dominik and Tielens (1997), would be higher, strengthening the aggregate against fragmentation. Also here, the experimental verification is still pending.

The work of Paszun and Dominik (2008) is to empathize because this can be regarded as an approach to close the gap between MD simulations, which are confined to small aggregates, and *Smooth Particle Hydrodynamics* (SPH) simulations which are better suited for larger aggregates and rely on exactly the properties computed by Paszun and Dominik (2008). The SPH method is known in the astrophysical context e.g. for the simulation of collisions of larger, brittle bodies (i.e. planetesimals and asteroids, Benz and Asphaug, 1994, Benz, 2000) and has lately been modified for the treatment of porous bodies colliding at small velocities, e.g. meters per second (Sirono, 2004). In the porosity model developed by Sirono (2004), a dust aggregate is treated as a continuous medium whose behavior is determined by the bulk modulus, the compressive strength, the tensile strength, and the shear strength. Smoothing over micro structures (i.e. dust grains and void space) discrete mass packages, persisting the above mentioned properties, are the smallest unit of the SPH code. Based on experimental data for toner particles (Valverde et al., 1998), Sirono (2004) found collision parameters which are favorable for sticking collisions. One interesting example is that Sirono (2004) predicts sticking if the compressive strength is smaller than the other strengths (tensile and shear). In that case, the kinetic energy is absorbed by compression and the two colliding aggregates merge (Fig. 1.4). Qualitatively, this growth mechanism of embedding a small aggregate into a larger one can be confirmed by the experiments of Langkowski et al. (2008). Schäfer et al. (2007) were able to reproduce the main results of Sirono (2004) and realized that *(i)* the critical input parameters for the SPH code must be measured for realistic protoplanetary dust aggregate analogs (e.g. Blum and Schräpler, 2004) and that *(ii)* the code must be cross-calibrated with impact experiments of these. This calibration will be presented in Chapter 3.

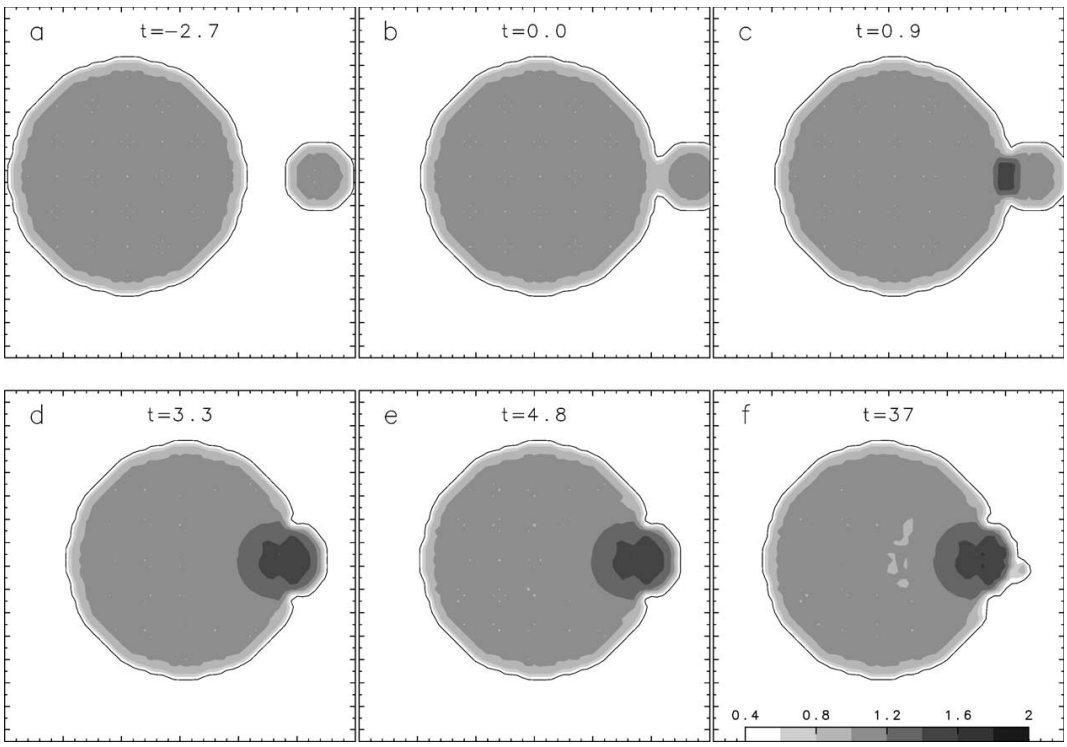

Figure 1.4: An SPH simulation of two colliding aggregates performed by Sirono (2004). If the strength parameters of the aggregate are appropriate, i.e. the compressive strength must smaller than shear strength and tensile strength, a smaller aggregate can be embedded in the larger one, leading to growth. The contour colors indicate densities in units of the initial aggregate density (0.1 g cm^{-3}) and the time in units of the passage time of a sound wave across the target radius (i.e. a/c_0, where a is the target radius and c_0 the sound speed). Details on the input parameters of this simulation can be found in Sirono (2004).

1.4 Coagulation Models

Collision experiments and simulation as described above (Sect. 1.2 and 1.3) only give an incomplete picture of the processes involved in the aggregation under realistic PPD conditions. These methods treat individual collisions where the input parameters are the sizes and porosities of the two colliding aggregates and their relative velocity. But without a complete study of the evolution of these aggregates, beginning with single dust grains, it is hard to say whether these parameters ever occur, i.e. which evolution path nature really takes.

This problem can be solved by coagulation models which compute the evolution of dust in the protoplanetary nebula. The pioneers in the field where Weidenschilling (1977b) and Hayashi et al. (1985) by constructing the minimum mass solar model as described above. Such model is the basis for any coagulation model as it determines the amount of mass (i.e. number density of aggregates) and the gas density (determines the collision velocities of aggregates) at a certain distance to the star. Hayashi et al. (1985) developed a full bottom-up model for the growth of (sub-)micrometer-sized dust grains into kilometer-sized

planetesimals, assuming that the dust coagulates into centimeter-sized aggregates while settling to the midplane, where it gravitationally collapses into planetesimals. The simple gravitational collapse for these aggregate sizes is unrealistic (Weidenschilling, 1995), but the focus here shall be on the first coagulation phase. Without better knowledge, Hayashi et al. (1985) assumed a sticking probability of unity up to aggregate sizes as large as 18 cm (the same assumption can e.g. be found in Mizuno et al., 1988), which is too optimistic as experiments in Sect. 1.2 show.

A more realistic approach was thus accomplished by Weidenschilling (1980, 1984). He pointed out that the results of coagulation are very sensitive to the assumed mechanical properties of the dust aggregates, thus, he implemented not only sticking but also erosion and fragmentation of the dust aggregates in his model. This was based on experimental data of Hartmann (1978, 1980, 1985), who performed laboratory impact experiments to study the effect of erosion, cratering, and fragmentation for dust targets as protoplanetary dust analogs. With this physics included, Weidenschilling (1984) found growth up to 0.1 – 1 cm aggregates. However, there was a severe lack of experimental data at that time and, as Weidenschilling (1984) emphasized, the picture was expected to change with more accurate collision physics included.

Promoted by new coagulation experiments and numerical collision models (see Sect. 1.2 and 1.3), recent growth calculations have become more and more realistic. Thereupon, solving the coagulation equation, Dullemond and Dominik (2005) found that the grain growth is way too efficient to be in agreement with infrared observation of T Tauri disks that show large amounts of small grains. A quasi-stationary aggregate size distribution as a result of a continuous growth-fragmentation cycle could be able to explain these findings. Following up this work, Brauer et al. (2008a) included a more realistic fragmentation model with a power-law size distribution, based on experimental results (Davis and Ryan, 1990, Blum and Münch, 1993) as well as on theoretical considerations (Tanaka et al., 1996). They found growth up to only a few millimeters although they implemented a fragmentation threshold of 10 m s^{-1}. It must be noted that they used the low density nebula as introduced above instead of the MMSN, which leads to much higher collision velocities. An also very interesting approach is the Monte-Carlo growth model of Ormel et al. (2007) who were able to treat the aggregate porosity as an additional free parameter and demonstrated it to be a very important one. They found the growth to be enhanced by an order of magnitude (e.g. aggregate sizes up to 10 cm in their model) before aggregates settle to the midplane. In a further work, Ormel et al. (2009) combined their coagulation model with an MD model to compute the individual collisional outcomes. This is a very appreciated approach because the included physics enormously increases the reliability of the coagulation model. They chose the environment of the interstellar medium with much lower densities, smaller aggregates, and higher collision velocities and found a growth- fragmentation cycle similar to the one proposed by Dullemond and Dominik (2005), Brauer et al. (2008a), and Zsom and Dullemond (2008) for the PPD environment.

1.5 This Thesis

The focus of this thesis is to understand from an experimental perspective the aggregation of dust from the 100 μm scale (non-fractal) up to sizes as far as dust can grow by aggregation. This goal cannot be achieved by only doing dust collision experiments but this approach has to go hand in hand with theory. Thus, it is also of importance that experimental results are being made available and applicable for state-of-the-art computer models to improve the understanding and interpretation of these.

In Chapter 2 the effect of bouncing aggregates will be reviewed in a new experiment. Since the experiments of Blum and Münch (1993) showed that macroscopic dust aggregates will not stick to each other but bounce even for velocities as low as 0.15 m s^{-1}, it is known that bouncing must be an important effect in the evolution of protoplanetary dust aggregates. Apart from not sticking, the effect was not further analyzed but it was obvious that a compaction of these highly porous dust aggregates might be possible in bouncing collisions. This was supported by the considerable loss of kinetic energy in the bouncing collision, which was in the order of 95 % in central collisions (Blum and Münch, 1993). Compaction decreases the porosity, which was nominated as a key parameter in the coagulation model by Ormel et al. (2007) as it influences the coupling of the dust to the gas and therefore the relative velocities of dust aggregates. Thus, in Chapter 2, an experiment is presented to measure the compaction of highly porous dust aggregates in bouncing collisions. The main advantage of this experiment compared to previous bouncing experiments (Blum and Münch, 1993, Heißelmann et al., 2007) is that the aggregate is observed over as many as 2 000 collisions where compaction becomes really visible. From the laboratory measurement, a recipe for the compaction in arbitrary collisions is derived which will be utilized in the forthcoming Chapters 4 and 5.

Chapter 3 deals with a new approach for a dynamic collision model of dust aggregates. The parameter range for possible dust aggregate collisions is huge and will probably never be fully covered by laboratory experiments. Moreover, aggregates under the conditions in PPDs may grow so exotic that they cannot be produced in the laboratory (i.e. meter-sized aggregates with extreme high porosity) or collision velocities can be too low to be achieved in the laboratory. These parameter ranges can be covered by a numerical collision model, if this is thoughtfully calibrated and trustworthy. Therefore, the aim in this chapter is to follow Schäfer et al. (2007) and calibrate an SPH collision model with static and dynamic laboratory experiments (also see Geretshauser et al., 2009). Macroscopic material parameters of protoplanetary dust aggregate analogs are measured as an input parameter for the computer code. Moreover, a simple collision experiment is performed to compare the laboratory results with results of a simulation with the same setup. Apart from developing the collision model, this approach helps in the understanding of the physics of protoplanetary dust aggregates which is the essential basis to perform extrapolations for laboratory experiments within a small parameter range.

There is a manifold of different laboratory collision experiments but these could so far not directly be utilized for any coagulation model in order to determine their impact on the growth on a global scale. So, in Chapter 4, existing and new collision experiments are

consolidated to construct a model that predicts the collisional outcome for any arbitrary collision that might occur. First, the possible collisional outcomes (i.e. types of sticking, bouncing, fragmentation) are classified and quantified according to what has been *observed* in laboratory collision experiments. Then, a model is constructed to arrange these outcomes within the parameter range (i.e. collision velocities, aggregates masses, aggregate porosities) that really *occurs* in protoplanetary dust collisions. The coverage of the full parameter range by the 19 included experiments is still quite small; therefore, wide extrapolations need to be performed which are based on the physics of protoplanetary dust aggregates as they were developed in previous experiments (e.g. Blum and Münch, 1993, Blum et al., 2006, Langkowski et al., 2008) and especially in Chapters 2 and 3.

In Chapter 5, this 'collision kernel' is implemented into a growth simulation based on the advanced Monte Carlo method developed by Zsom and Dullemond (2008). This method is capable of directly implementing the complexity of the experiment-based model without making too many simplifications. Apart from the coagulation kernel, the key ingredient that determines the growth are the relative velocities between the dust aggregates, and these are mainly determined by the gas density, i.e. the nebula model. As presented in Sect. 1.1, various models are under discussion and therefore all three presented models (MMSN, low density, high density) with a moreover variable turbulence are applied to have a wide range of different relative velocities. This model does not only compute the mass and porosity evolution of the aggregates, but also the parameters of collisions that really occur can be visualized. First, this is a measure for the quality of the results, as collisions that occur at parameters that were experimentally studied are more trustworthy than those where the collisional outcome is predicted by the extrapolation with a physical model that can be wrong. Secondly, this is an important feedback for the further development of the collision kernel. Collisions that are hardly backed by experiments will guide us to design and perform new experiments exactly where they are needed.

Chapter 2

Compaction in Multiple Collisions

René Weidling, Carsten Güttler, Jürgen Blum, Frithjof Brauer
The Astrophysical Journal, 696, pages 2036 – 2043[1]

Abstract

To study the evolution of protoplanetary dust aggregates, we performed experiments with up to 2 600 collisions between single, highly-porous dust aggregates and a solid plate. The dust aggregates consisted of spherical SiO_2 grains with 1.5 μm diameter and had an initial volume filling factor (the volume fraction of material) of $\phi_0 = 0.15$. The aggregates were put onto a vibrating baseplate and, thus, performed multiple collisions with the plate at a mean velocity of 0.2 m s^{-1}. The dust aggregates were observed by a high-speed camera to measure their size which apparently decreased over time as a measure for their compaction. After 1 000 collisions the volume filling factor was increased by a factor of two, while after $\sim$ 2 000 collisions it converged to an equilibrium of $\phi \approx 0.36$. In few experiments the aggregate fragmented, although the collision velocity was well below the canonical fragmentation threshold of $\sim$ 1 m s^{-1}. The compaction of the aggregate has an influence on the surface-to-mass ratio and thereby the dynamic behavior and relative velocities of dust aggregates in the protoplanetary nebula. Moreover, macroscopic material parameters, namely the tensile strength, shear strength, and compressive strength, are altered by the compaction of the aggregates, which has an influence on their further collisional behavior. The occurrence of fragmentation requires a reassessment of the fragmentation threshold velocity.

2.1 Introduction

The formation of planets in the accretion disks around young stars starts with the growth of (sub-)micrometer-sized dust grains. Embedded in the thin gas of the disk, the dust grains collide due to a Brownian relative motion and inevitably stick at the small collision

[1]Reproduced by permission of the AAS.

velocities (Blum et al., 2000, Krause and Blum, 2004). By this mechanism, dust grains can grow to fractal aggregates of ~ 100 μm before systematic drift significantly increases the collision velocities (Weidenschilling and Cuzzi, 1993). Numerical simulations as well as laboratory experiments have shown that for these increasing collision velocities, aggregates are restructured and grow to non-fractal but still very porous bodies (Dominik and Tielens, 1997, Blum and Wurm, 2000) so that growth can continue to larger sizes.

Once the aggregation has reached millimeter sizes, further growth due to sticking collisions between similar-sized dust aggregates slows down. Different experiments have shown that collisions of mm-sized aggregates result in bouncing or fragmentation: Blum and Münch (1993) performed collision experiments with $ZrSiO_4$ dust aggregates with a volume filling factor (the fraction of volume filled with material) of $\phi = 0.26$. For velocities exceeding ~ 1 m s^{-1} they found fragmentation as the dominant process, whereas for smaller velocities the aggregates bounced. Heißelmann et al. (2007) performed similar experiments with highly porous aggregates ($\phi = 0.15$) of $1 - 5$ mm diameter, which collided with a dusty target at a velocity of 0.2 m s^{-1} or with each other at 0.4 m s^{-1}. In both types of collisions the results were dominated by bouncing. Langkowski et al. (2008), performed impact experiments of the same highly porous dust aggregates of 0.2 to 3 mm diameter and different materials onto equally porous targets of 25 mm diameter. For intermediate velocities (0.5 to 2.5 m s^{-1}) and projectile sizes (0.5 to 2 mm) they found bouncing of the aggregate which was even more likely if the target was "molded" to a non-flat surface (see Fig. 1c in Langkowski et al., 2008). Smaller projectiles and lower velocities led to sticking of the dust aggregate on the target surface, whereas larger projectiles and higher velocities resulted in a deep penetration of the projectiles with no possibility for escape (Langkowski et al., 2008). All those experiments were performed without the influence of gravity (free fall, drop tower or parabolic flight) and in all experiments the coefficient of restitution ε (the velocity after the impact divided by the velocity before impact) was rather small ($\varepsilon \lesssim 0.4$).

Many experiments of Langkowski et al. (2008) and Heißelmann et al. (2007) were performed with the same sample material. While Langkowski et al. (2008) used different compositions (SiO_2 (monodisperse spheres), irregular SiO_2, and irregular diamond), Heißelmann et al. (2007) focussed on porous aggregates of 1.5 μm diameter SiO_2 monospheres. They were formed by the random ballistic deposition mechanism introduced by Blum and Schräpler (2004) and Blum et al. (2006), had a diameter of 25 mm, and a volume filling factor of $\phi = 0.15$. The dust samples could be cut or broken into mm-sized aggregates to perform the collision experiments. Although pure silica is not the most abundant material in protoplanetary nebulae, Blum et al. (2006) and Langkowski et al. (2008) showed that the material properties of the dust (composition, size distribution, and shape) do not significantly alter the experimental outcome. Therefore, we regard the material representative according to their mechanical properties of aggregates made of a broad collection of refractory grains and use the same material in the experiments presented below.

The motivation for this work is the explanation of the coefficient of restitution in the collisions of the described mm-sized SiO_2 aggregates, which is as low as $\varepsilon = 0.2$ in

aggregate-aggregate as well as in aggregate-target collisions (Heißelmann et al., 2007). This means that only a few percent of the translational energy are conserved, whereas the bulk of energy is dissipated in an unknown manner. Although the aggregates of Heißelmann et al. (2007) do not show apparent deformation after the collisions, the obvious assumption is that the energy is consumed by compression. In a microscopic view, compression results from the rolling, breaking and restructuring of inter-grain contacts which dissipates energy (e.g. Paszun and Dominik, 2008). In a macroscopic view, compression can be described by a compressive strength curve $p(\phi)$ (Blum et al., 2006, Blum and Schräpler, 2004, Güttler et al., 2009). The dissipated energy in this context is $\Delta E = p\,\Delta V$, where ΔV is the decrease of a volume inside the dust aggregate with internal pressure p.

In this work, we describe an experiment, in which a dust aggregate with ~ 2 mm diameter is placed on a vibrating baseplate and is thus forced to perform multiple collisions with this plate. Although this is not a zero gravity experiment, gravity is not important for the individual collisions as Heißelmann et al. (2007) have shown that even under microgravity conditions sticking never occurs at the relevant velocities of ~ 0.2 m s^{-1} and that the collision time is too short for substantial gravitational influence (see the image sequence in Figs. 4 and 5 of Heißelmann et al., 2007). The velocities are the same as those between aggregate and target in the experiments of Heißelmann et al. (2007). Performing multiple collisions, the cumulative compaction is larger than in a single collision and can, thus, be assessed.

In Sect. 2.2 we describe the experimental setup for the measurement of the aggregate compaction in multiple collisions. The results are presented in Sect. 2.3 and the relevance and consequences for dust aggregates in the protoplanetary nebula are discussed in Sect. 2.4.

2.2 Experimental Setup

As a starting material for a mm-sized, highly porous protoplanetary dust aggregate we chose the well-defined dust aggregates introduced and characterized by Blum and Schräpler (2004). They consist of 1.5 μm diameter monodisperse SiO_2 spheres, possess a volume filling factor of $\phi_0 = 0.15$ and were formed by random ballistic deposition (Blum and Schräpler, 2004). From these 25 mm aggregates we cut out cubes of $\sim$2.5 mm diameter with a compaction of the aggregate rim to a maximum of $\phi = 0.16$ (Heißelmann et al., 2007). Each small aggregate was weighed (mass m_0) and put into a box with plexiglass walls and an aluminum baseplate of 40×40 mm^2 size (Fig. 2.1). The aggregate was observed with a high-speed camera at a frame rate of 380 frames per second in back-light illumination while the box was vibrated in the vertical direction at a frequency of 100 Hz with a peak-to-peak amplitude of 0.4 mm for different durations (10 to 80 s). This led to a jumping motion of the aggregate and 200 to 2600 bouncing collisions, after which the aggregate (final mass $m_{\rm end}$) and the eroded material in the box (total mass of the debris $m_{\rm er}$) were again weighed.

In each image, the cross-sectional area and the position of the aggregate were measured.

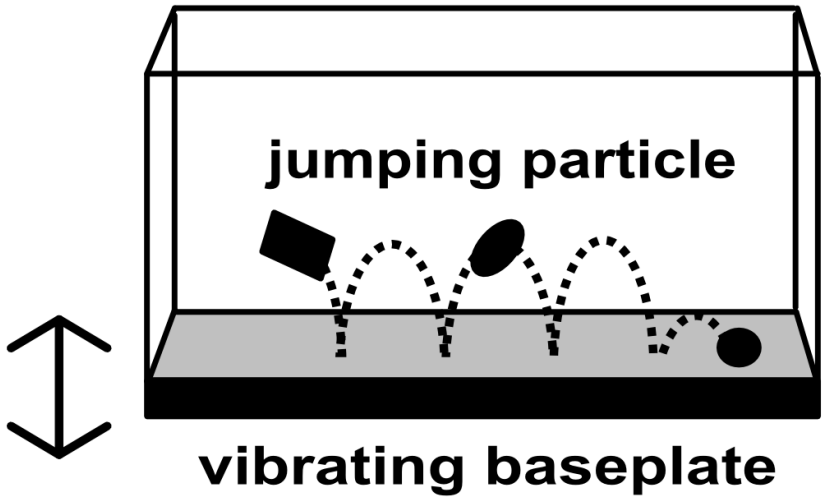

Figure 2.1: Experimental setup: The dust aggregate in the box is continuously colliding with the vibrating baseplate , while it is observed by a high-speed camera. The aluminum baseplate vibrates with a frequency of 100 Hz with a peak-to-peak amplitude of 0.4 mm.

The position measurements yield the number of collisions, which are underestimated by ∼20 %, because collisions near the edge of the box were not illuminated well. From the maximum height between two collisions the aggregate's velocity at the time of the collision can be determined assuming a free fall motion of the aggregate. Although the experiments were performed in air, the frictional effect of the ambient gas is negligible, as the maximum friction force $F_{\rm air} = 6\pi\eta a v = 9.5 \cdot 10^{-8}$ N is much smaller than the projectile's weight $F_{\rm grav} = mg = 3.9 \cdot 10^{-5}$ N. Here m, a, v, and η are a typical aggregate mass ($m \approx 4$ mg), the corresponding aggregate size ($a \approx 1.5$ mm), an average aggregate velocity ($v \approx 0.2$ m s^{-1}), and the viscosity of air ($\eta = 17.2$ μPa s); g is the gravitational acceleration.

As the velocity of the baseplate is unknown for the exact time of collision, a statistical collision velocity distribution is presented in Sect. 2.3. The imaged cross-sectional area of the aggregate was converted into a volume by assuming a sphere which is a coarse approximation at the onset of the experiments but a good approximation after $\sim$ 150 collisions (Fig. 2.2). A total of 18 individual bouncing experiments was performed (Table 2.1).

2.3 Results

In this section, we present the calculation of the distribution of collision velocities. We will then quantify the compaction of the dust aggregates and give an analytical approximation for practical use. Moreover, we will present further consequences of the structural change of the aggregates, namely the fragmentation of a dust aggregate at small velocities and the development of the coefficient of restitution.

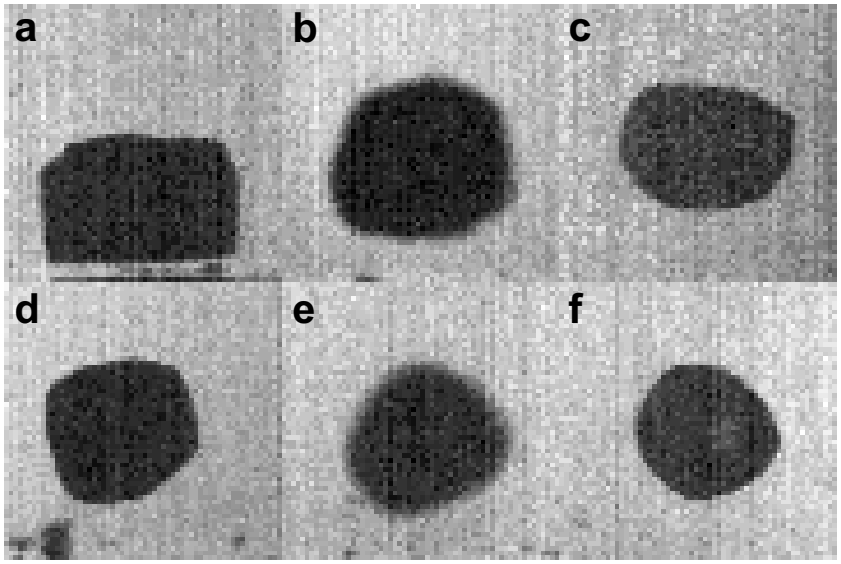

Figure 2.2: Sequence of a bouncing aggregate with ~ 150 collisions between two successive images. The aggregate is rounded first and is then clearly getting smaller. The width of the single frames is 4.6 mm. The example is taken from experiment 1 in Table 2.1.

2.3.1 Collision Velocities

The maximum height h of the dust aggregate between two collisions can be measured from the image with the highest aggregate position and it determines the aggregate's velocity at the time of impact, $v = \sqrt{2gh}$. As the impact time is only known with an error of 2.6 ms , as the maximum plate velocity of 0.13 m s^{-1} is in the same range as the collision velocity, and as the baseplate velocity rapidly changes, we make a statistical approach to calculate the distribution of collision velocities. The probability of a given plate velocity is given as

$$P(v)\,\mathrm{d}v = \nu \cdot (t(v) - t(v + \mathrm{d}v))\,, \tag{2.1}$$

where $\nu = 100$ Hz is the oscillation frequency of the plate and $\mathrm{d}v$ determines a velocity interval around v. $t(v)$ is the inverse velocity cosine function

$$t(v) = \frac{1}{\omega} \arccos\left(\frac{v}{A_0\omega}\right)\,, \tag{2.2}$$

where $A_0 = 0.2$ mm is the amplitude of the plate and $\omega = 2\pi\nu$ is the angular frequency. For an aggregate with velocity $v_{\mathrm{ag.}}$ plate velocities $v < -v_{\mathrm{ag.}}$ do not lead to a collision while the maximum plate velocity $v_{\mathrm{pl.}}$ is the likeliest. Thus, the velocity distribution of the plate (Eq. 2.1) is convolved with a linear collision probability, cropped for $v < -v_{\mathrm{ag.}}$ and shifted by $v_{\mathrm{ag.}}$. This is the velocity distribution of a single collision. The same procedure is performed for each collision and all normalized distributions summed up yield the overall velocity distribution for one experiment. Figure 2.3 shows the mean of the velocity distributions of all experiments (solid line) with the standard deviation (grey shaded area). All velocities are smaller than 0.35 m s^{-1}, the median velocity is

Table 2.1: Experimental results for all performed experiments. In the experiments marked with [a] the aggregate fragmented shortly after the given number of collisions.

experiment	initial mass m_0 [mg]	duration [s]	number of collisions	eroded mass [% of m_0]	mean collision velocity v [$\frac{\mathrm{m}}{\mathrm{s}}$]	resulting filling factor ϕ_{end}
1[a]	4.96	71	2400	20	$0.213^{+0.042}_{-0.055}$	0.50
2	3.62	33	1 200	9	$0.191^{+0.039}_{-0.055}$	0.32
3	3.90	43	1 400	0	$0.199^{+0.042}_{-0.055}$	0.38
4	2.68	30	1 050	34	$0.189^{+0.042}_{-0.055}$	0.25
5	2.64	13	550	9	$0.186^{+0.035}_{-0.052}$	0.28
6	2.88	14	250	12	$0.181^{+0.035}_{-0.049}$	0.21
7	2.10	10	200	24	$0.189^{+0.029}_{-0.047}$	0.16
8	2.34	15	500	-9	$0.186^{+0.037}_{-0.052}$	0.24
9	1.92	14	550	23	$0.206^{+0.039}_{-0.052}$	0.21
10	3.46	12	300	10	$0.189^{+0.035}_{-0.047}$	0.21
11	4.46	46	1 750	6	$0.194^{+0.045}_{-0.052}$	0.39
12	4.40	57	2 150	13	$0.191^{+0.039}_{-0.057}$	0.35
13	4.04	43	1 650	8	$0.196^{+0.042}_{-0.057}$	0.32
14	4.60	77	2 600	19	$0.201^{+0.039}_{-0.057}$	0.32
15[a]	5.86	47	1 700	14	$0.189^{+0.037}_{-0.055}$	0.34
16[a]	3.86	17	500	7	$0.164^{+0.037}_{-0.057}$	0.23
17[a]	4.44	53	2 300	10	$0.199^{+0.042}_{-0.057}$	0.32
18	4.88	44	1 600	8	$0.199^{+0.042}_{-0.052}$	0.34

0.19 m s^{-1}, while 50 % of all collisions are within 0.14 and 0.23 m s^{-1}. The velocity range for the individual experiments given in Table 2.1 is the 50 % range from the individual distributions.

2.3.2 Compaction of the Dust Aggregate

The prime objective of the experiments is to measure the increase of the averaged volume filling factor of the dust aggregate after n collisions, i.e.

$$\phi(n) = \phi_0 \cdot \frac{m(n)}{m_0} \cdot \frac{V_0}{V(n)}. \tag{2.3}$$

Here, m_0 is the initial mass of the aggregate, and V_0 is the initial volume calculated from m_0 by assuming an initial volume filling factor of $\phi_0 = 0.15$ (Blum and Schräpler, 2004). The volume $V(n)$ was calculated from the projectile's cross section $\sigma_{\mathrm{a}}(n)$ by assuming a sphere, thus, $V(n) = \frac{4}{3}\pi^{-1/2}\sigma_{\mathrm{a}}(n)^{3/2}$. The mass $m(n)$ slightly decreases due to erosion at the target. However, experiments with different durations did not show any change in the relative erosion (see Table 2.1) and most of the eroded fragments were sticking to the baseplate at the place of the first few collisions. Thus, assuming that the erosion took

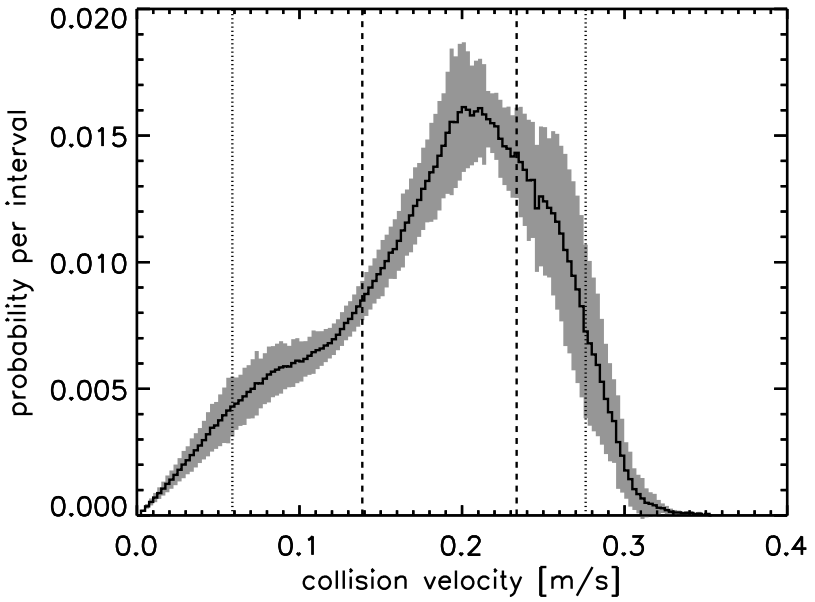

Figure 2.3: The mean of the impact velocity probabilities of all experiments (solid line) and the standard deviation from this distribution (grey shaded area). 50 % of the collision velocities are between the dashed lines, 90 % are between the dotted lines.

place in the very first collisions and was caused by the preparation of the sample, we take $m(n) = m_{\mathrm{end}}$.

The decrease of the volume of the dust aggregate over the course of collisions with the baseplate is obvious as presented in the image sequence of Fig. 2.2. From each experiment we calculated the volume filling factor $\phi(n)$ from Eq. 2.3 and took a boxcar average over 100 collisions to reduce stochastical scattering from the rotation of the aggregate. The mean filling factor and the standard deviation of all experiments are presented in Fig. 2.4 (solid line and grey shaded area).

The filling factor for $n < 150$ is greater than the initial filling factor of $\phi_0 = 0.15$, which is due to a combination of various systematic errors: The scaling is inaccurate if the aggregate is in the front or back of the box which results in an error of ± 3 % in ϕ, and the choice of the threshold for estimating the size yields an error of $^{+5\,\%}_{-0\,\%}$. In three experiments, the aggregate appeared from the smallest side in the beginning which overestimates ϕ, and the assumption of a sphere instead of the cuboid underestimates the filling factor until the aggregate is significantly rounded. Due to those uncertainties it is reasonable to regard the data only for $n > 150$ and assume $\phi(n = 0) = \phi_0$.

We give an analytic approximation which represents the filling factor for $n > 150$ (dashed line, Fig. 2.4):

$$\phi(n) = \phi_{\mathrm{max}} - \Delta\phi \cdot e^{-n/\nu} \tag{2.4}$$

with $\phi_{\mathrm{max}} = 0.365$, $\Delta\phi = \phi_{\mathrm{max}} - \phi_0$ and $\nu = 700$. Accounting for the systematic error in the collision number n, which is underestimated by 20 % (Sect. 2.2), we take $\nu = 850$ for

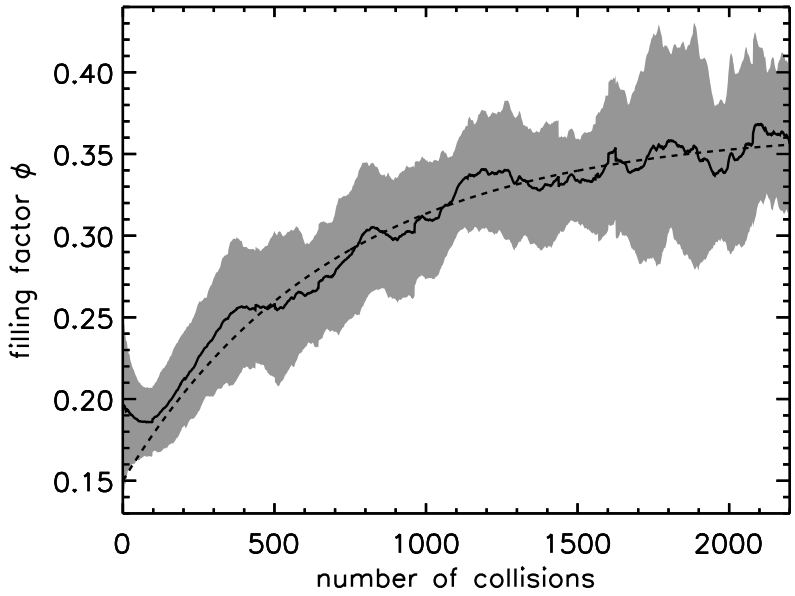

Figure 2.4: Mean increase of the volume filling factor from 18 individual experiments (solid line) and the standard deviation (grey shaded area). The dashed line represents an analytic approximation (Eq. 2.4) which converges to a filling factor of $\phi = 0.37$. The deviation for small collision numbers is determined by systematic errors in the experiments while the analytic curve is constrained to $\phi(n = 0) = \phi_0$.

practical use. For later application, we can calculate the volume of the aggregate (from Eqs. 2.3 and 2.4) as a function of the collision number

$$V(n) = \frac{\phi_0 \cdot V_0}{\phi_{\max} - \Delta\phi \cdot e^{-n/\nu}} \,, \tag{2.5}$$

where we ignore the mass loss in the first collisions and take $m(n) = m_0$.

In a very simple model, we assume that the compression is the cause for the loss of kinetic energy, thus

$$\left(1 - \varepsilon^2\right) \cdot \frac{1}{2} \cdot m \cdot v^2 = p \cdot \Delta V, \tag{2.6}$$

where ΔV for the first collision can be calculated by deriving Eq. 2.5 for $n = 0$ and $\Delta n = 1$:

$$\Delta V = \frac{V_0 \cdot \Delta\phi}{\phi_0 \cdot \nu}. \tag{2.7}$$

Thus, we can calculate the pressure in the aggregate (first collision) as

$$p = \frac{(1 - \varepsilon^2) \cdot m \cdot v^2 \cdot \phi_0 \cdot \nu}{2 \cdot V_0 \cdot (\phi_{\max} - \phi_0)} \,. \tag{2.8}$$

For an aggregate with $m = 4.24$ mg, $V_0 = 14.1$ mm^3, $v = 0.2$ m s^{-1}, and $\varepsilon = 0.2$ this yields a pressure of 3424 Pa. Using the compressive strength curve proposed by Güttler

et al. (2009) we can calculate the volume filling factor ϕ_c in the compressed volume ΔV_c to be

$$\phi_c(p) = \phi_2 - \frac{\phi_2 - \phi_1}{\exp\left(\frac{\lg p - \lg p_m}{\Delta}\right) + 1} \,. \tag{2.9}$$

For omindirectional dynamic compression, Güttler et al. (2009) developed the empirical parameters $\phi_1 = 0.12$, $\phi_2 = 0.58$, $\Delta = 0.58$, and $p_m = 1300$ Pa, which yields a volume filling factor $\phi_c = 0.43$, which is slightly higher than the end compression $\phi_{max} = 0.365$ of the aggregate.

The relation between the volume decrease of the agglomerate ΔV and the volume ΔV_c with compressed material is determined by the mass balance in the volume $(\Delta V + \Delta V_c)$:

$$\frac{\Delta V_c}{\Delta V} = \frac{\phi_0}{\phi_c - \phi_0} \tag{2.10}$$

If we assume that this relation holds for every collision, we can calculate the volume fraction of the compressed material for the equilibrium situation $n \to \infty$ to be:

$$\begin{aligned} f_c &= \frac{\int \Delta V_c \, \mathrm{d}n}{V(n \to \infty)} && (2.11)\\ &= \frac{\frac{\phi_0}{\phi_c - \phi_0} \cdot \int \Delta V \, \mathrm{d}n}{\frac{\phi_0}{\phi_{max}} \cdot V_0} && (2.12)\\ &= \frac{\phi_{max}}{\phi_c - \phi_0} \cdot \frac{V_0 - V(n \to \infty)}{V_0} && (2.13)\\ &= \frac{\phi_{max} - \phi_0}{\phi_c - \phi_0} && (2.14) \end{aligned}$$

Inserting the given values, we learn that the volume of the compressed material for $n \to \infty$ is 77 % of the end volume of agglomerate. Thus, the aggregate is inhomogeneously compacted and has an unaltered core of 61 % in radius.

2.3.3 Influence of the Compaction on the Mechanical Properties

The change of the volume filling factor must clearly have an influence on the mechanical properties of the dust aggregate. One related finding is that in four experiments the aggregate fragmented during the succession of impacts (Fig. 2.5). Those experiments are marked in Table 2.1 and do not show a clear systematic difference to the other experiments in which the aggregate did not fragment. The number of collisions and the filling factors in those experiments are rather high – except for experiment 16. A possible explanation is a decrease of the critical fragmentation velocity with increasing volume filling factor or, at least, an increasing breakup probability. Figure 2.5 shows very gentle fragmentation in contrast to the broad size distribution of fragments found at higher velocities (Blum and Münch, 1993). This breakup is usually found when fragmentation occurs at velocities near the fragmentation threshold. However, as the dependence on the number of collisions

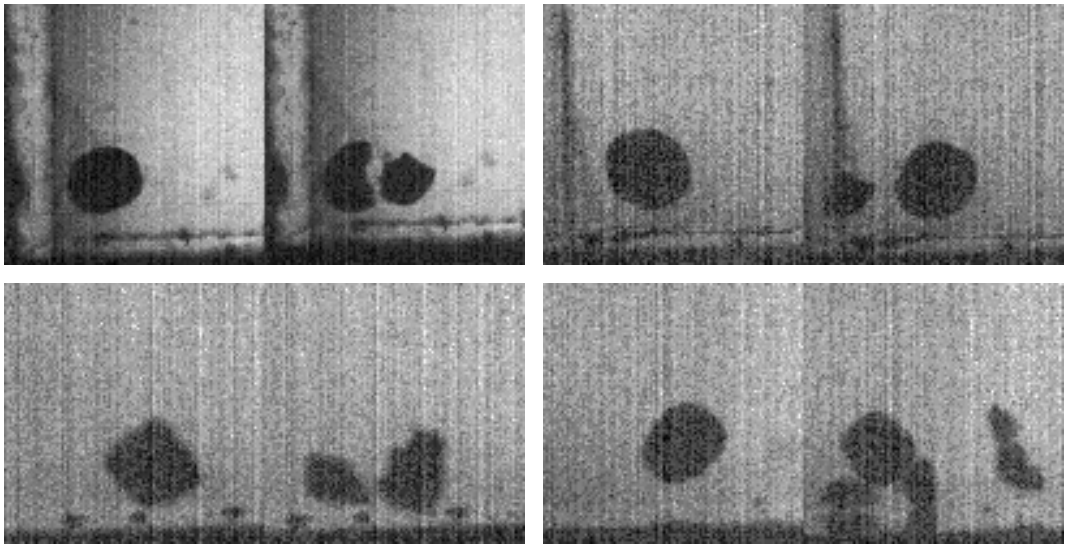

Figure 2.5: Four cases in which the aggregate fragmented (from top left to bottom right: experiments 1, 15, 16, and 17). The fragmentation is rather gentle, such that the aggregates only break into few fragments instead of producing a broad size distribution (see, e.g., Blum and Münch, 1993). The width of a single frame is 7.7 mm.

does not show a clear tendency, a second explanation is a general breakup probability for which we can give a rough estimate for mm-sized dust aggregates in low-velocity collisions as:

$$P_{\mathrm{frag}} = \frac{4 \pm 2}{\sum n_{\mathrm{coll}}} = (1.8 \pm 0.9) \cdot 10^{-4} \text{ per collision}, \tag{2.15}$$

where $\sum n_{\mathrm{coll}} = 22\,650$ is the total number of collisions in all experiments (Table 2.1).

Another influence of the structural change might be expected for the coefficient of restitution: the coefficient of restitution is a measure for the dissipation of energy and from Sect. 2.3.2 we know that compaction is a plausible dissipation mechanism. However, as the compaction is not constant over time, the coefficient of restitution is not expected to be either. As the mean baseplate velocity does not change with time, a change in the coefficient of restitution would result in a variation of the maximum height of the aggregate. Figure 2.6 shows that the jump height of the aggregate does only slightly increase with time for $n > 150$. A linear fit of all heights for $200 < n < 2\,000$ yields a mean slope of 40 μm / 1 000 collisions. The increasing height in the very beginning might be due to structural changes but concurrently the aggregate always collides with a broad side in these first collisions, which must have a substantial but unknown influence on the height.

2.4 Discussion

In this section we discuss the relevance for the protoplanetary nebula, namely, scaling the results for different sizes and velocities and estimating whether multiple bouncing

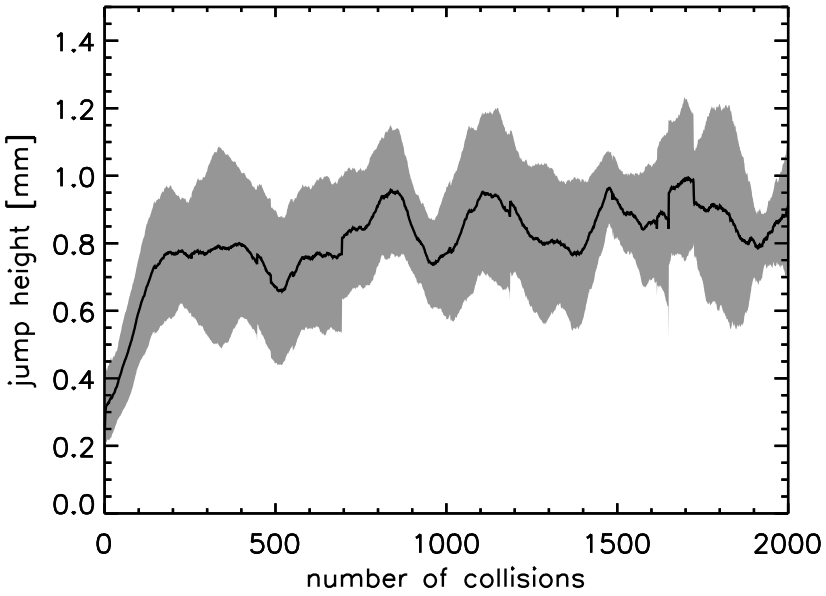

Figure 2.6: The jump height of the aggregate (mean of all experiments) over the number of collisions. The averaging was taken for as many experiments as possible: While for the first collisions all experiments could be utilized, for collision numbers of more than 2 000 only few experiments were available. For $n > 150$ the jump height only slightly increases with the number of collisions (also meaning compactness), which unexpectedly indicates a constant coefficient of restitution.

collisions can occur in a reasonable timescale. Furthermore, we discuss the consequences of the aggregate compaction for their further evolution.

2.4.1 Collision Model

We will develop a scaling relation for the aggregate compaction in size and collision velocity. From the momentum balance of the colliding aggregate, we can give the pressure in the aggregate as

$$p = \frac{(1+\varepsilon)\cdot m\cdot v}{\tau\cdot A} \tag{2.16}$$

$$= \frac{(1+\varepsilon)\cdot m\cdot v\cdot \nu}{\tau\cdot 4\cdot \pi\cdot a^2}\,, \tag{2.17}$$

where $(1+\varepsilon)\cdot m\cdot v$ is the change of momentum of the colliding aggregate, taking place within the collision time τ, and A is the contact area with the baseplate. For the contact area we make the assumption that the total surface of the aggregate interacted after ν collisions ($A = 4\pi a^2/\nu$), where ν is the e-folding width of the exponential function in Eq. 2.4. Indeed, this simple model of maximum compaction of a $1/\nu$ fraction of the aggregate volume only if a previously passive site on the aggregate surface is hit, yields the very same behavior as Eq. 2.4, which justifies this assumption (see Fig. 2.7). Thus, we can

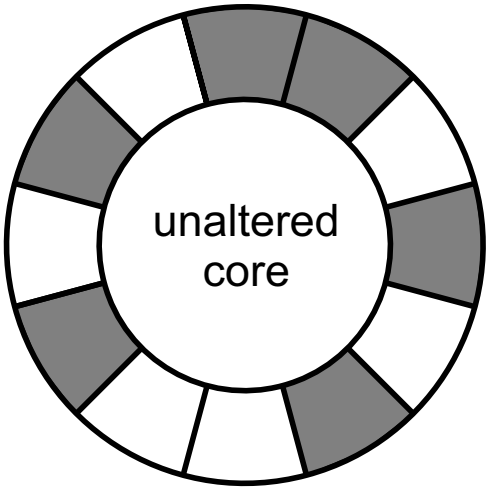

Figure 2.7: A simple 2D sketch of the compacted aggregate after some collisions. According to Eq. 2.14, 39 % of the aggregate radius are compacted around an unaltered core. The compacted rim is only compressed at the sites where the aggregate collided (grey volumes), and a second collision at the same site does not lead to further compaction. This simple model is capable to explain the increase of the volume filling factor according to Eq. 2.4.

combine Eqs. 2.8 and 2.17 to calculate the contact time

$$\tau = \frac{V_0 \cdot \Delta\phi}{(1-\varepsilon) \cdot v \cdot \phi_0 \cdot 2 \cdot \pi \cdot a^2} \,. \tag{2.18}$$

For the parameters of the $a = 1.5$ mm aggregate in Sect. 2.3.2 this leads to a contact time of $\tau = 8.9$ ms, which is a realistic result. Indeed, the collision time in the experiments of Heißelmann et al. (2007) can be confined to less than 20 ms (see their image sequence) and preliminary studies dedicated to measure the collision time of aggregates with $\phi \approx 0.35$ with a solid plate yield approximately 5 ms (Heißelmann et al., pers. comm.).

We approximate the situation by an elastic sphere with a Poisson number of zero, colliding with a wall and take the relation for the contact time from Hertz (1881) as

$$\tau = 3.85 \cdot \sqrt[5]{\frac{m^2}{v \cdot a \cdot G^2}} \,, \tag{2.19}$$

where G is the shear modulus of the sphere. Dintwa et al. (2008) compile the assumptions made in the Hertz model and value the importance of frictional contact, non-flat contact surface and large strains. As for the aimed accuracy in our model, the deviations from the Hertz model they found (and only for large strains) are rather small (within a few percent) so that we use Eq. 2.19 to calculate the shear modulus of the dust aggregate to be $G = 944$ Pa. Combining Eqs. 2.18 and 2.19, we get a scaling relation for the compression of an aggregate as

$$\Delta\phi_{\mathrm{sc}} \;=\; \frac{24.2 \cdot (1-\varepsilon) \cdot v \cdot \phi_0 \cdot a^2}{V_0} \cdot \sqrt[5]{\frac{m^2}{v \cdot a \cdot G^2}} \tag{2.20}$$

$$\propto \quad a^0 \cdot v^{4/5} \tag{2.21}$$

The upper velocity limit for this extrapolation is 0.56 m s^{-1} as for this velocity the volume filling factor $\phi_{\max} = \Delta\phi_{\rm sc} + \phi_0$ reaches the physical maximum of $\phi_{\rm RCP} \simeq 0.64$, which is the random close packing of spheres. This high filling factor is, however, unlikely to be reached in collisional compression, because the aggregate will then rather fragment. Thus, the model predicts a fragmentation threshold for ~ 0.5 m s^{-1} in multiple collisions. Velocities below a few mm s^{-1} lead to an insignificant compaction of $\Delta\phi_{\rm sc} \lesssim 0.01$.

We follow the same Hertzian ansatz to derive a scaling relation for the the e-folding collision number $\nu_{\rm sc} = 4\pi a^2/A$. The radius of the contact area A in the Hertz model is

$$s_0 = 0.86 \cdot \sqrt[5]{\frac{ma^2v^2}{\sqrt{G}}} \ . \tag{2.22}$$

Thus, the the e-folding collision number $\nu_{\rm sc}$ scales like

$$\nu_{\rm sc} \quad = \quad 5.42 \cdot \sqrt[5]{\frac{Ga^6}{m^2v^4}} \tag{2.23}$$

$$\propto \quad a^0 \cdot v^{-4/5} \tag{2.24}$$

With the scaling relations in Eqs. 2.21 and 2.24 we get $\Delta\phi_{\rm sc} = \Delta\phi \cdot \left(\frac{v}{0.2{\rm m/s}}\right)^{4/5}$ and $\nu_{\rm sc} = \nu \cdot \left(\frac{v}{0.2{\rm m/s}}\right)^{-4/5}$ and we are able to give the increase of the aggregate's volume filling factor in each collision as

$$\phi^+(\phi) = \frac{\phi_0 + \Delta\phi \cdot \left(\frac{v}{0.2\ {\rm m/s}}\right)^{4/5} - \phi}{\nu \cdot \left(\frac{v}{0.2\ {\rm m/s}}\right)^{-4/5}} \tag{2.25}$$

with $\phi_0 = 0.15$, $\Delta\phi = 0.215$, and $\nu = 850$ for $v \lesssim 0.5$ m s^{-1}. For a constant velocity this description is equivalent to Eq. 2.4 but it has the advantage that it is independent of the collision history of an aggregate (e.g. independent of n) and is therefore capable to account for non-constant bouncing velocities.

2.4.2 Collision Timescale

To value the importance of the bouncing and compacting collisions, we estimate the timescale on which subsequent collisions occur in the protoplanetary nebula. For simplicity we make the best-case assumption that the entire mass is in the relevant aggregate size. A comparable sharp size distribution was found for the first growth of fractal aggregates (Krause and Blum, 2004) but is unknown for the mm-size range. The mean collision timescale is then

$$\tau_{\rm c} = \frac{1}{nv\sigma} \ , \tag{2.26}$$

Table 2.2: The calculation of collision timescales τ_c for different solar-nebula models. For all models we use $\rho_d = 300$ kg m^{-3}, $r = 1$ AU, $T_0 = 280$ K, $M_\star = M_\odot$, and $\alpha = 10^{-5}$.

solar-nebula model	Σ_0 [g cm^{-2}]	δ	a [mm]	n [m^{-3}]	v [cm s^{-1}]	τ_c [years]	$\tau_c \cdot \nu$ [years]
Weidenschilling (1977b)	1700	1.50	1.50	$2.57 \cdot 10^{-1}$	0.27	1.62	1374
			2.66	$6.13 \cdot 10^{-2}$	20.00	0.03	24
Andrews and Williams (2007)	20	0.80	1.50	$2.79 \cdot 10^{-2}$	40.20	0.10	85
			0.11	$1.79 \cdot 10^{1}$	20.00	0.06	46
Desch (2007)	50500	2.17	1.50	1.40	0.02	4.00	3398
			77.50	$7.29 \cdot 10^{-5}$	20.00	0.03	24

where n is the number density of dust aggregates, $\sigma = 4\pi a^2$ is the collisional cross-section of two colliding aggregates, and v is the relative velocity. A broad size distribution does not extremely alter the effect of collisional compaction. If we consider such a wide size distribution and concentrate on the compaction of an aggregate at the high-mass end by collisions with smaller aggregates, the collision timescale decreases due to the increasing number density of smaller particles, $n \propto m^{-1}$, whereas the collision cross section and the relative velocity do not significantly change (see Fig. 2.8). The decrease in collision time is (partly) compensated by the smaller contact area in the collision (see Eq. 2.22) so that the number of collisions required to cover the whole surface of the large aggregate scales like $\nu \propto m^{-2/3}$. Thus, the relevant timescale for the total compaction scales as $\propto m^{1/3}$. Therefore the data given in Table 2.2 are upper limits. If we assume a gas-to-dust ratio of 100, we can give a general number density of dust aggregates in the midplane of the protoplanetary disk as

$$n = 1.88 \cdot 10^{-3} \frac{\Sigma_0}{\rho_d a^3} r^{\frac{\epsilon-3}{2}-\delta} \sqrt{\frac{M_\star}{T_0}\left(1 + \frac{a\rho_d r^\delta}{4\Sigma_0 \alpha}\right)} \text{ m}^{-3}. \tag{2.27}$$

This equation follows directly from the expressions for the dust particle density in the midplane, Eqs. A16 and A18 in Brauer et al. (2007). Here, Σ_0 is the surface density of the gas in units of [g cm^{-2}] at 1 AU in the disk, r is the distance to the star in [AU], δ and ϵ are the power indices for the surface density and temperature, respectively, $M_\star$ is the mass of the star in $[M_\odot]$, T_0 is the temperature at 1 AU in units of [280 K], and a and ρ_d are the radius in [mm] and mass density in [kg m^{-3}] of a representative dust aggregate. We assume that the dust particles are always in equilibrium between vertical dust settling towards the midplane of the disk and turbulent diffusion which mixes the dust up again into the higher regions of the protoplanetary disk (Dubrulle et al., 1995, Cuzzi and Weidenschilling, 2006). Larger particles settle closer to the midplane and, hence, lead to higher dust number densities. The last square root term in Eq. 2.27 accounts for this effect.

We assume to be in a nearly non-turbulent region in the midplane of the disk, the so-called dead zone. Due to the high dust opacity in the midplane the ionization degree in this region is too low for the magneto rotational instability to operate (Balbus and Hawley, 1991, Reyes-Ruiz, 2001). However, there are other sources for turbulence, such as Kelvin Helmholtz instability (Weidenschilling, 1979, Johansen et al., 2006), baroclinic

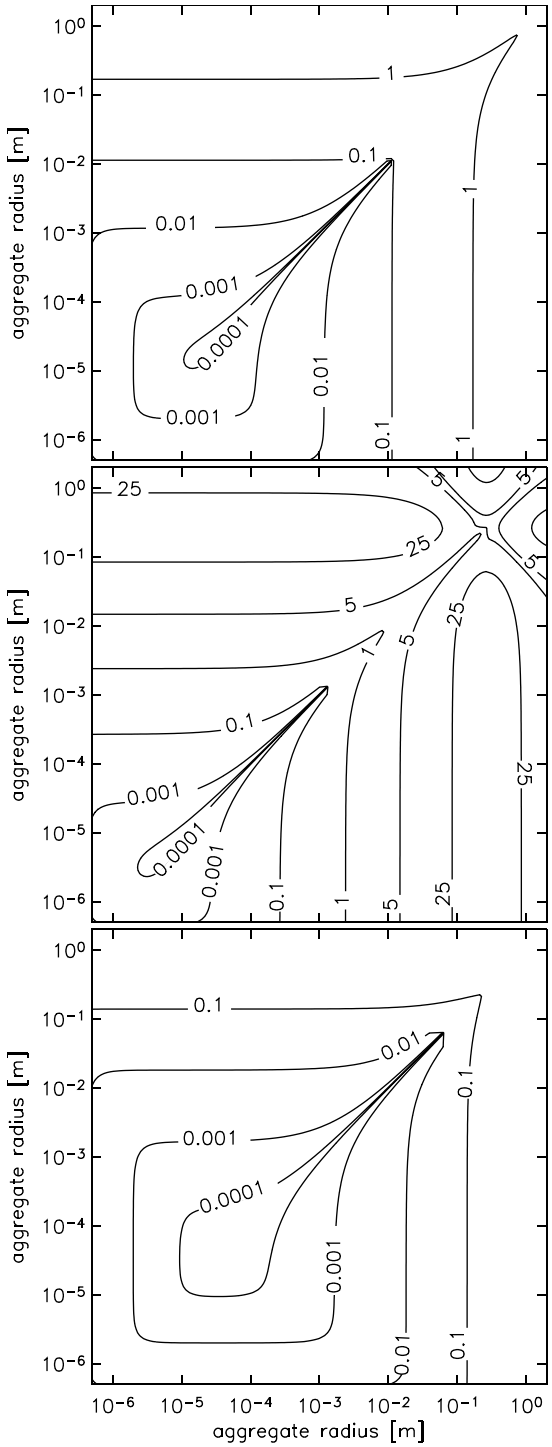

Figure 2.8: Relative velocities of dust aggregates in the protoplanetary disk midplane at 1 AU for different nebula models. Top to bottom Weidenschilling (1977b), Andrews and Williams (2007), Desch (2007). The contour lines indicate velocities in m s^{-1}. The turbulence value is $\alpha = 10^{-5}$ (dead zone), and, accounting for porosity, the bulk density of the aggregates is 300 kg m^{-3}. The applied values for the surface density can be found in Table 2.2.

instabilities (Klahr, 2004, Petersen et al., 2007), and possibly free charges mixed to the interior of the disk from the upper layers leading to a slight coupling of the midplane gas to the magnetic fields (Turner et al., 2007). Therefore, we assume a low, but non-zero turbulent α-value of $\alpha = 10^{-5}$ (Cuzzi and Weidenschilling, 2006). This low turbulent α-value influences the number densities of the dust as well as the relative velocities of solid particles in the disk (Ormel and Cuzzi, 2007).

We identify three solar nebula models which significantly spread the space of parameters in surface density. The first model is the minimum mass solar nebula (MMSN) model as calculated by Hayashi et al. (1985) and Weidenschilling (1977b). We adopt a second model based on recent interferometric millimeter observation of disks in the Taurus-Auriga and Ophiuchus-Scorpius star formation regions (Andrews and Williams, 2007). These observations suggest much flatter surface density distributions than in the MMSN model. Finally, we consider a revised MMSN model which accounts for planetary migration in the early solar system (Desch, 2007). In this new MMSN model, most of the mass is in the inner parts of the disk which leads to very high surface densities of several 10^4 g cm^{-2}, raising the question of gravitational instability. The surface densities at 1 AU and the power law indices δ of each disk model are given in Table 2.2. From these surface densities we can calculate the number density of aggregates (Eq. 2.27), also given in Table 2.2. For this calculation and also further on we use $T_0 = 280$ K, $\epsilon = 0.5$, $M_\star = M_\odot$, and $\rho_\mathrm{d} = 300$ kg m^{-3}.

Different surface densities lead to different relative particle velocities in the protostellar disk. Figure 2.8 shows the relative velocities in the midplane of the disk at 1 AU for all three models. For calculating these velocities, we followed Brauer et al. (2008a) and included Brownian motion, relative radial drift velocities, and relative velocities caused by turbulent gas motion as calculated by Ormel and Cuzzi (2007). We remark that these relative velocities may differ from earlier works due to the fact that we adopt more recent calculations of relative particle velocities in turbulence (Ormel and Cuzzi, 2007), and because the solid particle density used here is only 300 kg m^{-3} accounting for porous particle growth.

To deduce the mean collision velocities of two nearly equal sized aggregates with radius a, we calculate relative velocities in the interval $[\frac{2}{3}a, \frac{4}{3}a]$, accounting for a not perfectly sharp size distribution, and take the mean relative velocity in this interval. Thus, collision velocity, number density (Eq. 2.27) and cross section yield the collision timescale τ_c for different models. We also scale the size of the aggregate (cf. Sect. 2.4.1) so that we get a mean relative velocity of 0.2 m s^{-1}. For these sizes and velocities, we get collision timescales of less than a year. After the time $\tau_\mathrm{c} \cdot \nu$, the aggregates are significantly compacted and all these times are short in terms of planet formation.

2.4.3 Consequences for Further Protoplanetary Growth

We address three important consequences of the results of this work: *(i)* The aggregates are compacted and therefore change their surface-to-mass ratio. This has consequences for their coupling to the gas and their relative velocities. *(ii)* The compacted aggregate

possesses macroscopic parameters like tensile strength, compressive strength and shear strength different to the strengths of the non-compacted aggregate. *(iii)* The finding of unexpected fragmentation requires a review of the fragmentation threshold.

(i) The friction time, the time in which a protoplanetary dust aggregate is coupled to the surrounding rarified gas, is in the free molecular flow regime defined as (Epstein, 1924)

$$\tau_\mathrm{F} = \frac{m}{\sigma_\mathrm{a}} \frac{1}{\rho_\mathrm{g} \overline{v}} \,, \tag{2.28}$$

where ρ_g and $\overline{v}$ are the mass density and the mean thermal velocity of the gas. m and σ_a are properties of the dust aggregate, namely, its mass and its geometrical cross section $\sigma_\mathrm{a} = \pi a^2$. In Sect. 2.3.2 we found that the aggregate volume decreases by a factor of two within 1 000 collisions without changing its mass, which increases its friction time by a factor of 1.6. The friction time determines the aggregate's velocity relative to the nebular gas and, thus, relative to other aggregates (Weidenschilling and Cuzzi, 1993). As the size of the aggregate decreases from the compaction, its relative velocity would be that of an uncompacted aggregate with twice its diameter.

(ii) The macroscopic material parameters are clearly connected to the coordination number (number of contacts per dust grain) and thus to the volume filling factor. The compressive strength curve $\phi(p)$ (Blum and Schräpler, 2004, Blum et al., 2006, Güttler et al., 2009) gives the relation for the compressive strength as a function of the filling factor. Blum and Schräpler (2004) measured the tensile strength for differently-compressed dust aggregates and found an increasing tensile strength, closely linear to the coordination number. The shear strength (so far not measured for dust aggregates) is also believed to be depending on the filling factor (Sirono, 2004, Schäfer et al., 2007, Güttler et al., 2009). Güttler et al. (2009) perform Smooth Particle Hydrodynamics simulations using macroscopic material parameters to develop a collision model for protoplanetary dust aggregates. Sirono (2004) found the occurrence of fragmentation to be depending on the ratio between tensile strength and compressive strength. As the compressive strength is much more sensitive to compaction than the tensile strength (Blum and Schräpler, 2004), the compaction will clearly have an influence on the fragmentation threshold which is qualitatively shifted to smaller velocities.

(iii) The occurrence of fragmentation is rather surprising. Earlier experiments (Blum and Münch, 1993, Langkowski et al., 2008) show fragmentation for velocities $\gtrsim 1$ m s^{-1}, which is well above the maximum velocity of the experiments presented here (0.3 m s^{-1}). One possible explanation is a decreased fragmentation threshold due to the change of macroscopic parameters (see *(ii)*). However, Blum and Münch (1993) performed experiments with intermediate porosities ($\phi = 0.26$), still with a different material ($ZrSiO_4$), and found the same threshold. Explanations based on cracking and cumulative damage of the aggregate in multiple collisions are thinkable to reduce the aggregate strength but this – although of major importance – remains open for further investigation. A second possibility is a low but non-zero fragmentation probability, which would clearly be depending on velocity and material parameters, and has a finite value $P_\mathrm{frag} = 1.8 \cdot 10^{-4}$

per collision for $v \approx 0.2$ m s^{-1}. Although this probability disregards the history of the aggregate, it is so far the only possible treatment of the breakup in multiple collisions.

Chapter 3

Towards a Dynamical Collision Model

Carsten Güttler, Maya Krause, Ralf J. Geretshauser, Roland Speith, Jürgen Blum
The Astrophysical Journal, 701, pages 130 – 141[1]

Abstract

Recent years have shown many advances in our knowledge of the collisional evolution of protoplanetary dust. Based on a variety of dust-collision experiments in the laboratory, our view of the growth of dust aggregates in protoplanetary disks is now supported by a deeper understanding of the physics involved in the interaction between dust agglomerates. However, the parameter space, which determines the collisional outcome, is huge and sometimes inaccessible to laboratory experiments. Very large or fluffy dust aggregates and extremely low collision velocities are beyond the boundary of today's laboratories. It is therefore desirable to augment our empirical knowledge of dust-collision physics with a numerical method to treat arbitrary aggregate sizes, porosities and collision velocities. In this article, we implement experimentally-determined material parameters of highly porous dust aggregates into a Smooth Particle Hydrodynamics (SPH) code, in particular an omnidirectional compressive-strength and a tensile-strength relation. We also give a prescription of calibrating the SPH code with compression and low-velocity impact experiments. In the process of calibration, we develop a dynamic compressive-strength relation and estimate a relation for the shear strength. Finally, we define and perform a series of benchmark tests and find the agreement between experimental results and numerical simulations to be very satisfactory. SPH codes have been used in the past to study collisions at rather high velocities. At the end of this work, we show examples of future applications in the low-velocity regime of collisional evolution.

3.1 Introduction

3.1.1 Protoplanetary dust growth

The formation of planetesimals, the km-sized solid bodies whose further growth is controlled by mutual gravitational attraction, is still enigmatic. Collisions among the dust aggregates are controlled by Brownian motion, drift motions with respect to the gas of the protoplanetary disk, and turbulence in the gas (Weidenschilling, 1977a, Weidenschilling and Cuzzi, 1993). Once in contact, two dust grains experience a mutual van der Waals force (Heim et al., 1999). From the theoretical and experimental standpoints, it is evident that the (sub-)micrometer-sized protoplanetary dust grains initially undergo hit-and-stick collisions, which lead to the formation of fractal aggregates (Weidenschilling and Cuzzi, 1993, Blum et al., 2000, Krause and Blum, 2004). As the collision energy increases, due to increasing aggregate mass and collision velocity, dust aggregates undergo a restructuring phase, in which they acquire denser structures (Dominik and Tielens, 1997, Blum and Wurm, 2000, Wada et al., 2007, 2008, Weidling et al., 2009). Laboratory experiments showed that collisions among the dust aggregates result in fragmentation, i.e. in mass loss, if the impact velocities exceed ~ 1 m s^{-1} (Blum and Wurm, 2008). Depending on the disk model, this means that the direct collisional growth process ends (at the latest) at aggregate sizes for which this velocity is exceeded. For a minimum-mass solar nebula model (Weidenschilling, 1977b, Hayashi et al., 1985), this size is approximately 10 cm.

The further growth is still highly speculative. Wurm et al. (2001) and Blum (2004) proposed the accretion of collisional fragments by aerodynamic and electrostatic effects, respectively. Wurm et al. (2005b) and **?** showed experimentally that a fraction of a dust projectile can stick to a solidified larger dust target even at very large velocities. None of these processes, however, seem to work globally and under all circumstances so that very specific conditions are required for the dust aggregates to grow at high impact velocities. There is clearly a lack of understanding the detailed physics involved in the collisions between macroscopic dust aggregates of arbitrary composition and porosity. Without better knowledge of the collisional physics of these bodies, any attempt to model the formation of planetesimals as an aggregation process will have to fail.

3.1.2 Previous work

In the three previous papers of this series, we described the collisional physics of high-porosity protoplanetary dust aggregates up to the cm-size regime. In (Blum et al., 2006), we introduced a method to experimentally produce monolithic dust aggregates with diameters of 2.5 cm. By choosing either monodisperse spherical monomer particles, quasi-monodisperse irregular particles, or polydisperse irregular grains, we produced dust aggregates with volume filling factors (i.e. packing densities) $\phi = \rho/\rho_s$ of $\phi = 0.15$, $\phi = 0.11$, and $\phi = 0.07$, respectively (see Table 1 in Blum et al. (2006) for more details about the monomer-particle properties). Here, ρ and ρ_s are the aggregate and the monomer density. Static uniaxial compression of these dust samples revealed that the maximum

compaction for these high-porosity dust aggregates is $\phi_{\max} = 0.20 \ldots 0.33$, a value very close to the overall porosity found in comets. The tensile strengths of our dust samples were determined to $|T| = 200 \ldots 6\,300$ Pa, depending on the monomer properties and the compaction. Also these values are close to those found for comets. Langkowski et al. (2008) concentrated on low-velocity impacts into these high-porosity dust samples. We showed that sticking by penetration is the dominating process for impacts above a threshold velocity of ~ 1 m s^{-1} for projectiles in the mm-size regime and flat dust targets. For shallow penetration, i.e. for impacts below the threshold velocity, the projectiles bounce off, leaving a well-defined crater. It is obvious that the collisions result in the compaction of the target. Weidling et al. (2009) investigated the compaction for high-porosity mm-sized dust aggregates in bouncing collisions. Bouncing collisions among dust aggregates show considerable energy losses (Blum and Münch, 1993) so that it was natural to assume some degree of compaction. Weidling et al. (2009) found that – although a single collision leads only to very localized compaction of the dust aggregate – mm-sized dust aggregates in protoplanetary disks can reach volume filling factors of $\phi \approx 0.35$ within a few dozen years.

3.1.3 Objectives

All previous experiments (see Sects. 3.1.1 and 3.1.2) were limited by the experimentally available dust-aggregate sizes and morphologies and the achievable collision velocities. In the astrophysical context, the need for numerical simulations of collisions between dust aggregates of arbitrary composition, size and impact velocity arises from the fact that only a limited parameter space can be covered by experiments. The ongoing debate about threshold velocities for sticking, bouncing, compaction, and fragmentation as well as the fragment size distribution requires a thorough investigation of a wide range of collisions, varied over supposedly critical parameters, such as collision velocity, porosity, size, impact parameter, impact angle and shape of the colliding dust aggregates. An extensive parameter study of that kind is not feasible under laboratory conditions for the parameter ranges in question. Therefore, we aim to calibrate a Smooth Particle Hydrodynamics (SPH) code and validate this model thoroughly with a series of independent benchmark tests. Hence, the SPH code gains a deeper reliability and the conducted numerical simulations provide well-grounded insight into the physical behavior of dust aggregates.

3.2 SPH in Dust Collisions

SPH is a meshless Lagrangian particle method originally developed for astrophysical hydrodynamics applications. A detailed description of the original SPH method may, e.g., be found in Monaghan (2005). The SPH code we utilize for the simulations in this work and the underlying porosity model are introduced and described in full depth in Geretshauser et al. (2009). In the 1990s, SPH has been extended to model the elastic and plastic behavior of solids, see e.g. Libersky et al. (1993) and Randles and Libersky (1996). The

continuous solid objects are discretized into interacting mass packages called particles, which form a natural frame of reference for any deformation and fragmentation that may occur.

The SPH code solves the equations of continuum mechanics in Lagrangian form, in particular the continuity equation

$$\frac{\mathrm{d}\rho}{\mathrm{d}t} + \rho \frac{\partial v_\alpha}{\partial x_\alpha} = 0, \tag{3.1}$$

and the equation of motion

$$\frac{\mathrm{d}v_\alpha}{\mathrm{d}t} = \frac{1}{\rho} \frac{\partial \sigma_{\alpha\beta}}{\partial x_\beta}. \tag{3.2}$$

Here, Einstein's summing convention holds throughout and Greek indices denote spatial coordinates. The variables have their usual meanings, i.e., ρ denotes the density, v the velocity, and $\sigma_{\alpha\beta}$ the stress tensor. The latter is defined according to

$$\sigma_{\alpha\beta} = -p\delta_{\alpha\beta} + S_{\alpha\beta}, \tag{3.3}$$

consisting of a pressure part with pressure p and and a shear part given by the traceless deviatoric stress tensor $S_{\alpha\beta}$.

The deviatoric stress is defined by the constitutive equations. To model elastic behavior according to Hooke's law we adopt the approach by Benz and Asphaug (1994) for the time evolution of the deviatoric stress,

$$\frac{\mathrm{d}S_{\alpha\beta}}{\mathrm{d}t} = 2\mu \left(\dot{\epsilon}_{\alpha\beta} - \frac{1}{d}\delta_{\alpha\beta}\dot{\epsilon}_{\gamma\gamma} \right) + S_{\alpha\gamma}R_{\gamma\beta} + S_{\beta\gamma}R_{\gamma\alpha}, \tag{3.4}$$

where μ is the shear modulus and d denotes the dimension. The rotation rate tensor $R_{\alpha\beta}$ reads

$$R_{\alpha\beta} = \frac{1}{2} \left(\frac{\partial v_\alpha}{\partial x_\beta} - \frac{\partial v_\beta}{\partial x_\alpha} \right) \tag{3.5}$$

and the strain rate tensor $\dot{\epsilon}_{\alpha\beta}$ accordingly

$$\dot{\epsilon}_{\alpha\beta} = \frac{1}{2} \left(\frac{\partial v_\alpha}{\partial x_\beta} + \frac{\partial v_\beta}{\partial x_\alpha} \right). \tag{3.6}$$

This set of equations is closed by a suitable equation of state and describes the elastic behavior of a solid body.

In order to simulate also the plastic behavior of porous bodies, we adopt a modified version of the porosity model by Sirono (2004) (Fig. 3.1). According to this approach, plasticity is modeled within the equation of state, which is divided into three different regimes. In the first regime, plastic behavior is caused by compression that exceeds a critical limit, the compressive strength $\Sigma(\rho)$, while in the second regime, tension exceeds the tensile strength limit $T(\rho)$. In between these limits, the third, the elastic regime of

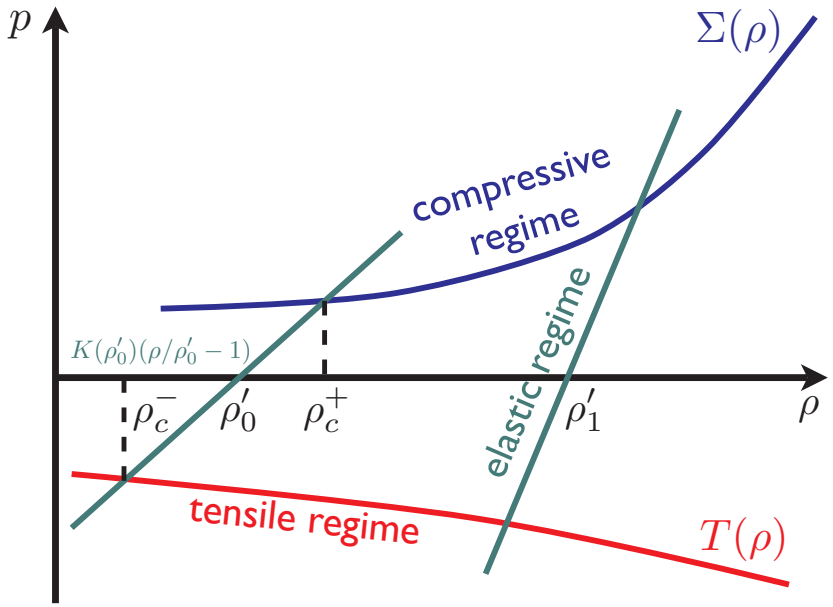

Figure 3.1: The modified Sirono porosity model is divided into the elastic, compressive and tensile regimes. The latter two are reached by exceeding the compressive and tensile strength, respectively, which leads to irreversible plastic deformation.

the material is described by a special version of the Murnaghan equation of state. Thus, the full equation of state reads

$$p(\rho) = \begin{cases} \Sigma(\rho) & \rho > \rho_c^+ \\ K(\rho'_0)(\rho/\rho'_0 - 1) & \rho_c^- \leq \rho \leq \rho_c^+ \\ T(\rho) & \rho < \rho_c^- \end{cases} . \tag{3.7}$$

The quantity ρ'_0 denotes the reference density, which is the density of the material without any external stress. ρ_c^+ and ρ_c^- are limiting quantities, where the transition between the elastic and plastic regime for compression and tension, respectively, takes place. Once these limits are exceeded, the material leaves the elastic path which represents the path where energy is conserved, and loses internal energy by following the paths of the compressive and tensile strength (Fig. 3.1).

3.3 Towards an Equation of State for Dust Aggregates

In this laboratory section, we will provide the macroscopic material parameters, which are necessary for the SPH model introduced in section 3.2. We recapitulate the tensile strength measurements of Blum and Schräpler (2004) and give an interpolation for different volume filling factors. The compressive strength for unidirectional (1D) compression was also measured by Blum and Schräpler (2004), while in this paper we will present

measurements on omnidirectional (3D) compression. Moreover, we will introduce a simple impact experiment, which will be used for calibrating the SPH model: A mm-sized glass bead (or a glass bead analog) impacts into a well-defined 2.5 cm dust sample at a collision speed of 0.1 to 1 m s^{-1}. The dust sample, consisting of 1.5 μm SiO_2 monodisperse spheres, was formed by random ballistic deposition (RBD) and has therefore a volume filling factor of $\phi_0 = 0.15$ (see Blum and Schräpler (2004) and references therein). The deceleration curve, penetration depth and impact duration of the glass bead are measured as well as the compression of the dust beneath the glass bead to compare these results with an impact computed by the SPH model.

3.3.1 Tensile Strength

In Blum and Schräpler (2004) and Blum et al. (2006), we reported on measurements of the tensile strength of dust samples of various constitutions (i.e. monomer size distribution, morphology, composition, volume filling factor). The best set of data was collected for the dust aggregates consisting of spherical 1.5 μm SiO_2 monomers (see above). For packing densities of $\phi = 0.15$, $\phi = 0.41$, $\phi = 0.54$ and $\phi = 0.66$, we found tensile strengths of $|T| = 1\,000$ Pa, $|T| = 2\,400$ Pa, $|T| = 3\,700$ Pa and $|T| = 6\,300$ Pa, respectively. To a good approximation, these values can be expressed by a relation of the form

$$T(\phi) = -\left(10^{2.8+1.48\,\phi}\right) \ . \tag{3.8}$$

This expression will be used throughout this paper for the packing-density-dependence of the tensile strength.

3.3.2 Static Measurement of Compressive Strength Curves

The compression curve of a given material tells us how the material behaves under an applied pressure Σ in changing its volume filling factor ϕ. If the material can be described by macroscopic parameters, the volume filling factor is representative for the material density and so the development of the compression curve $\phi(\Sigma)$ (cf. Eq. 3.7) is essential to establish a collision model and learn about collisions of protoplanetary dust aggregates.

Measurements of the compression curve were already performed by Blum and Schräpler (2004) and Blum et al. (2006). We will again focus on the dust samples made of 1.5 μm SiO_2 spheres, whose properties are compiled in Table 1 in Blum and Schräpler (2004). In the compression experiments of Blum and Schräpler (2004), a dust sample was fixed between two parallel glass plates, which were then pushed together with an increasing force. The measurement of the dust mass, dust volume, compression force, and, thus, pressure yield the compression curve $\phi(\Sigma)$. The force was applied in one direction, which is therefore called unidirectional compression. The dust sample flattens in the direction of the force but, at the same time, also expands in the other directions. For dust samples made of 1.5 μm SiO_2 spheres, this leads to an equilibrium filling factor of 0.33 for pressures exceeding 10^5 Pa. This compression curve is only applicable to protoplanetary dust

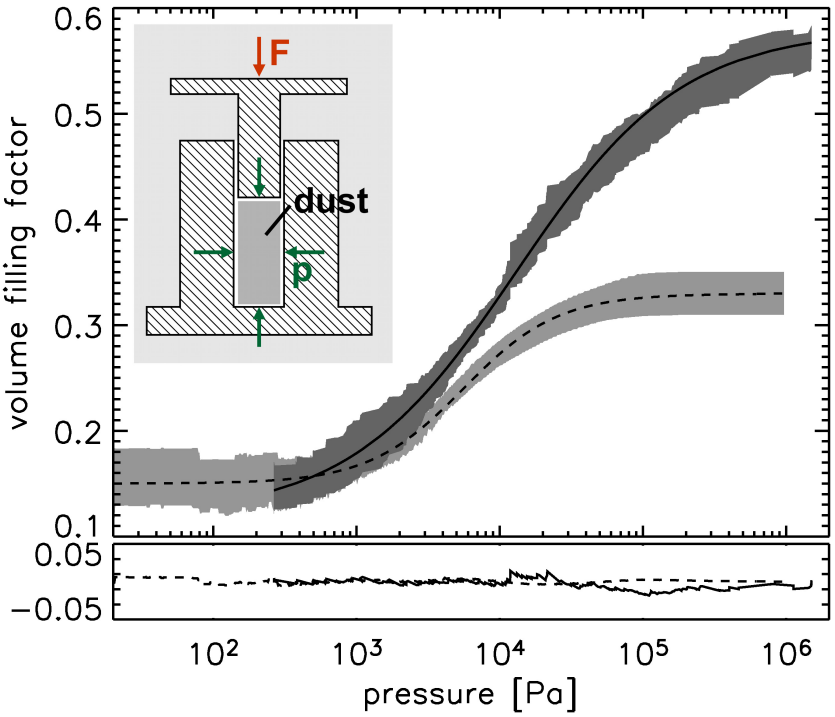

Figure 3.2: The omnidirectional (solid line) and unidirectional (dashed line) static compression curves and the standard deviations of the measurements (gray shaded areas). The upper plot shows the analytical approximations from Eq. 3.9 and Table 3.1, while the lower plot gives the deviation between approximation and measurement. The inset describes the setup for the omnidirectional measurement.

collisions, if the material compressed in the impact zone creeps sideways as it did in the static experiments. As we will show later by x-ray analysis of the compression next to an impact site, this is not the case.

Consequently, a second way to measure the compressive strength curve is to fix the dust sample at the sides with closed walls. In this case, the pressure cannot be released and acts from all sides, thus omnidirectional compression. We performed experiments in which we cut a cylindrical section from an RBD dust sample with a thin-walled plastic tube of 7 mm diameter. This cylindrical dust sample of approximately 1 cm height was then put into a 7 mm borehole in an aluminum block. Carefully pushing a piston into this borehole leads to an omnidirectional pressure onto the dust sample (see inset in Fig. 3.2). The setup was put onto a balance and the piston was loaded with weights of increasing mass. This weight force, divided by the piston area, yields the pressure Σ, while the mass and height of the dust sample determine the volume filling factor ϕ (Fig. 3.2). Due to the fact that the dust sample is not a frictionless fluid, force chains inside the sample might locally reduce the pressure. Thus, the pressure for the idealized compression curve can be slightly lower.

The solid line in Fig. 3.2 denotes an analytical approximation of the mean filling factor of nine individual experiments as a function of the applied pressure and the gray shaded area is the standard deviation of the measurements. The analytical function is based on

Table 3.1: Parameters of the analytical approximation for the two compression curves

	ϕ_1	ϕ_2	p_m [kPa]	Δ [dex]
unidirectional	0.15	0.33	5.6	0.33
omnidirectional	0.12	0.58	13.0	0.58

a Fermi distribution with logarithmic pressure in the energy term

$$\phi(\Sigma) = \phi_2 - \frac{\phi_2 - \phi_1}{\exp\left(\frac{\lg \Sigma - \lg p_\mathrm{m}}{\Delta}\right) + 1} \tag{3.9}$$

and is only valid for $\phi \geq \phi_0$. For pressures below $\Sigma(\phi_0)$ the dust aggregate behaves elastically. The parameters for the unidirectional and omnidirectional compression curve are given in Table 3.1. The bottom plot in Fig. 3.2 gives the deviation between the analytical approximation and the data, which is within $\phi_\mathrm{err} = \pm 0.02$. Often, the inverse function $\Sigma(\phi)$ is used (see Eq. 3.7), which is here

$$\Sigma(\phi) = p_\mathrm{m} \cdot \left(\frac{\phi_2 - \phi_1}{\phi_2 - \phi} - 1\right)^{\Delta \cdot \ln 10} \quad . \tag{3.10}$$

Compared with the unidirectional compression curve (dashed line) of Blum and Schräpler (2004), the filling factor also starts off at the original dust sample filling factor of $\phi_0 = 0.15$ (cf. Blum and Schräpler, 2004), but diverges from the unidirectional curve for pressures $p \gtrsim 10^3$ Pa. For those pressures, the filling factor is systematically higher, meaning on the other hand that the same filling factor is much easier to achieve if the pressure acts from all sides. So far there was no equilibrium filling factor found like in the case of the unidirectional compression experiments. The filling factor still significantly increases for the highest applied pressure of 10^6 Pa. However, the analytical approximation indicates an equilibrium for $\phi_2 = 0.58$, which is not far from random close packing of monodisperse spheres ($\phi \simeq 0.64$, see e.g. Torquato et al., 2000), the maximal possible compression without breaking the dust grains.

The new compression curve is still a static measurement. It is applicable for omnidirectional static pressures like the hydrostatic equilibrium inside planetesimal bodies. It is questionable if this compression curve is valid for dynamic collisions but it is a second attempt to assume that surrounding material, which does not interact in a collision, acts as a confining wall to the active impact volume instead of creeping sideways.

3.3.3 Deceleration Experiments

Experimental Setup

The experimental setup consists of a vacuum chamber (gas pressure ~ 0.5 mbar) in which a projectile is suspended on a thin fiber (Fig. 3.3) with negligible mass to prevent rotation

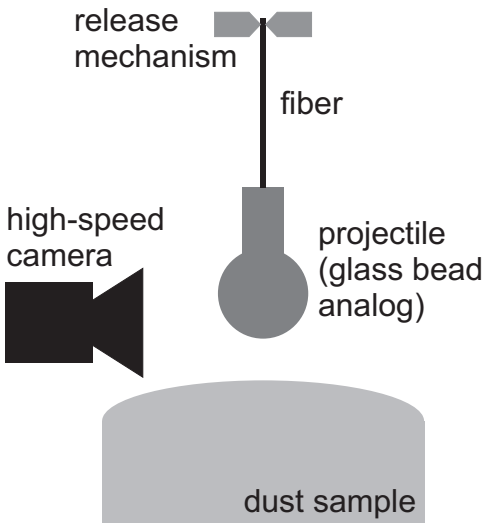

Figure 3.3: Setup for the deceleration measurement: An elongated projectile as a glass bead analog was dropped into the dust sample. Before dropping from a height of 1 to 40 mm, it was suspended on a fiber with negligible mass to avoid rotational motion. A high-speed camera observes the deceleration of the projectile.

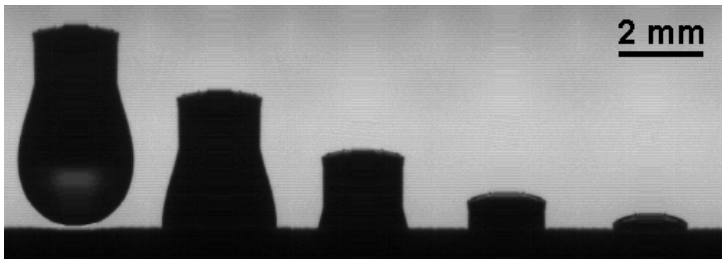

Figure 3.4: Image sequence of a decelerated projectile. The time between two images is 1.7 ms.

and lateral velocities. The distance between the suspended projectile and the surface of the dust sample determines the impact velocity v_0. The projectile consists of an elongated solidified epoxy droplet at the bottom and a cylindrical plastic tube at the top end. After the release of the projectile, it is accelerated by gravity and decelerated once it is in contact with the dust sample. The deceleration within the dust sample is observed by a high-speed camera (Fig. 3.4). From the deceleration curve of the projectile we can derive fundamental dynamic properties of the target dust aggregate.

The bottom shapes of the projectiles were spherical with radii of $a \approx 0.5$ mm and $a \approx 1.5$ mm and masses of $m \approx 1$ mg and $m \approx 30$ mg, respectively (see Table 3.2). The effective densities of the projectiles of $\rho = 2\,400 \ldots 3\,100$ kg m^{-3} match those of the astronomically relevant silicates, while the combination of low-density epoxy and plastic tube made sure that the top of the projectile was always visible to the camera even if the intrusion depth was larger than the projectile diameter. The high-speed camera was operated at a frame rate of 12 000 frames per second with a resolution of ~ 30 μm/pixel

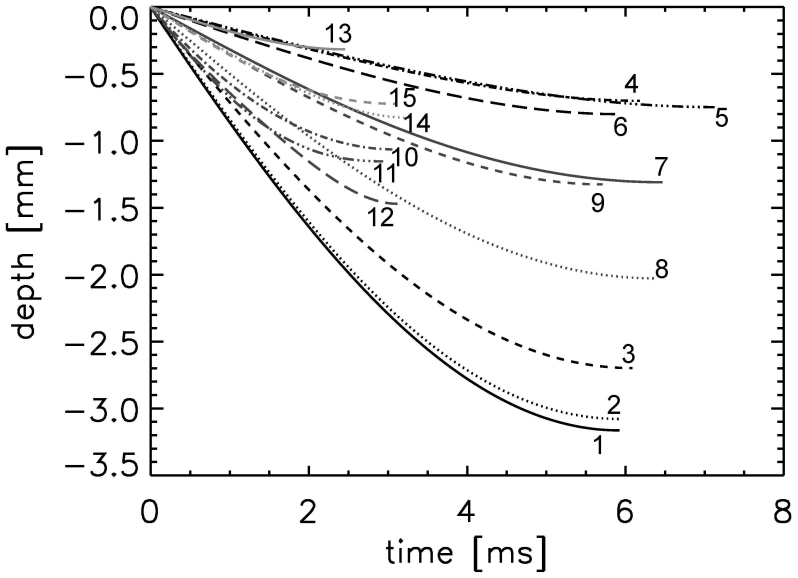

Figure 3.5: Fitted deceleration curves in absolute units. The experiment numbers at the deceleration curves confer to those in Table 3.2.

and the position of the upper edge of the projectile was measured with sub-pixel accuracy of ~ 3 μm. The first touch of the projectile with the surface of the dust sample marks the time $t = 0$ and can clearly be determined from the deviation of the trajectory compared to a free falling projectile. After its deepest penetration, the projectile bounces back (by ~ 100 μm) and oscillates in the vertical direction, which we will not take into account in the further discussion.

Experimental Results

We performed 15 impacts of our projectiles into the porous dust samples, which are compiled in Table 3.2. The time-resolved deceleration data $h(t)$ were cleaned from gravitational influence by adding $\frac{1}{2}gt^2$ to the negative intrusions so that the gravity-independent deepest penetration depth D and stopping time T could be determined. The intrusion curves were normalized in space and time through $h'(t') = h(t)/D$ and $t' = t/T$ so that $h'(t' = 0) = 0$ (first contact) and $h'(t' = 1) = -1$ (deepest intrusion), and can then be well represented by a sine function

$$h'(t') = -\sin\left(t' \cdot \frac{\pi}{2}\right) \ . \tag{3.11}$$

Alternatively, a fourth order polynomial with only one free parameter was used for fitting the data, where the mean standard deviation between the fit and the N data points $\sigma = \sqrt{\frac{1}{N}\sum_{i=1}^{N}(h'(t'_i) - h'_i)^2}$ amounts to only 2 – 4 μm in absolute units (cf. Table 3.2). Although the standard deviation for the sine function is rather of the order of 10 μm, we take the sine function because it has no free parameter and the standard deviation is

Table 3.2: Experimental results of the deceleration experiments.

experiment number	projectile diameter $2 \cdot a$ [mm]	projectile mass m [mg]	effective projectile density [kg/m^3]	impact velocity v_0 [m s^{-1}]	penetration depth D [mm]	stopping time T [ms]	standard deviation σ for polynomial [μm]	standard deviation σ for sine [μm]
1	2.73	25.7	2 412	0.89	3.16	5.92	2.43	21.48
2	2.94	32.0	2 404	0.85	3.08	5.93	2.99	22.64
3	2.77	26.4	2 372	0.73	2.70	6.09	1.87	17.29
4	2.94	32.0	2 404	0.17	0.70	6.18	4.63	10.78
5	2.94	32.0	2 404	0.16	0.75	7.13	2.84	7.69
6	2.94	32.0	2 404	0.20	0.80	5.92	2.96	8.95
7	2.94	32.0	2 404	0.32	1.31	6.47	1.62	2.53
8	2.77	27.6	2 480	0.50	2.03	6.38	1.82	3.57
9	2.77	26.4	2 372	0.37	1.33	5.71	3.65	6.26
10	0.99	1.5	2 854	0.67	1.06	3.09	3.48	27.77
11	0.99	1.5	2 854	0.76	1.15	2.94	1.41	23.24
12	0.99	1.5	2 854	0.79	1.47	3.12	14.29	5.62
13	0.85	1.0	3 109	0.19	0.32	2.46	1.94	3.79
14	0.85	1.0	3 109	0.35	0.83	3.28	2.60	11.15
15	0.85	1.0	3 109	0.36	0.72	3.11	2.71	3.73

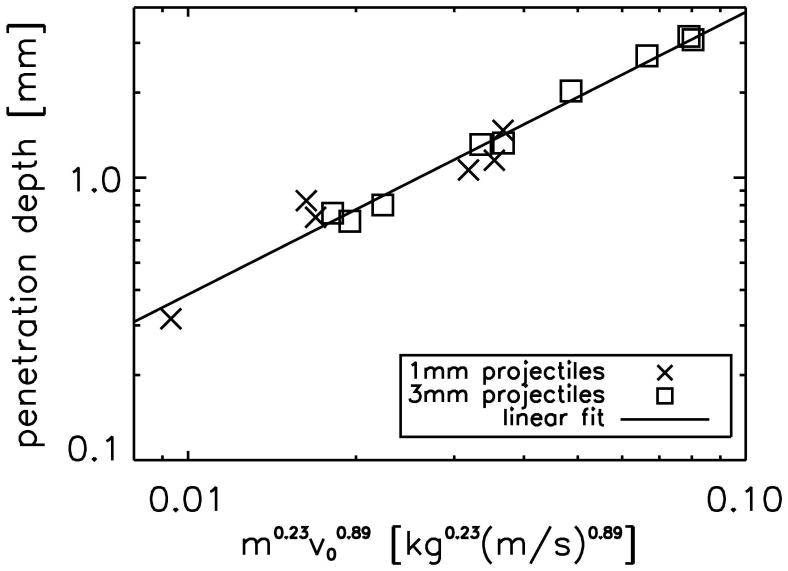

Figure 3.6: The best relation for the penetration depths from a χ^2 test yields a dependence of $D \propto m^{0.23} v_0^{0.89}$. The intuitive relation $D \propto mvA^{-1}$ is possible within the uncertainties.

still less than the pixel size of 30 μm. In few experiments, the 1 mm projectiles canted over before coming to rest. In these cases, the data was used as long as reliable and the remaining deceleration curve and, thus, the penetration depth was extrapolated.

Figure 3.5 shows all measured deceleration curves in absolute units. Different intrusion depths and stopping times can clearly be distinguished in this plot. The intrusion depths increase with increasing impact velocities (i.e. with the absolute values of the initial slopes of the curves), while the stopping times are rather constant for one projectile size ($T \sim$ 6 ms for 3 mm projectiles [nos. 1-9 in Fig. 3.5] and $T \sim 3$ ms for 1 mm projectiles [nos. 10-15 in Fig. 3.5]) and, thus, independent from the impact velocity v_0. A χ^2 test yielded the best-fitting power-law relation between the penetration depth, impact velocity and mass of the form

$$D = \gamma_\mathrm{D} \cdot m^{\alpha_\mathrm{D}} \cdot v_0^{\beta_\mathrm{D}} \ , \tag{3.12}$$

with $\alpha_\mathrm{D} = 0.23 \pm 0.13$, $\beta_\mathrm{D} = 0.89 \pm 0.34$, and $\gamma_\mathrm{D} = (3.86 \pm 0.11) \cdot 10^{-2}$ $\mathrm{kg}^{-0.23}\mathrm{m}^{0.11}\mathrm{s}^{-0.89}$ (Fig. 3.6). The respective errors denote the 1σ uncertainties. A more intuitive relation would be $D \propto mv_0A^{-1}$, with $A = \pi a^2$ being the cross section of the projectile. This relation has a clear physical meaning as the penetration depth is determined by the quotient of the momentum mv_0 as driving force and the cross sectional area A as resistive parameter. With $\alpha_\mathrm{D} = \frac{1}{3}$ and $\beta_\mathrm{D} = 1$ being possible within the uncertainties, the linear relation $D \propto mv_0A^{-1} \propto \rho_\mathrm{p}^{1/3} a v_0$ is also possible. However, constraining the exponent δ_D as $D \propto \rho_\mathrm{p}^{\delta_\mathrm{D}}$ in Eq. 3.12 was unfortunately not feasible due to the too small variations in the effective projectile density ρ_p (cf. Table 3.2).

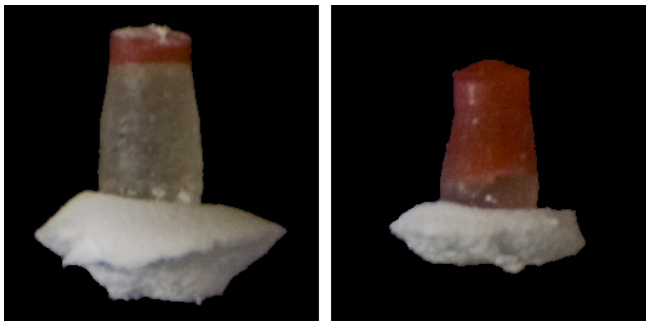

Figure 3.7: Dust sticks to the projectiles after pulling them out of the dust sample. This is an indication of compacted material under the projectile as will be confirmed in Sect. 3.3.4.

For the stopping time, we found

$$T = \gamma_T \cdot m^{\alpha_T} \cdot v_0^{\beta_T} \tag{3.13}$$

with $\alpha_T = 0.23 \pm 0.08$, $\beta_T = 0.01 \pm 0.23$, and $\gamma_T = (6.77 \pm 0.20) \cdot 10^{-2}$ $\mathrm{kg}^{-0.23}\mathrm{m}^{-0.01}\mathrm{s}^{1.01}$ was found for the stopping time.

After pulling the projectiles out of the dust sample, dust stuck to the surface with which it had been in contact before (Fig. 3.7). With the preliminary assumption that this is compacted dust and the layer where it broke off is the transition from compacted to non-compacted dust (transition in tensile-strength), this gives an indication for the compressed volume which will be analyzed in detail in the forthcoming section.

3.3.4 Dynamic Compression Experiments

Experimental Setup

In order to investigate in more detail the compression behavior of the dust aggregates by collisions, we performed impact experiments with subsequent x-ray micro-tomography measurements to analyze the degree of compaction.

Under vacuum conditions we dropped a single glass spherule with a diameter of ~ 1 mm from a given height of ~ 75 mm into an RBD dust sample within a plastic tube with 7 mm diameter. To ensure the sphere to preferably hit the center of the dust sample within the narrow plastic tube, the released projectile was guided by falling through a tube. Due to friction and collisions with the tube's walls the impact velocity of (0.8 ± 0.1) m s^{-1}, that was independently measured by high-speed imaging in 10 drops, is much lower than expected from free fall. However, the velocity in the specific experiment was not measured and can well be in the lower range of the error. From comparison of the observed penetration depth (see Fig. 3.9) with the results in Fig. 3.6 we expect a velocity of $v = 0.65$ m s^{-1}, which we will use for the further study.

For analyzing the density distribution of the dust sample cutout with the embedded glass sphere, the dust sample was scanned by an x-ray micro-computer-tomograph (Micro-CT SkyScan 1074) at the University of Osnabrück. The dust sample was positioned

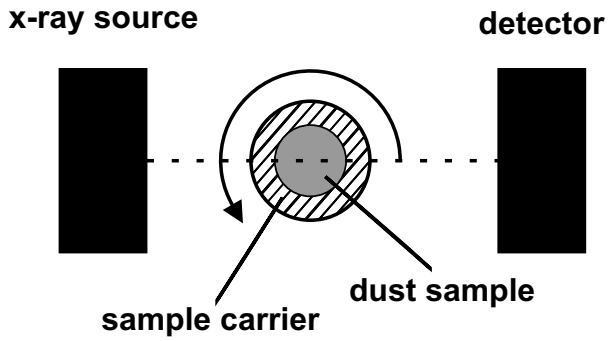

Figure 3.8: Setup of the x-ray micro-CT measurement: the sample is rotated between an x-ray source and a detector. A 3D density reconstruction can be computed from the transmission images.

on top of a rotatable sample carrier between the x-ray source and the detector (CCD camera) (Fig. 3.8). While rotating stepwise around by 360°, 400 transmission images were captured. Based on this data set, a 3-dimensional density reconstruction was calculated by the SkyScan Cone-Beam Reconstruction Software provided with the x-ray micro-CT instrument.

Experimental Results

In the following we present the results of two impact experiments. Further experiments with differently sized spheres and different impact velocities are intended. To visualize the spatial density distribution of the observed dust sample with the impacted glass sphere, the 3-dimensional reconstruction data was cylinder-symmetrically averaged with the vertical axis aligned with the sphere center. Figure 3.9 displays the mean volume filling factor as a function of height and radius, whereas the data is mirrored with respect to the vertical center line of the diagram. The color gradient from yellow to light blue underneath the impacted sphere (red color: saturated density values of the considerably denser glass spherule) clearly shows the densification of the porous dust sample with an initial volume filling factor of $\phi_0 \approx 0.15$. The compressed area, emphasized by overplotted contour-lines, is located almost cylindrically shaped beneath the sphere and extends only slightly to the lateral borders of the sphere. Thus, the assumption of an omnidirectional compression curve, made in Sect. 3.3.2, seems to be justified.

Analysis of the distribution of occurring volume filling factors related to their fraction of volume within an uncompressed dust sample provides a Gaussian-shaped distribution with a mean value of $\phi \approx 0.15$ (Fig. 3.10). Figure 3.11 (top) shows the volume fraction (normalized by the sphere volume) of volume filling factors, which we determined only regarding the compacted volume underneath the impacted sphere for the two impact experiments. In both curves the most prominent volume filling factor is around $\phi = 0.23$,

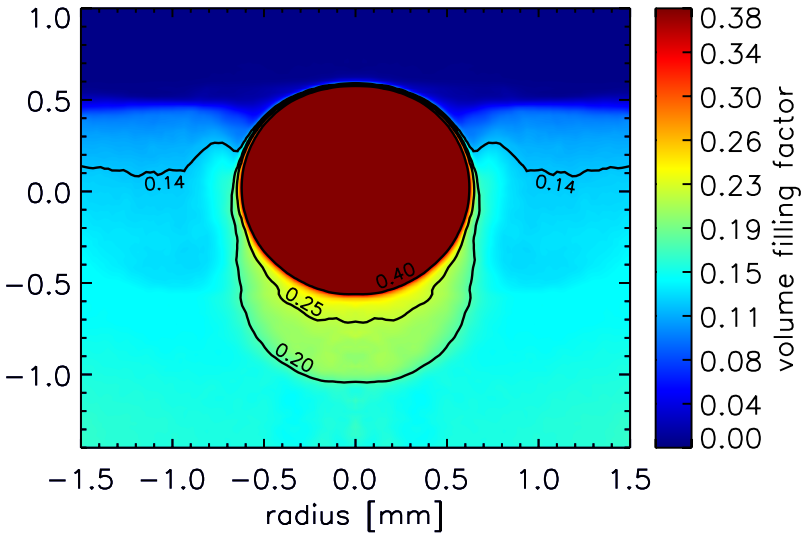

Figure 3.9: Spatial averaged volume filling factors mirrored at the vertical center line. The volume under the sphere is compacted to a volume filling factor > 0.2 (yellow), while the surrounding material is nearly unaffected (light blue).

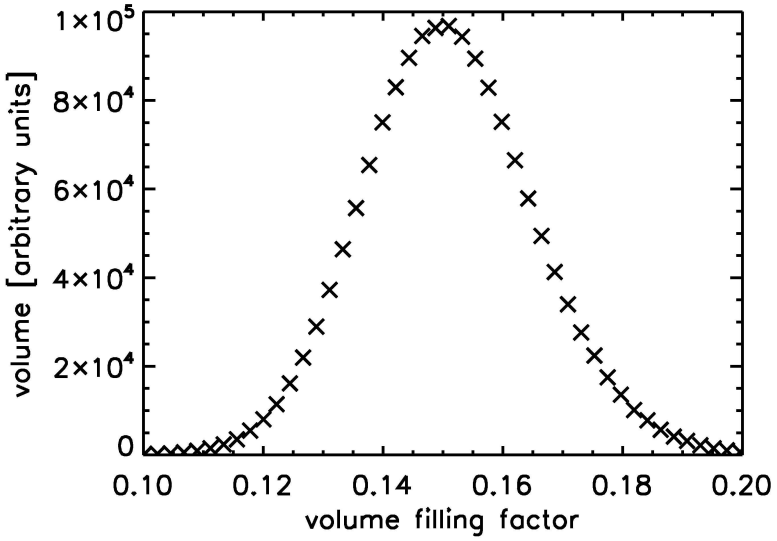

Figure 3.10: Distribution of volume filling factors for an uncompressed dust sample, which follows a Gaussia distribution with a mean value of $\phi \approx 0.15$.

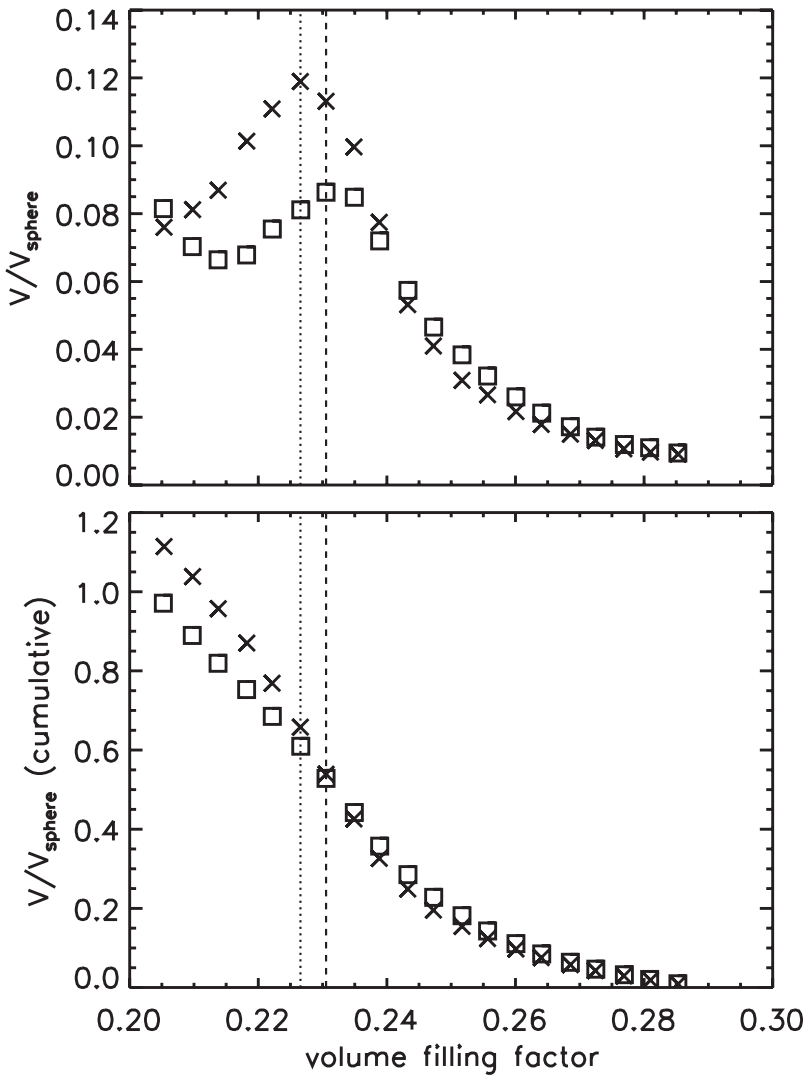

Figure 3.11: Top: Distribution of volume filling factors only for the compressed area underneath the impacted sphere for two experiments. The dashed and dotted lines mark the most occurring volume filling factors for each curve, lying at $\phi \approx 0.23$. **Bottom:** Normalized volume fraction of compacted area corresponding to a volume filling factor $> \phi$.

indicated by the dashed and dotted lines. The decreasing left flank of the curves corresponds to the transition region between compressed and uncompressed dust material (see right curve flank of Fig. 3.10). The same data plotted in a cumulative way (Fig. 3.11, bottom), represent the amount of compacted volume in units of the sphere volume that complies with a volume filling factor greater than a certain value. According to the volume filling factor values at the boundary to the uncompressed dust, given by the minima of the left side of the curves in Fig. 3.11 (top), we can conclude from the cumulative curves (Fig. 3.11, bottom) that the compressed volume due to an impacting sphere of 1 mm size into a high-porosity dust sample ($\phi \approx 0.15$) fills the volume of $\sim 0.8-1.2$ sphere volumes.

3.3.5 Requirements of a Dynamic Compressive Strength Curve

As seen in the previous sections, we have abundant indirect information about the compression behavior of loose dust samples. However, the basic question how the dynamic compressive strength curve, $\phi(\Sigma)$, looks, remains unanswered. We approach this problem the following way: (1) For low compressions, $\Sigma \to 0$, the volume filling factor is given by the initial properties of the material, i.e. $\phi \to \phi_1$ (see Table 3.1). (2) The maximum compression for $\Sigma \to \infty$ is given by the value ϕ_2 in Table 3.1 for the omnidirectional case, because the XRT analysis shows no material creeping sideways as was the case for the unidirectional flow (see Blum and Schräpler, 2004). (3) With these two limits in mind, we apply Eq. 3.9 as an approximation to the functionality of the dynamic compressive strength, which leaves us with the two free parameters Δ and p_m. The maximum slope of the compression at $\Sigma = p_\mathrm{m}$ is given by $\mathrm{d}\phi/\mathrm{d}\lg\Sigma = (\phi_2 - \phi_1)/\Delta$. For the unidirectional and omnidirectional static curves, we get slope values of 0.55 and 0.79, respectively (see Table 3.1). These are in fact not so different so that we adopt for the dynamic case the slope of the omnidirectional compression. Thus, we assume $\Delta = 0.58$ dex for the dynamic case. A refined study that takes both, Δ and p_m, as free parameters will be conducted in Geretshauser et al. (2009), but in this paper we only vary p_m.

3.4 Calibrating the SPH code

The laboratory experiments in the previous section provided the static omnidirectional compressive strength Σ and the tensile strength relation T as most important ingredients for the Sirono porosity model implemented in the SPH code by Geretshauser et al. (2009). However, as it was already pointed out in the laboratory section, the compressive strength relation has to be considered dynamically. The only free parameter p_m (see Sect. 3.3.5) cannot be determined by experiments. Hence it has to be constrained by a numerical parameter study. We will use the stopping time of the impacting glass bead as reference for this parameter.

In addition, a relation for the shear strength is also very hard to measure in the laboratory. Therefore, we suggest three simple relations depending on the dynamic compressive strength and tensile strength relations and use the qualitative comparison of the filling

factor profile under the glass bead after impact to constrain this unknown quantity.

Finally, we utilize the remaining experimentally measured independent features of the experiments described in the laboratory section to validate our calibration.

3.4.1 Benchmark test - setup

The given experimental setup (see Sect. 3.3.4) was modeled with high resolution in two dimensions. Initially, the SPH particles were put on a triangular grid. All simulations were performed with the influence of gravity taken into account.

The projectile was modelled with a circle of 1.1 mm in diameter consisting of 1519 SPH particles. Its material properties were simulated using the Murnaghan equation of state

$$p = \left(\frac{K_0}{n}\right)\left[\left(\frac{\rho}{\rho_0}\right)^n - 1\right] \tag{3.14}$$

with $\rho_0 = 2\,540$ kg m^{-3} (total 2D mass per unit length $m_{2\mathrm{D}} = 2.4 \cdot 10^{-3}$ kg m^{-1}), $K_0 = 5.0 \cdot 10^9$ Pa and $n = 4$. The density has been chosen such that it matches the experimental specifications. The other material parameters are similar to those of sandstone. They can be found together with the Murnaghan equation of state in Melosh (1989). The exact choice of the bulk modulus K_0 and the Murnaghan exponent n does not have significant effects. The glass bead was treated as fully elastic. The impact velocity was 0.65 m s^{-1}.

The dust sample was modelled as a 8×5 mm^2 rectangle with 64 421 SPH particles. About 0.15 mm at the bottom and 0.56 mm at each side of the rectangle were used as reflecting boundary by setting their acceleration to zero at each time step. The porous material was simulated by using the modified version of the Sirono model presented in Sect. 3.2. The initial density was expressed via the filling factor $\phi = \rho/\rho_0$ with $\phi = 0.15$ and $\rho_0 = 2\,000$ kg m^{-3}. For the tensile strength we used the semianalytical relation, derived in Sect. 3.3.1 (Eq. 3.8) that matches the findings of Blum and Schräpler (2004) and Blum et al. (2006). The bulk modulus was modeled by a power law

$$K(\rho) = K_0 \left(\frac{\rho}{\rho_\mathrm{i}}\right)^4 \tag{3.15}$$

with $K_0 = 300$ kPa and the initial density of the dust aggregate $\rho_i = 300$ kg m^{-3}. The bulk modulus $K_0 = \rho_\mathrm{i} c^2$ for uncompressed material was determined by the measurement of the sound speed, which is $c = 30$ m s^{-1} (Blum and Wurm, 2008, Paszun and Dominik, 2008).

For the compressive strength, several different relations were tested. At first we adopted the relation from the uniaxial experiments by Blum and Schräpler (2004). Secondly we used the omnidirectional compression curve presented in this paper. After it turned out that a modified relation for the dynamical compressive strength curve had to be considered, the omnidirectional compression curve (Eq. 3.10) was shifted towards lower pressure regimes using the free parameter p_m (see Sect. 3.3.5).

Since no experimental data was available for the shear strength Y, parameter studies were carried out with three different relations $Y(|T|, \Sigma)$: $Y = |T|$, $Y = \Sigma$ and, following Sirono (2004), $Y = \sqrt{\Sigma |T|}$, which represents the geometric mean of both quantities.

Due to reasons of stability, the two materials in contact (solid projectile, dusty target) have to be separated by artificial viscosity. We use the approach by Monaghan and Gingold (1983) and apply an α-viscosity of 1.0 to all particles of the sphere and all particles interacting with the sphere. All other dust-sample particles were simulated without artificial viscosity following Sirono (2004). All details regarding the SPH code can be found in Geretshauser et al. (2009).

3.4.2 Calibration procedure

With the aim of reproducing the experimental results presented in the laboratory section, an SPH simulation using the omnidirectional compressive strength curve (ODC) was conducted. In the resulting pressure regime the ODC relation and the relation from Blum and Schräpler (2004) are almost identical. Therefore they can be treated as one case.

The impact velocity of the 1.1 mm glass bead was 0.65 m s^{-1} and we will compare the results of the simulation with the vertical density profile along a line through the center of the sphere perpendicular to the bottom of the dust sample, which was measured with x-ray micro-tomography as described in Sect. 3.3.4. Figure 3.12 shows the results for three different shear strength models, which are compared to two density profiles as measured in the experiments (lines with blue and green crosses). The initial surface of the dust sample is at 0 mm.

For the original ODC relation (p_m = 13 kPa), the simulations for all shear strength models resulted in a much too shallow intrusion depth and an insufficient maximum filling factor underneath the sphere. These findings indicated, that the compressive strength curve had to be modified in order to reproduce the experimental data. Therefore, we performed a parameter study varying the parameter p_m, i.e. shifting the compressive strength curve to lower pressures for the different shear strength models. For the complete study see Geretshauser et al. (2009). Independent experiments (Weidling et al., 2009) also support a lower p_m which can quantitatively explain the amount compression in bouncing collisions.

A significant increase of the intrusion depth was only observed in case of $Y = \sqrt{\Sigma |T|}$ and $Y = \Sigma$ (see Fig. 3.12, top and center). In case of $Y = |T|$ the intrusion depth hardly changed with decreasing p_m (Fig. 3.12, bottom). Since the shear strength remained constant and changing p_m did not have a significant effect, it can be concluded that shearing plays an important role during the intrusion.

Compared to the other cases, the shear strength reaches its highest values in the $Y = |T|$ case. Hence, the material can hardly be pushed away due to shear and has to be compressed. Therefore, the highest filling factors can be found in this case (see Fig. 3.12, bottom). The $Y = \Sigma$ model yields the lowest shear strength values. Hence, material is

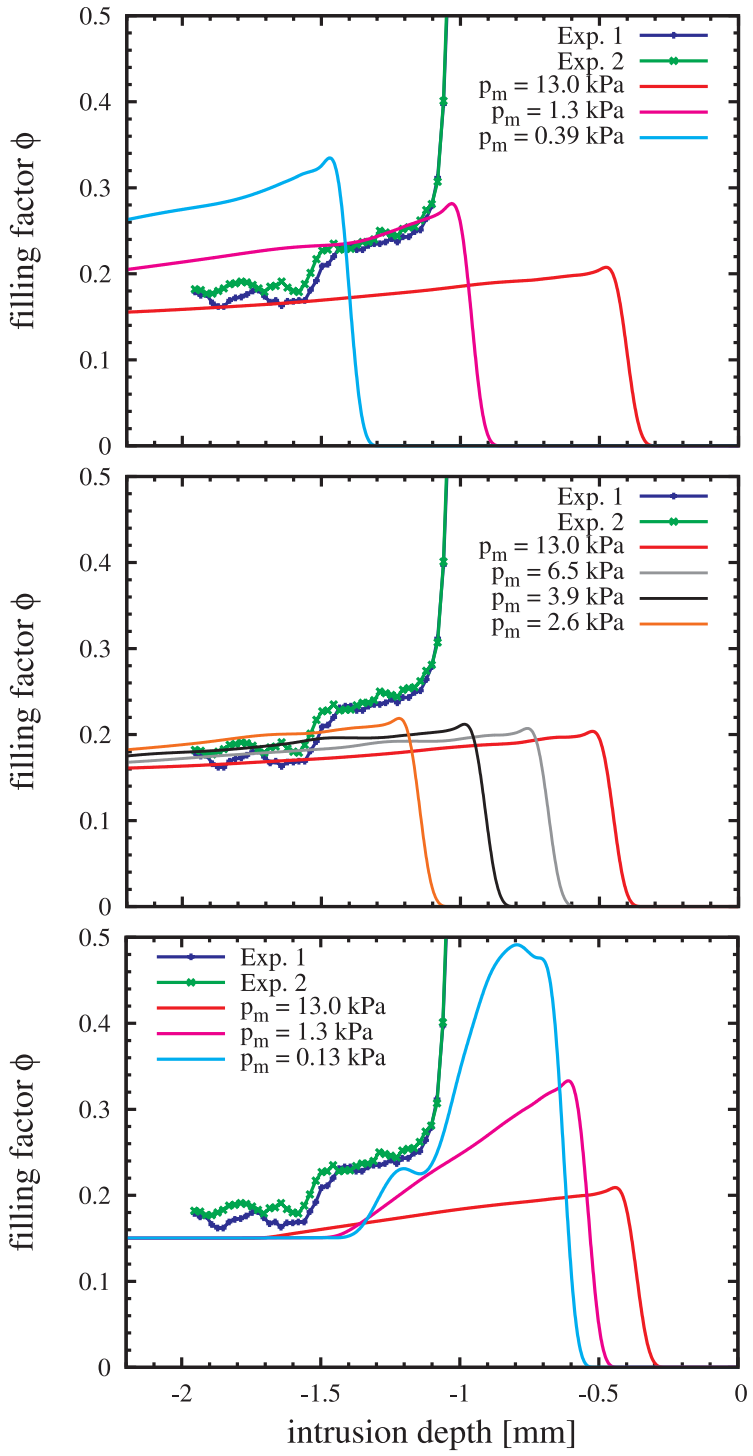

Figure 3.12: The filling factor measured along a line through the center of the sphere, perpendicular to the bottom of the dust sample (lines with blue and green crosses). The initial surface of the dust sample is situated at 0 mm and the steep slope at the right end of the experimental curves marks the transition from the dust sample to the glass sphere. The other curves are numerical simulations, varying the shear strength model and the material softness p_m. The shear strength relation was **(top)** $Y = \sqrt{\Sigma |T|}$, **(center)** $Y = \Sigma$, and **(bottom)** $Y = |T|$.

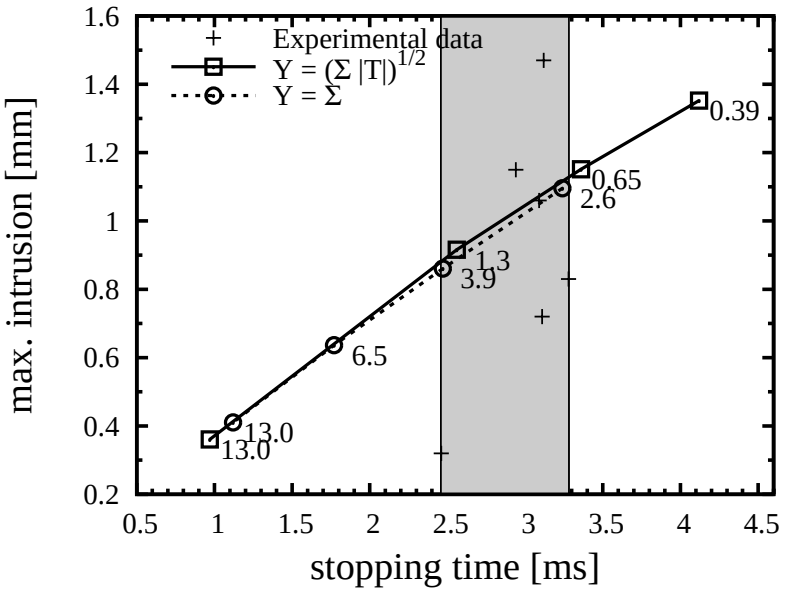

Figure 3.13: Stopping time - intrusion diagram. Experimental data for spheres of 1 mm radius. Labels indicate the p_m values (in kPa) for the modification of the compressive strength curve. For the $Y = \Sigma$ model the best match in stopping time and intrusion depth is found for $p_\mathrm{m} = 3.9$ kPa. For the $Y = \sqrt{\Sigma|T|}$ model the best approximation is given for $p_\mathrm{m} = 1.3$ kPa.

mostly sheared aside, less material is compressed and therefore this model leads to filling factors below the reference data (see Fig. 3.12, center).

Figure 3.13 shows intrusion depth over stopping time regarding the shear strength models $Y = \Sigma$ and $Y = \sqrt{\Sigma|T|}$ for all p_m. Since $Y = |T|$ did only yield insufficient intrusion depths, this model was omitted here. A good time/depth match was achieved for $p_\mathrm{m} = 3.9$ kPa using $Y = \Sigma$ and for $p_\mathrm{m} = 1.3$ kPa using $Y = \sqrt{\Sigma|T|}$. However, the $Y = \Sigma$ model cannot reproduce the high values in the vertical filling factor profile (Fig. 3.12, center) whereas the $Y = \sqrt{\Sigma|T|}$ model yields an almost perfect match (Fig. 3.12, top). Therefore, the latter with $p_\mathrm{m} = 1.3$ kPa gives a good match in Fig. 3.12 (top) as well as in Fig. 3.13 and is therefore used for further simulations. A more detailed study on the determination on the p_m value can be found in Geretshauser et al. (2009).

Hereby, we have determined parameters for all previously unknown material relations and thus have calibrated the SPH model with respect to the presented experiments. The resulting strength curves of compression (Eq. 3.10, $p_\mathrm{m} = 1.3$ kPa), tension (Eq. 3.8) and shear ($Y = \sqrt{\Sigma|T|}$) are illustrated in Fig. 3.14.

However, the fact that the filling factor does not rapidly drop to ~ 0.15 at a depth of 1.5 mm requires further investigation.

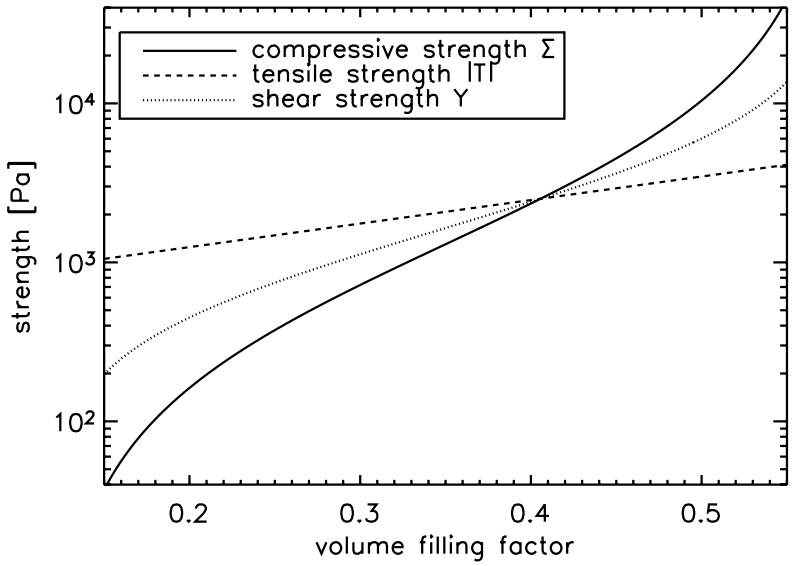

Figure 3.14: Compressive strength curve $\Sigma(\phi)$ (Eq. 3.10) for $p_\mathrm{m} = 1.3$ kPa, tensile strength $|T|$ (Eq. 3.8), and shear strength $Y = \sqrt{\Sigma \cdot |T|}$.

3.4.3 Reproducing Experimental Features

Since intrusion time and depth as well as the filling factor profile underneath the sphere have been used to determine p_m and the correct shear strength model, further features have to be reproduced in order to validate the calibration.

One of these features is the cumulated volume over filling factor relation (Fig. 3.15). While the filling factor profile only displays a cut through the compressed volume, this curve represents the total compressed volume with its filling factors. Both curves are not fully, but mostly independent from each other. The chosen model and p_m value yield an almost perfect match for filling factors > 0.22. The deviation for lower filling factors is due to the larger amount of compressed volume. This effect was already seen in the filling factor profile and is also very prominent in the comparison of the spatially density distribution plots (compare Figs. 3.9 and 3.16).

Another feature to be reproduced is the relation $D \propto mvA^{-1}$ found in a similar way in the drop experiments (cf. Fig. 3.6). We performed a series of 2D simulations with spheres of 1 mm and 3 mm diameter and evaluated the maximum intrusion depth with respect to the impact velocity v. The latter was varied from 0.1 m s^{-1} to 1.0 m s^{-1} in steps of 0.1 m s^{-1}.

2D simulation and experiment cannot be compared directly due to the different geometry (the 2D setup represents a cut through an infinitely long cylinder). The advantage of using the quantity mvA^{-1} instead of the more accurate Eq. 3.12 is given by the fact that the former can be "converted" into 2D by the following correction:

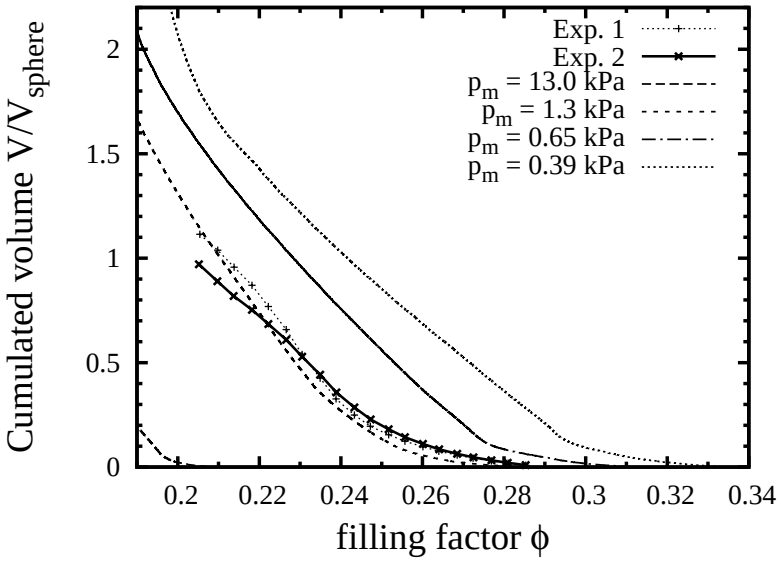

Figure 3.15: Cumulated volume over filling factor. While $p_\mathrm{m} = 13$ kPa, i.e. the unmodified ODC relation, and $p_\mathrm{m} = 0.39$ kPa as well as $p_\mathrm{m} = 0.65$ kPa yield too small and too high compression values, respectively, $p_\mathrm{m} = 1.3$ kPa matches very well for $\phi \gtrsim 0.22$. The experimental data are identical to those shown in Fig. 3.11 (bottom)

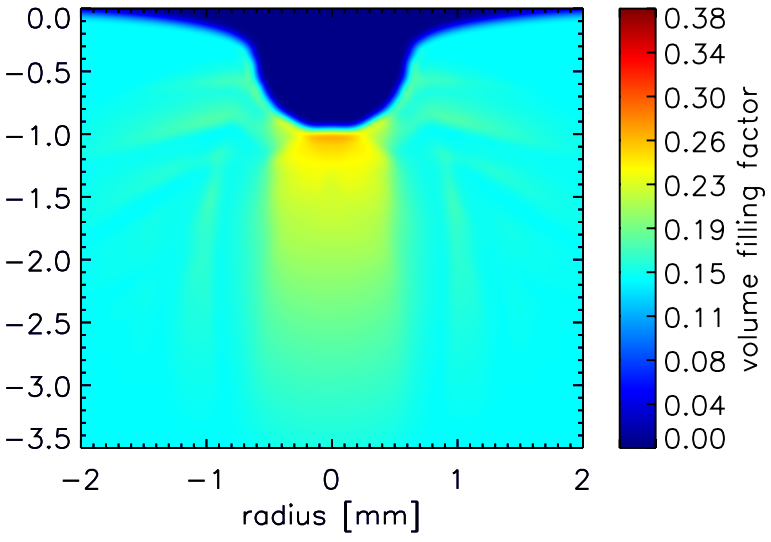

Figure 3.16: Spatially distributed compression as calculated in the SPH simulation with $Y = \sqrt{\Sigma \cdot |T|}$ and $p_\mathrm{m} = 1.3$ kPa; same color scale as Fig. 3.9; the projectile is not plotted. Although the filling factor of compressed material is comparable to the one in the experiments, the compressed volume reaches significantly deeper.

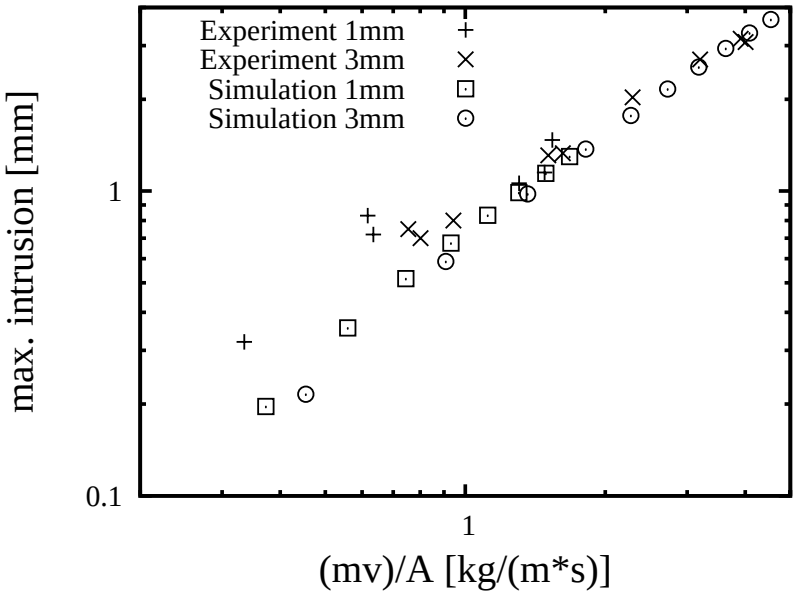

Figure 3.17: In the momentum-intrusion relation, the agreement between simulation and experimental results is very good for values of $mvA^{-1} \gtrsim 1$ kg m^{-1} s^{-1}.

$$\frac{m_{3D}v}{A_{3D}} = \frac{\frac{4}{3}\pi a^3 \rho \cdot v}{\pi a^2} = \frac{8}{3\pi}\,\frac{\pi a^2 \rho \cdot v}{2a} = \frac{8}{3\pi}\,\frac{m_{2D}v}{A_{2D}} \tag{3.16}$$

In comparison with the experimental results, the data from the simulation matches very well for $mvA^{-1} > 1.0$ kg m^{-1} s^{-1} (Fig. 3.17). For smaller values the simulation yields a shallower intrusion than the reference experiments, which, however, also show significant scattering in this range.

Comparing the simulated and experimentally acquired normalized deceleration curves (Fig. 3.18), the simulated data slightly deviate from the experimental mean but remain within standard derivation limits. The deviation could arise from the geometric difference of the 2D and 3D case and has to be investigated in future works.

3.5 Application of SPH to Dust Collisions in PPDs, Conclusions, and Outlook

In this section we will present some preliminary applications of SPH simulations to dust collisions in protoplanetary disks. We will present two examples of previously unfeasible calculations of inter-particle collisions among macroscopic dust aggregates and will qualitatively compare them to similar dust experiments performed in the laboratory. Then, we will speculate about how the SPH code should be used in research on protoplanetary growth. Finally we will sketch future work in preparation.

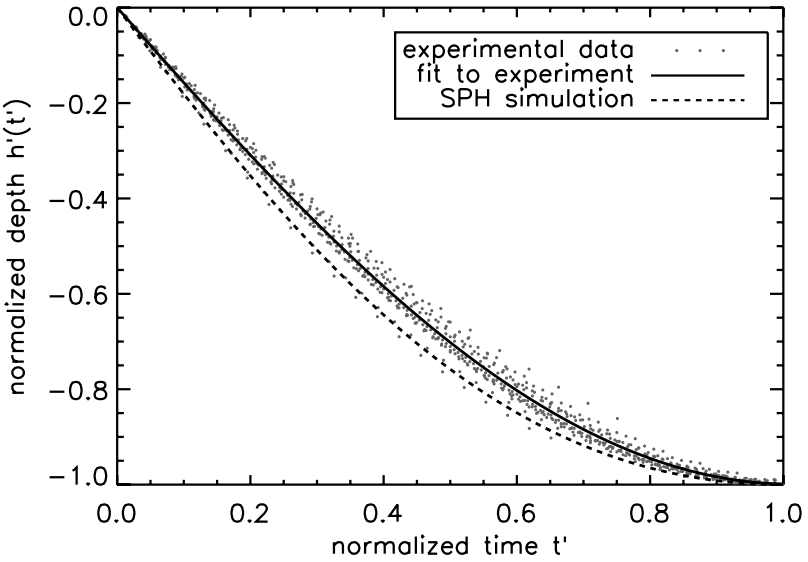

Figure 3.18: Normalized deceleration curve compared to the results. The deceleration curve in the SPH simulation is slightly lower than the experimentally observed sine curve, but well within the errors. This effect will be be analyzed in future work. However, the range of experimental data encompasses the simulation results.

3.5.1 Qualitative comparison between SPH simulations and laboratory experiments

The strength of the SPH simulations – besides the well-known examples in hyper-velocity collisions – over laboratory experiments and molecular-dynamics simulations is that low-velocity collisions among arbitrary dust aggregates can be investigated. Here, we show two examples recently observed in the lab, which can so far not be described by any other model. Example 1 deals with the frequently-observed bouncing collisions in aggregate-aggregate interactions. Example 2 describes the impact of a single dust aggregate onto a solid flat target, which shows the co-occurrence of (partial) sticking *and* fragmentation.

Example 1

Bouncing in collisions between dust aggregates has been observed in many laboratory experiments (Blum and Münch, 1993, Langkowski et al., 2008, Weidling et al., 2009, Heißelmann et al., 2007), although molecular-dynamics simulations always show a direct transition from sticking to fragmentation when the collision energy exceeds a threshold value (Dominik and Tielens, 1997, Wada et al., 2007, 2008). Nature obviously chooses a wider bouncing transition between those two stages, at least for aggregates above a certain size. It turns out that the SPH method is capable of describing the bouncing phase quite well. We have run a 3D SPH simulation of a low-velocity impact of a 1 mm (diameter) fluffy aggregate onto a flat target. Due to symmetry arguments, this is identical to a two-

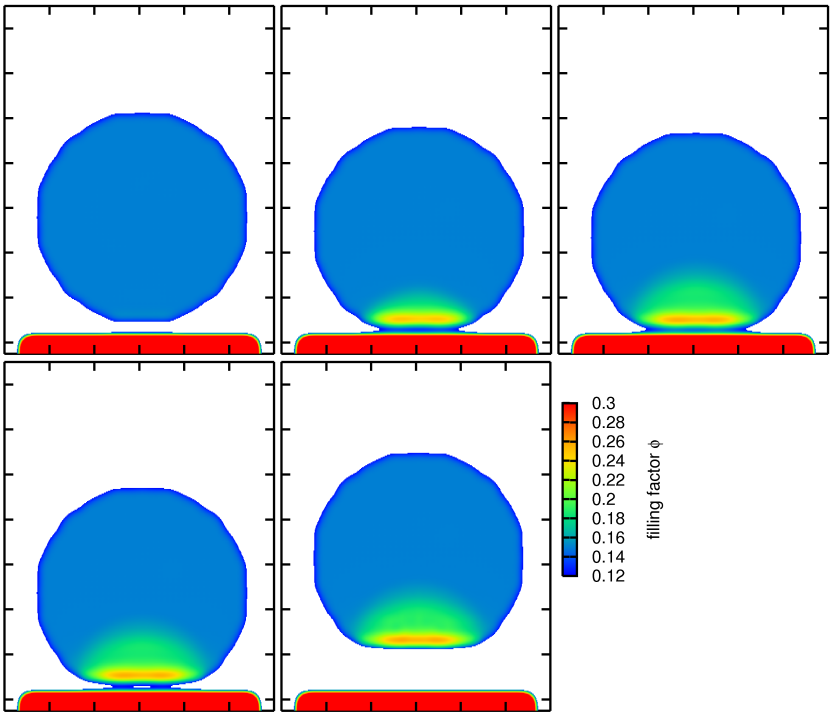

Figure 3.19: Sequence of snapshots of an SPH simulation of a fluffy dust aggregate with a radius of 0.5 mm, impacting a solid target at a velocity of 0.2 m s^{-1}. The time differences between subsequent images are 0.35 ms, 0.32 ms, 0.23 ms, and 4.45 ms, respectively. The colors denote different degrees of internal compaction.

aggregate (central) collision with twice the collision velocity. In our case, the aggregate was composed of 33 377 SPH particles and had an initial volume filling factor of 0.15. All other material parameters were identical to those in the previous section, i.e. $K_0 = 300$ kPa, $p_m = 1.3$ kPa, $Y = \sqrt{\Sigma|T|}$. The impact velocity was 0.2 m s^{-1}, matching exactly the situation in the aggregate-wall experiments performed by Weidling et al. (2009) and also those in the aggregate-aggregate collisions investigated by Heißelmann et al. (2007) with a collision speed of 0.4 m s^{-1}. Fig. 3.19 shows a sequence of snapshots with a cut through the center of the aggregate, indicating the internal compaction due to the impact. Our simulation can correctly predict the coefficient of restitution of ~ 0.2 (Blum and Münch, 1993, Heißelmann et al., 2007), although details in the compaction behavior still deviate from the laboratory results, which might be caused by insufficient resolution in the SPH simulation.

Example 2

In the previous example, we have seen that bouncing marks the broad transition regime between sticking and fragmentation. However, in the case of the impact of a dust aggregate onto a solid target, laboratory experiments have shown that, for impact experiments above the fragmentation threshold, fragmentation is always accompanied by partial sticking of

the aggregate to the target. This effect was first found by Wurm et al. (2005b) for compacted dust aggregates and impact velocities above 25 m s^{-1} and later confirmed in our laboratory for $\phi = 0.35$ aggregates and impact velocities above 1 m s^{-1}. Fig. 3.20 shows an image sequence of an impact experiment with fragmentation and partial sticking. An average of 10 % of the projectile mass sticks to an initially smooth target at normal impact, which is consistent with the low velocity results of Wurm et al. (2005b). The remainder of the projectile mass is fragmented into a power-law mass distribution (see Blum and Münch, 1993). The fragments leave the target under extremely flat angles. Our SPH simulation (Fig. 3.21, left) featuring the calibration parameters of Sect. 3.4.2 cannot reproduce the fragmentation behavior seen in the experiments. Here, the predominant part of the dust sample sticks to the target. Only a few bigger chunks and single SPH particles burst off. However, a simulation with the same setup, but using the shifted unidirectional compressive strength relation (Sect. 3.3.2) and a shear strength that is equal to the tensile strength, matches the experimental observations at least qualitatively (Fig. 3.21, right). From that we conclude that the SPH code is in principle capable of simulating fragmentation of highly-porous aggregates, even without the damage model adopted in the original Sirono (2004) porosity model.

We conclude that the shear model $Y = \Sigma^{0.5} \cdot |T|^{0.5}$ tested for the dynamic compression experiments (Sect. 3.4.1) is unable to explain the fragmentation findings which are rather dominated by shear and tension, whereas a shear model $Y = \Sigma^0 \cdot |T|^1$ shows qualitative agreement. The imperfect shear model can also be responsible for the narrow but deep compressed volume in Fig. 3.16 compared to Fig. 3.9. A future task will therefore be to refine the shear calibration in a way that we will use $Y = C \cdot \Sigma^\alpha \cdot |T|^{1-\alpha}$ with the free parameters C and α. Comprising both experiments for calibration we will be able to find a shear model that can reproduce both cases.

3.5.2 Use of the SPH code in research on protoplanetary growth

The above examples show that the SPH method is a powerful tool to investigate the outcomes of protoplanetary dust collisions. When properly calibrated with laboratory experiments, SPH calculations allow access to parameter-space regions that are unavailable to laboratory experiments. Whereas molecular-dynamics simulations can be used for studying collisions of very small dust aggregates, SPH is most useful for very large samples. Such samples, particularly those with fluffy compositions, cannot be built or treated in laboratories, and the experimental study of collisions seems impossible.

A particularly interesting and still unsolved problem is the dichotomy in the collision behavior of pairs of dust aggregates with similar and different sizes, respectively. Langkowski et al. (2008) found sticking by deep penetration for impacts of mm-sized dusty projectiles into flat, cm-sized dusty targets ("projectile-target" collisions) above $\sim$ 1 m s^{-1}. Both dust aggregates, projectile and target, consisted of identical particles and had equal porosity. Using similar dust aggregates, but giving projectile and target comparable size ("projectile-projectile" collisions), Blum and Münch (1993) and Heißelmann et al. (2007) found that collisions either lead to bouncing or to fragmentation.

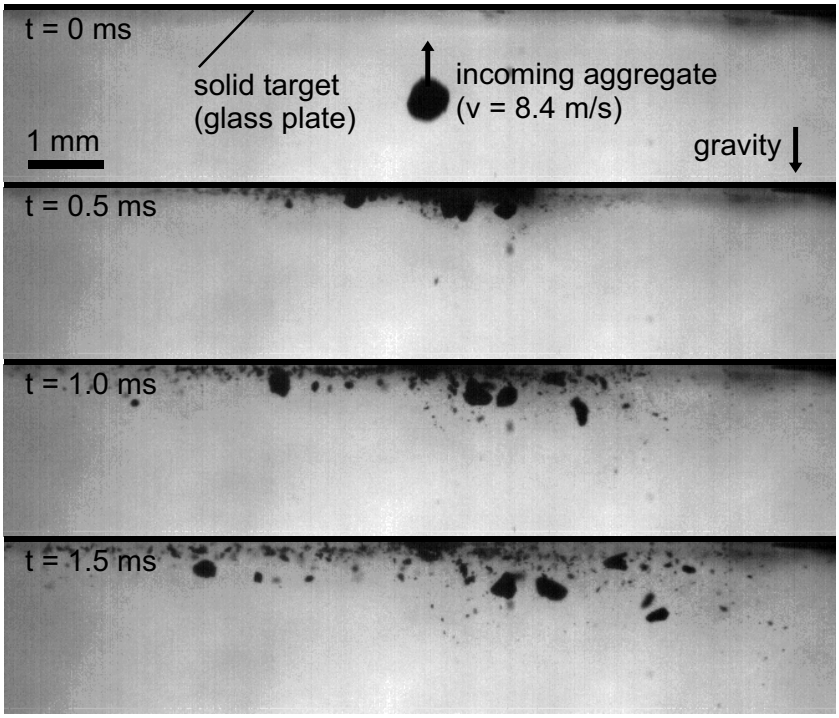

Figure 3.20: Image sequence of an experiment, in which a fluffy dust aggregate impacts a solid target at 8.4 m s^{-1}. Part of the aggregate sticks to the target after the collision.

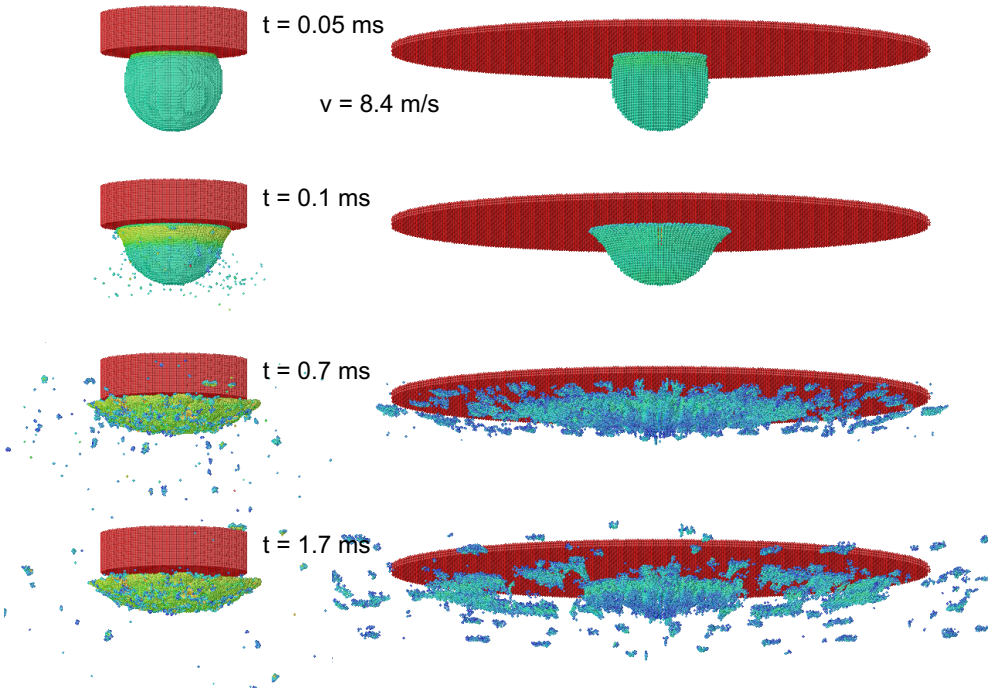

Figure 3.21: Image sequence of an SPH simulation, identical to the experiment shown in Fig. 3.20. The simulation with the calibrated parameters **(left)** cannot reproduce the experimental results, whereas a simulation using an unidirectional compression curve and $\Sigma = |T|$ **(right)** can reproduce the qualitative findings of Fig. 3.20.

Bouncing instead of sticking was also observed by Langkowski et al. (2008) when the target aggregates were prepared such that the local radius of curvature corresponded to the projectile's radius. To find out where the boundary between "projectile-target" and "projectile-projectile" collisions occurs, will be one of our future applications of our SPH code.

3.5.3 Future work

We have only begun to explore the potentials of SPH simulations of collisions between protoplanetary dust aggregates. Before we can start to investigate the full parameter space in protoplanetary dust collisions, i.e. before we can begin to find out what the collisional outcome is for all combinations of aggregate size, porosity, collision velocity, impact angle, state of rotation, temperature and state of sintering, material and size (distribution) of the constituent dust grains, etc., the material parameters of macroscopic dust aggregates have to be fully explored. This will be the next task in our investigation. To achieve this, we will perform more calibration experiments of the type described in this paper for dust aggregates of various compositions and porosities. In addition to that, other calibration experiments will be explored, like the ones described in Sects. 3.5.1 and 3.5.1.

Chapter 4

Mapping the zoo of laboratory collision experiments

Carsten Güttler, Jürgen Blum, Andras Zsom, Chris W. Ormel, Cornelis P. Dullemond
Submitted to Astronomy & Astrophysics

Abstract

The growth processes from protoplanetary dust to planetesimals are not fully understood. Laboratory experiments and theoretical models have shown that collisions among the dust aggregates can lead to sticking, bouncing, and fragmentation. However, no systematic study on the collisional outcome of protoplanetary dust has been performed so far so that a physical model of the dust evolution in protoplanetary disks is still missing. We intend to map the parameter space for the collisional interaction of arbitrarily porous dust aggregates. This parameter space encompasses the dust-aggregate masses, their porosities and the collision velocity. With such a complete mapping of the collisional outcomes of protoplanetary dust aggregates, we will – in Chapter 5 – follow the collisional evolution of dust for different protoplanetary disk models. We use literature data, perform own laboratory experiments, and apply simple physical models to get a complete picture of the collisional interaction of protoplanetary dust aggregates. In our study, we found four different types of sticking, two types of bouncing, and three types of fragmentation as possible outcomes in collisions among protoplanetary dust aggregates. Our best collision model distinguishes between porous and compact dust. We also differentiate between collisions among similar-sized and different-sized bodies. All in all, eight combinations of porosity and mass ratio can be discerned. For each of these cases, we present a complete collision model for dust-aggregate masses between 10^{-12} and 10^{2} g and collision velocities in the range $10^{-4} \ldots 10^{4}$ cm s^{-1} for arbitrary porosities. This model comprises the collisional outcome, the mass(es) of the resulting aggregate(s) and their porosities. We present the first complete collision model for protoplanetary dust. This collision model can be used for the determination of the dust-growth rate in protoplanetary disks. This will be the subject of Chapter 5.

4.1 Introduction

The first stage of protoplanetary growth has still not been fully understood. Although our empirical knowledge on the collisional properties of dust aggregates has considerably widened over the past years (Blum and Wurm, 2008), there is no self-consistent model for the growth of macroscopic dust aggregates in protoplanetary disks (PPDs). A reason for such a lack of understanding is the complexity in the collisional physics of dust aggregates. Earlier assumptions of perfect sticking have been experimentally proven false for most of the size and velocity ranges under consideration. Recent work also showed that fragmentation and porosity play important roles in mutual collisions between protoplanetary dust aggregates. In their review paper, Blum and Wurm (2008) show the complex diversity that is inherent to the collisional interaction of dust aggregates consisting of micrometer-sized (silicate) particles. This complexity is the reason why the outcome of the collisional evolution in PPDs is still unclear and why no 'grand' theory on the formation of planetesimals, based on firm physical principles, has so far been developed.

The theoretical understanding of the physics of dust aggregate collisions has seen major progress in recent decades. The behavior of aggregate collisions at low collisional energies – where the aggregates show a fractal nature – is theoretically described by molecular dynamics simulations of Dominik and Tielens (1997). The predictions of this model – concerning aggregate sticking, compaction, and catastrophic disruption – could be quantitatively confirmed by laboratory collision experiments of Blum and Wurm (2000). Also, the collision behavior of macroscopic dust aggregates was successfully modeled by a smooth particle hydrodynamics method, calibrated by laboratory experiments (Güttler et al., 2009, Geretshauser et al., 2009). These simulations were able to reproduce bouncing collisions, which were observed in many laboratory experiments (Blum and Wurm, 2008).

However, as laboratory experiments have shown, collisions between dust aggregates at intermediate energies and sizes are characterized by a plethora of outcomes: ranging from (partial) sticking, bouncing, mass transfer, to catastrophic fragmentation (see Blum and Wurm, 2008). From this complexity, it is clear that the construction of a simple theoretical model that agrees with all these observational constraints is very challenging. However, in order to understand the formation of planetesimals, it is imperative to describe the entire phase-space of interest, i.e., to consider a wide range of aggregate masses, aggregate porosities, and collision velocities. Likewise, the collisional outcome is the key ingredient of any model that computes the time evolution of the dust size distribution.

These concerns lay behind the approach we adopt in this and subsequent papers. That is, instead of first 'funneling' the experimental results through a (perhaps ill-conceived) theoretical collision model and then to calculate the collisional evolution, we will directly use the experimental results as input for the collisional evolution model. The drawback of such an approach is of course that experiments on dust aggregate collisions do not cover the whole parameter space and therefore need to be extrapolated by orders of magnitude, based on simple physical models which accuracy might be challenged. However, we feel that this drawback is more than justified by the prospects that our new approach will provide: through a direct mapping of the laboratory experiments, collisional evolution

models can increase enormously in their level of realism.

In this work, we will classify all existing dust-aggregate collision experiments for silicate dust, including three additional original experiments not published before, according to the above parameters (Sect. 4.2). We will show that we have to distinguish between nine different collision types, which we physically describe in Sect. 4.3. For the later use in a growth model, we will sort these collision types into a mass-velocity parameter space for all eight combinations of porous and compact dust-aggregate projectiles and targets. We will present our collision model in Sect. 4.4 and the consequences for the porosities of the dust aggregates in Sect. 4.5. In Sect. 4.6, we conclude our work and give a critical review on our model and the involved necessary simplifications and extrapolations.

Zsom et al. (2009) will then, based upon the results presented here, follow the dust evolution using a recently invented Monte-Carlo approach (Zsom and Dullemond, 2008) for three different disk models. This is the first fully self-consistent growth simulation for PPDs. The results presented in Chapter 5 represent the state-of-the-art modeling and will give us important insight into questions, such as if the meter-size barrier can be overcome and what the maximum dust-aggregate size in PPDs is, i.e. whether pebbles, boulders, or planetesimals can be formed.

4.2 Collision Experiments with Relevance to Planetesimal Formation

In the past years, numerous laboratory and space experiments on the collisional evolution of protoplanetary dust have been performed (Blum and Wurm, 2008). Here, we concentrate on the dust evolution around a distance of 1 AU from the solar-type central star where the ambient temperature is such that the dominating material class are the silicates. This choice of 1 AU reflects the kind of laboratory experiments that are included in this paper, which were all performed with SiO_2 grains or other refractory materials. The solid material in the outer solar nebula is dominated by ices, which possibly have very different material properties than silicates, but only a small fraction of laboratory experiments have dealt with these colder (ices, organic materials) or also warmer regions (oxides). In Sect. 4.6.2, we will discuss the effect that another choice of material might potentially have, but as we are far away from even basically comprehending the collisional behavior of aggregates consisting of these materials, we concentrate in this study on the conditions relevant in the inner solar nebula around 1 AU.

Table 4.1 lists all relevant experiments that address collisions between dust aggregates of different masses, mass ratios, and porosities, consisting of micrometer-sized silicate dust grains, in the relevant range of collision velocities. Experiments 1 – 16 are taken from the literature (cited in Table 4.1), whereas experiments 17 – 19 are new ones not published before. In the following two subsections we will first review the previously published experiments (Sect. 4.2.1) and then introduce the experimental setup and results of new experiments that were performed to fill some regions of interest (Sect. 4.2.2). All these

Table 4.1: Table of the experiments which are used for the model.

	projectile mass m_p [g]	collision velocity v [cm s^{-1}]	micro-gravity	collision type (see Fig. 4.1)	reference
Exp 1	$7.2 \cdot 10^{-12}$ – $7.2 \cdot 10^{-9}$	0.1 – 1	yes	S1	Blum et al. (1998, 2002), Wurm and Blum (1998)
Exp 2	$7.2 \cdot 10^{-12}$ – $2.0 \cdot 10^{-10}$	10 – 50	yes	S1	Wurm and Blum (1998)
Exp 3	$3.5 \cdot 10^{-12}$ – $3.5 \cdot 10^{-10}$	0.02 – 0.17	yes	S1	Blum et al. (2000),
	$1.0 \cdot 10^{-12}$ – $1.0 \cdot 10^{-10}$	0.04 – 0.46	yes	S1	Krause and Blum (2004)
Exp 4	$1.2 \cdot 10^{-10}$ – $4.3 \cdot 10^{-10}$	7 – 1 000	yes	S2	Blum and Wurm (2000)
Exp 5	$2 \cdot 10^{-3}$ – $7 \cdot 10^{-3}$	15 – 390	yes	B1, F1	Blum and Münch (1993)
	10^{-5}– 10^{-4}	15 – 390	yes	B1, F1	
Exp 6	10^{-6} – 10^{-4}	10 – 170	yes	S2, S3	Langkowski et al. (2008)
	10^{-4} – $3 \cdot 10^{-3}$	50 – 200	yes	B2, S2, S3	
	$2.5 \cdot 10^{-5}$ – $3 \cdot 10^{-3}$	200 – 300	yes	S3	
Exp 7	10^{-3} – $3 \cdot 10^{-2}$	20 – 300	yes	S3	Blum and Wurm (2008)
Exp 8	10^{-3} – $3.2 \cdot 10^{-2}$	16 – 89	no	S3	Güttler et al. (2009)
Exp 9	10^{-3} – 10^{-2}	10 – 40	yes	B1	Heißelmann et al. (in prep.)
	10^{-3} – 10^{-2}	5 – 20	yes	B1	
Exp 10	$2 \cdot 10^{-3}$ – $5 \cdot 10^{-3}$	1 – 30	no	B1	Weidling et al. (2009)
Exp 11	$1.6 \cdot 10^{-4}$ – $3.4 \cdot 10^{-2}$	320 – 570	yes	F1	Lammel (2008)
Exp 12	$3.5 \cdot 10^{-15}$	1 500 – 6 000	no	F2	Schräpler and Blum (in prep.)
Exp 13	0.2 – 0.3	1 650 – 3 750	no	F2	Wurm et al. (2005a)
Exp 14	0.2 – 0.3	350 – 2 150	yes	F2	Paraskov et al. (2007)
Exp 15	0.39	600 – 2 400	no	S4	Wurm et al. (2005b)
Exp 16	$4 \cdot 10^{-7}$ – $5 \cdot 10^{-5}$	700 – 850	no	S4	**?**
Exp 17	$1.6 \cdot 10^{-4}$ – $2.0 \cdot 10^{-2}$	100 – 1 000	no	S4	Sect. 4.2.2
Exp 18	10^{-9} – 10^{-4}	10 – 1 000	no	B1, S2, S4	Sect. 4.2.2
Exp 19	$1.5 \cdot 10^{-3}$ – $3.2 \cdot 10^{-3}$	200 – 700	yes	S4, F3	Sect. 4.2.2

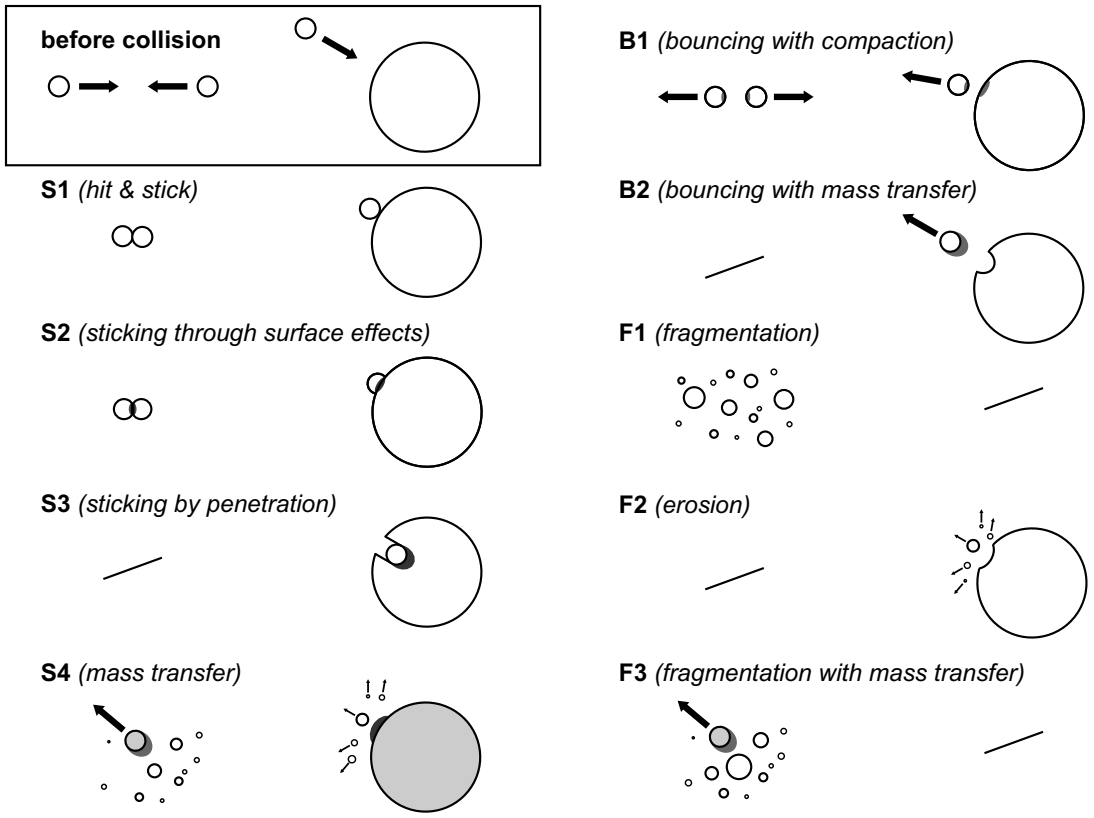

Figure 4.1: We classify the variety of laboratory experiments into nine types of collisional outcomes, involving sticking (S), bouncing (B) and fragmenting (F) collisions. All these collision types have been observed in laboratory experiments and detailed quantities on the outcomes can be given in Sect. 4.3. These experiments also showed that we have to distinguish between collisions of similar-sized aggregates (left columns) and different-sized aggregates (right columns) and some types only occur for one of these cases (e.g. S3).

collisions show a diversity of different outcomes for which we classify nine different collision types as displayed in Fig. 4.1. Details on these collision types are presented in Sect. 4.3.

4.2.1 A Short Review on Collision Experiments

We briefly review published results of dust-collision experiments here since these determine the collisional mapping in Sect. 4.3 and 4.4. The interested reader is referred to the review by Blum and Wurm (2008) for more information. All experiments are compiled and referenced in Table 4.1 where we also list the collision velocities and projectile masses as these will be used in Sect. 4.4. Most of the experiments in Table 4.1 (exception: Exp 10) were performed under low gas pressure conditions to match the situation in PPDs and most of the experiments were carried out in the absence of gravity (i.e. free falling aggregates or micro-gravity facilities), see column 4 of Table 4.1. For the majority of

the experiments, spherical monodisperse SiO_2 monomers with diameters between 1.0 μm and 1.9 μm were used; some experiments used irregular SiO_2 grains with a wider size distribution centered around $\sim$ 1.0 μm, and Exp 5 used irregular $ZrSiO_4$ with monomer diameters in the range $0.2 \ldots 1.0$ μm.

Exp 1 – 4: A well-known growth mechanism for small dust aggregates is the hit-and-stick growth, in which the aggregates collide with such a small kinetic energy that they stick at each other upon first contact without any restructuring. The first experiments to unambiguously show that the hit-and-stick process is relevant to protoplanetary dust aggregation were those by Wurm and Blum (1998), Blum et al. (1998, 2000, 2002) and Krause and Blum (2004). These proved that, as long as the collision velocities for small dust aggregates stay well below 100 cm s^{-1}, sticking collisions lead to the formation of fractal aggregates. This is in agreement with the molecular-dynamics simulations by Dominik and Tielens (1997) and Wada et al. (2007, 2008). The various experimental approaches for Exp 1 – 3 used all known sources for relative grain velocities in PPDs, i.e. Brownian motion (Exp 3), relative sedimentation (Exp 1), and gas turbulence (Exp 2). In these papers it was also shown that the hit-and-stick growth regime leads to a quasi-monodisperse evolution of the mean aggregate masses, depleting small grains efficiently and rapidly. For collisions between these fractal aggregates and a solid or dusty target, Blum and Wurm (2000, Exp 4) found growth at even higher velocities, in which the aggregates were restructured. This is also in agreement with molecular-dynamics simulations (Dominik and Tielens, 1997), and so this first stage of protoplanetary dust growth has so far been the only one that could be fully modeled.

Exp 5: Blum and Münch (1993) performed collision experiments between free falling $ZrSiO_4$ aggregates of intermediate porosity ($\phi = 0.35$, where ϕ is the volume fraction of the solid material) at velocities in the range 15 – 390 cm s^{-1}. They never found sticking, but, depending on the collision velocity, the aggregates bounced ($v < 100$ cm s^{-1}) or fragmented into a power-law size distribution ($v > 100$ cm s^{-1}). The aggregate masses were varied over a wide range (10^{-5} to 7×10^{-3} g) and also the mass ratio of the two collision partners ranged from 1:1 to 1:66. The major difference to experiments 1 – 4 which inhibited sticking in these collisions were the aggregate masses and their non-fractal but still very porous nature.

Exp 6 – 8: A new way of producing highly porous, macroscopic dust aggregates ($\phi = 0.15$ for 1.5 μm diameter SiO_2 monospheres) as described by Blum and Schräpler (2004) allowed new experiments, using the 2.5 cm diameter aggregates as targets and fragments of these as projectiles (Langkowski et al., 2008, Exp 6). In their collision experiments in the Bremen drop tower, Langkowski et al. (2008) found that the projectile may either bounce off from the target at intermediate velocities (50 – 250 cm s^{-1}) and aggregate sizes (0.5 – 2 mm), or stick to the target for higher or lower sizes and velocities, respectively. This bouncing went with a previous slight intrusion and a mass transfer from the target to the projectile. In the case of small and slow projectiles, the projectile stuck to the target, while large and fast projectiles penetrated into the target and were geometrically embedded. They also found that the surface roughness plays an important role for the sticking efficiency. If a projectile hits into a surface depletion it sticks while it

bounces off when hitting onto a hill with a small radius of curvature comparable to that of the projectile. A similar behavior for the sticking by deep penetration was also found by Blum and Wurm (2008, Exp 7) when the projectile aggregate is compact – a mm-sized glass bead in their case. Continuous experiments on the penetration of a solid projectile (1 to 3 mm diameter) into the highly porous target (Blum and Schräpler, 2004) were performed by Güttler et al. (2009, Exp 8) who studied this setup for the calibration of a smoothed particle hydrodynamics (SPH) collision model. We will use their measurement of the penetration depth of the projectile.

Exp 9 – 10: As a follow-up experiments of the study of Blum and Münch (1993), Heißelmann, Fraser and Blum (in prep., Exp 9) used 5 mm cubes of these highly porous dust aggregates and collided them with each other ($v = 40$ cm s^{-1}) or with a compact dust target ($v = 20$ cm s^{-1}). In both cases they also found bouncing of the aggregates and were able to confirm the low coefficient of restitution ($v_{\mathrm{after}}/v_{\mathrm{before}}$) of $\varepsilon = 0.2$ for central collisions. In their experiments they could not see any deformation of the aggregates, due to the limited resolution of their camera, which could have explained the dissipation of energy. This was followed up by Weidling et al. (2009, Exp 10) who studied the compaction of the same aggregates, which repeatedly collided with a solid target. They found that the aggregates decreased in size (without losing significant amounts of mass) which is a direct measurement of their porosity. After only 1 000 collisions the aggregates were compacted by a factor of two in volume filling factor and the maximum filling factor for the velocity used in their experiments (1 – 30 cm s^{-1}) was found to be $\phi = 0.36$. In four out of 18 experiments, the aggregate broke into few pieces and they derived a fragmentation probability of $P_{\mathrm{frag}} = 10^{-4}$ for the aggregate to break in a collision.

Exp 11: Also using fragments of the high porosity dust aggregates of Blum and Schräpler (2004) as well as intermediate porosity ($\phi = 0.35$) aggregates, Lammel (2008, Exp 11) followed up the fragmentation experiments of Blum and Münch (1993). For velocities from 320 to 570 cm s^{-1} he found fragmentation and measured the size of the largest fragment as a measure for the fragmentation strength.

Exp 12 – 14: Exposing the same highly porous dust aggregate to a stream of single monomers with a velocity from 1 500 to 6 000 cm s^{-1}, Schräpler and Blum (in prep., Exp 12) found a significant erosion of the aggregate. One monomer impact can easily kick out tens of monomers for the higher velocities examined. From an analytic model, they estimated the minimum velocity for this process to be approx. 350 cm s^{-1}. On a larger scale, Wurm et al. (2005a, Exp 13) and Paraskov et al. (2007, Exp 14) impacted dust projectiles with masses of 0.2 to 0.3 g and solid spheres into loosely packed dust targets. In the drop-tower experiments of Paraskov et al. (2007) they were able to measure the mass loss of the target which was – velocity dependent – up to 35 projectile masses. The lowest velocity in these experiment was 350 cm s^{-1}.

Exp 15 – 16: In a collision between a projectile of intermediate porosity and a compressed dust target at a velocity above 600 cm s^{-1}, Wurm et al. (2005b, Exp 15) found fragmentation of the projectile but also an accretion of mass onto the target. Depending on the collision velocity, this accretion was up to 0.6 projectile masses in a single collision. **?**, Exp 16 studied this partial sticking in many collisions, where solid targets of variable

sizes were exposed to 100 to 500 μm diameter dust aggregates with a mean velocity of 770 cm s^{-1}. Although they cannot give an accretion efficiency in a single collision, they found a large amount of mass accretion onto the targets, which is a combination of the pure partial sticking and the effects of the Earth's gravity. **?** argue that this acceleration is equivalent to the acceleration that micron-sized particles would experience as a result of their erosion from a much bigger body that had been (partially) decoupled from the gas motion in the solar nebula.

4.2.2 New Experiments

In this section, we will present new experiments which we performed to fill some parameter regions where no published data existed so far. All experiments cover collisions between porous aggregates with a solid target and were performed with the same experimental setup, consisting of a vacuum chamber (less than 0.1 mbar pressure) with a dust accelerator for the porous projectiles and an exchangeable target. The accelerator comprises a 50 cm long, 3 cm diameter plastic rod in a vacuum feed through. The pressure difference between the ambient air and the pressure in the vacuum chamber drives a constant acceleration, leading to a projectile velocity of up to 900 cm s^{-1}, when the accelerator is abruptly stopped. The porous projectile flies on and collides either with a solid glass plate (Sect. 4.2.2 and 4.2.2) or with a free falling glass bead which is dropped when the projectile is accelerated (Sect. 4.2.2). The collision is observed with a high-speed camera to determine aggregate and fragment sizes and to distinguish between the collisional outcomes (i.e. sticking, bouncing, and fragmentation). The experiments in this section are also listed in Table 4.1 as Exp 17 to 19.

Fragmentation with Mass Transfer (Exp 17)

In this experiment, mm-sized aggregates of different volume filling factors ($\phi = 0.15$ and $\phi = 0.35$) collided with a flat and solid glass target and fragmented as the collision velocity was above the fragmentation threshold of approx. 100 cm s^{-1}. The projected projectile size and its velocity were measured by a high-speed camera (see Fig. 4.2). In few experiments, the sizes of the produced fragments were measured for those fragments that were sharply resolved, which yielded a size distribution of a representative number of fragments (the number of resolved fragments varied from 100 to 400). Assuming a spherical shape of the fragments and an unchanged porosity from the original projectile, we calculated a cumulative mass distribution as shown in Fig. 4.3, where the cumulative mass fraction $\sum_{i=0}^{k}(m_\mathrm{i}/M_\mathrm{F})$ is plotted over the normalized fragment mass $m_\mathrm{k}/m_\mathrm{p}$. Here, m_i and $M_\mathrm{F} = \sum_{i=1}^{N} m_\mathrm{i}$ are the mass of the i-th smallest fragment and the total mass of all visible fragments and N is the total number of fragments. We found that the cumulative distribution can well be described by a power law

$$\int_0^m n(m')m' \,\mathrm{d}m' = \left(\frac{m}{\mu}\right)^{\kappa}, \tag{4.1}$$

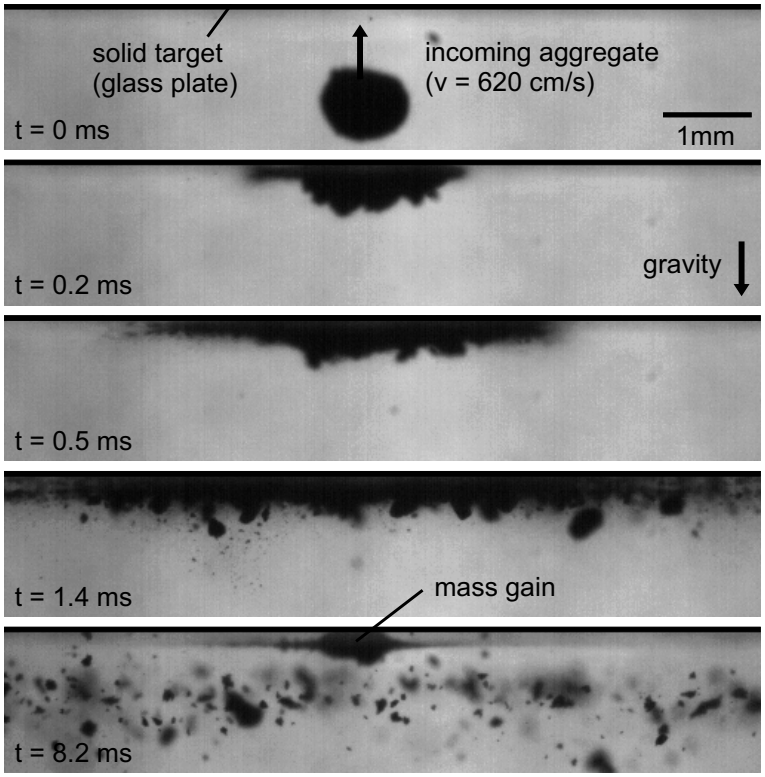

Figure 4.2: Example for a collision of a porous ($\phi = 0.35$) aggregate with a solid target at a velocity of 620 cm s^{-1}. The aggregate fragments according to a power-law size distribution and some mass sticks to the target (bottom frame).

where m' and m are the mass of the fragments in units of the projectile mass and μ is a parameter to measure the strength of fragmentation, being defined as the mass of the largest fragment divided by the mass of the original projectile. The deviation between data and power-law for low masses (see Fig. 4.3) is due to the finite resolution of the camera, which could not detect fragments with sizes $\ll 50$ μm. In the 10 experiments where the mass distribution was determined, the power-law index κ was nearly constant from 0.64 to 0.93, showing no dependence in velocity which was varied from 120 to 840 cm s^{-1}. However, a clear dependence on the velocity was found for the parameter μ, which decreased with increasing velocity as shown in the inset of Fig. 4.3. This increasing strength of fragmentation can be described as

$$\mu(v) = 1.27 \left(\frac{v}{100 \text{ cm s}^{-1}} \right)^{-1.87} \tag{4.2}$$

for $v \geq 114$ cm s^{-1}.

It is important to know that the number density of fragments of a given mass follows from Eq. 4.1 as

$$n(m') = \frac{\kappa}{\mu^{\kappa}} m'^{\kappa-2}, \tag{4.3}$$

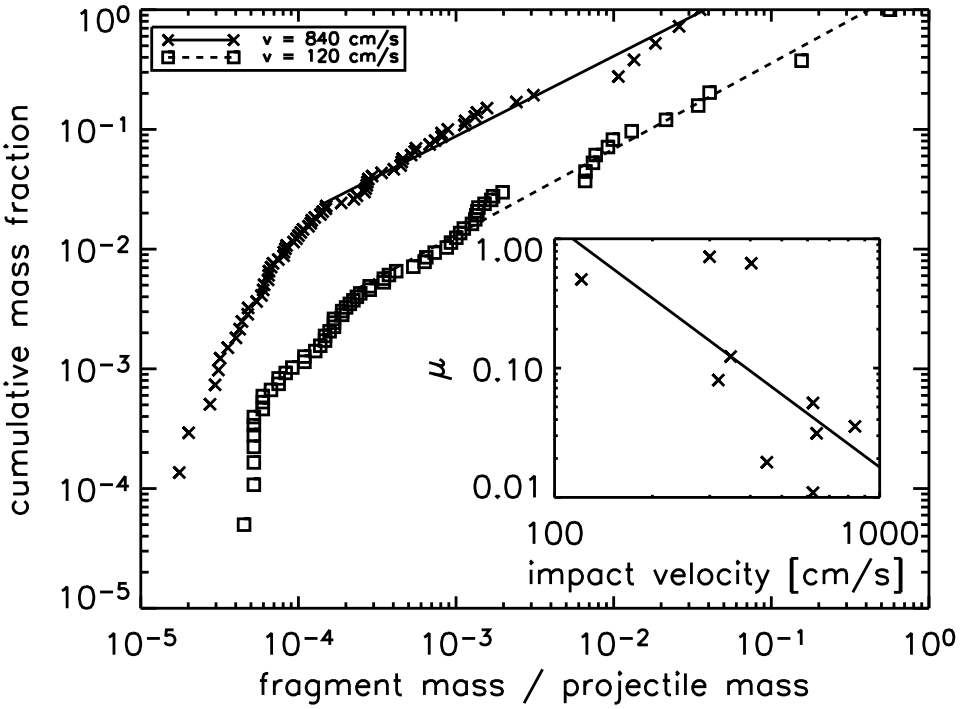

Figure 4.3: Mass distribution for two experiments at the extreme velocities of 120 and 840 cm s^{-1}. For the higher masses, the distribution follows a power law while the lower masses are depleted due to the finite camera resolution. The slopes are the same for both experiments and there is only an offset (pre-factor) between the two. The inset describes this pre-factor μ (cf. Eq. 4.1) which is a measure for the strength of the fragmentation. The value clearly decreases with increasing velocity.

and that the power law for this mass distribution can be translated into a power-law size distribution $n(a) \propto a^{\lambda}$ with $\lambda = 3\kappa - 4$. This yields λ values from -2.1 to -1.2, much flatter than the power-law index of -3.5 from the MRN distribution (Mathis et al., 1977), which is widely used for the description of high-speed fragmentation of *solid* materials. Moreover, this power-law index is consistent with measurements of Blum and Münch (1993) who studied aggregate-aggregate collisions between millimeter-sized $ZrSiO_4$ aggregates (see Sect. 4.2). Their power-law index, equivalent to λ was -1.4, and for different velocities they also found a constant power-law index and a velocity-dependent pre-factor (their Fig. 8a).

While most of the projectile mass fragmented into a power-law distribution, some mass fraction stuck to the target (see bottom frame in Fig. 4.2). Therefore, the mass of the target was weighed before the collision and again after 19 shots on the same spot. The mass of each projectile was weighed which yielded a mean value of 3.34 ± 0.84 mg per projectile. The increasing mass of the target in units of the projectile mass is plotted in Fig. 4.4. After 57 collisions, dust chipped off the target which can clearly be accounted to the gravitational influence. For the following measurements we therefore added one projectile mass to the target because we found good agreement with the foregoing values

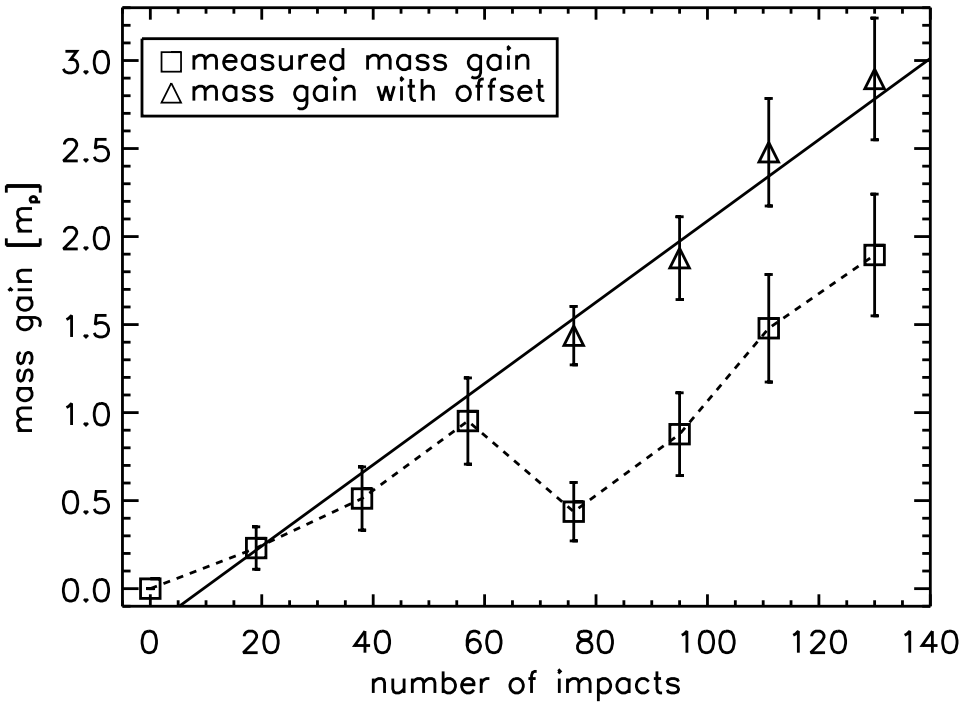

Figure 4.4: Mass gain of a solid target in 133 collisions (S. Kothe, C. Güttler & J. Blum, unpublished data). The target was weighed after every 19 collisions. After 57 collisions, one projectile mass of dust chipped off from the target, which is a clear effect of gravity. Thus, we added this mass to the following measurements (triangles) and fitted a linear mass gain, which is $0.023 \times m_\mathrm{p}$ in every collision (solid line).

for this offset. The measurements were linearly fitted and the slope, which determines the mass gain in a single collision, is 2.3 % (S. Kothe, C. Güttler & J. Blum, unpublished data).

Impacts of Small Aggregates (Exp 18)

Using exactly the same setup as in the previous section, we performed collision experiments with very small (20 μm to 1.4 mm diameter) but non-fractal projectiles. Those aggregates were fragments of larger dust samples as described by Blum and Schräpler (2004) and had a volume filling factor of $\phi = 0.15$. In this experiment we observed not only fragmentation but also bouncing and sticking of the projectiles to the solid glass target. Thus, the analysis with the high-speed camera involved the measurement of projectile size, collision velocity, and collisional outcome, where we distinguished between (1) perfect sticking, (2) perfect bouncing without mass transfer, (3) fragmentation with partial sticking, and (4) bouncing with partial sticking. The difference between the cases (3) and (4) is that in a fragmentation event at least two rebounding aggregates were produced, whereas in the bouncing collision only one aggregate bounced off.

For the broad parameter range in diameter (20 to 1 400 μm) and velocity (10 to

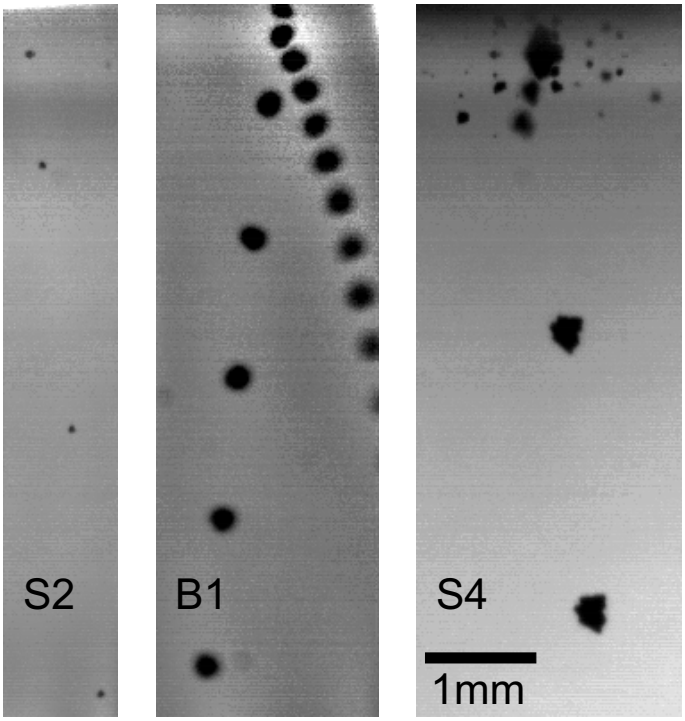

Figure 4.5: Examples for the experimental outcomes in the collisions of small aggregates with a solid target. The collision can lead to sticking, bouncing, or fragmentation (from left to right). The time between two exposures is 2 ms.

1 000 cm s^{-1}), we performed 403 individual collisions in which we were able to measure size, velocity, and collisional outcome. Examples for sticking, bouncing, and fragmentation are shown in Fig. 4.5. The full set of data is plotted in Fig. 4.6, where different symbols were used for different collisional outcomes. Clearly, collisions of large aggregates and high velocities lead to fragmentation, while small aggregates rather bounce off the target. For intermediate aggregate mass (i.e. $m_\mathrm{p} = 10^{-7}$ g), all types of collisions can occur. The background color shows a sticking probability which was calculated as a boxcar average (logarithmic box) at every node where an experiment was performed. Blue color denotes a poor sticking probability while a green to yellow color shows a sticking probability of approx. 50 %. We draw the solid lines in a polygon [$(100, 70, 800, 200, 200, 17)$ cm s^{-1}, $(1.6\cdot10^{-4}, 5\cdot10^{-7}, 1\cdot10^{-7}, 8\cdot10^{-10}, 1\cdot10^{-8}, 1\cdot10^{-8})$ g] to mark the border between sticking and non-sticking as we will use it in Sect. 4.4. For the higher masses, this accounts for a bouncing-fragmentation threshold of 100 cm s^{-1} at $1.6\cdot10^{-4}$ g (Exp 18) and for the lower masses, we assume a constant fragmentation threshold of 200 cm s^{-1}, which is in rough agreement with the restructuring-fragmentation threshold of Blum and Wurm (2000, Exp 4). For lower velocities outside the solid-line polygon, bouncing collisions are expected, whereas for higher velocities outside the polygon, we expect fragmentation. Thus, an island of enhanced sticking probability for 10^{-7} – 10^{-7} g aggregates at a broad velocity range from 30 to 500 cm s^{-1} was rather unexpected before. The dotted box is just a

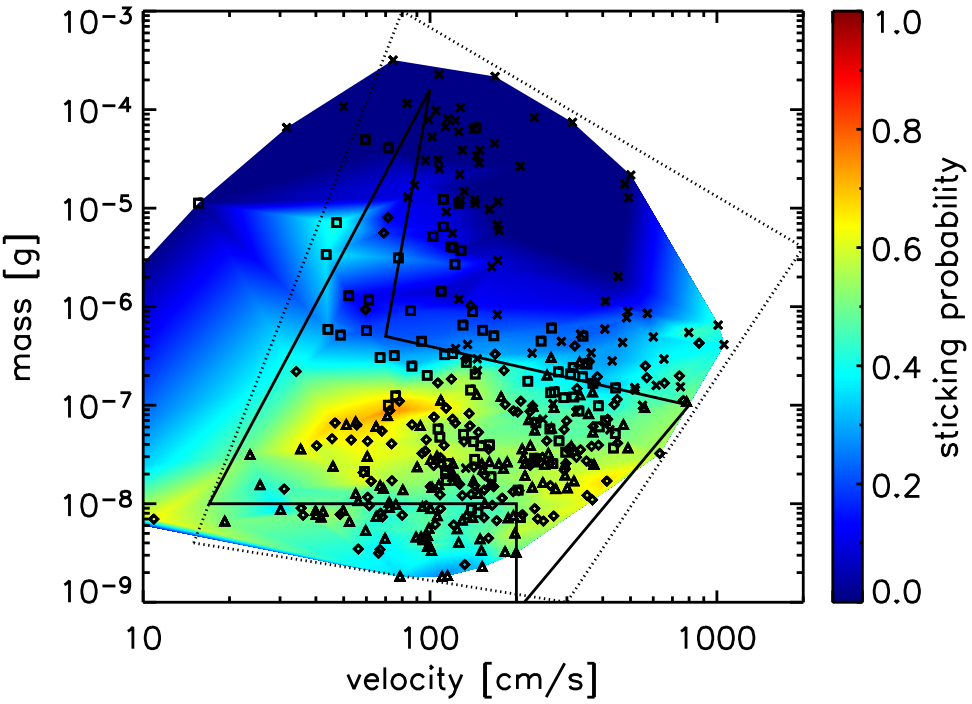

Figure 4.6: Overview on collision experiments between 20 to 1 400 μm diameter aggregates and a solid target, which leads to sticking (diamonds), bouncing (triangles), or fragmentation (crosses). The intermediate sticking-bouncing collision type is indicated by the squared symbols. The color indicates the sticking probability, i.e. the fraction of sticking events in a logarithmic bin around every node. The dotted box denotes the approximated parameter range and the solid lines denote the threshold between sticking, bouncing and fragmentation as also used in Fig. 4.11.

rough borderline showing for which parameters the experiments were performed as it will also be used in Sect. 4.4.

Collisions Between Similar Sized Solid and Porous Aggregates (Exp 19)

In a collision between a free falling glass bead of 1 mm diameter and a porous ($\phi = 0.15$) dust aggregate of 1.5 to 8.5 mg mass, we observed fragmentation of the porous aggregate while some mass was growing on the compact and indestructible glass bead (S. Olliges & J. Blum, unpublished data). In this case, the high-speed camera was used with a 3D optics that allowed to image the collision from two angles, separated by 90°. On the one hand, this made it possible to exactly measure the impact parameter b, also if the offset of the two collision partners is in the line of sight of one viewing angle. Moreover, observing the mass growth of the compact projectile is not only a projection in one direction but can be reconstructed to get a 3D measurement. So, the relative velocity and aggregate size were measured from the images before the collision and the mass gain of the compact glass bead was measured after the collision. Figure 4.7 shows a diagram of volume gain in

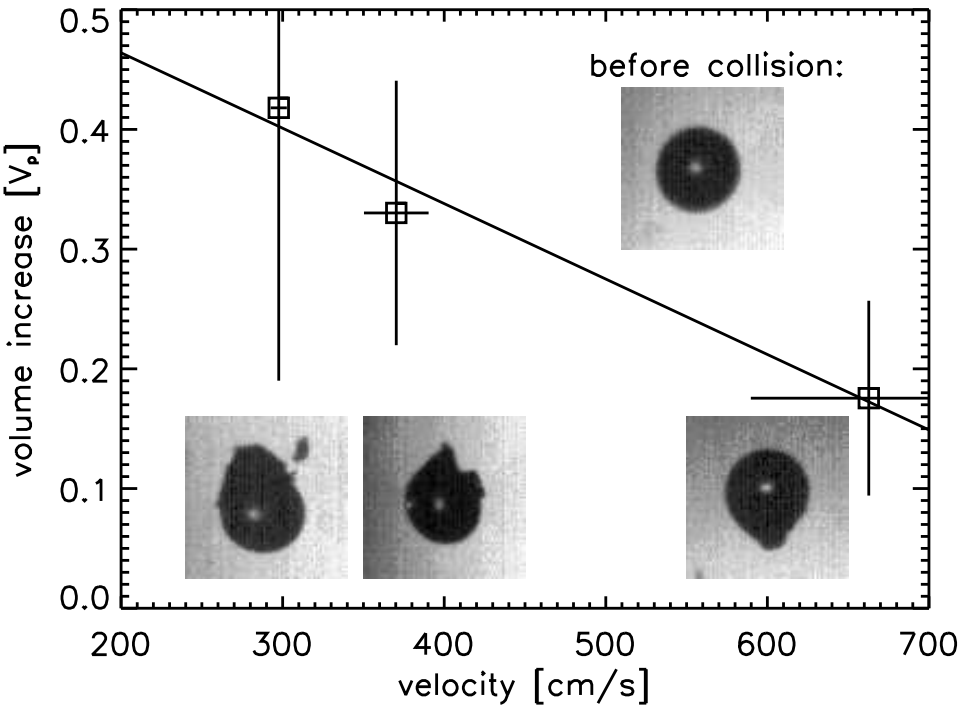

Figure 4.7: The volume gain of a compact particle colliding with a porous aggregate depends on the collision velocity. The data points are mean values of 11, 8, and 7 individual experiments (left to right), thus, the error bars show the 1σ standard deviation of velocities and volume gain in these. The images with a width of 1.9 mm show the original 1 mm glass bead and examples for the mass gain in the three corresponding collision velocities (S. Olliges & J. Blum, unpublished data).

units of projectile volume (projectile: porous aggregate) over the collision velocity. The three data points are averaged over a number of experiments at the same velocity. The error bars denote the 1σ standard deviation of collision velocities and projectile volume, respectively. A clear trend shows that the volume gain of the compact target decreases with velocity and we fitted the data points with

$$\Delta V = V_\mathrm{p} \left(0.59 - 6.3 \times 10^{-4} \frac{v}{\mathrm{cm\ s^{-1}}} \right) \tag{4.4}$$

where V_p is the volume of the glass bead. In this experiment we were not able to measure the size distribution of the fragments because the absolute velocity is determined by the projectile velocity (up to 600 cm s^{-1}), and the faster fragments were out of the frame before they were clearly separated from each other.

4.3 Classification of the Laboratory Experiments

In this section, the experiments outlined above will be categorized according to their physical outcomes in the respective collisions. In Sect. 4.2, we saw that various kinds of

sticking, bouncing, and fragmentation can occur. Here, we will keep all these experiments in mind and classify them according to nine types of possible collisional outcomes that were observed in laboratory experiments. These collisional outcomes are displayed in Fig. 4.1. The denomination of the classification follows S for sticking, B for bouncing, and F for fragmentation. S and F are meant with respect to the target, i.e. the more massive of the two collision partners. We will discuss each of the pictograms in Fig. 4.1, describe the motivation for the respective collision type and physically quantify the outcome of these collisions.

(1) *Sticking Collisions:* A well known growth mechanism is due to hit-and-stick (S1) collisions. Hit-and-stick growth was observed in the laboratory (Blum and Wurm, 2000, Blum et al., 2000) and numerically described (Dominik and Tielens, 1997). Experiments show that the mass distribution during the hit-and-stick (S1) phase is always quasi-monodisperse. The evolution of the mean mass within an ensemble of dust aggregates due to hit-and-stick collisions was calculated to follow a power law in time, in good agreement with the experiments (Wurm and Blum, 1998, Krause and Blum, 2004). Dominik and Tielens (1997) showed theoretically and Blum and Wurm (2000) confirmed this experimentally that small fractal aggregates stick at first contact if their collision energy is smaller than a threshold energy. For higher energies, experiments showed that an aggregate is elastically and plastically deformed at the contact zone (Blum and Münch, 1993, Weidling et al., 2009). This increases the number of contacts, which then can lead to sticking at higher velocities, an effect we call sticking through surface effects (S2). Langkowski et al. (2008) found that sticking can occur for even larger velocities, if the target aggregate is porous and significantly larger than the projectile. In this case, the projectile sticks by deep penetration (S3) into the target and cannot rebound, simply because of geometrical considerations. This effect holds also true if the projectile aggregate is compact, which has been shown by Blum and Wurm (2008) and further studied by Güttler et al. (2009). In Sect. 4.2.2, we saw that the growth of a solid target can occur if a porous projectile fragments and partially sticks to the target surface (S4). This growth mechanism was already described by Wurm et al. (2005b). **?** found it to be an efficient growth mechanism in multiple collisions.

(2) *Bouncing Collisions:* If the collision velocity of two dust aggregates is too low for fragmentation and too high for sticking to occur, the dust aggregates will bounce (B1). Heißelmann et al. (in prep.) found highly inelastic bouncing between similar-sized porous dust aggregates and between a dust aggregate and a dusty but rather compact target, where 95 % of the kinetic energy were dissipated. Weidling et al. (2009) showed that the energy can effectively be dissipated by a significant (and for a single collision undetectable) compaction of the porous aggregates after multiple collisions (collision type bouncing with compaction (B1)). Another type of bouncing occurred in the experiments of Langkowski et al. (2008) in which a porous projectile collided with a significantly bigger and also highly porous target aggregate. If the penetration of the aggregate was too shallow for the S3 sticking to occur, the projectile bounced off and took away mass from the target aggregate. This bouncing with mass transfer (B2) was also observed in the case of compact projectiles (Blum and Wurm, 2008).

(3) *Fragmenting Collisions:* Fragmentation (F1), i.e. the breakup of the dust aggregates, occurs in collisions between similar-sized dust aggregates at a velocity above the fragmentation threshold. Blum and Münch (1993) showed that both aggregates are then disrupted into a power-law size distribution. If a target aggregate is exposed to impacts of single monomer grains or very small dust aggregates, Schräpler and Blum (in prep.) found that the target aggregate is efficiently eroded (F2) if the impact velocities exceed 1 500 cm s^{-1}. This mass loss of the target was also observed in the case of larger projectiles into porous targets (Wurm et al., 2005a, Paraskov et al., 2007). Similar to the F1 fragmentation, it may occur that one aggregate is porous while the other one is compact. In that case, the porous aggregate fragments but cannot destroy the compact aggregate. The compact aggregate accretes mass from the porous aggregate (Sect. 4.2.2). We call this fragmentation with mass transfer (F3).

These nine fundamental types of collisions are all based on firm laboratory results. Future experiments will almost certainly modify this picture and potentially add so far unknown collision types to this list. However, at the present time this is the complete picture of possible collisional outcomes. In the following we will quantify the thresholds and boundaries between the different collision regimes as well as physically characterize the collisional outcomes therein.

S1: Hit-and-Stick Growth

Hit-and-stick growth occurs when the collisional energy involved is less than $5 \cdot E_{\rm roll}$ (Dominik and Tielens, 1997, Blum and Wurm, 2000), where $E_{\rm roll}$ is the energy which is dissipated when one dust grain rolls over another by an angle of 90°. We can calculate the upper threshold velocity for the hit-and-stick mechanism of two dust grains by using the definition relation between rolling energy and rolling force, i.e.

$$E_{\rm roll} = \frac{\pi}{2} a_0 F_{\rm roll} \ . \tag{4.5}$$

Here, a_0 is the radius of a dust grain and $F_{\rm roll}$ is the rolling force. Thus, we are inside the hit-and-stick regime if

$$\frac{1}{2} m_\mu v^2 \leq 5 E_{\rm roll}, \tag{4.6}$$

where m_μ is the reduced mass of the aggregates. The hit-and-stick velocity range is then given by

$$v \leq \sqrt{5 \frac{\pi a_0 F_{\rm roll}}{m_\mu}} \ . \tag{4.7}$$

S2: Sticking by Surface Effects

For velocities exceeding the hit-and-stick threshold velocity (Eq. 4.7), we assume sticking because of an increased contact area due to surface flattening and, therefore, an increased number of sticking grain-grain contacts. For the calculation of the contact area, we take

an elastic deformation of the aggregate (Hertz, 1881) and get a radius for the contact area of

$$s_0 = \left[\left(\frac{15}{32} \right) \frac{m_\mu a_\mu^2 v^2}{G} \right]^{\frac{1}{5}} . \tag{4.8}$$

Here, v is the collision velocity, G is the shear modulus, and a_μ is the reduced radius. The energy of a pair of bouncing aggregates after the collision is

$$E_{\text{rest.}} = \varepsilon^2 \frac{1}{2} m_\mu v^2 \tag{4.9}$$

with the coefficient of restitution ε. The contact energy of the flattened surface in contact is

$$E_{\text{cont.}} = s_0^2 \frac{\phi^{\frac{2}{3}} E_0}{a_0^2}, \tag{4.10}$$

where E_0 is the sticking energy of a monomer grain with radius a_0. We expect sticking for $E_{\text{cont.}} \geq E_{\text{rest.}}$, thus,

$$\left[\left(\frac{15}{32} \right) \frac{m_\mu a_\mu^2 v^2}{G} \right]^{\frac{2}{5}} \frac{\phi^{\frac{2}{3}} E_0}{a_0^2} \geq \varepsilon^2 \frac{1}{2} m_\mu v^2 \quad \text{or} \tag{4.11}$$

$$v \leq \left[\left(\frac{15}{32} \right) \frac{m_\mu a_\mu^2}{G} \right]^{\frac{1}{3}} \left[\frac{2\phi^{\frac{2}{3}} E_0}{a_0^2 m_\mu \varepsilon^2} \right]^{\frac{5}{6}} . \tag{4.12}$$

This is the sticking threshold velocity for sticking through surface effects (S2), which is based on the Hertzian deformation which is of course a simplified model but has proven as a good concept in many attempts to describe slight deformation of porous dust aggregates (Langkowski et al., 2008, Weidling et al., 2009).

We have to ensure that the centrifugal force of two rotating aggregates, sticking like above, does not tear them apart, which is the case if

$$F_{\text{cent}} > T \pi s_0^2, \tag{4.13}$$

where T is the tensile strength of the aggregate material. The centrifugal force in the worst case of a perfectly grazing collision is

$$F_{\text{cent}} = \frac{m_\mu \varepsilon^2 v^2}{2 a_\mu} , \tag{4.14}$$

where $2a_\mu$ is a conservative estimation for the radial distance of the masses with tangential velocity εv. Thus, only collisions with velocities

$$v < \left[\left(\frac{15}{32} \right) \frac{m_\mu a_\mu^2}{G} \right]^{\frac{1}{3}} \left[\frac{2\pi T a_\mu}{m_\mu \varepsilon^2} \right]^{\frac{5}{6}} \tag{4.15}$$

can lead to sticking. For the relevant parameter range (see Table 4.2 below), the threshold velocity in Eq. 4.15 is always significantly greater than the sticking velocity in Eq. 4.12, thus, we can take Eq. 4.12 as the relevant velocity for process S2.

We will use this type of sticking not only within the mass and velocity threshold as defined by Eq. 4.12 but also for collisions where we see sticking which can so far not be explained by any model like in experiment 6 or 18. For all these cases, we assume the porosity of target and projectile to be unchanged, disregarding any slight compaction as needed for the deformation. One exception is the sticking of small, fractal aggregates, which clearly goes together with a compaction of the projectile (Dominik and Tielens, 1997, Blum and Wurm, 2000). In these cases we assume a projectile compaction by a factor of 1.5 in volume filling factor as there is no precise measurement on this compaction.

S3: Sticking by Deep Penetration

If the target aggregate is much larger than the projectile, porous and flat, an impact of a (porous or compact) projectile results in its penetration into the target. Sticking is inevitable if the penetration of the projectile is deep enough, i.e. deeper than one projectile radius. In that case, the projectile cannot bounce off the target from geometric considerations. This was found in experiments of Langkowski et al. (2008) in the case of porous projectiles and Blum and Wurm (2008) in the case of compact projectiles. The result of the collision for penetration depths $D_\mathrm{p} \geq a_\mathrm{p}$ is that the mass of the target is augmented by the mass of the projectile and the volume of the new aggregate reads

$$V = V_\mathrm{t} - \pi a_\mathrm{p}^2 \left(D_\mathrm{p} - a_\mathrm{p}\right) + \frac{1}{2} V_\mathrm{p} \tag{4.16}$$

$$= V_\mathrm{t} + \frac{5}{4} V_\mathrm{p} - \pi a_\mathrm{p}^2 D_\mathrm{p} \,, \tag{4.17}$$

with V_p and V_t being the volume of the projectile and target, respectively. We distinguish between compact and porous projectiles and take the experiments of Güttler et al. (2009) and Langkowski et al. (2008) for impacts into $\phi = 0.15$ dust aggregates and calculate the sticking threshold velocities.

For *compact* projectiles, we use the linear relation for the penetration depth of Güttler et al. (2009)

$$D_\mathrm{p} = \gamma \frac{m_\mathrm{p} v}{A_\mathrm{p}} \,, \tag{4.18}$$

where $m_\mathrm{p} = \frac{4}{3}\pi\rho_0\phi_\mathrm{p} a_\mathrm{p}^3$ and $A_\mathrm{p} = \pi a_\mathrm{p}^2$ are the projectile mass and cross section, respectively. Although Güttler et al. (2009) suggest a power-law relation for the penetration depth, i.e. $D_\mathrm{p} = \gamma m_\mathrm{p}^{0.23\pm0.13} v^{0.89\pm0.34}$, we choose the linear relation in Eq. 4.18 for simplicity which is also in agreement with the data within the error bars. For such a linear fit, the slope to the data in Güttler et al. (2009) is $\gamma = 8.3 \cdot 10^{-3}$ cm^2 s g^{-1}. We assume sticking for $D_\mathrm{p} \geq a_\mathrm{p}$ and get sticking due to process S3 in the velocity range

$$v \geq \left(\frac{4}{3}\gamma\rho_0\phi_\mathrm{p}\right)^{-1} \,, \tag{4.19}$$

which only depends on the projectile bulk density ρ_0 and filling factor ϕ_p and not on projectile radius.

A *porous* projectile, colliding with a porous target, makes a visible indentation into the target aggregate if the kinetic energy is $E > E_\mathrm{min}$, with a material-dependent minimum energy E_min. The crater volume is then given by

$$V_\mathrm{cr.} = \left(\frac{E}{E_\mathrm{t}}\right)^{\frac{3}{4}} \mathrm{cm}^3 \,, \tag{4.20}$$

(see Fig. 15 in Langkowski et al., 2008). Again, from geometrical considerations, we assume that sticking occurs if the projectile penetrates at least one radius deep, thus, $V_\mathrm{cr.} \geq 0.5 V_\mathrm{p}$, where $V_\mathrm{p} = \frac{4}{3}\pi a_\mathrm{p}^3$ is the volume of the projectile. Thus,

$$\left(\frac{E}{E_\mathrm{t}}\right)^{\frac{3}{4}} \geq \frac{1}{2} V_\mathrm{p} \tag{4.21}$$

$$\frac{1}{2} m v^2 \geq E_\mathrm{t} \left(\frac{1}{2}\frac{m}{\rho}\right)^{\frac{4}{3}} \tag{4.22}$$

$$v \geq \left(\frac{m E_\mathrm{t}^3}{2\rho_0^4 \phi_\mathrm{p}^4}\right)^{\frac{1}{6}} \,. \tag{4.23}$$

For these velocities, the projectile is inevitably embedded into the target aggregate. However, if the impact energy is less than E_min, the collision will not lead to a penetration so that the final condition for sticking of a porous projectile according to process S3 is

$$v \geq \max\left(\sqrt{\frac{2E_\mathrm{min}}{m}}, \left(\frac{m E_\mathrm{t}^3}{2\rho_0^4 \phi_\mathrm{p}^4}\right)^{\frac{1}{6}}\right) \,. \tag{4.24}$$

S4: Partial Sticking in Fragmentation Events

As introduced in Sect. 4.2.2, a fragmenting collision between a porous aggregate and a solid target can lead to a partial growth of the target. The mass transfer from the projectile to the target is typically 2.3 % of the projectile mass (Fig. 4.4) and without better knowledge we assume that the transferred mass has a volume filling factor of $1.5\phi_\mathrm{p}$. The remaining mass of the projectile fragments according to the power-law mass distribution given in Eq. 4.3 for velocities $v \geq 134$ cm s^{-1}, with the fragmentation strength from Eq. 4.2.

For a compact projectile aggregate impacting a compact target, the threshold velocity for the S4 process is identical to that of the F1 process (see Eq. 4.38). The fragmentation strength is given by Eq. 4.36.

B1: Bouncing with Compaction

In a bouncing collision we find compaction of the two collision partners. For similar-sized aggregates, the increase of the volume filling factor was formulated by Weidling et al.

(2009, their Eq. 25) to be

$$\phi^+(\phi) = \frac{\phi_{\max}(v) - \phi}{\nu(v)} \; ; \;\; \phi^+(\phi, v) > 0 \tag{4.25}$$

with $\nu(v) = \nu_0 \cdot (v/20 \text{ cm s}^{-1})^{-4/5}$, $\phi_{\max}(v) = \phi_0 + \Delta\phi \cdot (v/20 \text{ cm s}^{-1})^{4/5}$ and $\nu_0 = 850$, $\phi_0 = 0.15$, $\Delta\phi = 0.215$ for $v \leq 50$ cm s^{-1}. Here, $\phi_{\max}$ is the saturation of the filling factor after many collisions, which follows an exponential function with the e-folding width ν (Weidling et al., 2009). In their experiments, v was the velocity of a porous projectile colliding with a solid target (infinite mass). In the case of similar-sized colliding aggregates, the velocity would be $0.5 \cdot v$ for each aggregate in a center-of-mass system. Therefore, we scale the velocity as

$$v_{\rm p} = \frac{v}{1 + \frac{m_{\rm p}}{m_{\rm t}}} \tag{4.26}$$

$$v_{\rm t} = \frac{v}{1 + \frac{m_{\rm t}}{m_{\rm p}}} \; , \tag{4.27}$$

where $v_{\rm p}$ ($v_{\rm t}$) is the center-of-mass velocity of the projectile (target). In the case of $m_{\rm p} \ll m_{\rm t}$ we have the situation of Weidling et al. (2009) with $v_{\rm p} = v$, thus, these velocities are chosen to calculate the scaling of $\nu(v)$ and $\phi_{\max}(v)$ for projectile and target compaction, respectively. This means that a projectile with negligible mass with respect to the target cannot compact the target but is only compacted by itself, while two aggregates of the same mass are equally compacted.

For $\phi_{\max}(v)$, Weidling et al. (2009) gave the above relation which is biased by the experimentally used dust samples and overestimates the compression for very low velocities. Therefore, we propose an alternative scaling relation for $\phi_{\max}(v)$. In a collision with velocity v we can calculate a dynamic pressure

$$p_{\rm dyn} = \nu(v) \cdot \frac{1}{2}\rho v^2 \; . \tag{4.28}$$

This pressure is increased by a factor $\nu(v)$ as we know from the experiments of Weidling et al. (2009) that the contact area is very small (factor $1/\nu$ of the aggregate surface) and that only a very confined volume is compressed. For $v = 20$ cm s^{-1} the pressure calculated from Eq. 4.28 is very close to the value given by Weidling et al. (2009). From this pressure we calculate the compression from the compressive strength curve which Güttler et al. (2009) derived for collisions:

$$\phi_{\rm comp}(p) = \phi_2 - \frac{\phi_2 - \phi_1}{\exp\left(\frac{\lg p - \lg p_{\rm m}}{\Delta}\right) + 1} \tag{4.29}$$

with $\phi_1 = 0.12$, $\phi_2 = 0.58$, $\Delta = 0.58$, and $p_{\rm m} = 1.3 \times 10^4$ dyn cm^{-2}. This compressive strength curve is also biased from the experiments as its lowest value is $\phi_1 = 0.12$. Assuming the saturation part of the compressive strength curve to be general, we propose

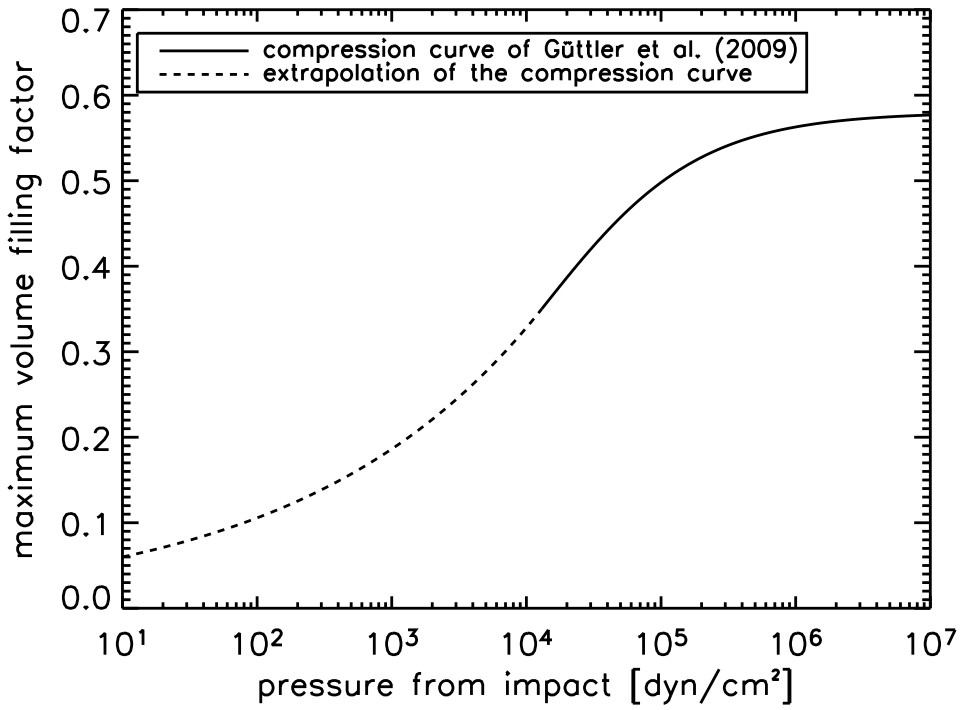

Figure 4.8: The original compressive strength curve measured by Güttler et al. (2009) (Eq. 4.29, solid line) is biased by the dust samples used in the experiments. To describe also the compression of dust aggregates with a volume filling factor lower than those used by Güttler et al. (2009), we extrapolate the curve with a power law (Eq. 4.30, dashed line) for $p < p_\mathrm{m}$.

a power law for $p < p_\mathrm{m}$ with the same slope as in Eq. 4.29 for $\phi_\mathrm{comp}(p_\mathrm{m})$ which is then given by

$$\phi_\mathrm{comp}(p) = \frac{\phi_1 + \phi_2}{2} \cdot \left(\frac{p}{p_\mathrm{m}} \right)^{\frac{\phi_2 - \phi_1}{\phi_2 + \phi_1} \cdot \frac{1}{2\Delta \ln 10}} \tag{4.30}$$

and is able to treat the lowest filling factors and pressures. Equations 4.29 and 4.30 determine the compression in a confined volume. Taking into account that after many collisions only an outer rim of the aggregate is compressed, we reduce the compression by a factor $f_\mathrm{c} = 0.79$ to fit the $\phi_\mathrm{max}(v = 20 \text{ cm s}^{-1}) = 0.365$ experimentally measured by Weidling et al. (2009).

Conclusively, we calculate the increase of the volume filling factor from Eq. 4.25, where ϕ_max is now provided by the dynamical pressure curve as

$$\phi_\mathrm{max}(v) = f_\mathrm{c} \cdot \phi_\mathrm{comp}(p_\mathrm{dyn}) \,, \tag{4.31}$$

where ϕ_comp is given by Eqs. 4.29 and 4.30. For the pressure we use Eq. 4.28 and for the corresponding velocities we use Eqs. 4.26 and 4.27 to calculate projectile and target compression, respectively. The maximum compression $\phi_\mathrm{max}(v)$, which an aggregate can achieve in many collisions at a given velocity, is shown in Fig. 4.8.

Weidling et al. (2009) found that in this bouncing regime, the aggregates can also fragment with a low probability. We adopt this fragmentation probability of

$$P_{\mathrm{frag}} = 10^{-4} \tag{4.32}$$

and assume that an aggregate breaks into two similar-sized fragments as suggested by their Fig. 5.

B2: Bouncing with Mass Transfer

Langkowski et al. (2008) and Blum and Wurm (2008) found, that the collision between a projectile (porous or compact) and a porous target aggregate can lead to a slight penetration of the projectile into the target followed by the bouncing of the projectile. This leads to a mass transfer from the target to the projectile (see Fig. 7 in Langkowski et al., 2008). We assume that the transferred mass is one projectile mass (Fig. 8 in Langkowski et al., 2008), thus,

$$\Delta m_{\mathrm{t}\rightarrow\mathrm{p}} = m_{\mathrm{p}} \tag{4.33}$$

and that the filling factor of the transferred (compacted) material is 1.5 times that of the original target material, i.e.

$$\phi_{\mathrm{t}\rightarrow\mathrm{p}} = 1.5 \times \phi_{\mathrm{t}} \ . \tag{4.34}$$

Although the filling factor of the transferred material was not measured, we know that the material is significantly compacted in the collision (see x-ray micro tomography (XRT) analysis of Güttler et al., 2009) so that the above assumption seems justified.

F1: Fragmentation

When two similar-sized dust aggregates collide at a velocity which is greater than the fragmentation velocity of

$$v_{\mathrm{frag}} = 100 \text{ cm s}^{-1}, \tag{4.35}$$

they will both be disrupted. Blum and Münch (1993) found fragmentation for mm-sized $ZrSiO_4$ dust aggregates with a porosity of $\phi = 0.35$ at a velocity greater than 100 cm s^{-1}. In their experiments, the aggregates fragmented according to a power-law size distribution with an exponent of $\lambda = -1.4$ (see Sect. 4.2.2) which we will use hereafter. The two largest fragments together have a mass of $\mu(v)(m_{\mathrm{p}} + m_{\mathrm{t}})$, where we can determine $\mu(v)$ from the experiments of Blum and Münch (1993, $ZrSiO_4$ aggregate collisions with $\phi = 0.35$) and Lammel (2008, SiO_2 aggregates of different porosities). These values are plotted in Fig. 4.9 and a power-law fit for velocities $v \geq 100$ cm s^{-1}

$$\mu(v) = 0.965 \left(\frac{v}{100 \text{ cm s}^{-1}} \right)^{-0.282} \tag{4.36}$$

is shown by the solid line.

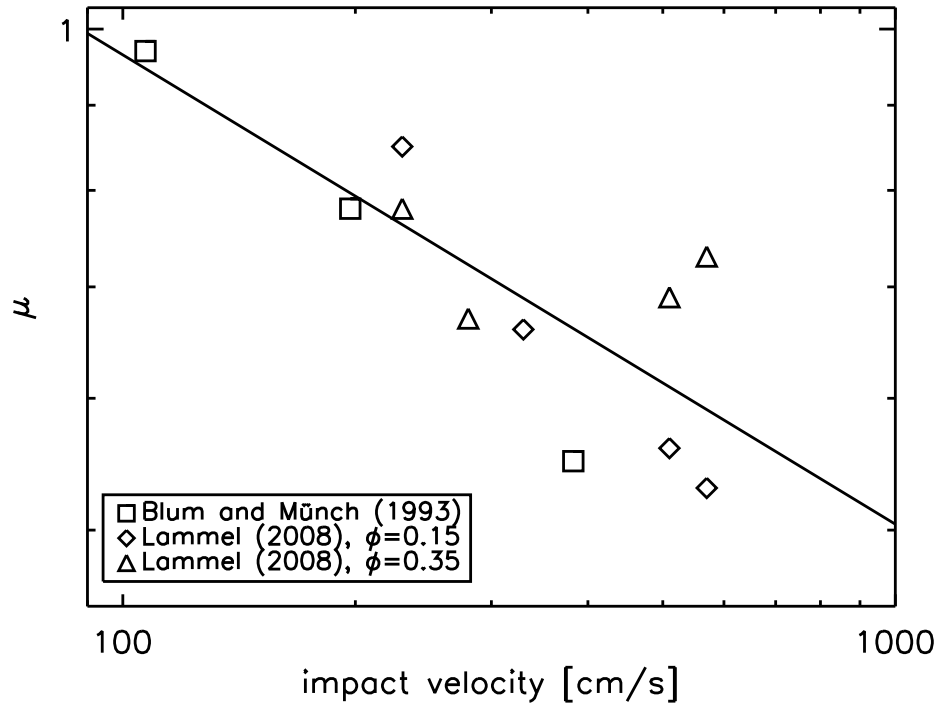

Figure 4.9: The impact strength for aggregate-aggregate collision also increases for higher velocities (decreasing μ, cp. inset in Fig. 4.3). The fitted power law is given by Eq. 4.36.

The fragmentation threshold we generally assume to be 100 cm s^{-1}. However, as most experiments were performed with approximately mm-sized dust aggregates, a slight dependence of the fragmentation threshold in size or mass would not have been observed in these experiments. Such a threshold, based on the strength of the colliding bodies, is however well known for the disruption of kilometer-sized bodies (Benz and Asphaug, 1999). In these studies, a strength parameter Q_D, defined as the collision energy per unit mass that is required to fragment the body such that the largest fragment has half the mass of the original projectile, can be described by a power law $Q_\mathrm{D} \propto a^{-0.4}$ (see Table 3 in Benz and Asphaug, 1999). Thus, taking

$$Q_\mathrm{D} = \frac{E}{m_\mathrm{tot}} \propto \frac{m_\mu}{m_\mathrm{tot}} v^2 \propto a^{-4/10} \propto m^{-4/30} \tag{4.37}$$

and approximating $m_\mu/m_\mathrm{tot} = \mathrm{const.}$, we get a relation $m \propto v^{-15}$. Here, E and m_tot are the collision energy and the total mass of the colliding bodies. By treating $m_\mu/m_\mathrm{tot} = \mathrm{const.}$, we obtain a lower threshold velocity for the transition to the fragmentation regime. Fitting this power law to the dust fragmentation experiments and a fragmentation threshold of 100 cm s^{-1} for dust aggregates of 5 mg mass, we get fragmentation for velocities

$$v \geq t_\mathrm{f}\ m^{-1/15} \tag{4.38}$$

with a material-dependent fragmentation parameter $t_\mathrm{f} = 70.2\ \mathrm{g}^{1/15}\ \mathrm{cm\ s}^{-1}$ for porous dust aggregates. Due to the lack of measurements, we are neglecting the expected porosity dependence of t_f and use it for any porosity.

F2: Erosion

If a projectile collides with a significantly larger *porous* target aggregate at a sufficiently high impact velocity, the target may be eroded. Schräpler and Blum (in prep.) found erosion of porous ($\phi = 0.15$) aggregates which were exposed to 1.5 μm diameter SiO_2 monomers (mass m_0) at velocities from 1 500 to 6 000 cm s^{-1}. Their numerical model, which fits the experimental data very well, predicts an onset of erosion for a velocity of 350 cm s^{-1}. The eroded mass grows roughly linear with impact velocity, i.e.

$$\frac{\Delta m}{m_\mathrm{p}} = \frac{6}{80} \left(\frac{v}{100\ \mathrm{cm\ s}^{-1}} \right) \ , \tag{4.39}$$

where Δm is the amount of eroded mass and $m_\mathrm{p} = m_0$ is the projectile mass. Paraskov et al. (2007) also found mass loss of a porous target aggregate for velocities from 350 to 2 150 cm s^{-1}, although the process involved is widely different. They used porous and solid projectiles and their results (Fig. 4 in Paraskov et al., 2007) are consistent with

$$\frac{\Delta m}{m_\mathrm{p}} = \frac{15}{20} \left(\frac{v}{100\ \mathrm{cm\ s}^{-1}} \right) \ , \tag{4.40}$$

which is in agreement with non zero-gravity experiments of Wurm et al. (2005a), who estimated a mass loss of 10 projectile masses for velocities larger than 1650 cm s^{-1}. Due to the small variation in projectile mass within each of the two experiments, we apply a power law in mass and merge both experiments to

$$\frac{\Delta m}{m_\mathrm{p}} = \frac{6}{80} \left(\frac{v}{100\ \mathrm{cm\ s}^{-1}} \right) \left(\frac{m_\mathrm{p}}{m_0} \right)^{0.092} \ . \tag{4.41}$$

The velocity range for erosion is therefore

$$v_\mathrm{er} \geq 350\ \mathrm{cm\ s}^{-1} \tag{4.42}$$

and is consistent in both experiments.

For *compact* targets, Schräpler and Blum (in prep.) were able to measure the velocity range for erosion at

$$v_\mathrm{er} \geq 2\,500\ \mathrm{cm\ s}^{-1}. \tag{4.43}$$

Due to the nature of the compact target, far less material was eroded, i.e.

$$\frac{\Delta m}{m_\mathrm{p}} = \frac{8}{550} \left(\frac{v}{100\ \mathrm{cm\ s}^{-1}} \right) \left(\frac{m_\mathrm{p}}{m_0} \right)^{0.092} \ . \tag{4.44}$$

Here, we applied the same power-law index as in Eq. 4.41 due to the absence of large-scale experiments in this case. We assume a mass distribution of the eroded material according to Eq. 4.2.

F3: Fragmentation with Mass Transfer

In Sect. 4.2.2 we described the volume transfer from a porous to a compact aggregate above the fragmentation threshold velocity (see Eq. 4.4). Without better knowledge, we assume that the transferred mass has a volume filling factor of 1.5 times that of the porous collision partner (ϕ_p) and cannot exceed the mass of the porous aggregate, thus

$$\Delta m = m_{\mathrm{p(t)}} 1.5 \phi_\mathrm{p} \left(0.59 - 6.3 \times 10^{-4} \frac{v}{\mathrm{cm\ s^{-1}}} \right) , \tag{4.45}$$

where $m_{\mathrm{p(t)}}$ is the mass if the porous aggregate which can either be projectile or target in our definition, depending on its actual mass. For the fragmentation of the porous aggregate we assume a power-law distribution following the F1 case. If the collision velocity is higher than 940 cm s^{-1}, Eq. 4.45 yields no mass gain for the compact aggregate, thus, the mass of the compact aggregate is conserved and only the porous aggregate fragments.

4.4 Collision Regimes

In this Section we intend to build on the physical descriptions, which we have derived in the previous Section, and develop a complete collision model for determination of the collisional outcome in protoplanetary dust interactions (Fig. 4.1). This means that for each collision that may occur, a set of collision parameters will be provided as input for a numerical model of the evolution of protoplanetary dust (see Zsom et al., 2009). The most crucial parameters that mainly determine the fate of the colliding dust aggregates in each collision are the respective dust-aggregate masses and their relative velocity.

Moreover, in Sect. 4.2 and 4.3, we saw that the porosity difference between the two collision partners also has a big impact on the collisional outcome. The only difference between the types F1 and F3 (and between S3 and S4) is that the target aggregate is either porous or compact. Thus, we define a critical porosity ϕ_c to distinguish between porous or compact aggregates. This value can only roughly be confined between $\phi = 0.15$ (S3 sticking, clearly an effect of porosity, Langkowski et al., 2008) and $\phi = 0.64$ (random close packing, clearly compact Torquato et al., 2000) and without better knowledge we will choose $\phi_\mathrm{c} = 0.4$.

Another important parameter is the mass ratio of the collision partners. Again, the sticking by deep penetration (S3) occurs for the same set of parameters as the fragmentation (F1) and only the critical mass ratio $r_\mathrm{m} = m_\mathrm{t}/m_\mathrm{p}$ is different. From the work of Blum and Münch (1993) and Langkowski et al. (2008), we can confine this parameter to the range $10 \leq r_\mathrm{m} \leq 1\,000$ and will also treat it as a free parameter (with fixed values $r_\mathrm{m} = 10, 100, 1\,000$) in Chapter 5 .

A further parameter, which has an impact on the collisional outcome, is the impact angle but at this stage, due to a lack of information of the actual influence of the impact angle on the collisional result, we will treat all collisions as central collisions. Experiments by Blum and Münch (1993), Langkowski et al. (2008), or Lammel (2008) indicate rather

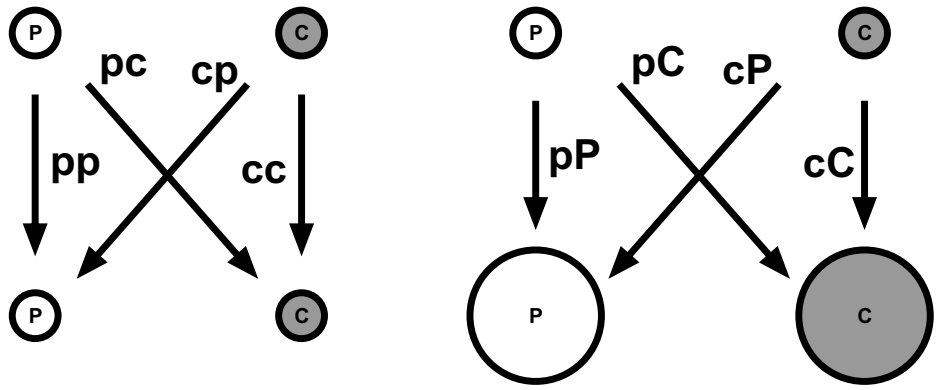

Figure 4.10: Experiments suggest that collisions between dust aggregates with different porosities lead to a different outcome than those between aggregates of similar porosity. Thus, our model distinguishes between porous and compact aggregates, which leads to the displayed four types of collisions (*'pp'*, *'pc'*, *'cp'*, *'cc'*) if the collision partners are not too different in size (left). The size ratio of projectile and target aggregate was identified as another important parameter and we distinguish between similar-sized and different-sized collision partners. Thus, in addition to the four collision types on the left, impacts of projectiles into much larger targets (*'pP'*, *'pC'*, *'cP'*, *'cC'*; the target characterized by a capital letter) can also occur (right). The boundary between similar-sized and different-sized aggregates is given by the critical mass-ratio parameter r_m. Collisions on the left are restricted to $m_\mathrm{p} \leq m_\mathrm{t} \leq r_\mathrm{m} m_\mathrm{p}$, collisions on the right happen for $m_\mathrm{t} > r_\mathrm{m} m_\mathrm{p}$.

small differences between central and grazing collisions so that we feel confident that the error due to this simplification is small. Another parameter, which we also neglect at this point due to a lack of experimental data, is the surface roughness of the aggregates. Langkowski et al. (2008) showed its relative importance, but a quantitative treatment of the surface roughness is currently not possible.

The binary treatment of the parameters ϕ_c and r_m leads to Fig. 4.10 whereafter we have four different porous-compact combinations and, if we take into account that the collision partners can either be similar-sized or different-sized, we have a total of eight collision combinations. We will call these *'pp'*, *'pP'*, *'cc'*, *'cC'*, *'cp'*, *'cP'*, *'pc'*, and *'pC'*. Here, the first small letter denotes the porosity of the projectile (*'p'* for porous and *'c'* for compact) and the second letter denotes the target porosity which can be either similar-sized (small letter) or different-sized (capital letter). Aggregates with porosities $\phi < \phi_\mathrm{c}$ are *'porous'*, those with $\phi \geq \phi_\mathrm{c}$ are *'compact'*. If the mass of the target aggregate $m_\mathrm{t} \leq r_\mathrm{m} m_\mathrm{p}$, we treat the collisions as equal-sized, for $m_\mathrm{t} > r_\mathrm{m} m_\mathrm{p}$, the collisions are treated as different-sized.

For each combination depicted in Fig. 4.10, we have the most important parameters (1) projectile mass m_p and (2) collision velocity v, which then determine the collisional outcome. As shown in Fig. 4.11, we treat each combination from Fig. 4.10 separately and define the collisional outcome as a function of projectile mass and collision velocity. For the threshold lines and the quantitative collisional outcomes we use a set of equations, which were given in Sect. 4.3. For a quantitative analysis and application to PPDs (see

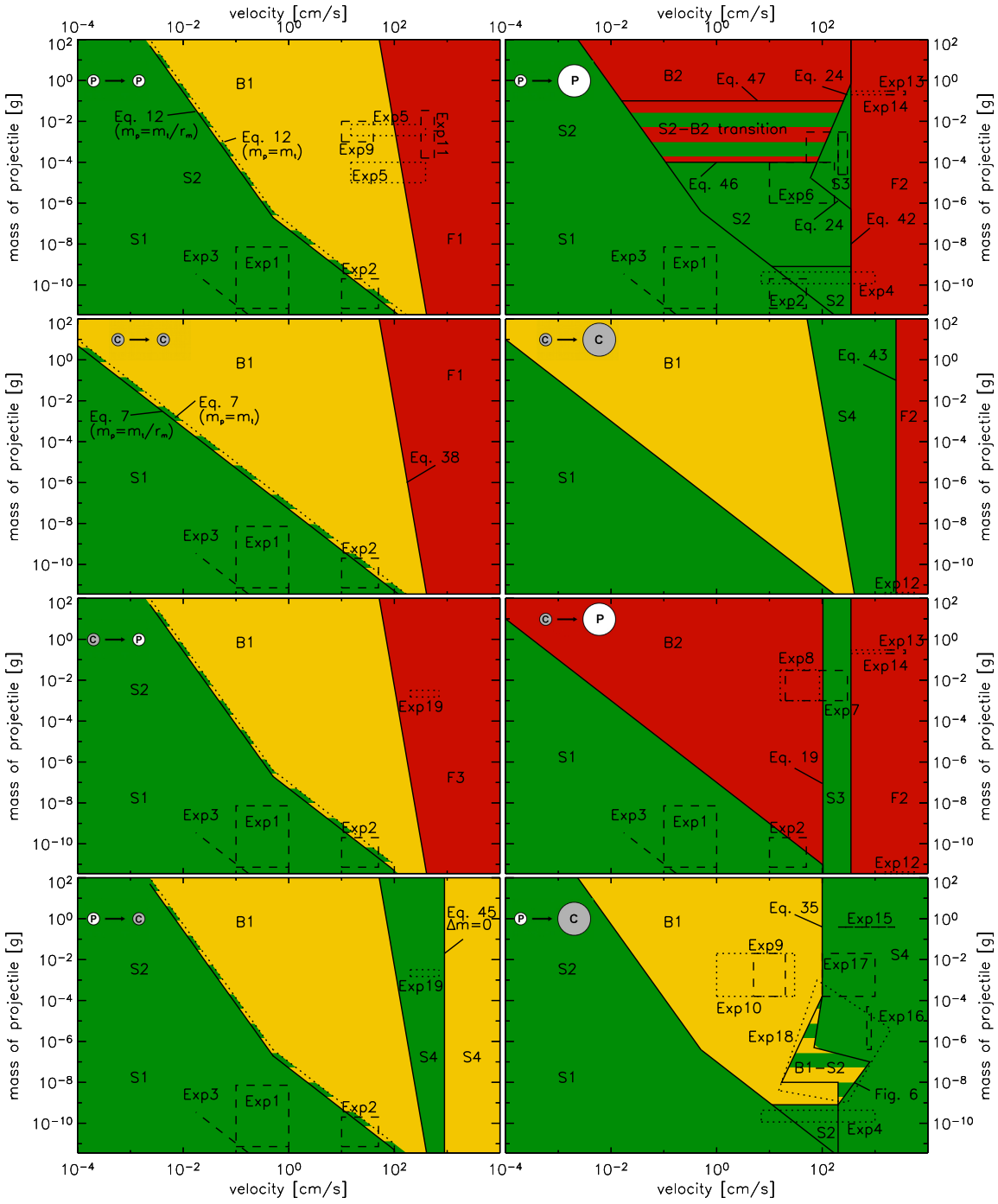

Figure 4.11: The resulting collision model as described in this paper. We distinguish between similar-sized (left column) and different-sized (right column) collision partners, which are either porous or compact (also see Fig. 4.10). For each case, the important parameters to determine the collisional outcome are the projectile mass and the collision velocity. collisions within green regions can lead to the formation to larger bodies while red regions denote mass loss. Yellow regions are neutral in terms of growth. The dashed and dotted boxes show where experiments directly support this model.

Table 4.2: Particle and aggregate material properties used for generating Fig. 4.11.

symbol	value	reference
monomer-grain properties:		
a_0	0.75 μm	
m_0	3.18×10^{-12} g	
ρ_0	2 g cm^{-3}	
E_0	2.2×10^{-8} erg	Blum and Wurm (2000), Poppe et al. (2000)
$F_{\rm roll}$	10^{-4} dyn	Heim et al. (1999)
aggregate properties:		
ε	0.05	Blum and Münch (1993), Heißelmann et al. (in prep.)
G	6320 dyn cm^{-2}	this work
T	10^4 dyn cm^{-2}	Blum and Schräpler (2004)
$\phi_{\rm c}$	0.40	this work
$r_{\rm m}$	10 – 1 000	this work
γ	8.3×10^{-3} s cm^2 g^{-1}	Güttler et al. (2009)
$E_{\rm t}$	3.5×10^4 erg	Langkowski et al. (2008)
$E_{\rm min}$	3.1×10^{-2} erg	Langkowski et al. (2008)
ϕ_1	0.12	Güttler et al. (2009)
ϕ_2	0.58	Güttler et al. (2009)
Δ	0.58	Güttler et al. (2009)
$p_{\rm m}$	1.3×10^4 dyn cm^{-2}	Güttler et al. (2009)
$f_{\rm c}$	0.79	this work
$t_{\rm f}$	70.2 g$^{1/15}$ cm s^{-1}	this work
ν_0	850	Weidling et al. (2009)
λ	-1.4	this work

Zsom et al., 2009), knowledge of the material parameters of the monomer dust grains and dust aggregates is required. In Table 4.2 we list all relevant parameters for 1.5 μm SiO_2 spheres, for which most experimental data are available. However, we believe that the data in Table 4.2 is also relevant for most types of micrometer-sized silicate particles.

The only collision type, which is the same in all regimes, is the hit-and-stick (S1) process, which, due to its nature, does not depend on porosity or mass ratio but only on mass and collision velocity. Thus, all collision combinations in Fig. 4.11 have the same region of sticking behavior for a mass-velocity combination smaller than defined by Eq. 4.7. This parameter region is marked in green because hit-and-stick (S1) can in principle lead to the formation of arbitrary large aggregates. Marked in yellow are collision types, which do not lead to further growth of the *target* aggregate, but conserve the mass of the target aggregate, which is only the case for bouncing with compaction (B1). For simplicity, the weak fragmentation probability of $P_{\rm frag} = 10^{-4}$ (see Sect. 4.3) has been neglected in the coloring. The red-marked regions are parameter sets for which the *target* aggregate loses mass.

The dashed and dotted boxes in Fig. 4.11 mark the mass and velocity ranges of the experiments from Table 4.1. In Chapter 5, this plot will help us to see in which parameter regions collisions occur and how well they are supported by experiments. We will now go through all of the eight plots in Fig. 4.11 and explain the choice for the thresholds between the collision types.

'pp': In addition to the omnipresent hit-and-stick (S1) regime, which is backed by experiments 1 – 3 in Table 4.1, collisions of porous projectiles can also lead to sticking through surface effects (S2), whose threshold is determined by Eq. 4.12. For higher velocities, fragmentation sets in, where the threshold velocity is given by Eq. 4.38. Bouncing (B1) and fragmentation (F1) in this regime are well tested by experiments 5, 9, and 11 in Table 4.1.

'pP': As the projectiles are also porous here, we have the same sticking through surface effects (S2) threshold as in *'pp'*. The same collision type (but with compaction of the projectile) was found for collisions of small aggregates (Blum and Wurm, 2000, experiment 4 in Table 4.1). Langkowski et al. (2008) (experiment 6) found the S2 collision type for projectile masses

$$m_\mathrm{p} < 10^{-4} \text{ g}. \tag{4.46}$$

thus we have a horizontal upper limit for S2 in the *'pp'* plot of Fig. 4.11. Extrapolation of experiment 6 to large aggregate masses

$$m_\mathrm{p} > 0.1 \text{ g} \tag{4.47}$$

results in bouncing with mass transfer (B2). A linear interpolation between perfect sticking for $m_\mathrm{p} < 10^{-4}$ g and perfect bouncing for $m_\mathrm{p} > 0.1$ g, justified by the sticking probabilities shown in Fig. 5 of Langkowski et al. (2008), gives a sticking probability for the mass range $10^{-4} \text{ g} \leq m_\mathrm{p} \leq 0.1$ g (striped region in the *'pP'* of Fig. 4.11) of

$$P_\mathrm{stick} = -\frac{1}{3} \log_{10} \left(\frac{m_\mathrm{p}}{0.1 \text{ g}} \right) \tag{4.48}$$

In Sect. 4.3 we defined the threshold for sticking by deep penetration (S3) by Eqs. 4.23 and 4.24, which are prominent in the *'pP'* plot for high velocities. For even higher velocities, we have erosion of the porous aggregate (F2), defined by the threshold velocity in Eq. 4.41 and based on experiments 12 – 14 in Table 4.1.

'cc': Our knowledge about collisions between similar-sized, compact dust aggregates is rather limited. Blum and Münch (1993) performed collisions between similar-sized aggregates with $\phi = 0.35$. Although this is lower than the critical volume filling factor ϕ_c as defined in Table 4.2, we assume a similar behavior also for aggregates with higher porosity. Therefore, without better knowledge, we define a fragmentation threshold line as in the *'pp'* regime, and take the hit-and-stick (S1) threshold for low energies. We omit the sticking through surface effects (S2) in this regime because of the significantly lower compressibility of the compact aggregates.

'cC': Also in this collision regime, the experimental background is very limited. For low collision energies we assume a hit-and-stick (S1) growth, for higher velocities bouncing with compaction (B1) and, if the fragmentation threshold (Eq. 4.38) is exceeded, fragmentation with mass transfer (S4). Based on experiment 12, we have an erosion (F2) limit for velocities higher than 2 500 cm s^{-1} (Eq. 4.43).

*'cp'*and *'pc'*: These two cases are almost identical with the only difference that the compact aggregate can either be the projectile or the target (i.e. slightly lower or higher

in mass than the target aggregate). However, the mass ratio of both aggregates is within the critical mass ratio $r_{\rm m}$. Besides the already-discussed cases S1, S2, and B1, we assume fragmentation above the threshold as defined in Eq. 4.38. Due to the nature of the collision between a compact and a porous aggregate, only the porous aggregate is able to fragment, whereas the compact aggregate stays intact. If the compact aggregate is the projectile, the target mass is always reduced, thus we have fragmentation with mass transfer (F3) from the target to the projectile. If the target is compact, it grows by fragmentation with mass transfer (S4), if the velocity is less than 940 cm s^{-1} (see Eq. 4.45). For higher velocities, Eq. 4.45 yields no mass gain and so this region is neutral in terms of growth. Collisions at high velocities are confirmed by experiment 19 in this regime.

'cP': While small collision energies lead to hit-and-stick (S1) higher energies result in bouncing with mass transfer (B2) (Exp. 8, Blum and Wurm, 2008). This region is confined by the sticking by deep penetration (S3) threshold velocity as defined in Eq. 4.19, based on experiment 7 (Güttler et al., 2009). At even higher velocities above 350 cm s^{-1} (Eq. 4.41), we get erosion of the target aggregate as seen in experiments 12 – 14.

'pC': This plot in Fig. 4.11 looks the most complicated but it is supported by a large number of experiments. For low collision velocities, we again have hit-and-stick (S1) and sticking through surface effects (S2), and a transition to bouncing with compaction (B1) for larger collision energies. The existence of the B1 bouncing region has been shown in experiments 9 and 10 (Heißelmann et al., in prep.; Weidling et al., 2009). For higher velocities and masses above $1.6 \cdot 10^{-4}$ g we assume a fragmentation threshold of 100 cm s^{-1} with mass transfer to the target (S4), as seen in experiment 16 (Sect. 4.2.2). For lower masses, the odd-shaped box of experiment 18 is a direct input from Sect. 4.2.2 (see Fig. 4.6). In the striped region between B1 and S4, we found in experiment 18 a sticking probability of $P_{\rm stick} = 0.5$. For lower masses, experiment 4 showed sticking through surface effects (S2) with a restructuring (compaction) of the projectile. As in the *'pP'* regime, we set the threshold for a maximum mass to $8 \cdot 10^{-10}$ g, while the upper velocity threshold – which must be a transition to a fragmentation regime (Blum and Wurm, 2000) – is 200 cm s^{-1} from experiments 4 and 18.

4.5 Porosity Evolution of the Aggregates

Since the porosity of dust aggregates is a key factor for the outcome of dust aggregate collisions (Blum and Wurm, 2008), it is paramount that collisional evolution models follow its evolution (Ormel et al., 2007, Zsom et al., 2009). Therefore, in this section, we want to stress on the evolution of the dust aggregates' porosities and recapitulate the porosity recipe as used in Sect. 4.3. In this paper we have used the volume filling factor ϕ as a quantitative value, being defined as the volume fraction of material (one minus porosity). Zsom et al. (2009) will also use the enlargement parameter Ψ as introduced by Ormel et al. (2007), which is the reciprocal quantity $\Psi = \phi^{-1}$.

Starting the growth with solid dust grains, we have a volume filling factor of 1, which

will however rapidly fall due to the hit-and-stick (S1) growth, producing highly porous, fractal aggregates. Here, we use the porosity recipe of Ormel et al. (2007), who describe this fractal growth by their enlargement parameter as

$$\Psi_{\rm new} = \frac{m_{\rm p}\Psi_{\rm p} + m_{\rm t}\Psi_{\rm t}}{m_{\rm p} + m_{\rm t}} \times \left(1 + \frac{m_{\rm t}\Psi_{\rm t}}{m_{\rm p}\Psi_{\rm p}}\right)^{0.425} + \Psi_{\rm add} \ , \tag{4.49}$$

where $\Psi_{\rm add}$ is a correction factor in case of $m_{\rm p} \approx m_0$ and otherwise zero (for details see their Sect. 2.4). This equation predicts an increasing porosity in every hit-and-stick (S1) collision. In collisions that lead to sticking through surface effects (S2), we assume that the compaction of the aggregates is so little, that their porosity is unaffected. So the aggregates are merged and only the mass and volume of both are being added, thus,

$$\phi_{\rm new} = \frac{V_{\rm t}\phi_{\rm t} + V_{\rm p}\phi_{\rm p}}{V_{\rm t} + V_{\rm p}} \ . \tag{4.50}$$

One exception for the sticking through surface effects (S2) occurs in a small parameter space which is determined by the experiments of Blum and Wurm (2000). For the smallest masses and a velocity around 100 cm s^{-1}, Blum and Wurm (2000) found sticking of fractal aggregates in the *'pP'* and *'pC'* regimes that goes with a restructuring and, thus, compaction of the projectiles. In this case, we assume a compaction of the projectile by a factor of 1.5 in volume filling factor, thus

$$\phi_{\rm new} = \frac{V_{\rm t}\phi_{\rm t} + \min\left(1.5V_{\rm p}\phi_{\rm p},\ \phi_{\rm c}\right)}{V_{\rm t} + V_{\rm p}} \ . \tag{4.51}$$

An increasing filling factor is also applied for sticking by deep penetration (S3). Here, the mass of the projectile is added to the target while the new volume must be less than $V_{\rm t} + V_{\rm p}$. The new volume filling factor will be

$$\phi_{\rm new} = \frac{V_{\rm t}\phi_{\rm t} + V_{\rm p}\phi_{\rm p}}{V_{\rm new}} \ , \tag{4.52}$$

where $V_{\rm new}$ is taken from Eq. 4.17 (compact projectile) or as $V_{\rm new} = V_{\rm t} - V_{\rm cr.}$ with $V_{\rm cr.}$ from Eq. 4.20 (porous projectile). In the cases where we transfer mass from one aggregate to the other, we always assume that this mass is previously compacted by a factor of 1.5 in volume filling factor, but cannot be compacted higher than the critical filling factor $\phi_{\rm c}$. For the bouncing with mass transfer (B2) we have good arguments for this assumption as this compaction is consistent with XRT measurements of Güttler et al. (2009), who also showed that it is likely that this compacted material is transferred to the projectile (see their Figs. 7 and 9). Without better knowledge, we assume the same compaction of transferred material for fragmentation with mass transfer (F3 and S4) and for these three cases we again use Eq. 4.51. Here, we have to note that in the case of bouncing with mass transfer (B2) and fragmentation with mass transfer (F3) the indices of target and projectile need to be swapped as the projectile is accreting mass in this

Table 4.3: Overview on the porosity evolution in the different collision types.

collision type	porosity evolution	equation
S1	fluffier	4.49
S2	neutral or compaction	4.50 or 4.51
S3	compaction	4.17, 4.20, 4.52
S4 (target)	fluffier	4.51
S4 (projectile)	neutral	–
B1	compaction	4.25 – 4.31
B2 (target)	neutral	–
B2 (projectile)	both	4.51[a]
F1	neutral	–
F2	neutral	–
F3 (target)	fluffier	4.51[a]
F3 (projectile)	neutral	–

[a]The indices of target and projectile must be swapped here.

collision type. For the fragments in S4 and F3 as well as for those in the case of F1 and F2, we assume an unchanged porosity with respect to the destroyed aggregate. The most sophisticated compaction model is used for collisions that lead to bouncing with compaction (B1). Although Weidling et al. (2009) measured the compaction only for a small range of aggregate sizes and collision velocities, they derived an analytic model to scale this compaction in collision velocity and showed that it is independent in aggregate mass. We follow this model but release it from the experimental bias due to the $\phi = 0.15$ samples they used. As outlined in detail in Sect. 4.3, we basically use Eq. 4.25, and scale the $\phi_{\max}(v)$ according to Eq. 4.31 (furthermore using Eqs. 4.26 – 4.30).

In summary, one can say that the aggregates' porosities can only be increased by the collision types S1, S4, and F3 (see Table 4.3), where the hit-and-stick (S1) collisions will have the most effect. While some collision types are neutral in terms of porosity evolution (F1 and F2), the main processes which lead to more compact aggregates are S3 and B1.

4.6 Discussion

In the previous sections we have developed a comprehensive model for the collisional interaction between protoplanetary dust aggregates. The culmination of this effort is Fig. 4.11, which presents a general collision model based on 19 different dust-collision experiments, which will be adopted in Chapter 5. Since it plays a vital role, it is worth a critical appraisal. In a few examples, we want to discuss the main simplifications and shortcomings of our current model.

(1) The categorization into collisions between similar-sized and different-sized dust aggregates (see Figs. 4.10 and 4.11) is well-motivated as we pointed out in Sect. 4.4. However, we may ask ourselves whether this binarization is fundamentally correct, if we need more than two categories, or 'soft' transitions between the regimes. At this stage, a more complex treatment would be impractical due to the lack of experiments treating this problem.

(2) The binary treatment of porosity (i.e. $\phi < \phi_c$ for 'porous' and $\phi \geq \phi_c$ for 'compact' dust aggregates) is also a questionable assumption. Although we see fundamental differences in the collision behavior when we use, e.g., porous or compact targets, there might be a smooth transition from the more 'porous' to the more 'compact' collisions. In addition to that, the assumed value $\phi_c = 0.4$ is reasonable but not empirically affirmed. On top of that, the maximum compaction that a dust aggregate can achieve in a collision depends on many parameters, such as, e.g., the size distribution of the monomer grains (Blum et al., 2006) and the ability of the granular material to creep sideways inside a dust aggregate (Güttler et al., 2009).

(3) Although the total number of experiments, upon which our model is based, is unsurpassedly large, the total coverage of parameter space (see the experiment boxes in Fig. 4.11) is still small. Thus, we sometimes apply extrapolations into extremely remote parameter-space regions. Although not quantifyable, it must be clear that the error of each extrapolation grows with the distance to the experimentally confirmed domains (i.e. the boxes in Fig. 4.11). Clearly, more experiments are required to fill the parameter space, and the identification of the key regions in the mass-velocity plane is exactly one of the goals Chapter 5.

(4) With such new experiments, performed at the 'hot spots' predicted by Zsom et al. (2009), we will not only close gaps in our knowledge of the collision physics of dust aggregates but will most certainly reveal completely new effects. The rather simple *'cc'* panel in Fig. 4.11 as compared to the more complex *'pC'* is due to the fact that there are hardly any experiments that back-up the *'cc'* regime, whereas in the *'pC'* case we have a rather good experimental coverage of the parameter space.

In summary, the sophisticated nature of our collision model is both its strength and its weakness. The drawbacks of identifying four parameters that shape the collision outcome are that rather crude approximations and extrapolations have to be made. However, to acknowledge the role of, e.g., porosity through a binary treatment is still better than to not treat this parameter at all. Our new collision model represents the first attempt to include all existing laboratory experiments (for the material properties of interest); collisional evolution models can enormously profit from this effort.

4.6.1 The Bottleneck for Protoplanetary Dust Growth

In this paper, we have presented the framework and physical background for an extended growth simulation. What is to be expected from this? Here, we can speculate under which conditions growth in PPDs is most favorable. A view on Fig. 4.11 immediately shows that large dust aggregates can preferentially grow for realistic collision velocities in the *'cC'* and *'pC'* collision regimes (and to a lesser extent in the *'pc'* case), due to fragmentation with mass transfer (S4). For this to happen, a broad mass distribution of protoplanetary dust must be present. This prerequisite for efficient growth towards planetesimal sizes has also been suggested by **?**, see their Fig. 11. Agglomeration experiments with micrometer-sized dust grains and a sticking probability of unity (experiments 1 – 3 in Table 4.1) have shown that nature chooses a rather narrow size distribution for the initial fractal growth

phase. If this changes when the physical conditions leave no room for growth under quasi-monodisperse conditions, i.e. whether nature is so 'adaptive' and 'target-oriented' to find out that growth can only proceed with a wide size distribution, will be the subject of Chapter 5, in which we apply the findings of this paper to a collisional evolution model.

4.6.2 Influence of the Adopted Material Properties

The choice of material in our model is silica dust as most of the underlying experiments were performed with this material. Although many experiments (Langkowski et al., 2008, Blum and Wurm, 2008) showed that this material is at least in a qualitative sense representative for other silicatic materials – also for irregular grains with a broader size distribution – organic or icy material in the outer regions of PPDs or oxides and sintered material in the inner regions may have a big impact on the collisional outcome, i.e. in enhancing the stickiness of the material and thereby potentially opening new growth channels.

As for organic materials, Kouchi et al. (2002) found an enhanced sticking of cm-sized bodies covered with a 1 mm thick layer of organic material at velocities as high as 500 cm s^{-1} and a temperature of $\sim$ 250 K. Also icy materials are likely believed to have an enhanced sticking efficiency compared to silicatic materials. Hatzes et al. (1991) collided 5 cm diameter solid ice spheres, which were covered with a 10 – 100 μm thick layer of frost. They found sticking for a velocity of 0.03 cm s^{-1}, which is in a regime where our model for refractory silicatic material predicts bouncing (see *'pp'* or *'cc'* in Fig. 4.11). Sintering of porous dust aggregate may occur in the inner regions near the central star or – triggered by transient heating events (e.g. lightning, Güttler et al., 2008) – even further out. Ongoing studies with sintered dust aggregates (Poppe, 2003) show an increased material strength (e.g. tensile strength) by order of magnitude. This would at least make the material robust against fragmentation processes and qualitatively shift them from the porous to the compact regime in our model – without necessarily being compact. Due to a severe lack on experimental data for all these materials, it is necessary and justified to restrict our model to silicates at around 1 AU while it is to be kept in mind that these examples of rather unknown materials might potentially favor growth in other regions in PPDs.

Chapter 5

Introducing the Bouncing Barrier

Andras Zsom, Carsten Güttler, Chris W. Ormel, Jürgen Blum, Cornelis P. Dullemond
Submitted to Astronomy & Astrophysics

Abstract

The sticking of micron sized dust particles due to surface forces in circumstellar disks is the first stage in the production of asteroids and planets. The key ingredients that drive this process are the relative velocity between the dust particles in this environment and the complex physics of dust aggregate collisions. Here we present the results of a collision model, which is based on laboratory experiments of these aggregates. We investigate the maximum aggregate size and mass that can be reached by coagulation in protoplanetary disks. We use the results of laboratory experiments to establish the collision model (see Chapter 4). The collision model is based on some necessary assumptions: our aggregates have a fractal dimension of three, we model the aggregates as spheres having compact and porous 'phases' and a continuous transition between these two. We apply this collision model to the Monte Carlo method of Zsom and Dullemond (2008) and include Brownian motion, radial drift and turbulence as the sources of relative velocity between dust particles. We model the growth of dust aggregates at 1 AU at the midplane at three different gas densities. We find that the evolution of the dust does not follow the previously assumed growth-fragmentation cycles. Catastrophic fragmentation hardly occurs in the three disk models. Furthermore we see long lived, quasi-steady states in the distribution function of the aggregates due to bouncing. We explore how the mass and the porosity change upon varying the turbulence parameter and by varying the critical mass ratio of dust particles (see Chapter 4). Upon varying the turbulence parameter, the system behaves in a non-linear way and the critical mass ratio has a strong effect on the particle sizes and masses. Particles reach Stokes numbers of roughly 10^{-4} during the simulations. The particle growth is stopped by bouncing rather than fragmentation in these models. The final Stokes number of the aggregates is rather insensitive to the variations of the gas density and the strength of turbulence. The maximum mass of the particles is limited to ~ 1 g (chondrule sized particles). Planetesimal formation can proceed via the turbulent

concentration of these aerodynamically size-sorted chondrule-sized particles.

5.1 Introduction

In the core accretion paradigm of planet formation (Mizuno, 1980, Pollack et al., 1996) planets are the outcome of an accretion process that starts with micron-size dust grains and covers 40 magnitudes in mass. It can be divided into three stages. The first stage of the formation of rocky planets and the rocky cores of gas giant planets starts with the coagulation of dust in the protoplanetary disks surrounding many pre-main-sequence stars. The next stage of planet formation is the formation of protoplanetary cores from the planetesimals. The idea is that the kilometer size planetesimals are so large, that gravity starts to take over and leads to the gravitational agglomeration of these bodies to rocky planets. This scenario was studied already by Safronov (1969), and has since been modeled using numerical methods by Weidenschilling (1980), Nakagawa et al. (1983), Mizuno (1980), Schmitt et al. (1997), Wetherill (1990), Nomura and Nakagawa (2006), Garaud and Lin (2004), Tanaka et al. (2005) and several more authors. These models solve for the size distribution of dust aggregates in the disk as a function of time, and investigate if, where and how larger dusty bodies form, and how long that takes. Finally, in the third stage, gas accretes onto these protoplanets forming giant planets or – in the absence of gas – gravitational encounters between these protoplanets result in a chaotic, giant impact phase, until orbital stability has been achieved (Chambers, 2001, Kokubo et al., 2006, Thommes et al., 2008).

In this study, we focus on the first phase and address the fundamental question of how effective dust growth by surface forces really is; that is, how big do particles become by simple sticking processes only. It is known that initially, for micron size grains, the growth is driven by Brownian motion. This typically leads to slow collisions and forms aggregates of fractal structure (Kempf et al., 1999, Blum et al., 1996). In the current picture of dust growth, as these aggregates grow, at some point the growth will leave the fractal regime, and collisions will start to lead to compaction and breaking of the aggregates (Blum and Wurm, 2000), embedding of small bodies into larger aggregates leading to 'filling up' of these larger aggregates and compaction due to the force of the collision (Ormel et al., 2007). As the size of the dust aggregates increases, differential vertical settling (Safronov, 1969), radial drift (Whipple, 1972) and turbulence (Völk et al., 1980, Mizuno, 1980, Ormel et al., 2007) will become important new mechanisms driving relative velocities between aggregates. The increasing relative velocities caused by these mechanisms will at least partly compensate the lower collision probability due to lower surface-over-mass ratio of large aggregates. When the aggregates grow to sizes of millimeter to meter, however, the sticking efficiency drops strongly (e.g. Blum and Münch, 1993) and the relative velocities become so large that aggregates can fragment (Blum and Wurm, 2008), so called 'fragmentation barrier'. Another hurdle that the particles have to circumvent is the 'drift barrier' (Weidenschilling, 1977a), namely that millimeter, centimeter sized particles are lost to the star due to radial drift in a short timescale. Recently, Okuzumi

(2009) pointed out the existence of a 'charge barrier', which possibly halts the particle growth already at an early stage of fractal aggregates. Despite many years of efforts, it is not known if the coagulation process can overcome these barriers. These barriers have been and still are the main open question of the initial stages of planet formation: the growth from dust to planetesimals.

Several mechanisms have been proposed to overcome this problem, among which are the trapping of dust in vortices (Barge and Sommeria, 1995, Klahr and Henning, 1997, Lyra et al., 2009), trapping of decimeter-sized boulders in turbulent eddies and the subsequent gravitational collapse of swarms of these trapped boulders (Johansen et al., 2007), the trapping of particles in a pressure bump caused by the evaporation front of water (Kretke and Lin, 2007, Brauer et al., 2008b) and many more scenarios. However, the correct modeling of any of these scenarios requires the detailed knowledge of the collisional physics, and these models have so far relied either on simplified input physics or on simplified initial conditions.

Because of their complexity, collisional evolution models have to make simplifying assumptions concerning the outcome of dust aggregate collisions, for example that collisions always result in sticking, or otherwise use simple recipes for the collisional outcome. Ideally, one requires to know the detailed outcome of every collision. But modelling this microphysics within an evolution model is simply unpractical. There are computer programs that model such individual collisions in detail (e.g. Dominik and Tielens, 1997, Suyama et al., 2008, Geretshauser et al., 2009), but each model collision takes anywhere from hours to weeks to run on a computer. They are therefore not practical to use at run-time in a model that computes the overall time-dependent evolution of the dust size distribution inside protoplanetary disks. Moreover, such collision models themselves often depend on poorly known input physics.

Another approach to obtain the collisional outcome of dust aggregates is to model these collision in the laboratory. From the many experiments that have as of now been performed a picture emerges of the outcome of dust aggregate collision under a variety of conditions in the PPD. In Sect. 4, we have collected data from over 19 experiments, and constructed a set of formulae that reasonably well describe the outcomes of these collisions in such a way that they can be used as input for models that address the temporal evolution of the dust size distribution.

In this paper we will directly rely on the outcome of these laboratory experiments for modeling the dust aggregate size distribution. As described in Chapter 4, we have produced a mapping of all available collision experiments regarding silicate-like particles. This mapping therefore provides an outcome of collisions that represent conditions at 1 AU in the protoplanetary disks. For details regarding the collisional mapping, we will refer to Chapter 4, but we will summarize the elements of our new collision model in Sect. 5.3.1.

We build this collision kernel into a Monte Carlo code for modeling the size- and porosity distribution of dust in a protoplanetary disk (Zsom and Dullemond, 2008, hereafter ZsD08). The outcome of our laboratory-driven dust coagulation model is hard to a priori predict since the key variables involved depend on a non-trivial interplay between

the collision kernel (Chapter 4) and the velocity field. We can, however, anticipate two scenarios. In the first, particle growth will proceed beyond the meter-size barrier, all the way to planetesimals. In the second scenario, growth will terminate at an intermediate size. In this case further growth to planetesimal sizes may proceed through concentration and subsequent gravitational collapse of these particles (Johansen et al., 2007, Cuzzi et al., 2008). Thus, our model will provide the starting conditions for these concentration models. We do emphasize, however, that in this work we do not in any way 'optimize' the outcome by laboriously scanning all the parameter space or treating environments that may be more conducive for growth, like nebula pressure bumps or trapping of dust in vortices (Kretke and Lin, 2007, Lyra et al., 2009). These are obvious expansions of our work. But by considering the sensitivity of a few key parameters (e.g., gas density, and turbulence strength) on the outcome of the growth process, we do obtain a picture of where the arrow of coagulation typically points to in protoplanetary environments: pebbles, boulders or planetesimals.

In this paper we describe the three nebulae models used in this work and the sources of relative velocity between the aggregates (Sect. 5.2), how we build the coagulation/fragmentation model of Chapter 4 into the Monte Carlo code (Sect. 5.3), and what these first results look like (Sect. 5.4). We also test the sensitivity of the results with respect to variations in gas density, the velocity field, and other key model parameters. Section 5.5 reflect the importance of our result in the context of planetesimal formation and provide suggestions for future experiments. Finally, Sect. 5.6 lists our main conclusions.

5.2 The Nebulae Model

5.2.1 Disk Models

In this Section we briefly describe the disk models considered in this paper.

The low density model: Resolved millimeter emission maps of protoplanetary disks seem to indicate a shallow surface density profile (Andrews and Williams, 2007): $\Sigma_g(r) \propto r^{-0.5}$. Systematic effects of some of their assumptions, such as the disk inclinations or the simplified treatment of the temperature distribution, may suggest somewhat steeper profiles. Therefore, (Brauer et al., 2008a) adopted the following profile:

$$\Sigma_g(r) = 45 \frac{\mathrm{g}}{\mathrm{cm}^2} \left(\frac{r}{\mathrm{AU}} \right)^{-0.8}. \tag{5.1}$$

Here we assumed that the central star is of solar mass, the disk extends from 0.03 AU until 150 AU and that the total mass of the disk is 0.01 $M_\odot$. Assuming that the pressure scale-height is $H_p = 0.05 \times r$ and the vertical structure is gaussian:

$$\rho_g(z, r) = \frac{\Sigma_g(r)}{\sqrt{2\pi} H_p} \exp(-z^2/2H_p^2), \tag{5.2}$$

the density at 1 AU in the midplane ($z = 0$) is 2.4×10^{-11} g cm^{-3}, approximately two orders of magnitude lower than the MMSN value.

MMSN model: The Minimum Mass Solar Nebulae model (MMSN) was introduced by Weidenschilling (1977a) and Hayashi et al. (1985). From the present state of the Solar System today, it is possible to obtain a lower limit to the mass of the solar nebulae from which the planets were formed. The model assumes that the planets were formed where they are currently located (no migration included). It also assumes that all the solid material presented in the solar nebula had been incorporated in the planets. The loss of solid material due to radial drift is not taken into account. Despite these uncertainties, the MMSN model is frequently used as a benchmark. The surface density of the MMSN disk is given by:

$$\Sigma_g(r) = 1700 \frac{\mathrm{g}}{\mathrm{cm}^2} \left(\frac{r}{\mathrm{AU}} \right)^{-1.5}, \tag{5.3}$$

which corresponds to a total disk mass of 0.01 $M_\odot$ contained between 0.4 and 30 AU (between the orbits of Mercury and Neptune). Assuming that the vertical structure of the gas follows a gaussian distribution, leads to a midplane density at 1 AU of 1.4×10^{-9} g cm^{-3}.

The high density model: Desch (2007) introduced a 'revised MMSN model' by adopting the starting positions of the planets in the 'Nice' model of planetary dynamics (Tsiganis et al., 2005) thus taking into account planetary migration. The model predicts that the solar system started out in a much more compact configuration and its surface density profile is given by:

$$\Sigma_g(r) = 5.1 \times 10^4 \frac{\mathrm{g}}{\mathrm{cm}^2} \left(\frac{r}{\mathrm{AU}} \right)^{-2.2}. \tag{5.4}$$

This model is consistent with a decretion disk which is being photoevaporated by the central star. Although the model of Desch (2007) was defined for the outer solar system, we extrapolate the profile to 1 AU in order to cover a broad range of surface density values in our calculations. Assuming, as in the MMSN model, a gaussian vertical distribution, the density at 1 AU in the midplane is 2.7×10^{-8} g cm^{-3}.

For simplicity, we adopt a midplane temperature of 200 K (isothermal sound speed of $c_s = 8.5 \times 10^4$ cm s^{-1}) in all the three models.

5.2.2 Relative Velocities

We consider three sources for relative velocities between dust aggregates. These are Brownian motion, radial drift and turbulence. In the following, we discuss these sources.

The average relative velocity of two particles with mass m_1 and m_2 in a region of a disk with temperature T due to Brownian motion is

$$\Delta v_B(m_1, m_2) = \sqrt{\frac{8kT(m_1 + m_2)}{\pi m_1 m_2}}. \tag{5.5}$$

For micron sized particles, the relative velocity is of the order of 0.1 cm s^{-1}, but for cm sized particles this value drops several orders of magnitude. Therefore, Brownian motion is only effective for collisions between small particles during the initial stages of growth. Because of the low relative velocities, coagulation due to Brownian motion results in fluffy aggregates (Kempf et al., 1999, Blum et al., 1996). In practice there is no growth due to Brownian motion for aggregates larger than 100 micron.

The second source for relative velocity is turbulence. Relative velocity of aggregates due to the random motion of turbulent eddies were calculated numerically by Völk et al. (1980), Mizuno et al. (1988) and Markiewicz et al. (1991). We use the closed form expressions presented by Ormel et al. (2007). We assume that turbulence is parameterized by the Shakura and Sunyaev (1973) α parameter

$$\nu_T = \alpha c_s H_g, \tag{5.6}$$

where ν_T is the turbulent viscosity, c_s is the isothermal sound speed and H_g is the pressure scale height of the disk. The value of the α parameter reflects the strength of the turbulence in the disk. Typical values of α in this paper range between 10^{-3} and 10^{-5}. The turbulent relative velocity is a function of the stopping times of the two colliding particles. The stopping time (or friction time) is the time the particle needs to react to the changes in the motion of the surrounding gas. As long as the radius of the particle is smaller than the mean free path of the gas ($a < \frac{9}{4}\lambda_{\rm mfp}$), the particle is in the Epstein regime, where the stopping time is (Weidenschilling, 1977a)

$$t_s = t_{\rm Ep} = \frac{3m}{4v_{\rm th}\rho_g A}, \tag{5.7}$$

where m and A are the mass and the cross section of the particle, ρ_g and $v_{\rm th}$ are the gas density and the thermal velocity. At high gas densities, where the mean free path is low or in case of larger particles, the first Stokes regime applies and the stopping time is

$$t_s = t_{\rm St} = \frac{3m}{4v_{\rm th}\rho_g A} \times \frac{4}{9}\frac{a}{\lambda_{\rm mfp}}. \tag{5.8}$$

In the first Stokes regime the stopping time is independent of the particle-gas relative velocity as well as the gas density. This regime can be used as long as the particle Reynolds number is smaller than unity. The particle Reynolds number calculated as (Weidenschilling, 1977a):

$$Re_p = \frac{2a\Delta v_{\rm pg}}{\eta}, \tag{5.9}$$

where $\Delta v_{\rm pg}$ is the relative velocity between the particle and the gas, and η is the gas viscosity. For particles outside the Epstein regime, it can be assumed that the systematic velocity (radial drift) dominates over the random velocities (turbulence); therefore, $\Delta v_{\rm pg} \approx v_D$, where v_D is the drift velocity of the particle, defined in the next paragraph. The particle Reynolds number never exceeds unity in our simulations. Therefore, we do not include further Stokes regimes.

Radial drift also leads to relative velocities between aggregates. Radial drift (v_D) has two sources: drift of individual particles (v_d) and drift due to accretion processes of the gas (v_{da}), thus the total radial drift velocity is $v_D = v_d + v_{da}$. The radial drift of individual dust aggregates with mass m is (Weidenschilling, 1977a)

$$v_d = -\frac{2v_N}{St + 1/St}, \tag{5.10}$$

where St is the Stokes number of the aggregate ($St = t_s\Omega$, where Ω is the orbital frequency) and v_N is the maximum radial drift velocity (Whipple, 1972).

The second part of the radial velocity is due to the accretion of the gas. This part of the radial velocity is calculated as follows (Kornet et al., 2001):

$$v_{da} = \frac{v_{\text{gas}}}{1 + St^2}, \tag{5.11}$$

where v_{gas} is the accretion velocity of the gas (Takeuchi and Lin, 2002).

The relative velocity due to radial drift is then simply the difference between the radial velocity of particle 1 and particle 2. However, as the Stokes number of the aggregates is always smaller than 10^{-3} (see Sec. 5.4), the second term of the radial velocity (v_{da}) can be safely neglected:

$$\Delta v_D = |v_{D1} - v_{D2}| \approx |v_{d1} - v_{d2}|. \tag{5.12}$$

This study uses two quantities to describe the porosity of the aggregates. The volume filling factor is:

$$\phi = V^*/V_{\text{tot}} = (A^*/A)^{3/2}, \tag{5.13}$$

where V^* is the volume occupied by the monomers and V_{tot} is the total volume of the aggregate, including pores, and A and A^* are the surface area equivalents of these quantities. In this way, the filling factors also enters the definition of the friction time (Eqs. 5.7 and 5.8). The density of aggregates then follows as $\rho = \rho_0\phi$, where $\rho_0 = 2$ g cm^{-3} is the material density of the silicate. In this study we will also use the reciprocal parameter of the filling factor, which is denoted the enlargement parameter, $\Psi = \phi^{-1}$.

We illustrate the relative velocity between equal sized and different sized aggregates with $\Psi = 20$ ($\phi = 0.05$) in Fig. 5.1 for the disk models considered in this work. Adopting a threshold (fragmentation) velocity of 1 m s^{-1}, the maximum particle size, which can be reached in the models are: 0.025 cm in the low density model, 1.4 cm in the MMSN model and 1.7 cm in the Desch model. The Stokes numbers of these particles are the same in all the three models, 4.7×10^{-3}. The constant fragmentation velocity of 1 m s^{-1} is the typical velocity at which silicate particles will fragment Birnstiel et al. (2009). In our collision model this is not the case for all combinations of mass ratio and porosity (Chapter 4), but the m s^{-1} threshold is still a useful proxy for the point where fragmentation processes will become important.

Figure 5.2 shows the Stokes number as a function of particle radii in the three models. Initially, particles are in the Epstein regime, where the stopping time, thus the Stokes number, depends on the gas density. When the particles enter the Stokes regime, the

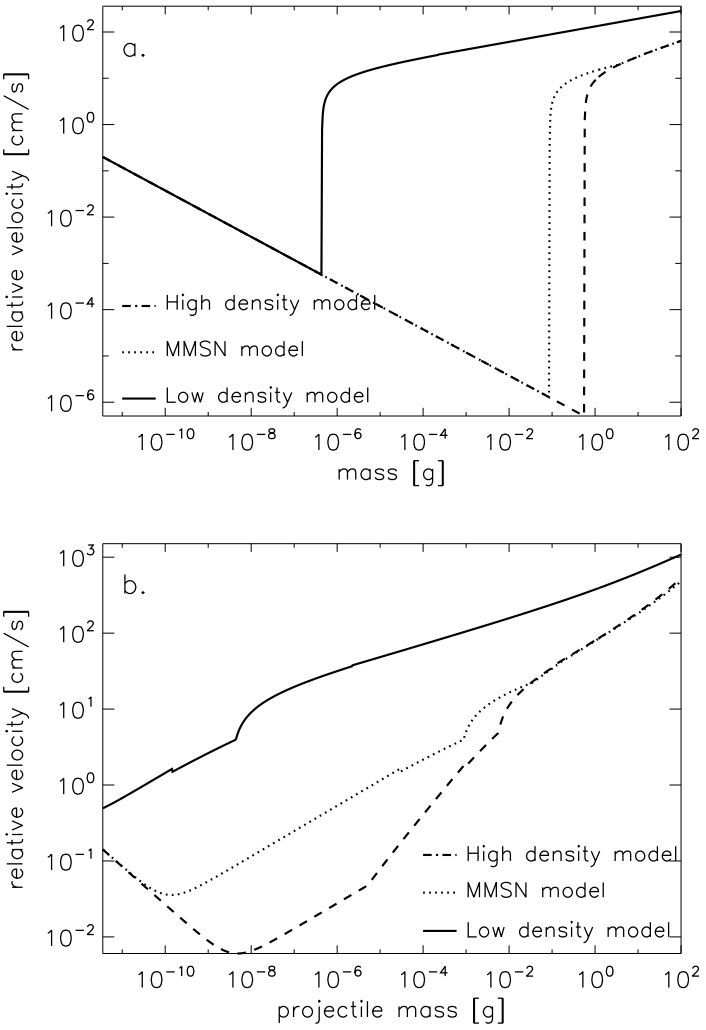

Figure 5.1: The combined relative velocities caused by Brownian motion, radial drift and turbulence for fluffy particles ($\Psi = 20$) in the three disk models for equal sized particles (a) and for different sized particles with a mass ratio of 100 (b). The solid line indicates the low density model of Brauer et al. (2008a). Physical parameters of the disk: the distance from the central star is 1 AU, temperature is 200 K, the density of the gas is 2.4×10^{-11} g cm^{-3}, and the turbulence parameter, $\alpha = 10^{-4}$. The dotted line represents the MMSN model. The density is 1.4×10^{-9} g cm^{-3}, the other parameters are the same. The dashed line corresponds to the high density disk. The gas density is 2.7×10^{-8} g cm^{-3}.

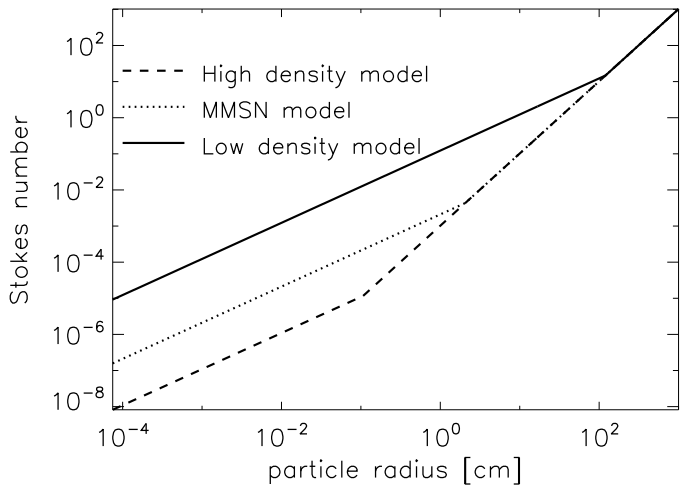

Figure 5.2: The Stokes number as a function of the particle radius in the three models. The parameters of the dust for all of the models are the following: monomer radius is $a_0 = 0.75$ μm, material density is $\rho_0 = 2$ g cm^{-3}, and $\Psi = 1$.

stopping time becomes independent of the gas density (see Eq. 5.8). One can see that particles in the Desch model are in the Stokes regime at Stokes number of 4.7×10^{-3} (when the particles have relative velocities of 1 m s^{-1}), while the aggregates in the MMSN model are close to it, which explains why the maximum particle size is almost the same in these two models.

As discussed in Ormel et al. (2007), particles are initially in the 'tightly coupled particle' regime, where the eddies are of class I type. A particle, upon entering a class I eddy, will forget its initial motion and align itself to the gas motions of the eddy before the eddy decays or the particle leaves it. This regime is apparent in Fig. 5.1a and b. Different sized particles are in this relative velocity regime as long as their masses are less than 10^{-8} g in the low density model, 10^{-3} g in the MMSN model and 10^{-2} g in the high density model assuming fluffy particles ($\Psi = 20$). If the particles leave this regime and enter the 'intermediate particle' regime, their relative velocity increases. This transition affects the particle evolution, as discussed in e.g. Sect 5.4.3.

5.3 Collision Model and Implementation

In this work we use a statistical or 'particle in a box' method to compute the collisional evolution. That is, we assume that all particles are homogeneously distributed within a certain volume (the simulation volume). In reality however, the particles could leave the simulated volume or new particles could enter from outside due to radial drift or random motions (turbulence and Brownian motion). Since we do not resolve the spatial dependence of the aggregates, we will simply assume that local conditions hold during the run. The gas and dust densities are kept constant and particles cannot leave or enter

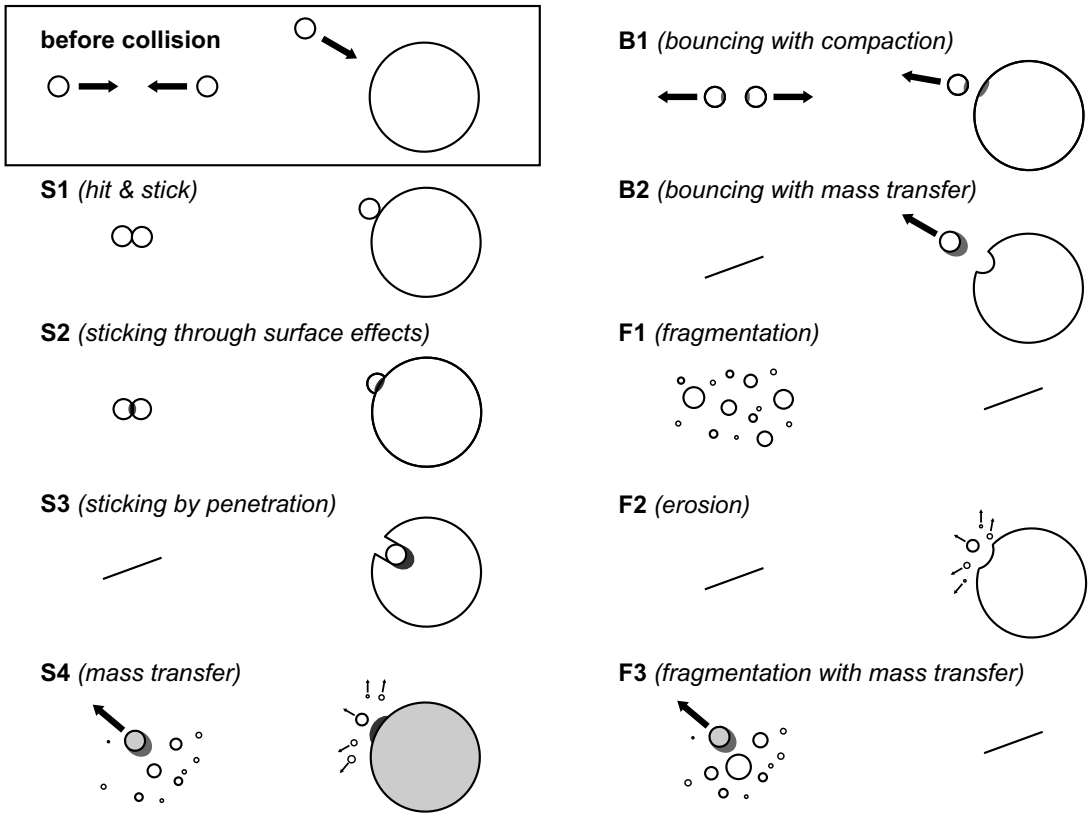

Figure 5.3: The collision types considered in this paper. We distinguish between similar sized and different sized particles. Some of the collision types only happens for one of the mass ratios. Grey color indicates that during the given collision type the particle is compact, or part of the mass will be compacted.

the simulation volume (hereafter 'local approach').

5.3.1 Short Overview of the Collision Model

Many laboratory experiments on dust aggregate collisions have been performed in the past years, see Blum and Wurm (2008). The growth begins as fractal growth and we use the recipe of Ormel et al. (2007) to describe this initial stage. However, once aggregates have restructured into non-fractal, macroscopic aggregates (e.g. $\gtrsim 100$ μm), laboratory experiments show that the collisional outcomes become very diverse. In this regime, many new experiments were performed with dust aggregates consisting of 1.5 μm diameter SiO_2 monomers either with high porosity $\phi = 0.15$ Blum and Schräpler (2004), or intermediate porosity ($\phi = 0.35$). Chapter 4 compiled 19 experiments with different aggregate masses, collision velocities, and aggregate porosities.

From these experiments we have identified nine different collisional outcomes involving sticking, bouncing, or fragmentation (see Fig. 5.3). The occurrence of these regimes

mainly depends on aggregate masses and collision velocities. However, it also depends on the porosity of the particles and on the critical mass ratio. For example, in Chapter 4 we find fragmentation in collisions between a porous aggregate and a solid wall, whereas Langkowski et al. (2008) find sticking of a porous projectile by penetrating an also porous target. Likewise, Heißelmann et al. (in prep.) find bouncing of two similar-sized, porous dust aggregates, while Langkowski et al. (2008) find sticking for the same velocity where one collision partner (target) was significantly bigger. To address the importance of the mass ratio and porosity, we have identified eight different collision regimes (look-up tables) based on a binary treatment of porosity and mass ratio: i.e., *(i)* similarly sized or differently sized collision partners and *(ii)* porous or compact collision partners. The further distinction between target, which we always define as the heavier collision partner, and projectile then results in eight different collision regimes. We denote these regimes as *'pP'* (porous projectile, porous target; target significantly bigger than the projectile), *'pc'* (porous projectile, compact target; target of similar size than the projectile), etc.

In Chapter 4 we have classified each of these 19 experiments into one or more of these eight regimes (see Fig. 4.10 in Chapter 4). Based on extrapolation of experimental findings, we decide in which mass and velocity range collisions results sticking, bouncing, or fragmentation. These results are presented in 4.11 in Chapter 4.

It should be noted that the critical mass ratio between the equal-size (*'pp'*, *'cc'*, etc.) and the different size regimes (*'pP'*, *'cC'*, etc.) is ill-constrained by experiments. Therefore, we use critical mass ratios of $r_m = 10$, 100 and 1000 to explore the effect of this parameter.

5.3.2 Porosity

In Chapter 4 we defined a binary representation of the porosity, particles are either porous or compact. Following the simple model of Weidling et al. (2009), we include a continuous transition between these two 'phases'. They showed that the compaction of particles due to bouncing can be described by porous and compacted sites on the surface of the aggregate. A site of the aggregate is porous if it did not encounter any collisions yet (e.g. bouncing), a compacted site encountered at least one collision already but any further collision happening at that part of the surface cannot change the porosity of this site anymore. We describe the probability of hitting a passive site of the aggregate in the following way:

$$P_p = \frac{\phi_c - \phi}{\phi_c - \phi_p}, \tag{5.14}$$

where ϕ is the volume filling factor of the aggregate, ϕ_c is the critical porosity ($\phi_c = 0.4$, see Chapter 4), and ϕ_p is the volume filling factor of the porous site, which is chosen to be 0.15. If ϕ is between 0.15 and 0.4, a random number decides whether the particle collided with a porous or a compact site. Such a treatment of the porosity ensures a continuous transition from porous to compact aggregates.

5.3.3 The Monte Carlo Method

Using the expressions for the relative velocity, the collisional cross section between the dust particles, and the collisional outcome, we solve for the temporal evolution of the dust size distribution. Traditionally, the Smoluchowski equation is solved to follow the evolution of the mass distribution function (e.g. Dullemond and Dominik, 2004, Dullemond and Dominik, 2005, Tanaka et al., 2005, Brauer et al., 2008a). The collision model typically used in these works is, by necessity, rather simple as in the Smoluchowski formulation the collision and time evolution steps are linked together. These collision models consist of sticking and fragmentation and only the mass of the particles is followed. The advantage of such a model is that it is computationally not too expensive: The entire disk can be modeled. Ormel et al. (2007) introduced a new Monte Carlo method to solve for the mass and the porosity distribution function simultaneously. Their collision model consists of sticking and compaction; ZsD08 added a simple fragmentation model as well. Although these models are more detailed, one can see that they still lack the full complexity which is observed at "the zoo" of laboratory collision experiments.

The MC-approach used in this study has previously been presented by ZsD08. It can be characterized by two key properties: (1) the number of MC-particles (also referred to as representative particles) is kept constant; (2) the method follows the mass of the particle distribution.

Property (1) is required to preserve good statistics. Because of the $\sqrt{N}$ noise of MC-methods, a large fluctuation of N would severely affect the accuracy of the method (Ormel and Spaans, 2008). The second property states that our primary interest lies in the particles that contain most of the mass of the system. Moreover, it has been shown that following the particle's mass distribution – rather than the number distribution – is also a prerequisite to preserve a good correspondence with systems that experience strong growth (Ormel and Spaans, 2008).

Property (2) ensures that the MC method samples the parameter space only where a significant portion of the total dust mass is. However, this is not always desirable. For instance, radiative transfer calculations require the surface area distribution of the aggregates, which determines the opacity. If most of the particle mass is contained in big particles (which are not observable) the amount of small particles (which could contain most of the surface area and determines the IR appearance of the disk) might be resolved with a bad statistics. But if we are interested in following the evolution of the dominant portion of the dust, then MC methods naturally focus on these parts of the phase space.

A required condition for the ZsD08 method to work is that the number of the representative particles N is much less than the number of actual aggregates present in the system under consideration – a condition that is safely met in any of our simulation runs. Then, a representative particle will collide only with the non-representative particles, whose distribution is assumed to be the same as that of the representative particles. We refer to ZsD08 for details regarding the precise implementation and accuracy of the method; here we further concentrate on how the method operates under the new collisional setup.

The collision kernel is defined as the product of the cross section of the colliding

particles and their relative velocity:

$$K_{i,k} = \sigma_{i,k} \Delta v_{i,k}, \tag{5.15}$$

where the index i corresponds to the representative particle and k is the index of the non-representative particle. The kernel is proportional to the probability of a collision. The value of $K_{i,k}$ is calculated for every possible particle pair, and random numbers determine which of the collision will occur first and at which time interval.

The above properties and conditions specify the essence of the ZsD08 method: one of the two collision particles is a representative particle and, by property (1), only one of the collisional products becomes the new representative particle. By property (2) the choice for the new representative particle is weighed by the mass of the collision products. A very helpful analogy here is that of the representative 'atom', which is contained within the representative particle. The choice for the new representative particle after the collision is then proportional to the probability of the representative 'atom' ending up in the collision products. If, for instance, a collision leads to the production of an entire distribution of debris particles, the chance that a particular debris fragment becomes the new representative particle is proportional to the likelihood of this fragment to contain the representative 'atom'.

5.3.4 Implementation of the Collision Types

We describe the implementation of the collision model using the representative 'atom' concept. We refer to Chapter 4 for details of the various collision types described below.

hit-and-stick (S1), sticking through surface effects (S2), sticking by deep penetration (S3): All three of these collision types result in sticking and increase the mass of the aggregate by that of the projectile, but the porosity changes in a different manner (see Chapter 4). The new mass of the representative particle i is then the sum of the original particle masses, $m_{i,\mathrm{new}} = m_i + m_k$, where m_i is the mass of the representative particle and m_k is the mass of the non-representative particle.

fragmentation with mass transfer (S4): In the case of fragmentation with mass transfer (S4), a certain percentage of the mass of the projectile sticks to the target, while the left-over mass of the projectile will fragment into a power law distribution (see Chapter 4)

There are two situations to consider:

1. The representative 'atom' is part of the target. The mass of the new aggregate will be the mass of the original aggregate plus the transferred mass from the non-representative particle ($m_{i,\mathrm{new}} = m_i + m_{\mathrm{trans}}$, where m_{trans} is the transferred mass calculated according to Chapter 4).

2. The representative 'atom' is part of the projectile. Again, we have two situations.

(a) The representative 'atom' will be transferred to the non-representative particle. The mass of the new representative particle will be the mass of the non-representative particle plus the transferred material ($m_{i,\mathrm{new}} = m_k + m_{\mathrm{trans}}$). The chance of transferring (removing) the representative atom from the projectile is simply $P = m_{\mathrm{trans}}/m_i$, the ratio between the transferred mass and the mass of the projectile.

(b) The representative 'atom' remains in one of the fragments. The chance of this event is $P = (m_i - m_{\mathrm{trans}})/m_i$, the ratio between the fragmented mass to the original mass of the representative particle. As discussed in Chapter 4, the fragments follow a power law mass distribution. The distribution is defined by the maximum mass of the fragments, which is a function of the relative velocity and the total mass of the fragments. The total mass of the fragments is $m_i - m_{\mathrm{trans}}$. We randomly choose from the fragment distribution to find the new mass of the representative particle (to find which of the fragments will contain the representative 'atom').

bouncing with compaction (B1): Upon bouncing with compaction (B1) particles collide and bounce. Bouncing itself does not change the mass of the particles, but it compactifies them according to Chapter 4. As observed in laboratory experiments (Weidling et al., 2009), there is a small probability ($P_{\mathrm{frag}} = 10^{-4}$) that the bouncing particle will break apart. If this happens, we break the particle into two equal mass pieces.

bouncing with mass transfer (B2): bouncing with mass transfer (B2) is, from the implementation point of view, similar to fragmentation with mass transfer (S4). The recipe to define the new representative particle is as in fragmentation with mass transfer (S4). The difference is that the projectile does not fragment during the collision, and that the porosity changes differently (see Chapter 4).

fragmentation (F1): Fragmentation only happens between similar sized aggregates in the *'pp'* and *'cc'* regimes. The fragments follow a power law mass distribution where the maximum mass of the fragments is determined by the relative velocity of the particles and the total mass that goes into the fragments (Chapter 4). We randomly choose from these distribution to determine the new mass of the representative particle.

erosion (F2): erosion (F2) happens between different sized particles only. During the collision the projectile"kicks out" pieces from the target aggregate. These pieces follow a power law distribution (see Chapter 4). We have to consider two cases.

1. The representative 'atom' is in the target. Again, we have two possibilities.

   (a) The representative 'atom' will stay in the target after the collision. The mass of the new particle will be $m_{i,\mathrm{new}} = m_i - m_{\mathrm{er}}$, where m_{er} is the eroded mass.

The probability of this event is $P = (m_i - m_{\rm er})/m_i$, that is the ratio between the left-over mass (which does not erode) and the mass of the original particle.

(b) The representative 'atom' is part of the eroded particles. As the eroded particles follow a power law distribution, we randomly pick from this distribution to determine the new mass of the representative particle. The chance for this event is the ratio between the eroded mass and the original mass of the particle ($P = m_{\rm er}/m_i$).

2. The representative 'atom' is part of the small particle which caused the erosion. As the particles do not stick and the small particle does not fragment, the representative particle remains unaffected.

fragmentation with mass transfer (F3): In fragmentation with mass transfer (F3) the porous particle gets destroyed by the compact one and transfers a certain amount of mass to the compact particle. fragmentation with mass transfer (F3) only happens in the *'cp'* regime. Again, we have two possibilities.

1. The representative 'atom' is part of the compact particle. In this case the representative 'atom' cannot leave the particle. The new mass of the representative particle will be $m_{i,\rm new} = m_i + m_{\rm trans}$, the sum of the original mass plus the transferred mass.

2. The representative 'atom' was part of the porous aggregate.

   (a) The representative 'atom' is part of the material which is transferred to the compact particle. In this case, the new mass of the particle will be that of the compact (non-representative) particle plus the transferred material ($m_{i,\rm new} = m_k + m_{\rm trans}$). The probability of this event is $P = m_{\rm trans}/m_i$.

   (b) The representative 'atom' is part of the fragments. As before, the mass distribution will follow a power law and we randomly pick from this distribution to determine the new mass of the representative particle. The probability of this event is $P = (m_i - m_{\rm trans})/m_i$.

5.3.5 Evolving the Particle Properties in Time

We summarize how the particle properties are evolved in time using the above described kernel. We start with the size and porosity distribution of the particles at a given time, t. At $t = 0$, we must give the initial size and porosity distribution, see Sect. 5.4.1. Knowing these:

- We calculate the cross sections of all possible collision partners, as well as their relative velocities using the equations described in Sect. 5.2.2. Both are used to determine the collision rates between the particle pairs.

- By using random numbers, we identify from the collision rates the representative particle, which is involved in the collision, as well as the non-representative particle it collides with and at what time the collision takes place ($t + \Delta t$).
- Knowing the masses (mass ratio) and porosities of the collision partners, we identify in which of the eight regimes the collision takes place (e.g. *'pP'*, or *'pC'*, etc.).
- Next, we identify which of the nine collision types materializes (Fig. 5.3) using the relative velocity of the particles and the mass of the projectile (see Chapter 4).
- Based on the collision recipe described in Chapter 4 and Sect. 5.3.4, the new mass and new porosity of the representative particle is calculated and the new size and porosity distribution of the particles at time $t + \Delta t$ is obtained.
- In the final step, we update the collision rates.

5.4 Results

5.4.1 Initial Conditions, Setup of Simulations

All simulation starts with silicate monomers of 1.5 μm diameter and 2 g cm^{-3} material density (monodisperse size distribution). We simulate the dust evolution at the midplane of our disk models at a distance of 1 AU from the central star. The gas density is obtained from the disk models described in Sect. 5.2.1. We assume a typical 1:100 dust to gas ratio. We follow the history of each collision: the mass and porosity of the colliding particles, their relative velocity, the occurred collision type and the new mass and porosity of the particles. In this way we can reconstruct the history of the dust evolution.

The parameters we vary in this study are the gas density ρ_g and the turbulence parameter α. We also treat the critical mass ratio r_m as a free parameter in order to explore its effect on the dust evolution.

We provide a detailed description of the low density model with $\alpha = 10^{-4}$ and critical mass ratio of 100 in Sect. 5.4.2. We then compare this with the MMSN model and the high density model using the same turbulence parameter and the critical mass ratio (Sects. 5.4.3 and 5.4.4). In Sects. 5.4.5 and 5.4.6 we discuss the effects of changing the turbulence parameter and critical mass ratio by comparing those results with the two example runs.

5.4.2 The Low Density Model

The gas density in this disk model at 1 AU is 2.4×10^{-11} g cm^{-3}, the turbulence parameter is $\alpha = 10^{-4}$, the critical mass ratio is $r_{\rm m} = 100$. As shown in Fig. 5.1, the particles reach the fragmentation velocity (1 m s^{-1}) already at sizes smaller than millimeter because the particles in low gas density environment decouple from the gas already at these small radii

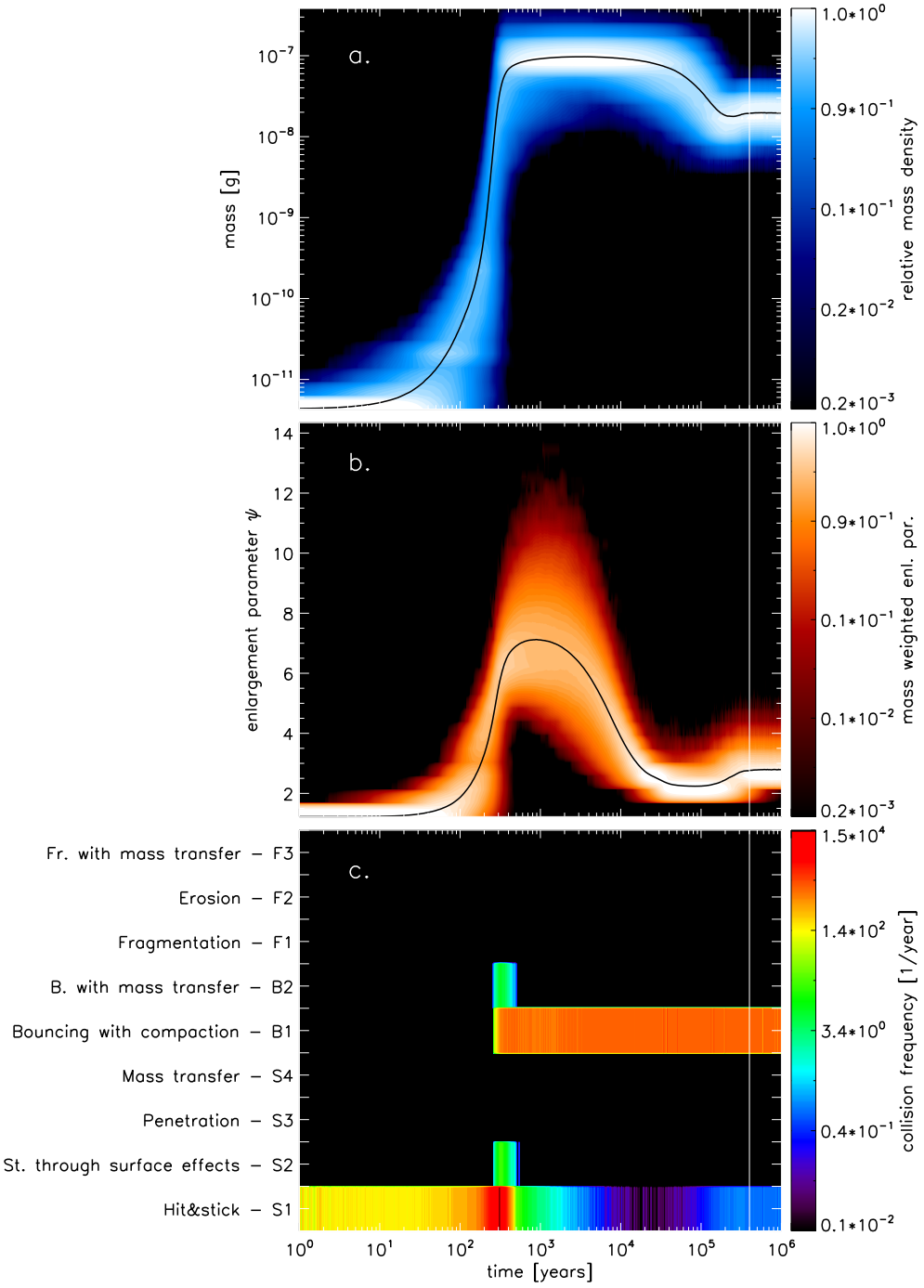

Figure 5.4: The evolution of the mass distribution (a), enlargement parameter distribution (b) and the collision frequency of the nine different collision types (c) in the low density model with $\alpha = 10^{-4}$ and critical mass ratio of 100. The x-axis shows the time. The y-axis of the (a) and (b) figures show the logarithmic mass and the linear enlargement parameter respectively. The contours represent the normalized mass density and the mass weighted enlargement parameter. The black lines represents the average of the mass and enlargement parameter at a given time. The y-axis on the (c) figure represents the nine collision types. Each stripe shows the total collision rate of the collision types. Two distinct phases can be distinguished. During the initial 300 yr particles grow by hit-and-stick (S1), after that the evolution is governed by bouncing with compaction (B1). The white lines indicate how long our 'local approach' assumption is valid (discussed in Sect. 5.3).

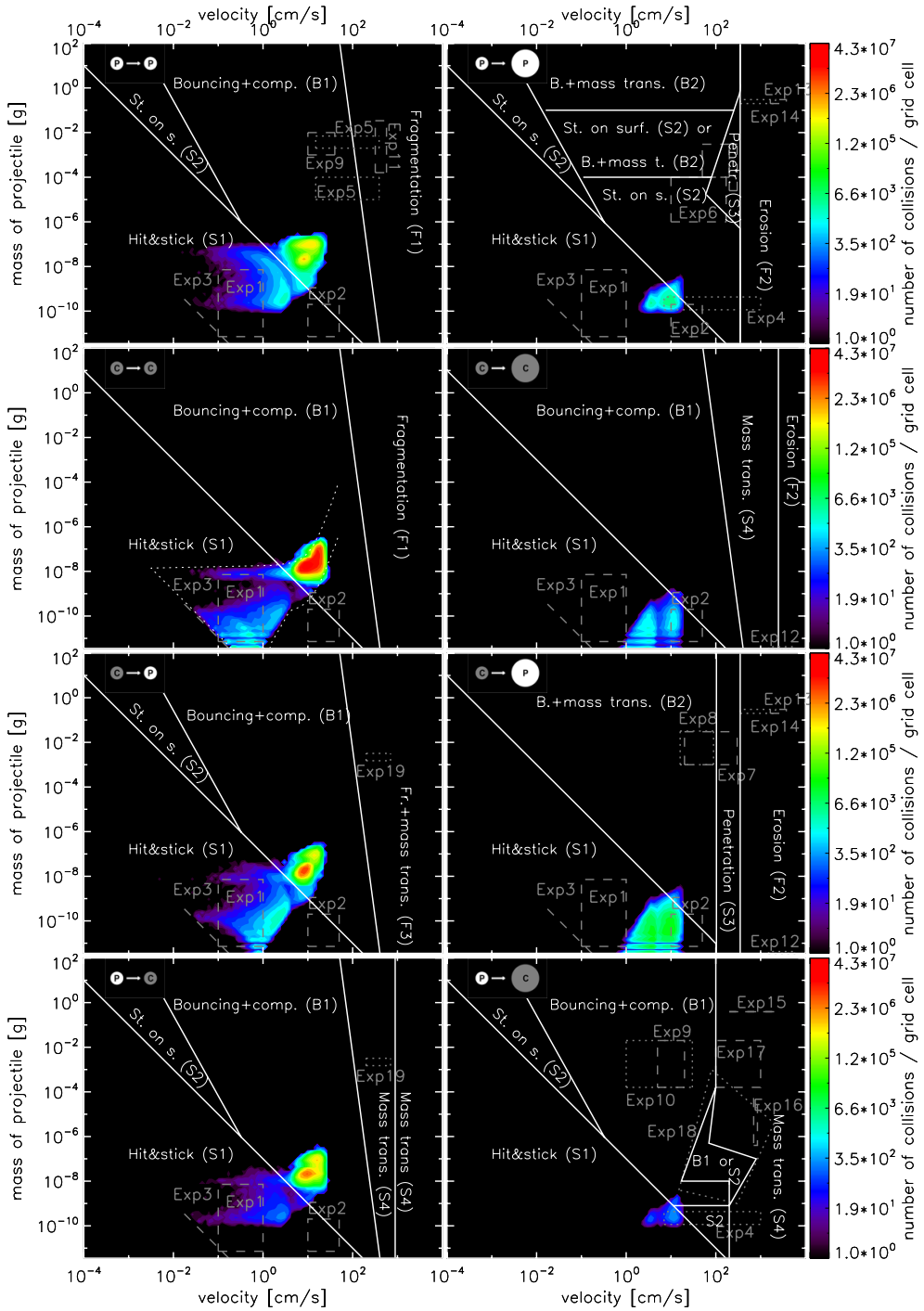

Figure 5.5: The collision history of the eight regimes in the low density model for $\alpha = 10^{-4}$. The x-axis is the relative velocity, the y-axis shows the projectile mass. The different collision types, their border lines, as well as the areas covered with laboratory experiments (grey) are plotted. A relative velocity - mass grid is created and in these grid cells we calculate how many collisions happened until the 'local approach' assumption is valid (4×10^5 yr). This is represented by the colors: yellow and red indicate a high collision frequency. The two dotted lines on the *'cc'* regime are evolution tracks. Assuming a constant (40%) volume filling factor, the relative velocity between equal sized particles (left curve) and particles with a mass ratio of 100 (right curve) can be calculated. The collisions in the simulation should lay between these two lines. The small deviations are due to the fact that the volume filling factor is not exactly 40% during the simulation.

Figure 5.4 shows the evolution of the mass distribution (a), the porosity distribution (b) and the collision frequency of the various collision types (c). The x-axis shows the time in a logarithmic scale. The y-axis of Fig. 5.4a, b shows the mass and enlargement distributions, respectively. Here, the intensity of the color reflects the number density of representative particles, which, as explained in ZsD08, measures the mass density of the distribution. Thus, in Fig. 5.4a the intensity levels directly reflect the mass density, while in Fig. 5.4b the colours indicate the mass weighted enlargement parameter. The black lines show the average of these quantities over the particle distribution. The y-axis in Fig. 5.4c represents the nine collision types used in this paper. Every stripe shows the total collision rate of the collision types at a given time

Figure 5.5 represents the collision history in the eight collision regimes. The x-axis is the velocity, the y-axis shows the mass of the projectile. A mass-velocity grid is created and for all grid cells we calculate how many collisions happened inside that given grid cell during which our 'local approach' assumption is correct, that is 4×10^5 yr. The different collision types and their border lines, as well as the areas which are covered with laboratory experiments (indicated with grey colors) are plotted. For more details on the experiments, see Chapter 4.

In the *'cc'* panel, we indicate two curves with dotted lines. These curves are evolution tracks. The left curve is obtained by calculating the relative velocity between equal sized particles with an enlargement parameter of 2.5 (volume filling factor of 40%). The right curve represent the relative velocity between particles having a mass ratio of 100. These two curves serve as a guide to our results, as collisions should happen between these two curves in the *'cc'* panel. The lower part of the left curve, where the relative velocity decreases with increasing mass, is a sign that relative velocities between equal sized particles are dominated by Brownian motion. For higher masses, the relative velocity is dominated by turbulence. These curves do not precisely match the contours because we assumed a constant enlargement parameter of 40% when calculating the evolution tracks, whereas Ψ is a free parameter in the simulation.

Early Evolution

We discuss here the evolution of the distribution functions until the 'local approach' assumption becomes invalid (4×10^5 yr). The long term evolution of the dust is discussed in Section 5.4.2.

We distinguish two distinct phases here. During the first 300 yr, particles grow by the hit-and-stick (S1) mechanism. The second phase is bouncing with compaction (B1) dominated; the particles leave the S1 regimes. During this phase the mass of the particles is slowly decreasing and the enlargement parameter asymptotically reaches a minimum value of 2.23. As discussed in Chapter 4, keeping the bouncing velocity of a particle constant, the porosity of the aggregate will asymptotically reach a maximum value, $\phi_{\max}$ (see Chapter 4). The relative velocity of a particle is a function of the friction time (Eq. 5.7), which depends on the ratio of the mass to surface area, m/A. Since particle growth is halted at this point in the simulation (m stays constant), only a decrease in A due

to compaction can further increase the velocity between particles. The particle radius can decrease until either $\phi_{\max}$ for the given relative velocity is reached, or until particles reach the maximum compaction possible. The latter limit, random close packing (RCP), corresponds to an enlargement parameter of 1.6 (volume filling factor of ∼60%)

We find that fragmentation does not play a role during the evolution of these particles indicated by Fig. 5.4c. As can be seen in Fig. 5.5, their evolution is halted by bouncing before the particles could reach the fragmentation barrier. The two dominant collision types are hit-and-stick (S1) and bouncing with compaction (B1).

Termination of Growth

As we can see from Fig. 5.5, sticking at higher energies than the hit-and-stick (S1) border lines is only possible inside the *'pP'* regime. As soon as we no longer have collisions inside this regime or the S1 regimes, the growth is halted. There can be two reasons why this is happening: 1.) All particles are compact; there are simply no collisions in the *'pP'* regime. 2.) The width of the particle mass distribution is less than the critical mass ratio (r_m), such that all collision take place in the equal-size regimes (*'pp'*, *'pc'*, etc.).

In the case of the current simulation, the small particles have been 'consumed'. Once the heavy particles grow into the bouncing with compaction (B1) area of the *'pp'* regime, their growth in the *'pp'* regime stops. The heavy particles collect the small ones via collisions in the *'pP'* regime and by doing so, the width of the distribution is reduced to a value which is less than r_m. Therefore, before particles could reach the fragmentation barrier, growth is halted. Due to B1, particles get compacted and collisions in the *'cc'*, *'cp'* and *'pc'* regimes appear.

Long Term Evolution

Before discussing the long term evolution of the distribution functions, we must consider for how long our starting assumptions ('local approach' and constant gas density) hold true.

Using Eq. 5.11, we calculate that a particle with Stokes number 10^{-4} drifts a distance of 1 AU in roughly 4×10^5 yr. This is the drift timescale beyond which the 'local approach' assumption (discussed in Sect. 5.3) is not valid anymore: particles become separated from each other on this timescale.

Another process through which particles separate is by viscous spreading. We determine the viscous timescale of the disk at 1 AU:

$$t_{\rm vis} = r^2/\nu_T, \tag{5.16}$$

where r is the distance from the central star (1 AU), ν_T is defined in Eq. 5.6. The viscous timescale in our model, using $\alpha = 10^{-4}$, is of the order of 10^6 yr.

One has to consider the results of the simulation with caution for longer times than the drift or viscous timescales. We find that the equilibrium state of the particles is hardly reached within these timescales. Upon neglecting these warnings, we find that the final

equilibrium state of the dust is reached at $t = 4 \times 10^5$ yr. The equilibrium is reached between the bouncing collisions resulting in breakage and hit-and-stick (S1) (see Fig. 5.4c). The equilibrium average mass and porosity of the particles are $\bar{m}_{\rm fin} = 2 \times 10^{-8}$ g, $\bar{\Psi}_{\rm fin} = 2.77$.

To be able to compare the distribution functions of different runs, we define some quantities using the mean of the distribution functions shown with black lines in Fig. 5.4a and b: $\max(\bar{m})$, the maximum of the mean mass; $\max(\bar{\Psi})$, maximum of the mean enlargement parameter; Ψ_{min}, the minimum mean enlargement parameter when particles do not compact anymore; $t_{\rm noc}$, the time when Ψ_{min} is reached, that is when the time derivative of $\bar{\Psi}$ is zero ($d\bar{\Psi}/dt = 0$); and $\max(\bar{St})$, the maximum average Stokes number reached during the simulation. The values of these quantities are listed in Table 5.1 (model id 'Lt1d-4m100'). In this table, Col. 1 describes the model names. 'L' stands for the low density model, 'M' is the MMSN model, 'H' is the high density model, the letter 't' and the following number indicates the value of the turbulence parameter, and the letter 'm' and the number shows the used critical mass ratio values. Columns 2, 3 and 4 show the gas density, turbulence parameter and the critical mass ratio respectively. Columns 5, 6, 7, 8 and 9 list the parameters defined to characterize the distribution functions. These are $\max(\bar{m})$ in Col. 5, $\max(\bar{\Psi})$ in Col. 6, Ψ_{min} in Col. 7, $t_{\rm noc}$ in Col. 8 and finally $\max(\bar{St})$ in Col. 9.

5.4.3 The MMSN Model

The gas density in the MMSN model at 1 AU at the midplane is 1.4×10^{-9} g cm^{-3}, $\alpha = 10^{-4}$, the critical mass ratio is 100. As shown in Fig. 5.1, the particles grow to bigger sizes than in the low density model, as they are better coupled to the gas and the relative velocities are suppressed. As in the previous Section, we first discuss the evolution of the distribution functions for as long as the 'local approach' assumption holds true (6×10^5 yr in this model).

Figure 5.6 shows again the time evolution of the mass (a), enlargement parameter (b), and the collision frequency (c). Figure 5.7 shows the collision history. These figures show a rather different evolution than the previous model.

Early Evolution

We find that during the fractal growth regime, the collision rate of hit-and-stick (S1) is much higher than in the low density model (Fig. 5.6c). This is due to the higher dust densities. We can see from Fig. 5.7, *'cc'* regime, that growth starts with Brownian motion because the relative velocity decreases with increasing particle mass for particle masses less than 10^{-9} g. As a result of these low velocity collisions, some particles reach enlargement parameter values higher than 30 (volume filling factor less than 3.3%). At 200 yr, some particles grow above the border line of hit-and-stick (S1) and enter the area of sticking through surface effects (S2) in the *'pP'* plot, and bouncing with compaction (B1) in the *'pp'* plot. Growth due to S1 and S2 continues until different sized particles enter the

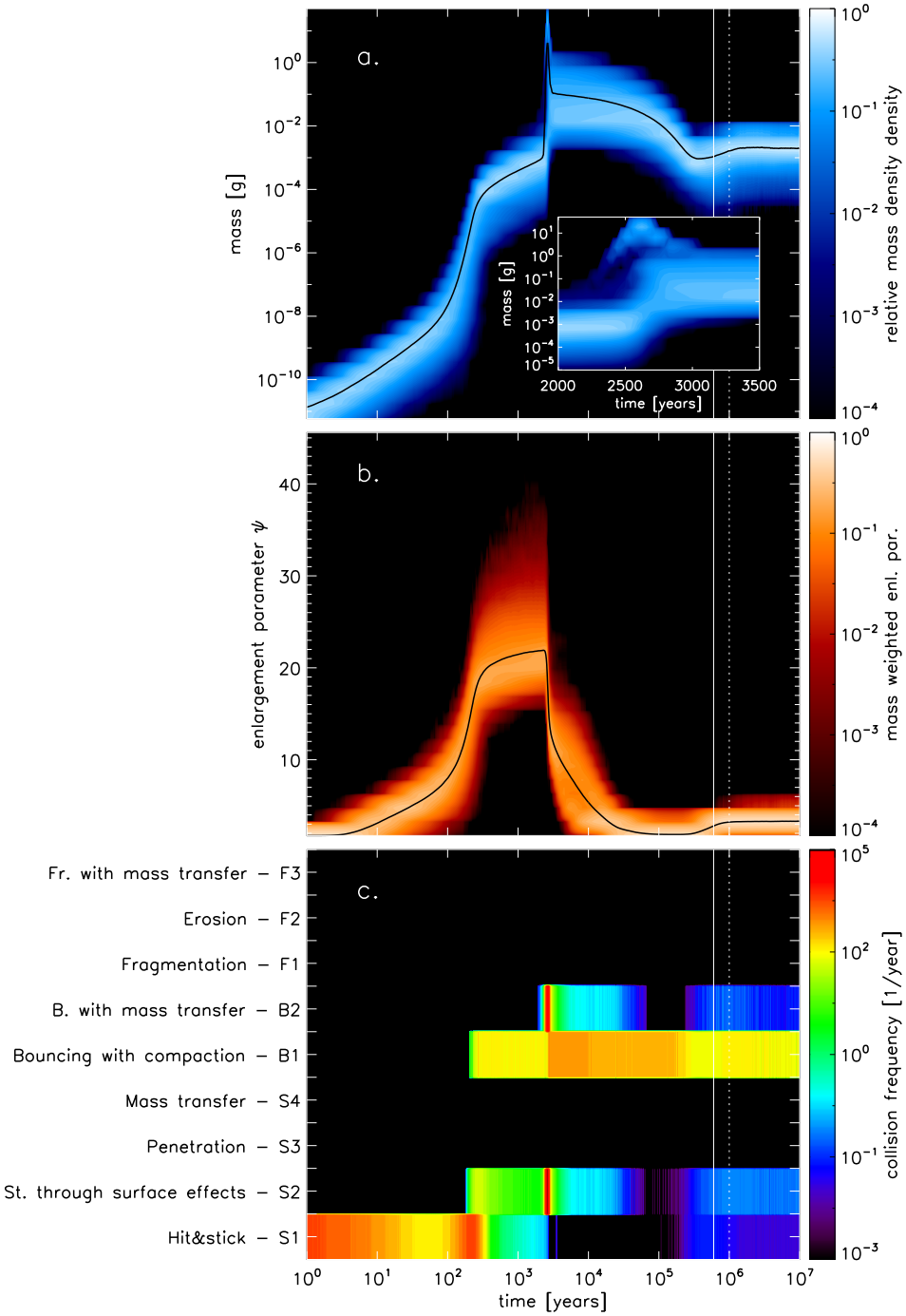

Figure 5.6: Same as Fig. 5.4 but for the MMSN model. We magnify the spike of the mass distribution at $\sim 2.5 \times 10^3$ yr in Fig. (a). Four phases can be distinguished here. Initially (first 300 yr) particles grow purely by hit-and-stick (S1). After this the growth slows down because Bouncing with compation (B1) starts and all particles leave the hit-and-stick (S1) regime. Between 3×10^3 and 10^4 yr, particles enter the transition regime between sticking through surface effects (S2) and bouncing with mass transfer (B2) on the *'pP'* regime. Some particles reach masses of 1 g, but their masses are fastly reduced by B2. The last phase is bouncing with compaction (B1) dominated. The solid/dotted white lines indicate how long our 'local approach' assumptions are valid (discussed in Sect. 5.3).

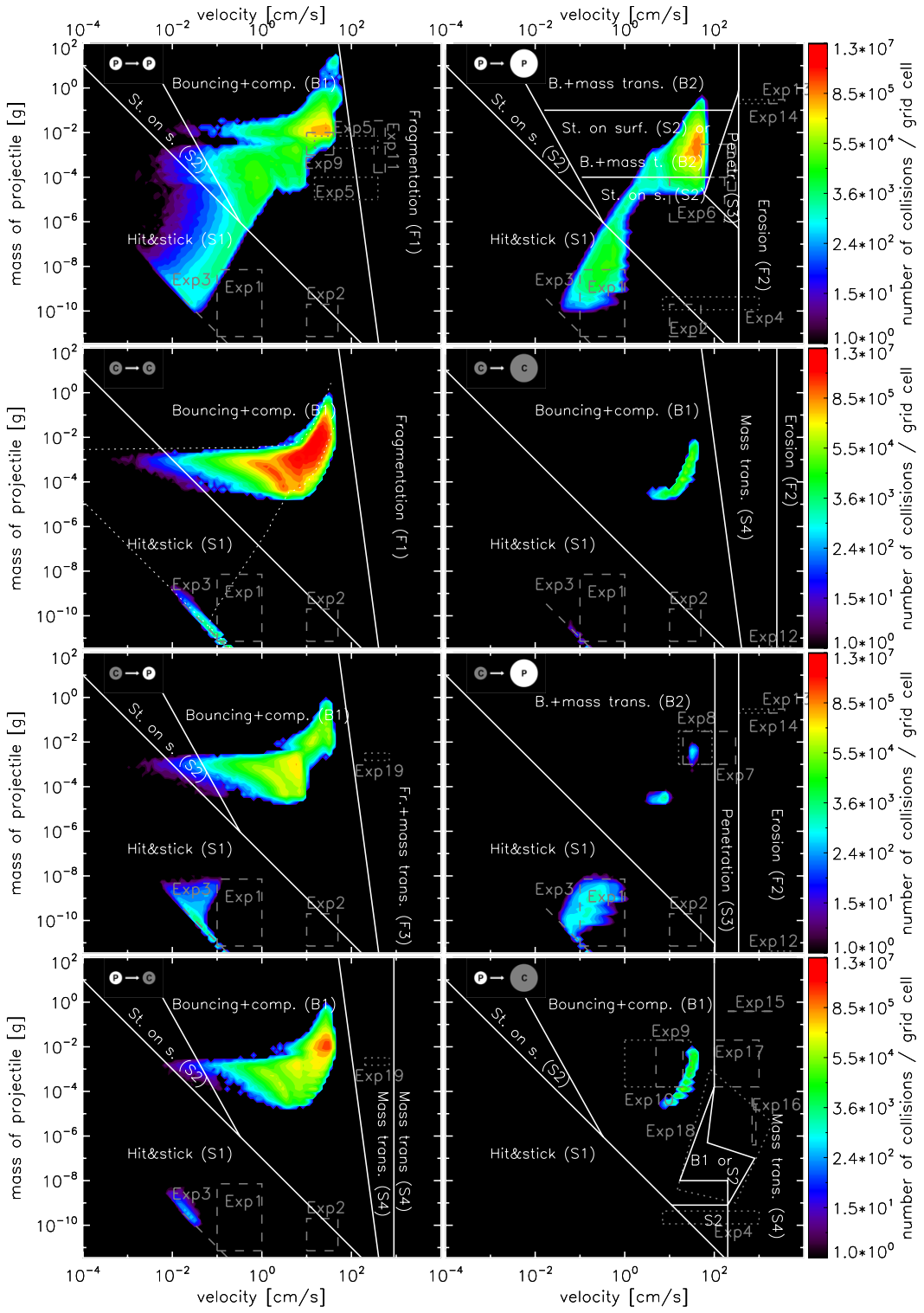

Figure 5.7: Same as Fig. 5.5 but for the MMSN model. The particles are better coupled to the gas due to the higher gas density. Therefore, they grow to bigger sizes than in the low density model.

transition regime in the *'pP'* plot. One can see in Fig. 5.6a, that some particles reach 1 g in mass. However when particle collisions enter the transition regime between bouncing with mass transfer (B2) and sticking through surface effects (S2) in the *'pP'* plot, their masses are equalized due to the mass transfer of the B2 collisions and the collisions shift to the similar sized regime (B1). We find that after roughly 10^4 yr particles mostly bounce and compact. The enlargement parameter reaches a minimum value of 1.85 (54% volume filling factor), the mass distribution function slowly decreases due to a small probability of breakage. Collisions at this point are mainly happening in the *'cc'* regime.

A peculiar feature of Fig. 5.6a is a peak at $t = 2.5 \times 10^3$ yr, which is accompanied by a fast decrease in the enlargement parameter in Fig. 5.6b and an increased collision rate of sticking through surface effects (S2) and bouncing with mass transfer (B2) in Fig. 5.6c. At this point, the relative velocity due to turbulence increases. As discussed in Sect. 5.2.2, particles leave the 'tightly coupled particle' regime and enter the 'intermediate particle' regime (see the relative velocity bump in Fig. 5.1b). We calculate the growth timescale of the heaviest particle with mass M in the simulation as follows:

$$t_{\rm gr} = \left(\frac{1}{M} \frac{dM}{dt} \right)^{-1} . \tag{5.17}$$

This is illustrated with a dotted line in Fig. 5.8. As a comparison, we also calculate the minimum growth timescale that a particle can have (solid line). That is:

$$t_{\rm max} = \left(\frac{M}{\rho_d \Delta v \sigma_M} \right)^{-1} , \tag{5.18}$$

where σ_M is the cross section of the largest particle. Here, we assume that the 'swept up' particles have masses of $M/100$, therefore we use the relative velocity curve presented in Fig. 5.1b, dotted line. The effect of the relative velocity bump and the increased growth rate is seen at 0.1 g.

The relative velocity 'boost' happens shortly after the particles enter the transition regime of S2 and B2 in the *'pP'* plot. The heaviest particle, which encounters the velocity transition the earliest, experiences higher relative velocities leading to an increased collision rate with the other particles. As the particles are initially located at the lower part of the S2-B2 transition regime (with masses of 10^{-3} g, see Fig. 5.6a), the heaviest particle experiences fast growth and reaches masses of 30 g. The simulated timescale, however, does not reach the minimum growth timescale due to the bouncing with mass transfer (B2) collisions which are reducing the mass of the heaviest particle. The rest of the particle population increases in mass because of B2 and the growth rate of the heaviest particle decreases. Eventually, the fast growth of the heaviest particle is halted, the growth timescale at $m = 30$ g is infinity. From this point on, the heaviest particle reduced in mass, and B2 equalizes the masses of the particles.

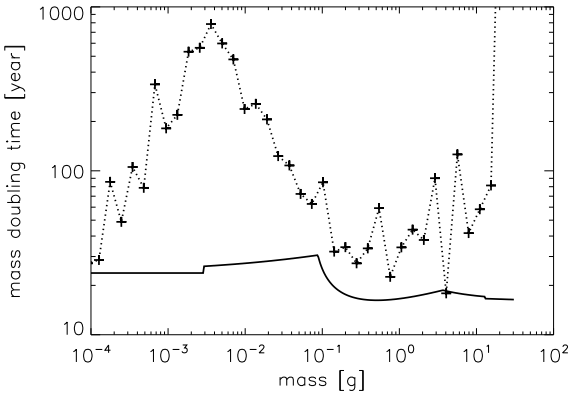

Figure 5.8: The dotted line and the '+' signs represent the growth timescale of the heaviest particle in the MMSN simulation with $\alpha = 10^{-4}$ and $r_m = 100$. As a comparison, we show the minimum growth timescale a particle can have in this simulation (solid line).

Long Term Evolution

We calculate the drift and viscous timescales to determine how long our assumptions of 'local approach' and constant gas density are valid. Assuming Stokes number 10^{-4} particles, we find that the drift timescale is of the order of 6×10^5 yr, the viscous timescale is 10^6 yr. These timescales are indicated with solid and dotted white lines in Fig. 5.6.

We find that the final equilibrium is reached at $t = 2 \times 10^6$ yr, which is longer than the drift and the viscous timescales. The equilibrium is reached between the growth mechanisms of hit-and-stick (S1), sticking through surface effects (S2) and the destruction mechanisms of bouncing resulting in breakage and bouncing with mass transfer (B2). The final average mass and porosity of the particles are $\bar{m}_{\rm fin} = 2 \times 10^{-3}$ g, $\bar{\Psi}_{\rm fin} = 3.3$.

We conclude that the dust evolution is more complex in the MMSN model than in the low density model because the complex interaction of the velocity field and the collision kernel is apparent in this model. As in the previous model, bouncing with compaction (B1) is the most frequent collision type and hit-and-stick (S1) determines the initial particle growth, but sticking through surface effects (S2) and bouncing with mass transfer (B2) are of importance in this model. The final equilibrium is not reached within the drift and viscous timescales.

5.4.4 The High Density Model

The gas density in this model is 2.7×10^{-8} g cm^{-3} at the midplane of the disk at 1 AU distance from the central star. The values of α, r_m and the dust to gas ratio are the same as in the previous models.

Figure 5.1, dashed line, shows the relative velocity field of fluffy aggregates in this model. As already discussed in Sect. 5.2.2, the aggregates reach 1 m s^{-1} relative velocities

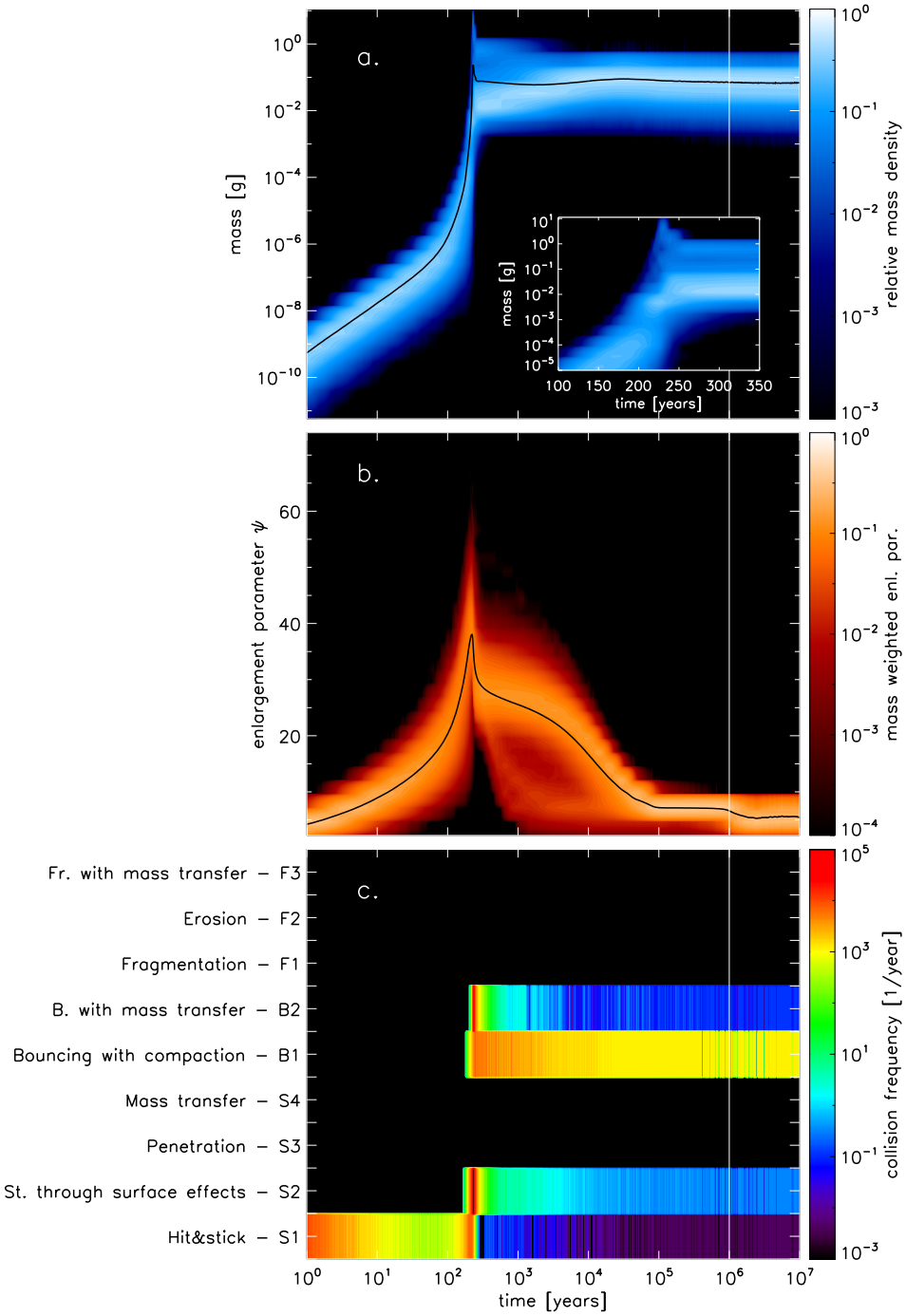

Figure 5.9: Same as Fig. 5.4 but for the high density model. As in Fig. 5.6a, we zoom in on the peak at the mass distribution. The solid white line indicate how long our 'local approach' assumptions are valid at $t = 10^6$ yr (discussed in Sect. 5.3).

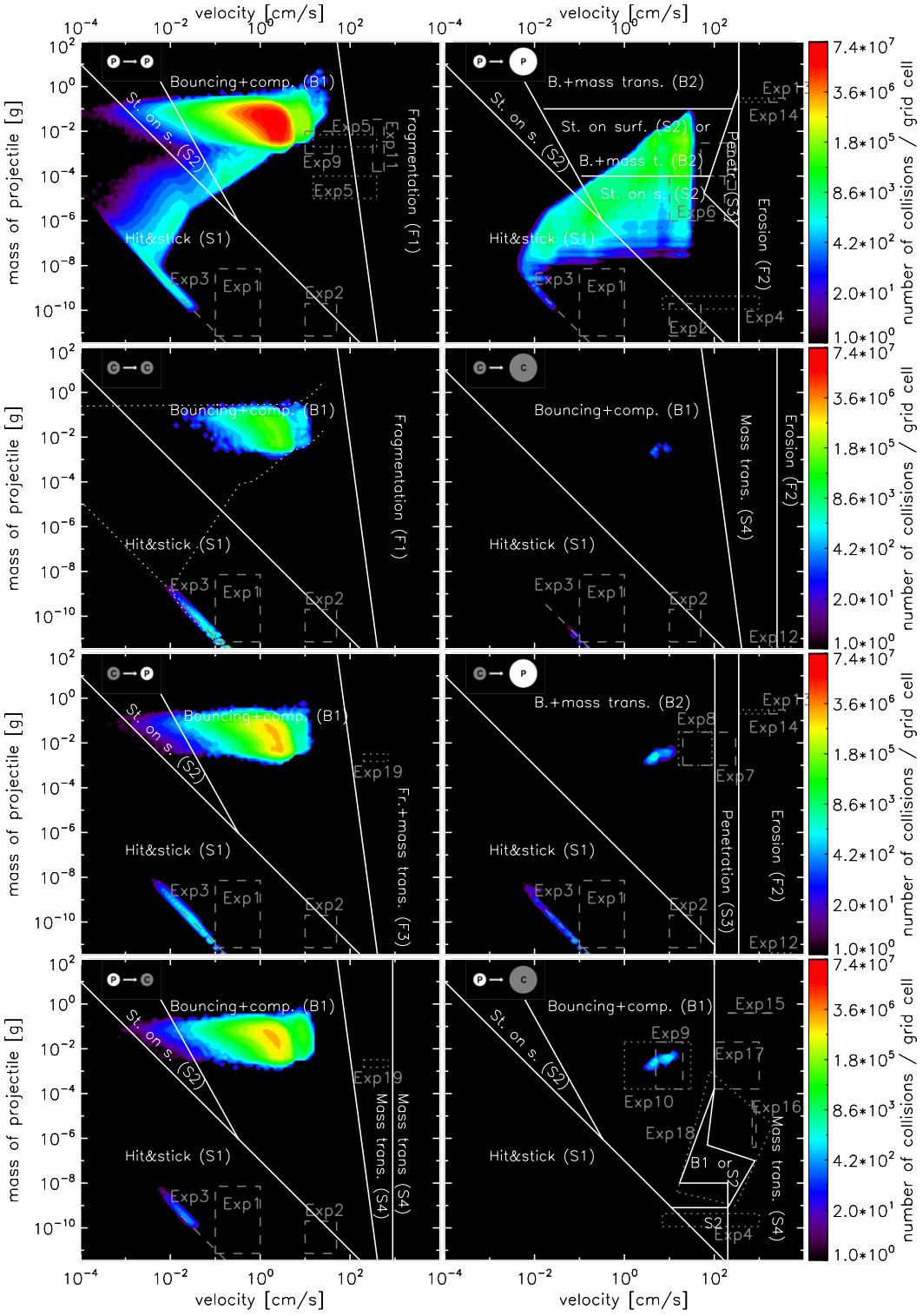

Figure 5.10: Same as Fig. 5.5 but for the high gas density model.

at similar masses as the MMSN model due to the Stokes drag. Therefore, we expect that the final aggregate sizes and masses will be similar to the particles produced in the MMSN model.

Figure 5.9 shows the time evolution of the mass (a), enlargement parameter (b) and the collision frequency (c). Figure 5.10 illustrates the collision history.

Early Evolution

As seen in Fig. 5.10, Brownian motion is the dominant source of relative velocity, as long as particles stay below masses of 10^{-8} g (that is an order of magnitude higher than in the MMSN model). Therefore, the enlargement parameter of the aggregates is also higher than in the MMSN model. As the hit-and-stick (S1) collisions are more frequent than in the MMSN model due to the higher dust densities, the particles reach the sticking through surface effects (S2) – bouncing with mass transfer (B2) transition regime earlier, at $t = 200$ yr. The peak in the mass distribution is not as pronounced as in the MMSN model. The relative velocity boost happens for heavier aggregates (10^{-2} g, see Fig. 5.1b) due to the higher gas density of the model. When the fast growth of the heaviest particle starts, most of the projectiles are already in the transition regime. Here, the B2 collisions soon reduce the mass of the heaviest particle and narrow the mass distribution.

In contrast to the MMSN model, the mass of the particles is not reduced due to the low probability of breakage in bouncing with compaction (B1), but is kept nearly constant in time. This is the result of the increased collision rate of sticking through surface effects (S2). The S2 collision rate increased because of low velocity collisions, which are occurring when particles are in the tightly couple regime and have similar stopping times. These S2 collisions are happening in the *'pp'* regime as seen in Fig. 5.10. These collisions cancel out the effect of breakage in B1.

The maximum Stokes number reached in this model is 3.6×10^{-5} (see Table 5.1, model id 'Ht1d-4m100'), lower than in the MMSN model. The growth in this model is halted by the bouncing with mass transfer (B2) collisions in the transition regime of the *'pP'* panel. This shows us that particles cannot reach masses much larger than 1 g independently from the gas density (or Stokes number), because at this point, particles enter the S2-B2 transition regime and the growth is halted. Further increasing the gas density would result in even lower Stokes numbers.

Long Term Evolution

The drift and the viscous timescales in the high density model are both 10^6 yr. As seen in Fig. 5.9a, the particle masses do not change significantly after $t = 10^3$ yr. The porosity is reduced due to bouncing with compaction (B1) and it reaches a final value of 5.41 at $t = 3 \times 10^6$ yr.

Table 5.1: Overview and results of all the simulations.

Model	ρ_g [g cm^{-3}]	α	$r_{\rm m}$	max($\bar{m}$) [g]	max(Ψ)	$\Psi_{\rm min}$	$t_{\rm noc}$ [yr]	max(St)
(1)	(2)	(3)	(4)	(5)	(6)	(7)	(8)	(9)
Lt1d-3m100	2.4×10^{-11}	10^{-3}	100	8×10^{-8}	7.27	1.77	2×10^4	2.5×10^{-4}
Lt1d-4m100	2.4×10^{-11}	10^{-4}	100	9.7×10^{-8}	7.12	2.23	8×10^4	2.2×10^{-4}
Lt1d-5m100	2.4×10^{-11}	10^{-5}	100	2.66×10^{-7}	7.72	3.78	3×10^5	2.1×10^{-4}
Mt1d-3m100	1.4×10^{-9}	10^{-3}	100	2.32	17.23	1.5	10^4	3.9×10^{-4}
Mt1d-4m100	1.4×10^{-9}	10^{-4}	100	4.18	21.9	1.85	2×10^5	2.8×10^{-4}
Mt1d-5m100	1.4×10^{-9}	10^{-5}	100	7.7×10^{-2}	30.0	4.13	7×10^5	2.1×10^{-4}
Ht1d-3m100	2.7×10^{-8}	10^{-3}	100	3.08	38.9	4.1	10^5	6.8×10^{-5}
Ht1d-4m100	2.7×10^{-8}	10^{-4}	100	0.23	38.0	5.41	3×10^6	3.6×10^{-5}
Ht1d-5m100	2.7×10^{-8}	10^{-5}	100	0.28	43.9	4.94	4×10^6	7.7×10^{-5}
Lt1d-4m10	2.4×10^{-11}	10^{-4}	10	1.3×10^{-3}	5.97	1.83	10^5	4.4×10^{-3}
Lt1d-4m100	2.4×10^{-11}	10^{-4}	100	9.7×10^{-8}	7.12	2.23	8×10^4	2.2×10^{-4}
Lt1d-4m1000	2.4×10^{-11}	10^{-4}	1000	9.7×10^{-8}	7.09	2.29	8×10^4	2.2×10^{-4}
Mt1d-4m10	1.4×10^{-9}	10^{-4}	10	2.5×10^{-2}	19.4	2.1	2×10^5	2.2×10^{-4}
Mt1d-4m100	1.4×10^{-9}	10^{-4}	100	4.18	21.9	1.85	2×10^5	2.8×10^{-4}
Mt1d-4m1000	1.4×10^{-9}	10^{-4}	1000	9.5×10^{-3}	23.1	2.9	2×10^5	1.3×10^{-4}
Ht1d-4m10	2.7×10^{-8}	10^{-4}	10	0.15	34.6	2.46	2×10^6	4.5×10^{-5}
Ht1d-4m100	2.7×10^{-8}	10^{-4}	100	0.23	38.0	5.41	3×10^6	3.6×10^{-5}
Ht1d-4m1000	2.7×10^{-8}	10^{-4}	1000	8.8×10^{-2}	40.0	7.1	10^5	3.5×10^{-5}

In this table, Col. 1 describes the model names. 'L' stands for the low density model, 'M' is the MMSN model, 'H' is the high density model, the letter 't' and the following number indicates the value of the turbulence parameter, the letter 'm' and the number shows the used critical mass ratio values. Columns 2, 3 and 4 shows the gas density, turbulence parameter and the critical mass ratio respectively. Columns 5, 6, 7, 8 and 9 list the parameters defined to characterize the distribution functions. These are the average maximum mass in Col. 5, the average maximum enlargement parameter in Col. 6, the minimum enlargement parameter in Col. 7, the end of the compaction phase in Col. 8 and finally the average maximum Stokes number in Col. 9.

5.4.5 Varying the Turbulence Parameter

To explore the effects of turbulence, we perform two more simulations in each of the disk models. We keep the critical mass ratio fixed (100) and vary only the turbulence parameter (α) to have values of 10^{-3}, 10^{-4} and 10^{-5}. The results are shown in Table 5.1, the first nine models and in Fig. 5.11a.

The work of Brauer et al. (2008a) suggests that in situations where fragmentation limits the growth, a lower turbulence strength results in bigger aggregates. This, of course, directly reflects the shift of the fragmentation threshold (1 m/s) to large sizes when α is lower (Fig. 5.1). In this study it is fragmentation that balances the growth, which results in a (quasi) steady-state. For the low density models we do see a decrease of the final

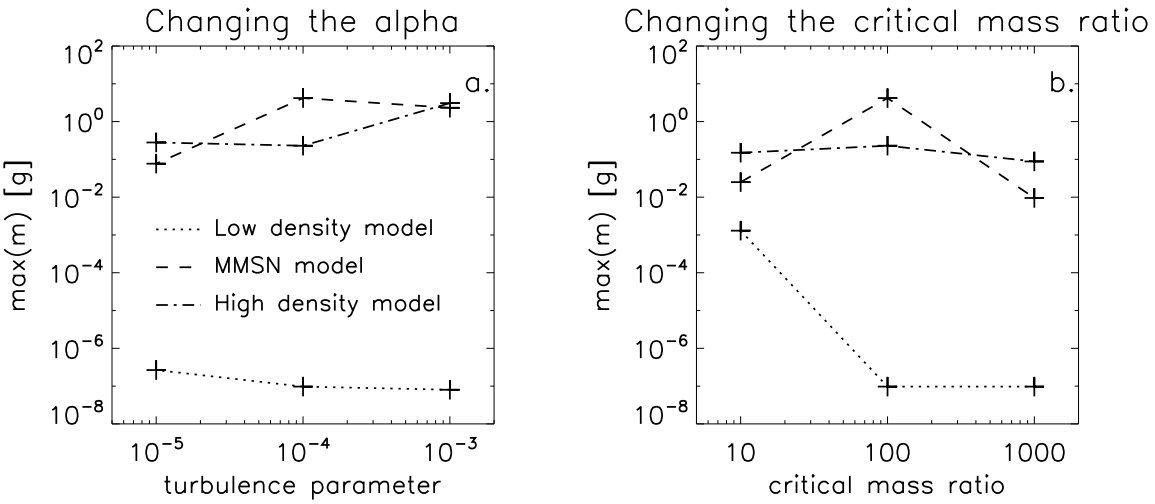

Figure 5.11: The maximum mean particle mass as a function of the turbulence parameter (a) and critical mass ratio (b).

particle mass, but it is bouncing that balances it. In the low density model, particles grow only in the hit-and-stick (S1) regimes. When particles leave these regimes, the growth stops due to bouncing. The border of the S1 regime is determined by the collision energy being lower than $5 \times E_{\rm roll}$, where $E_{\rm roll}$ is the rolling energy of monomers (see Chapter 4). As the collision energy is $E_{\rm coll} = 1/2\mu(\Delta v)^2$, particles in strong turbulence leave the S1 regimes at lower particle masses.

On the other hand, the MMSN and high density models show that the maximum mass of the particles can even increase with α. The precise value of the $\max(\bar{m})$ is determined by the intensity of the peak in the mass-density plots (Sect. 5.4.3) and this may vary somewhat between the simulations. In the 'Mt1d-4m100' model we have argued that the spike is exceptionally pronounced due to the high probability of sticking through surface effects (S2) collisions at the initial part of the fast growth. However the main point is that in the MMSN/high density simulations the maximum particle masses all end up around 1 g, independent of the turbulent strength.

The reason for this is the nature of the S2-B2 transition, which occurs at projectile masses of 10^{-4} g in the *'pP'* plot. As explained before, collisions in the *'pP'* plot are the only way by which particles can grow after the hit-and-stick (S1) phase is finished. Thus, we require a broad distribution for a high growth rate. However, a B2 collision works in the opposite way: it transfers mass from the target to the projectile, narrowing the distribution and decreasing the overall probability for the *'pP'* process. Thus, once B2 becomes effective, there is a shift from the *'pP'* panel to the *'pp'* panel. For the MMSN/high density models this behavior is always present and the important quantities involved (i.e., relative probability of B2 over S2) scale with mass and not with velocity. The result is that the maximum masses particles achieve are ~ 1 g and rather insensitive

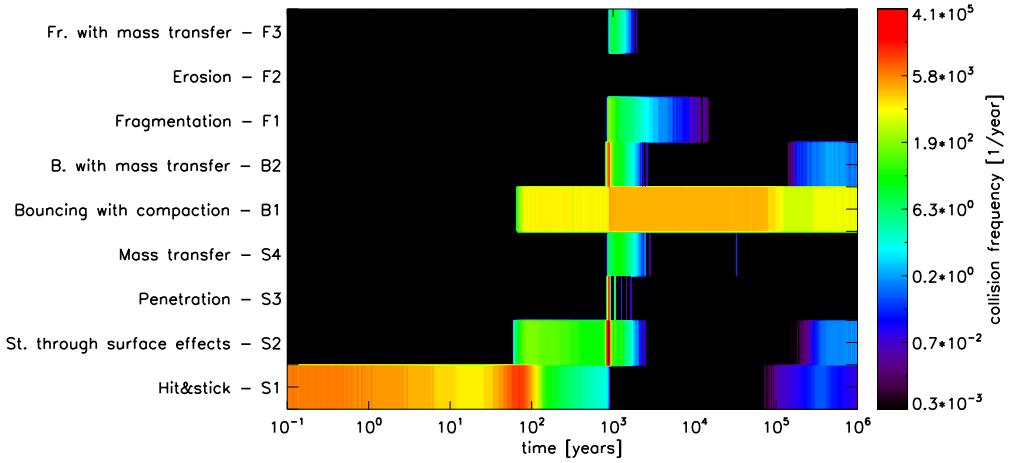

Figure 5.12: The collision frequencies of the 9 collision types in the MMSN model with $\alpha = 10^{-3}$ and $r_{\rm m} = 100$.

to the strength of the turbulence.

5.4.6 Varying the Critical Mass Ratio

We perform simulations in the disk models with $\alpha = 10^{-4}$ but with a varying critical mass ratio. We explore how the dust distributions change upon using $r_{\rm m} = 10$, 100 and 1000. Table 5.1, lines 10 to 18, shows the parameters describing the distribution functions, and Fig. 5.11b illustrates the maximum particle mass as a function of the critical mass ratio.

By examining Table 5.1 we see that using $r_{\rm m} = 10$ in the low density model ('Lt1d-4m10') results in heavier and more compact particles. The low critical mass ratio means that the biggest particles in the different sized regimes can sweep up the projectiles and grow to bigger sizes, eventually reaching the fragmentation line, where growth stops. As discussed in Sect. 5.2.2, assuming a fragmentation velocity of 1 m s^{-1}, the maximum Stokes number of the aggregates is 4.7×10^{-3}. This value is almost reached in this model.

We find that there is no significant difference between the $r_{\rm m} = 100$ and 1000 simulations in the low density model. The explanation for this can be found by examining the width of the mass distribution in the hit-and-stick (S1) phase. This initial phase is happening in the same way independently of the critical mass ratio. If the critical mass ratio r_m is equal to or larger than the width of the distribution function, collisions between different size particles in the *'pP'* regime are inhibited. After the S1 phase, the width of the distribution in the low density regime is approximately 100. Therefore, we do not see any difference when the mass threshold is shifted from $r_m = 100$ to $r_m = 1000$; in both cases collisions occur between equal-size particles only and these are either S1 or (when this stage is over) B1.

For the high density models (MMSN/Desch) we find that the outcome is again similar:

growth halts at $\sim$ 0.1 g (within a factor of 10) and no clear dependence on r_m is seen. For the high mass ratios, growth is always in the similar-size regime. Here, it is the gas density that determines the velocity, i.e., whether we have a sticking (S1) or a bouncing (B1) collision. Therefore, if $r_m = 1000$, the high density model produces heavier particles than the MMSN model (see Fig. 5.11b). For lower r_m it is again the nature of the S2-B2 transition regime that limits the maximum mass.

Thus, the critical mass ratio is an important parameter since it determines the relative likelihood of collisions occurring in the different-size regime, which are in general more conducive to growth. Conversely, in simulations where B2 collisions are important – which have the effect to narrow the distribution – the width of the distribution will correspond to the value of the r_m parameter, although we have also seen that the absolute size/mass is rather insensitive to it. Overall, these arguments indicate that a good knowledge of this parameter is important.

5.5 Discussion

We performed simulations with varying turbulence parameter and critical mass ratio values in three disk models having low, intermediate and high gas densities. We find that hit-and-stick (S1) and bouncing with compaction (B1) are the most dominant collision types. All simulations show the presence of long lived, quasi-steady states. Fragmentation is rarely present, but even then, only for a limited time period. The absence of fragmentation is due to the bouncing collisions.

5.5.1 The Sensitivity of the Results

As presented in Sect. 5.4, the outcome of our simulations is determined by the collision kernel and the relative velocity field. A significant change in one, or both can alter the evolution of the aggregates.

Here we present the results of a test simulation, where the sticking through surface effects (S2) – bouncing with mass transfer (B2) transition regime in the *'pP'* plot is neglected and replaced by S2 collisions. This alternative transition regime provides a good opportunity to further examine the fast growth presented in Sect. 5.4.3, as the kernel is now simplified. The new kernel also gives us the possibility to see how much the outcome of our simulations can be altered by changing critical areas of the parameter space. As the transition regime is only constrained by one experiment in a rather small area (see e.g. Fig. 5.5 or Fig. 4.11 in Chapter 4), further experiments may make it necessary to change this part of the parameter space. We use the same initial conditions as in the 'Mt1d-4m100' model described in Sect. 5.4.3.

In this case, the heaviest particle experiences increased relative velocities, as soon as it reaches $m = 0.1$ g, and the particle undergoes a fast growth period (as in the original MMSN simulation, Sect. 5.4.3). Figure 5.13 illustrates the growth timescale of the heaviest particle (dotted line) and the minimum growth timescale possible (solid

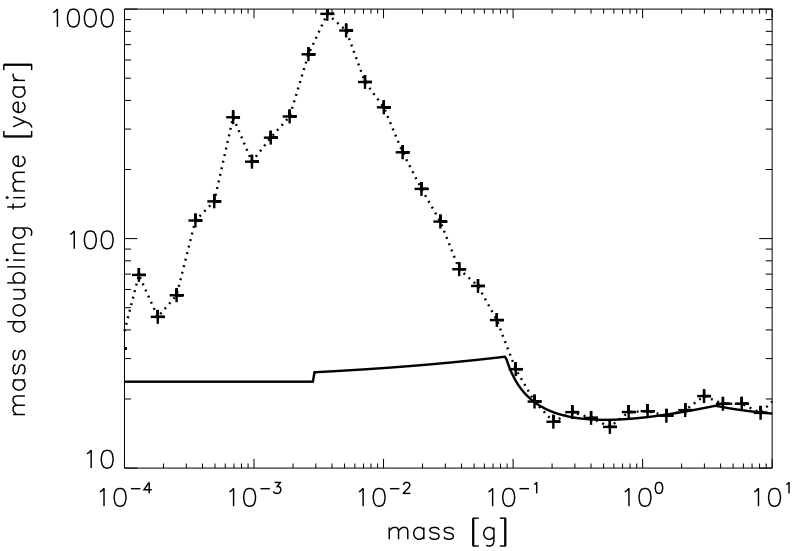

Figure 5.13: Growth timescale in the test simulation where the S2-B2 transition regime is replaced by S2 collisions only. The dotted line represents the growth timescale of the heaviest particles, the solid line is the minimum growth timescale. In this scenario, the growth timescale reaches the maximum possible value.

line). As there are no B2 collisions to reduce the mass of the heaviest particle, the growth timescale reaches the maximum that is possible. The heaviest particle increases in mass until the rest of the particle population enters the B2 regimes above 0.1 g in the *'pP'* plot. In this simulation, the maximum average mass is 27 g, whereas in the original simulation with the transition regime, the value is 4.18 g.

This work, together with Chapter 4, is the first attempt to calculate dust growth in protoplanetary disks on an empirical, thus realistic basis. However, a few more cycles of the feedback loop between the laboratory experiments, the models of the kind described in Chapter 4 and the models described in the paper have to be conducted before we can get near a truly reliable model of dust growth in protoplanetary disks.

5.5.2 Retention of Small Grains

Dullemond and Dominik (2005) showed that without a mechanism that reduces the sticking probability of particles in the upper layers of the disk or without a continuous source of small particles, the observed SEDs of TTauri stars would show very weak infrared excess. The SEDs of TTauri stars have strong IR excess (e.g. Furlan et al., 2005, Kessler-Silacci et al., 2006); therefore, some kind of grain-retention mechanism is needed to explain these SEDs. Previous models of grain growth assumed a continuous cycle of growth and fragmentation, which provides the necessary amount of small particles (Brauer et al., 2008a, Dullemond and Dominik, 2005, Birnstiel et al., 2009, see e.g.). Our simulations, however, showed that the mass distribution function is narrow. Small, monomer sized particles are

not present and fragmentation is ineffective in providing small particles, which could be transported to disk atmospheres. The question naturally arises: how can small grains be produced in our collision model?

One possible solution might come from bouncing. Weidling et al. (2009) performed bouncing experiments by putting an aggregate onto an oscillating metal plate and measuring the porosity of particles due to collisions with the plate. They observed that approximately 10% of the projectile mass eroded during the experiment (see Table 1 of their paper). This mass loss can happen due to the initial collisions; thus the eroded mass sticked to the baseplate. It is also possible that small pieces of fragments grind off when the aggregates bounce, which cannot be observed in the experiment. These ground off particles can then diffuse out of the midplane and provide the necessary amount of small particles to the upper layers of the disk. Future laboratory experiments are needed to quantify the level of ground off particles in bouncing collisions.

The second possible explanation is provided by dust growth at the upper layers of the disk. We performed two simulations at four pressure scale-heights in the low density model and in the MMSN model using $\alpha = 10^{-4}$. We find that the relative velocity of two monomers in the Brauer model is 2 m s^{-1}, thus monomers at these heights do not coagulate, only bounce. The particles in the MMSN model can form aggregates of maximum of 10 μm in size. Using a higher α (as is mostly assumed in the upper layers of the disk) can completely halt even this limited growth. Therefore, bouncing could be the key ingredient the mechanism that reduces the sticking probability of the particles. However, if substantial vertical turbulent mixing takes place, this may not help, because these monomers would then be "vacuum cleaned" away by the bigger particles at the interior of the disk. Further studies of 1D vertical slices of disk models are needed to investigate this scenario.

5.5.3 Implications for Planetesimal Formation Models

One can also see that coagulation only cannot produce planetesimals with the conditions presented in this work. Even if the turbulence parameter is taken to be zero, relative velocity due to radial drift is preventing particles to cross the so called 'meter size barrier'. An ideal environment for particle growth is a pressure bump in the dead zone where both the turbulent and radial relative velocities are reduced. Such an environment is located around the snow line (Kretke and Lin, 2007). Brauer et al. (2008b) showed that in these pressure bumps relative velocities stayed below a presumed fragmentation threshold of 10 m s^{-1}, presenting a window through which particles can overcome the m-size barrier, although they assumed perfect sticking (no bouncing) below the fragmentation barrier. Future studies have to verify whether planetesimals can be formed with the collision model presented in this study.

Another planetesimal forming mechanism is the gravitational collapse of swarms of boulders (Johansen et al., 2007). This scenario assumes that large amount of the solid material is present in dm sized boulders ($St \geq 0.1$) at the midplane of the disk. These boulders then concentrate in long-lived high pressure regions in the turbulent gas and

these initial over-densities are further amplified by the streaming instability. This mechanism forms 100 km sized objects on a very short timescale (some orbits). However, our simulations produce particles with $St \approx 10^{-4}$ which is due to bouncing with compaction (B1) and the low (1 m s^{-1}) fragmentation velocity of silicates. Using a 'stickier' material such as ices or particles with organic mantels may produce bigger particles. Molecular dynamic simulations (e.g. Dominik and Tielens, 1997, Wada et al., 2007, 2008) showed that icy aggregates could have fragmentation velocities of about 10 m s^{-1}, although these findings have yet to be confirmed by laboratory experiments. Similarly, it is conceivable that the enhanced sticking capabilities of ices will prevent the bouncing, which is so omnipresent for small particles in our simulations, or shifts it to larger sizes.

Cuzzi et al. (2008) outlined an alternative concentration mechanism to obtain GI-unstable clumps of particles. In this model turbulence causes dense concentrations of aerodynamically size-sorted, chondrule-size particles (Cuzzi et al., 2001)– more precisely, particles of Stokes numbers $St = Re^{-1/2} \approx 10^{-4}$ in our simulations. Since growth in our models is typically halted at these Stokes numbers, this concentration mechanism is an obvious successor to coagulation – at least where it concerns the conditions adopted in this paper (1AU, silicates).

However, it should be emphasized that fulfilling the GI criterion does not imply planetesimals will form unimpededly. An important question to address is how collisions will affect the collapse. In the Cuzzi et al. (2008) scenario the collapse occurs on a sedimentation timescale and for these high densities collisions between particles will be frequent. Likewise, in the Johansen scenario – where the collapse occurs on an orbital timescale and involves $St \sim 0.1$ particles – collisions can be rather violent. Collisional fragmentation or erosion may change the appearance of the collapse, because the small fragments are carried away by the gas. The role of collisions in these situations is certainly an important question, and our new collision model provides a tool to quantitatively address this issue in future studies.

5.5.4 Consequences for Laboratory Experiments

One can see from 4.11 (Chapter 4) that only a small part of the parameter space is covered by experiments. Although laboratory experiments cannot be made at every point of the parameter space, we suggest future ones based on Figs. 5.5, 5.7 and 5.10 in order to better understand dust growth in the early stages of planet formation.

- More experiments in the *'cc'* and *'cC'* regimes are needed as particles get compactified by the end of their evolution. Thus, most of the collisions happen in this regime, at velocities between 0.1 and 100 cm s^{-1}, at masses between 10^{-7} and 10 g.

- As seen in Figs. 5.5, 5.7 and 5.10, the 'hot spots', where most of the collisions are happening, are located in the equal sized regimes, at the left side of the fragmentation line. Therefore, it is important to map these areas of the parameter space in detail.

- We define a sharp border line between the hit-and-stick (S1) and bouncing with compaction (B1) collisions. If there is a continuous transition between S1 and B1, the growth of particles would not be halted by bouncing at such low particle sizes. As many collisions are happening in the *'pp'* and *'cc'* regimes, even a small probability of growth could increase the particle sizes.
- As seen in Fig. 5.6b, particles in high gas density environments can have enlargement parameters much higher than 6.6 ($\phi = 0.15$). An interesting question is whether the collision types and regimes are also valid for particles with such a low volume filling factors, or whether these particles have a different collision behavior?
- The sticking through surface effects (S2) – bouncing with mass transfer (B2) transition regime greatly affects the outcome of the simulations (see Sect. 5.5.1). However, the transition regime is only mapped at the high velocity and low mass regions. Therefore, it is essential to better constrain this part of the parameter space.
- The critical mass ratio affects the particle masses and porosities. Experiments are needed to constrain its value.
- The bouncing model, described in Chapter 4, has important implications for the evolution of dust aggregates in protoplanetary disks but it is unfortunately still based on too few experiments. Further experiments are needed to refine the model, as bouncing with compaction (B1) is the most frequent collision type in all of the simulations.

5.6 Summary

We performed simulations of dust growth using the Monte Carlo code of ZsD08 and a dust collision model based on laboratory experiments (Chapter 4). We performed simulations at the midplane of three disk models having low (2.4×10^{-11} g cm^{-3}), intermediate (1.4×10^{-9} g cm^{-3}) and high (2.7×10^{-8} g cm^{-3}) gas densities at 1 AU distance from the central star. We vary the turbulence parameter (α) and the critical mass ratio ($r_{\rm m}$) to explore their effects on the mass and porosity distribution functions. Our main results are:

- Upon using $\alpha = 10^{-4}$, the low density / MMSN / high density model produces particles with maximum mean mass of 9.7×10^{-8} g / 4.18 g / 0.23 g, the maximum average enlargement parameter of these particles are 7.12 / 21.9 / 38.0. The maximum average Stokes numbers are 2.2×10^{-4} / 2.8×10^{-4} / 3.6×10^{-5}.
- We find that particle evolution does not follow the previously assumed growth-fragmentation cycles. Although catastrophic fragmentation is present for a short period of time in some of the models (typically when $\alpha = 10^{-3}$), it has a fringe effect. Particles in most of the simulations do not reach the fragmentation barrier because their growth is halted by bouncing.

- We see long lived, quasi-steady states in the distribution function of the aggregates due to bouncing. The final equilibrium state is not reached within the drift or the viscous timescales.
- We performed simulations with varying turbulence strength. We find that the system is 'non-linear': The maximum mass of particles is not a decreasing function of the turbulence parameter and is not an increasing function of the gas density.
- We explored the effects of the critical mass ratio. We find that different critical mass ratios can affect the particle evolution. Small critical mass ratios can produce heavier particles, while big values of r_m can halt the growth earlier.
- The maximum Stokes number is rather independent of the gas density and the strength of the turbulence.
- The maximum mass of the aggregates is limited to ≈ 1 g due to the S2-B2 transition regime.
- The Stokes number 10^{-4} particles can be concentrated in turbulence by aerodynamical size-sorting, thus planetesimals can form from these particles.

Chapter 6

Conclusion

This work expands our knowledge on the post-fractal dust aggregation but it also reveals our limits in understanding. In Chapters 2 and 3, experiments and simulations were presented which are a direct contribution to understand the evolution of these aggregates. The dynamic compaction behavior of dust aggregates was previously only known for fractal aggregates (Dominik and Tielens, 1997, Blum and Wurm, 2000) whereas it was expected but never quantified for macroscopic aggregates. It was shown in Chapter 2 that bouncing collisions which were often observed in dust collision experiments (Blum and Münch, 1993, Heißelmann et al., 2007, Langkowski et al., 2008) do lead to a compaction of the aggregate. This becomes important after only a few hundred to 1 000 collisions which occur in a relatively short time (i.e. years) in the protoplanetary nebula. To understand the physics involved in the collision processes, the calibration of a computer model based on SPH was presented in Chapter 3. With the help of such a model, it will be possible to measure quantities that are hard or even impossible to measure in the laboratory. As an example, the reproduction of the bouncing experiment was presented. Here, quantities like the volume of compressed material in a collision can easily be accessed, which would be a laborious XRT-measurement for laboratory dust aggregates. A blind trust in these models would be dangerous, whereas a liaison between experiments and simulations is a fruitful approach to get an insight into the physics of protoplanetary dust aggregates.

All these results and models carry the weight of the collision model that was developed and utilized in Chapters 4 and 5. Based on the variety of laboratory collision experiments (Blum and Wurm, 2008) as well as on new experiments (Chapter 4), a model was constructed that predicts a quantified collisional outcome for any possible set of parameters, i.e. collision velocity, aggregate masses, and aggregate porosities. In spite of the many experiments that are included in this model, the parameter space is still poorly covered and experimental results needed to be extrapolated by orders of magnitude. However, based on concepts and physical models for protoplanetary dust aggregates as developed in previous works (e.g. Blum and Münch, 1993, Heißelmann et al., 2007, Langkowski et al., 2008) and in the foregoing Chapters, this model is the most advanced and reliable up to the present. Chapter 5 describes the implementation of this model into the Monte Carlo growth model developed by Zsom and Dullemond (2008). The results show that growth

is possible up to centimeter-sized aggregates (few grams, see Table 5.1) at 1 AU when solar nebula models with a sufficient mass density (i.e. MMSN, high density; see Sect. 1.1) are assumed. A growth-fragmentation cycle as expected from previous works (Zsom and Dullemond, 2008, Brauer et al., 2008a) could not be confirmed. Instead, growth is inhibited at a certain size because dust aggregates are neither sticking nor fragmenting but dominantly bounce. So the consequence of increasing the reliability of the growth model revealed another growth barrier: after the drift barrier (Weidenschilling, 1977b) and the fragmentation barrier (Brauer et al., 2008a, and others), the bouncing barrier is now inhibiting the growth to sizes before the other barriers become important. Fortunately, our understanding of bouncing dust aggregates is well-funded (Chapter 2 and references therein), but these experiments are still restricted to a small parameter range and must be extended in the future which is already ongoing (N. Rott, C. Güttler and J. Blum, in prep.). Also, the growth up to the biggest aggregates is passing through a bottleneck of sticking through surface effects (S2) growth (see Figs. 5.7 and 5.10, *'pP'* panel), which is rarely covered by experiments. Experiments to check this effect are also ongoing (I. von Borstel and J. Blum, in prep.).

Whatever future experiments will reveal, the mere existence of the bouncing barrier seems to be solid, as many experiments have shown this. Thus, we are facing a gap in the dust growth from centimeter-sized to meter-sized aggregates. Collisional aggregation works out up to centimeter sizes, whereas the successive growth may be explained if aggregates reach meter sizes. A growth mechanism with high potential to follow after the coagulation is a gravitational instability in locally overdense regions in the PPD. It has been shown by Johansen et al. (2007) that meter-sized bodies can concentrate in transient high-pressure regions, where the density can be further increased by the streaming instability (for streaming instability see Youdin and Goodman, 2005). As a consequence, a gravitationally bound cluster forms, which can collapse and directly form a large object with dwarf planet mass. However, the meter-sized bodies in this cluster collide, and in a follow-up simulation, Johansen et al. (2008) have shown that in case of fragmentation, small fragments are carried out of the cluster by the gas which inhibits the overdensities needed to become unstable. They used an oversimplified fragmentation model, assuming boulders to completely fragment into dust grains, which can be expected to be much too conservative. In a new simulation, Johansen et al. (2009) computed the distribution of relative velocities of dust aggregates inside a gravitationally bound cluster, which were around 1 m s^{-1}, but approximately half of the collisions occurred at higher velocities (i.e. up to 10 or 20 m s^{-1}). Thus, weak to intermediate fragmentation inside these clusters is likely but the influence of this is not clear. The implementation of a realistic aggregation kernel as described in Sect. 4 would be the preferred way to decide whether the instability as described by Johansen et al. (2007) can form these large bodies. A further question must then be the minimum aggregate size for which this instability can occur. It is shown that it might already work for centimeter to decimeter sized bodies (Chiang and Youdin, 2009, Johansen et al., 2009), especially if the host star is metal rich such that the PPD can be assumed to be denser (see Sect. 1.1).

Undoubtedly, it would be desirable to extend the collisional aggregation phase up to

much larger sizes and identify the conditions which benefit their growth. One possibility is the choice of material as outlined in Sect. 4.6.2: ices and organics in the outer regions of the disk may be stickier, whereas sintering in the inner parts increases the material strength to avoid destruction. In excess of material composition, the collision recipe of Dominik and Tielens (1997) predicts an enhanced strength for aggregates consisting of smaller grains as it has been pointed out by various authors (e.g. Zsom and Dullemond, 2008, Wada et al., 2009). The fragmentation criterion depends on the total number of grains involved, which overcompensates the smaller contact energy of the smaller grains. Sub-micrometer grains (i.e. 0.1 μm) may as well be the starting material for planet formation (see Sect. 1.1). An example for another discussed scenarios to enhance the growth is a pressure bump around a sublimation front like the snow line as proposed by Kretke and Lin (2007). A pressure-gradient avoids radial drift and particles concentrate in this region. A higher aggregate density results in more collisions per time and thus in a faster growth as described by Brauer et al. (2008b). However, the underlying assumption was that collisions do lead to growth in spite of bouncing, which is contradictory to the model presented in Chapter 4. So, also in this region, aggregates – though concentrated – would only grow until the bouncing barrier is reached. According to Chapters 4 and 5, a possible way to find a growth path through the labyrinth of the panels in Fig. 4.11 would be an appropriate velocity field for the relative velocities between aggregates. Testing different solar nebula models with different turbulence parameters in Chapter 5 is nothing else than changing the velocity field, and apart from the tested models there may be another way to enhance growth. Such a velocity field does not necessarily have to be globally existent but it may be valid in a special region in the disk comparable to the particle concentration at the snow line or resulting from the very low turbulence in a dead zone.

So far, the coagulation model as described in Chapter 5 is restricted to one confined region in the PPD without considering the dynamics of the disk, so it can be regarded as a 0D model. The next dimension that might change the result, would be the height of the disk, which includes differential settling of solids to the midplane. Due to the small relative velocities of settling aggregates, it is believed that dust aggregates, have decimeter sizes when they arrive at the midplane after 1 000 years of settling (i.e. Hayashi et al., 1985), which might possibly even lead to gravitational instability (Schräpler and Henning, 2004). These models assume sticking at velocities above the sticking threshold presented in the aggregation kernel in Chapter 4, thus, the growth to these sizes seems to be very unlikely. However, the differential settling clearly changes the velocity field which determines the evolution of dust aggregates (i.e. the growth path in Fig. 4.11). A non-linear effect might still unexpectedly enhance the growth to larger bodies. A second dimension that should be included in the model is the radial direction.

Also by further developing the aggregation kernel, possible ways for the growth up to larger bodies might become evident. The reliability of the growth model is unique and satisfactory at the moment, but it still needs to be improved. A single parametric region that might have been extrapolated by ill-conceived assumptions could change the whole growth path completely as Chapter 5 approved the expectation that the model is

highly non-linear. The weak points of the model were outlined in the end of Chapter 5 and these must be checked by new experiments for a more elaborated version of the model. Moreover, the whole growth model is only rarely covered by experiments. There are many blank spaces where a certain collisional outcomes is expected but this does not necessarily have to be the truth. Using the SPH code – although so far only calibrated in terms of compression – we can now effectively map these regions to check for unexpected collisional outcomes. Interesting simulation results should definitely be verified by laboratory experiments, but this would be much more effective way than performing every single experiments.

Bibliography

Andrews, S. M. and Williams, J. P. (2007). High-Resolution Submillimeter Constraints on Circumstellar Disk Structure. *The Astrophysical Journal*, 659:705–728.

Balbus, S. A. and Hawley, J. F. (1991). A powerful local shear instability in weakly magnetized disks. I - Linear analysis. II - Nonlinear evolution. *The Astrophysical Journal*, 376:214–233.

Barge, P. and Sommeria, J. (1995). Did planet formation begin inside persistent gaseous vortices? *Astronomy and Astrophysics*, 295:L1–L4.

Benz, W. (2000). Low Velocity Collisions and the Growth of Planetesimals. *Space Science Reviews*, 92:279–294.

Benz, W. and Asphaug, E. (1994). Impact simulations with fracture. I - Method and tests. *Icarus*, 107:98.

Benz, W. and Asphaug, E. (1999). Catastrophic Disruptions Revisited. *Icarus*, 142:5–20.

Birnstiel, T., Dullemond, C. P., and Brauer, F. (2009). Dust retention in protoplanetary disks. *Astronomy and Astrophysics*, 503:L5–L8.

Blum, J. (2004). Grain Growth and Coagulation. In Witt, A. N., Clayton, G. C., and Draine, B. T., editors, *Astrophysics of Dust*, volume 309 of *Astronomical Society of the Pacific Conference Series*, page 369.

Blum, J. (2006). Dust agglomeration. *Advances in Physics*, 55:881–947.

Blum, J. and Münch, M. (1993). Experimental investigations on aggregate-aggregate collisions in the early solar nebula. *Icarus*, 106:151.

Blum, J. and Schräpler, R. (2004). Structure and Mechanical Properties of High-Porosity Macroscopic Agglomerates Formed by Random Ballistic Deposition. *Physical Review Letters*, 93(11):115503.

Blum, J., Schräpler, R., Davidsson, B. J. R., and Trigo-Rodríguez, J. M. (2006). The Physics of Protoplanetesimal Dust Agglomerates. I. Mechanical Properties and Relations to Primitive Bodies in the Solar System. *The Astrophysical Journal*, 652:1768–1781.

Blum, J. and Wurm, G. (2000). Experiments on Sticking, Restructuring, and Fragmentation of Preplanetary Dust Aggregates. *Icarus*, 143:138–146.

Blum, J. and Wurm, G. (2008). The Growth Mechanisms of Macroscopic Bodies in Protoplanetary Disks. *Annual Review of Astronomy and Astrophysics*, 46:21–56.

Blum, J., Wurm, G., Kempf, S., and Henning, T. (1996). The Brownian Motion of Dust Particles in the Solar Nebula: an Experimental Approach to the Problem of Preplanetary Dust Aggregation. *Icarus*, 124:441–451.

Blum, J., Wurm, G., Kempf, S., Poppe, T., Klahr, H., Kozasa, T., Rott, M., Henning, T., Dorschner, J., Schräpler, R., Keller, H. U., Markiewicz, W. J., Mann, I., Gustafson, B. A., Giovane, F., Neuhaus, D., Fechtig, H., Grün, E., Feuerbacher, B., Kochan, H., Ratke, L., El Goresy, A., Morfill, G., Weidenschilling, S. J., Schwehm, G., Metzler, K., and Ip, W.-H. (2000). Growth and Form of Planetary Seedlings: Results from a Microgravity Aggregation Experiment. *Physical Review Letters*, 85:2426–2429.

Blum, J., Wurm, G., Poppe, T., and Heim, L.-O. (1998). Aspects of Laboratory Dust Aggregation with Relevance to the Formation of Planetesimals. *Earth Moon and Planets*, 80:285–309.

Blum, J., Wurm, G., Poppe, T., Kempf, S., and Kozasa, T. (2002). First results from the cosmic dust aggregation experiment codag. *Advances in Space Research*, 29:497–503.

Brauer, F., Dullemond, C. P., and Henning, T. (2008a). Coagulation, fragmentation and radial motion of solid particles in protoplanetary disks. *Astronomy and Astrophysics*, 480:859–877.

Brauer, F., Dullemond, C. P., Johansen, A., Henning, T., Klahr, H., and Natta, A. (2007). Survival of the mm-cm size grain population observed in protoplanetary disks. *Astronomy and Astrophysics*, 469:1169–1182.

Brauer, F., Henning, T., and Dullemond, C. P. (2008b). Planetesimal formation near the snow line in MRI-driven turbulent protoplanetary disks. *Astronomy and Astrophysics*, 487:L1–L4.

Brownlee, D., Tsou, P., Aléon, J., Alexander, C. M. O. ., Araki, T., Bajt, S., Baratta, G. A., Bastien, R., Bland, P., Bleuet, P., Borg, J., Bradley, J. P., Brearley, A., Brenker, F., Brennan, S., Bridges, J. C., Browning, N. D., Brucato, J. R., Bullock, E., Burchell, M. J., Busemann, H., Butterworth, A., Chaussidon, M., Cheuvront, A., Chi, M., Cintala, M. J., Clark, B. C., Clemett, S. J., Cody, G., Colangeli, L., Cooper, G., Cordier, P., Daghlian, C., Dai, Z., D'Hendecourt, L., Djouadi, Z., Dominguez, G., Duxbury, T., Dworkin, J. P., Ebel, D. S., Economou, T. E., Fakra, S., Fairey, S. A. J., Fallon, S., Ferrini, G., Ferroir, T., Fleckenstein, H., Floss, C., Flynn, G., Franchi, I. A., Fries, M., Gainsforth, Z., Gallien, J.-P., Genge, M., Gilles, M. K., Gillet, P., Gilmour, J., Glavin, D. P., Gounelle, M., Grady, M. M., Graham, G. A., Grant, P. G., Green, S. F.,

Grossemy, F., Grossman, L., Grossman, J. N., Guan, Y., Hagiya, K., Harvey, R., Heck, P., Herzog, G. F., Hoppe, P., Hörz, F., Huth, J., Hutcheon, I. D., Ignatyev, K., Ishii, H., Ito, M., Jacob, D., Jacobsen, C., Jacobsen, S., Jones, S., Joswiak, D., Jurewicz, A., Kearsley, A. T., Keller, L. P., Khodja, H., Kilcoyne, A. L. D., Kissel, J., Krot, A., Langenhorst, F., Lanzirotti, A., Le, L., Leshin, L. A., Leitner, J., Lemelle, L., Leroux, H., Liu, M.-C., Luening, K., Lyon, I., MacPherson, G., Marcus, M. A., Marhas, K., Marty, B., Matrajt, G., McKeegan, K., Meibom, A., Mennella, V., Messenger, K., Messenger, S., Mikouchi, T., Mostefaoui, S., Nakamura, T., Nakano, T., Newville, M., Nittler, L. R., Ohnishi, I., Ohsumi, K., Okudaira, K., Papanastassiou, D. A., Palma, R., Palumbo, M. E., Pepin, R. O., Perkins, D., Perronnet, M., Pianetta, P., Rao, W., Rietmeijer, F. J. M., Robert, F., Rost, D., Rotundi, A., Ryan, R., Sandford, S. A., Schwandt, C. S., See, T. H., Schlutter, D., Sheffield-Parker, J., Simionovici, A., Simon, S., Sitnitsky, I., Snead, C. J., Spencer, M. K., Stadermann, F. J., Steele, A., Stephan, T., Stroud, R., Susini, J., Sutton, S. R., Suzuki, Y., Taheri, M., Taylor, S., Teslich, N., Tomeoka, K., Tomioka, N., Toppani, A., Trigo-Rodríguez, J. M., Troadec, D., Tsuchiyama, A., Tuzzolino, A. J., Tyliszczak, T., Uesugi, K., Velbel, M., Vellenga, J., Vicenzi, E., Vincze, L., Warren, J., Weber, I., Weisberg, M., Westphal, A. J., Wirick, S., Wooden, D., Wopenka, B., Wozniakiewicz, P., Wright, I., Yabuta, H., Yano, H., Young, E. D., Zare, R. N., Zega, T., Ziegler, K., Zimmerman, L., Zinner, E., and Zolensky, M. (2006). Comet 81P/Wild 2 Under a Microscope. *Science*, 314:1711–1716.

Butler, R. P., Marcy, G. W., Fischer, D. A., Brown, T. M., Contos, A. R., Korzennik, S. G., Nisenson, P., and Noyes, R. W. (1999). Evidence for Multiple Companions to υ Andromedae. *The Astrophysical Journal*, 526:916–927.

Carpenter, J. M., Wolf, S., Schreyer, K., Launhardt, R., and Henning, T. (2005). Evolution of Cold Circumstellar Dust around Solar-type Stars. *The Astronomical Journal*, 129:1049–1062.

Chambers, J. E. (2001). Making More Terrestrial Planets. *Icarus*, 152:205–224.

Chiang, E. and Youdin, A. (2009). Forming Planetesimals in Solar and Extrasolar Nebulae. *Annual Reviews of Earth and Planetary Science*, 38. submitted.

Cuzzi, J. N., Hogan, R. C., Paque, J. M., and Dobrovolskis, A. R. (2001). Size-selective Concentration of Chondrules and Other Small Particles in Protoplanetary Nebula Turbulence. *The Astrophysical Journal*, 546:496–508.

Cuzzi, J. N., Hogan, R. C., and Shariff, K. (2008). Toward Planetesimals: Dense Chondrule Clumps in the Protoplanetary Nebula. *The Astrophysical Journal*, 687:1432–1447.

Cuzzi, J. N. and Weidenschilling, S. J. (2006). *Particle-Gas Dynamics and Primary Accretion*, pages 353–381. Meteorites and the Early Solar System II.

Davis, D. R. and Ryan, E. V. (1990). On collisional disruption - Experimental results and scaling laws. *Icarus*, 83:156–182.

Descartes, R. (1644). *Principia Philosophiae*. Elsevier, Amsterdam (in latin).

Desch, S. J. (2007). Mass Distribution and Planet Formation in the Solar Nebula. *The Astrophysical Journal*, 671:878–893.

Dintwa, E., Tijskens, E., and Ramon, H. (2008). On the accuracy of the Hertz model to describe the normal contact of soft elastic spheres. *Granular Matter*, 10(3):209–221.

Dominik, C., Blum, J., Cuzzi, J. N., and Wurm, G. (2007). Growth of Dust as the Initial Step Toward Planet Formation. In Reipurth, B., Jewitt, D., and Keil, K., editors, *Protostars and Planets V*, pages 783–800.

Dominik, C. and Tielens, A. G. G. M. (1995). Resistance to rolling in the adhesive contact of two elastic spheres. *Philosophical Magazine A*, 72:783–803.

Dominik, C. and Tielens, A. G. G. M. (1996). Resistance to sliding on atomic scales in the adhesive contact of two elastic spheres. *Philosophical Magazine A*, 73:1279–1302.

Dominik, C. and Tielens, A. G. G. M. (1997). The Physics of Dust Coagulation and the Structure of Dust Aggregates in Space. *The Astrophysical Journal*, 480:647.

Dubrulle, B., Morfill, G., and Sterzik, M. (1995). The dust subdisk in the protoplanetary nebula. *Icarus*, 114:237–246.

Dullemond, C. P. and Dominik, C. (2004). The effect of dust settling on the appearance of protoplanetary disks. *Astronomy and Astrophysics*, 421:1075.

Dullemond, C. P. and Dominik, C. (2005). Dust coagulation in protoplanetary disks: A rapid depletion of small grains. *Astronomy and Astrophysics*, 434:971–986.

Einstein, A. (1905). Über die von der molekularkinetischen Theorie der Wärme geforderte Bewegung von in ruhenden Flüssigkeiten suspendierten Teilchen. *Annalen der Physik*, 322:549–560.

Epstein, P. S. (1924). On the resistance experienced by spheres in their motion through gases. *Physical Review Letters*, 23(6):710–733.

Fischer, D. A. and Valenti, J. (2005). The Planet-Metallicity Correlation. *The Astrophysical Journal*, 622:1102–1117.

Furlan, E., Calvet, N., D'Alessio, P., Hartmann, L., Forrest, W. J., Watson, D. M., Uchida, K. I., Sargent, B., Green, J. D., and Herter, T. L. (2005). Colors of Classical T Tauri Stars in Taurus Derived from Spitzer Infrared Spectrograph Spectra: Indication of Dust Settling. *The Astrophysical Journal, Letters to the Editor*, 628:L65–L68.

Garaud, P. and Lin, D. N. C. (2004). On the Evolution and Stability of a Protoplanetary Disk Dust Layer. *The Astrophysical Journal*, 608:1050–1075.

Geretshauser, R. J., Speith, R., Güttler, C., Krause, M., and Blum, J. (2009). Numerical Simulations of Highly Porous Dust Aggregates in the Low-Velocity Collision Regime. *Astronomy and Astrophysics*. submitted.

Goldreich, P. and Ward, W. R. (1973). The Formation of Planetesimals. *The Astrophysical Journal*, 183:1051–1062.

Güttler, C., Krause, M., Geretshauser, R. J., Speith, R., and Blum, J. (2009). The Physics of Protoplanetesimal Dust Agglomerates. IV. Toward a Dynamical Collision Model. *The Astrophysical Journal*, 701:130–141.

Güttler, C., Poppe, T., Wasson, J. T., and Blum, J. (2008). Exposing metal and silicate charges to electrical discharges: Did chondrules form by nebular lightning? *Icarus*, 195:504–510.

Haisch, Jr., K. E., Lada, E. A., and Lada, C. J. (2001). Disk Frequencies and Lifetimes in Young Clusters. *The Astrophysical Journal, Letters to the Editor*, 553:L153–L156.

Hartmann, W. K. (1978). Planet formation - Mechanism of early growth. *Icarus*, 33:50–61.

Hartmann, W. K. (1980). Continued Low-Velocity Impact Experiments at AMES Vertical Gun Facility: Miscellaneous Results. In *Lunar and Planetary Institute Science Conference Abstracts*, volume 11 of *Lunar and Planetary Institute Science Conference Abstracts*, pages 404–406.

Hartmann, W. K. (1985). Impact experiments. I - Ejecta velocity distributions and related results from regolith targets. *Icarus*, 63:69–98.

Hatzes, A. P., Bridges, F., Lin, D. N. C., and Sachtjen, S. (1991). Coagulation of particles in Saturn's rings - Measurements of the cohesive force of water frost. *Icarus*, 89:113–121.

Hayashi, C., Nakazawa, K., and Nakagawa, Y. (1985). Formation of the solar system. In Black, D. C. and Matthews, M. S., editors, *Protostars and Planets II*, pages 1100–1153.

Heim, L.-O., Blum, J., Preuss, M., and Butt, H.-J. (1999). Adhesion and Friction Forces between Spherical Micrometer-Sized Particles. *Physical Review Letters*, 83:3328–3331.

Heißelmann, D., Fraser, H., and Blum, J. (2007). Experimental Studies on the Aggregation Properties of Ice and Dust in Planet-Forming Regions. In *Proceedings of the 58th International Astronautical Congress 2007*. IAC-07-A2.1.02.

Hertz, H. (1881). Über die Berührung fester elastischer Körper. *Journal für die reine und angewandte Mathematik*, 92:156–171.

Jessberger, E. K., Stephan, T., Rost, D., Arndt, P., Maetz, M., Stadermann, F. J., Brownlee, D. E., Bradley, J., and Kurat, G. (2001). *Properties of interplanetary dust: Information from collected samples*, page 253. Springer Verlag, Berlin.

Johansen, A., Brauer, F., Dullemond, C., Klahr, H., and Henning, T. (2008). A coagulation-fragmentation model for the turbulent growth and destruction of preplanetesimals. *Astronomy and Astrophysics*, 486:597–611.

Johansen, A., Henning, T., and Klahr, H. (2006). Dust Sedimentation and Self-sustained Kelvin-Helmholtz Turbulence in Protoplanetary Disk Midplanes. *The Astrophysical Journal*, 643:1219–1232.

Johansen, A., Oishi, J. S., Low, M.-M. M., Klahr, H., Henning, T., and Youdin, A. (2007). Rapid planetesimal formation in turbulent circumstellar disks. *Nature*, 448:1022–1025.

Johansen, A., Youdin, A., and MacLow, M.-M. (2009). Particle Clumping in Protoplanetary Disks Depends Strongly on Metallicity. *The Astrophysical Journal, Letters to the Editor*. submitted.

Johnson, K. L., Kendall, K., and Roberts, A. D. (1971). Surface Energy and the Contact of Elastic Solids. *Royal Society of London Proceedings Series A*, 324:301–313.

Kalas, P., Graham, J. R., Chiang, E., Fitzgerald, M. P., Clampin, M., Kite, E. S., Stapelfeldt, K., Marois, C., and Krist, J. (2008). Optical Images of an Exosolar Planet 25 Light-Years from Earth. *Science*, 322:1345–1348.

Kant, I. (1755). *Allgemeine Naturgeschichte und Theorie des Himmels*. W. Webel, Zeitz.

Kempf, S., Pfalzner, S., and Henning, T. K. (1999). N-Particle-Simulations of Dust Growth. I. Growth Driven by Brownian Motion. *Icarus*, 141:388–398.

Kessler-Silacci, J., Augereau, J.-C., Dullemond, C. P., Geers, V., Lahuis, F., Evans, II, N. J., van Dishoeck, E. F., Blake, G. A., Boogert, A. C. A., Brown, J., Jørgensen, J. K., Knez, C., and Pontoppidan, K. M. (2006). c2d Spitzer IRS Spectra of Disks around T Tauri Stars. I. Silicate Emission and Grain Growth. *The Astrophysical Journal*, 639:275–291.

Klahr, H. (2004). The Global Baroclinic Instability in Accretion Disks. II. Local Linear Analysis. *The Astrophysical Journal*, 606:1070–1082.

Klahr, H. H. and Henning, T. (1997). Particle-Trapping Eddies in Protoplanetary Accretion Disks. *Icarus*, 128:213–229.

Kokubo, E., Kominami, J., and Ida, S. (2006). Formation of Terrestrial Planets from Protoplanets. I. Statistics of Basic Dynamical Properties. *The Astrophysical Journal*, 642:1131–1139.

Kornet, K., Stepinski, T. F., and Różyczka, M. (2001). Diversity of planetary systems from evolution of solids in protoplanetary disks. *Astronomy and Astrophysics*, 378:180–191.

Kouchi, A., Kudo, T., Nakano, H., Arakawa, M., Watanabe, N., Sirono, S.-i., Higa, M., and Maeno, N. (2002). Rapid Growth of Asteroids Owing to Very Sticky Interstellar Organic Grains. *The Astrophysical Journal, Letters to the Editor*, 566:L121–L124.

Krause, M. and Blum, J. (2004). Growth and Form of Planetary Seedlings: Results from a Sounding Rocket Microgravity Aggregation Experiment. *Physical Review Letters*, 93(2):021103.

Kretke, K. A. and Lin, D. N. C. (2007). Grain retention and formation of planetesimals near the snow line in mri-driven turbulent protoplanetary disks. *The Astrophysical Journal*, 664:L55.

Lammel, C. (2008). Experimentelle Untersuchungen zur Fragmentation von Staubagglomeraten im Zweiteilchenstoß bei mittleren Geschwindigkeiten. Bachelor's thesis, Technische Universität Carolo Wilhelmina zu Braunschweig.

Langkowski, D., Teiser, J., and Blum, J. (2008). The Physics of Protoplanetesimal Dust Agglomerates. II. Low-Velocity Collision Properties. *The Astrophysical Journal*, 675:764–776.

Laplace, P. S. (1796). *Exposition du Système du Monde*. Circle-Solaire, Paris (in french). English translation: H.H. Harte (1830). The System of the World. University, Dublin.

Li, A. and Greenberg, J. M. (2003). In dust we trust: an overview of observations and theories of interstellar dust. In Pirronello, V., Krelowski, J., and Manicò, G., editors, *Solid State Astrochemistry*, pages 37–84.

Libersky, L. D., Petschek, A. G., Carney, T. C., Hipp, J. R., and Allahdadi, F. A. (1993). High strain lagrangian hydrodynamics: A three-dimensional sph code for dynamic material response. *Journal of Computational Physics*, 109(1):67–75.

Lyra, W., Johansen, A., Zsom, A., Klahr, H., and Piskunov, N. (2009). Planet formation bursts at the borders of the dead zone in 2D numerical simulations of circumstellar disks. *Astronomy and Astrophysics*, 497:869–888.

Markiewicz, W. J., Mizuno, H., and Voelk, H. J. (1991). Turbulence induced relative velocity between two grains. *Astronomy and Astrophysics*, 242:286–289.

Mathis, J. S., Rumpl, W., and Nordsieck, K. H. (1977). The size distribution of interstellar grains. *The Astrophysical Journal*, 217:425–433.

Mayor, M. and Queloz, D. (1995). A Jupiter-mass companion to a solar-type star. *Nature*, 378:355–359.

Melosh, H. J. (1989). *Impact cratering: A geologic process*. Oxford University Press.

Mizuno, H. (1980). Formation of the Giant Planets. *Progress of Theoretical Physics*, 64:544–557.

Mizuno, H., Markiewicz, W. J., and Voelk, H. J. (1988). Grain growth in turbulent protoplanetary accretion disks. *Astronomy and Astrophysics*, 195:183–192.

Monaghan, J. J. (2005). Smoothed particle hydrodynamics. *Reports of Progress in Physics*, 68:1703–1759.

Monaghan, J. J. and Gingold, R. A. (1983). Shock simulations by the particle method sph. *Journal of Computational Physics*, 52:374.

Nakagawa, Y., Hayashi, C., and Nakazawa, K. (1983). Accumulation of planetesimals in the solar nebula. *Icarus*, 54:361–376.

Nomura, H. and Nakagawa, Y. (2006). Dust Size Growth and Settling in a Protoplanetary Disk. *The Astrophysical Journal*, 640:1099–1109.

Okuzumi, S. (2009). Electric Charging of Dust Aggregates and its Effect on Dust Coagulation in Protoplanetary Disks. *The Astrophysical Journal*, 698:1122–1135.

Ormel, C. W. and Cuzzi, J. N. (2007). Closed-form expressions for particle relative velocities induced by turbulence. *Astronomy and Astrophysics*, 466:413–420.

Ormel, C. W., Paszun, D., Dominik, C., and Tielens, A. G. G. M. (2009). Dust coagulation and fragmentation in molecular clouds. I. How collisions between dust aggregates alter the dust size distribution. *Astronomy and Astrophysics*, 502:845–869.

Ormel, C. W. and Spaans, M. (2008). Monte carlo simulation of particle interactions at high dynamic range: Advancing beyond the googol. *The Astrophysical Journal*, 684:1291.

Ormel, C. W., Spaans, M., and Tielens, A. G. G. M. (2007). Dust coagulation in protoplanetary disks: porosity matters. *Astronomy and Astrophysics*, 461:215–232.

Paraskov, G. B., Wurm, G., and Krauss, O. (2007). Impacts into weak dust targets under microgravity and the formation of planetesimals. *Icarus*, 191:779–789.

Paszun, D. and Dominik, C. (2008). Numerical determination of the material properties of porous dust cakes. *Astronomy and Astrophysics*, 484:859–868.

Petersen, M. R., Julien, K., and Stewart, G. R. (2007). Baroclinic Vorticity Production in Protoplanetary Disks. I. Vortex Formation. *The Astrophysical Journal*, 658:1236–1251.

Pollack, J. B., Hubickyj, O., Bodenheimer, P., Lissauer, J. J., Podolak, M., and Greenzweig, Y. (1996). Formation of the Giant Planets by Concurrent Accretion of Solids and Gas. *Icarus*, 124:62–85.

Poppe, T. (2003). Sintering of highly porous silica-particle samples: analogues of early solar-system aggregates. *Icarus*, 164:139–148.

Poppe, T., Blum, J., and Henning, T. (2000). Experiments on Collisional Grain Charging of Micron-sized Preplanetary Dust. *The Astrophysical Journal*, 533:472–480.

Randles, P. W. and Libersky, L. D. (1996). Smoothed particle hydrodynamics: Some recent improvements and applications. *Computer Methods in Applied Mechanics and Engineering*, 139(1-4):375–408.

Reyes-Ruiz, M. (2001). The Magnetorotational Instability across the Dead Zone of Protoplanetary Disks. *The Astrophysical Journal*, 547:465–474.

Righter, K., Drake, M. J., and Scott, E. R. D. (2006). *Compositional Relationships Between Meteorites and Terrestrial Planets*, pages 803–828. University of Arizona Press, Tucson.

Ryan, E. V., Hartmann, W. K., and Davis, D. R. (1991). Impact experiments. III - Catastrophic fragmentation of aggregate targets and relation to asteroids. *Icarus*, 94:283–298.

Safronov, V. S. (1969). *Evolution of the Protoplanetary Cloud and Formation of the Earth and Planets*. Nauka, Moscow. English translation: NASA TTF-677 (1972).

Schäfer, C., Speith, R., and Kley, W. (2007). Collisions between equal-sized ice grain agglomerates. *Astronomy and Astrophysics*, 470:733–739.

Schmitt, W., Henning, T., and Mucha, R. (1997). Dust evolution in protoplanetary accretion disks. *Astronomy and Astrophysics*, 325:569–584.

Schräpler, R. and Henning, T. (2004). Dust Diffusion, Sedimentation, and Gravitational Instabilities in Protoplanetary Disks. *The Astrophysical Journal*, 614:960–978.

Scott, E. R. D. and Krot, A. N. (2005). Thermal Processing of Silicate Dust in the Solar Nebula: Clues from Primitive Chondrite Matrices. *The Astrophysical Journal*, 623:571–578.

Shakura, N. I. and Sunyaev, R. A. (1973). Black holes in binary systems. Observational appearance. *Astronomy and Astrophysics*, 24:337–355.

Sirono, S.-I. (2004). Conditions for collisional growth of a grain aggregate. *Icarus*, 167:431–452.

Suyama, T., Wada, K., and Tanaka, H. (2008). Numerical Simulation of Density Evolution of Dust Aggregates in Protoplanetary Disks. I. Head-on Collisions. *The Astrophysical Journal*, 684:1310–1322.

Takeuchi, T. and Lin, D. N. C. (2002). Radial Flow of Dust Particles in Accretion Disks. *The Astrophysical Journal*, 581:1344–1355.

Tanaka, H., Himeno, Y., and Ida, S. (2005). Dust Growth and Settling in Protoplanetary Disks and Disk Spectral Energy Distributions. I. Laminar Disks. *The Astrophysical Journal*, 625:414–426.

Tanaka, H., Inaba, S., and Nakazawa, K. (1996). Steady-State Size Distribution for the Self-Similar Collision Cascade. *Icarus*, 123:450–455.

Thommes, E. W., Matsumura, S., and Rasio, F. A. (2008). Gas Disks to Gas Giants: Simulating the Birth of Planetary Systems. *Science*, 321:814–817.

Torquato, S., Truskett, T. M., and Debenedetti, P. G. (2000). Is Random Close Packing of Spheres Well Defined? *Physical Review Letters*, 84:2064–2067.

Tscharnuter, W. M. (1987). A collapse model of the turbulent presolar nebula. *Astronomy and Astrophysics*, 188:55–73.

Tscharnuter, W. M., Schönke, J., Gail, H. ., and Lüttjohann, E. (2009). Protostellar collapse: rotation and disk formation. *Astronomy and Astrophysics*. in press.

Tsiganis, K., Gomes, R., Morbidelli, A., and Levison, H. F. (2005). Origin of the orbital architecture of the giant planets of the Solar System. *Nature*, 435:459–461.

Turner, N. J., Sano, T., and Dziourkevitch, N. (2007). Turbulent Mixing and the Dead Zone in Protostellar Disks. *The Astrophysical Journal*, 659:729–737.

Udry, S., Fischer, D., and Queloz, D. (2007). A Decade of Radial-Velocity Discoveries in the Exoplanet Domain. In Reipurth, B., Jewitt, D., and Keil, K., editors, *Protostars and Planets V*, pages 685–699.

Valverde, J. M., Ramos, A., Castellanos, A., and Watson, P. K. (1998). The tensile strength of cohesive powders and its relationship to consolidation, free volume and cohesivity. *Powder Technology*, 97(3):237–245.

Völk, H. J., Jones, F. C., Morfill, G. E., and Roeser, S. (1980). Collisions between grains in a turbulent gas. *Astronomy and Astrophysics*, 85:316–325.

Wada, K., Tanaka, H., Suyama, T., Kimura, H., and Yamamoto, T. (2007). Numerical Simulation of Dust Aggregate Collisions. I. Compression and Disruption of Two-Dimensional Aggregates. *The Astrophysical Journal*, 661:320–333.

Wada, K., Tanaka, H., Suyama, T., Kimura, H., and Yamamoto, T. (2008). Numerical Simulation of Dust Aggregate Collisions. II. Compression and Disruption of Three-Dimensional Aggregates in Head-on Collisions. *The Astrophysical Journal*, 677:1296–1308.

Wada, K., Tanaka, H., Suyama, T., Kimura, H., and Yamamoto, T. (2009). Collisional Growth Conditions for Dust Aggregates. *The Astrophysical Journal*, 702:1490–1501.

Weidenschilling, S. J. (1977a). Aerodynamics of solid bodies in the solar nebula. *The Monthly Notices of the Royal Astronomical Society*, 180:57–70.

Weidenschilling, S. J. (1977b). The distribution of mass in the planetary system and solar nebula. *Astrophysics and Space Science*, 51:153–158.

Weidenschilling, S. J. (1979). Self-Induced Turbulence and the Onset of Gravitational Instability in a Dust Layer. *Bulletin of the American Astronomical Society*, 11:552.

Weidenschilling, S. J. (1980). Dust to planetesimals - Settling and coagulation in the solar nebula. *Icarus*, 44:172–189.

Weidenschilling, S. J. (1984). Evolution of grains in a turbulent solar nebula. *Icarus*, 60:553–567.

Weidenschilling, S. J. (1995). Can gravitation instability form planetesimals? *Icarus*, 116:433–435.

Weidenschilling, S. J. and Cuzzi, J. N. (1993). Formation of planetesimals in the solar nebula. In Levy, E. H. and Lunine, J. I., editors, *Protostars and Planets III*, pages 1031–1060.

Weidling, R., Güttler, C., Blum, J., and Brauer, F. (2009). The Physics of Protoplanetesimal Dust Agglomerates. III. Compaction in Multiple Collisions. *The Astrophysical Journal*, 696:2036–2043.

Weizsäcker, C. F. v. (1944). Über die Entstehung des Planetensystems. *Zeitschrift für Astrophysik*, 22:319.

Wetherill, G. W. (1990). Comparison of analytical and physical modeling of planetesimal accumulation. *Icarus*, 88:336.

Whipple, F. L. (1972). On certain aerodynamic processes for asteroids and comets. In Elvius, A., editor, *From Plasma to Planet*, page 211.

Wurm, G. and Blum, J. (1998). Experiments on Preplanetary Dust Aggregation. *Icarus*, 132:125–136.

Wurm, G., Blum, J., and Colwell, J. E. (2001). NOTE: A New Mechanism Relevant to the Formation of Planetesimals in the Solar Nebula. *Icarus*, 151:318–321.

Wurm, G., Paraskov, G., and Krauss, O. (2005a). Ejection of dust by elastic waves in collisions between millimeter- and centimeter-sized dust aggregates at 16.5 to 37.5 m/s impact velocities. *Physical Review E*, 71(2):021304.

Wurm, G., Paraskov, G., and Krauss, O. (2005b). Growth of planetesimals by impacts at ∼25 m/s. *Icarus*, 178:253–263.

Wyatt, M. C. (2008). Evolution of Debris Disks. *Annual Review of Astronomy and Astrophysics*, 46:339–383.

Youdin, A. N. and Goodman, J. (2005). Streaming Instabilities in Protoplanetary Disks. *The Astrophysical Journal*, 620:459–469.

Zolensky, M. E., Zega, T. J., Yano, H., Wirick, S., Westphal, A. J., Weisberg, M. K., Weber, I., Warren, J. L., Velbel, M. A., Tsuchiyama, A., Tsou, P., Toppani, A., Tomioka, N., Tomeoka, K., Teslich, N., Taheri, M., Susini, J., Stroud, R., Stephan, T., Stadermann, F. J., Snead, C. J., Simon, S. B., Simionovici, A., See, T. H., Robert, F., Rietmeijer, F. J. M., Rao, W., Perronnet, M. C., Papanastassiou, D. A., Okudaira, K., Ohsumi, K., Ohnishi, I., Nakamura-Messenger, K., Nakamura, T., Mostefaoui, S., Mikouchi, T., Meibom, A., Matrajt, G., Marcus, M. A., Leroux, H., Lemelle, L., Le, L., Lanzirotti, A., Langenhorst, F., Krot, A. N., Keller, L. P., Kearsley, A. T., Joswiak, D., Jacob, D., Ishii, H., Harvey, R., Hagiya, K., Grossman, L., Grossman, J. N., Graham, G. A., Gounelle, M., Gillet, P., Genge, M. J., Flynn, G., Ferroir, T., Fallon, S., Ebel, D. S., Dai, Z. R., Cordier, P., Clark, B., Chi, M., Butterworth, A. L., Brownlee, D. E., Bridges, J. C., Brennan, S., Brearley, A., Bradley, J. P., Bleuet, P., Bland, P. A., and Bastien, R. (2006). Mineralogy and Petrology of Comet 81P/Wild 2 Nucleus Samples. *Science*, 314:1735.

Zsom, A. and Dullemond, C. P. (2008). A representative particle approach to coagulation and fragmentation of dust aggregates and fluid droplets. *Astronomy and Astrophysics*, 489:931–941.

Zsom, A., Ormel, C. W., Güttler, C., Blum, J., and Dullemond, C. P. (2009). The outcome of protoplanetary dust growth: pebbles, boulders, or planetesimals? II. Introducing the bouncing barrier. *Astronomy and Astrophysics*. submitted.

Acknowledgements

First and above all I want to thank Jürgen Blum for supervising this work in his very own inspiring and motivating manner. Always giving me the advise and the discussion I needed, he also gave me the freedom to do what I liked, which was the best motivation for me to do my very best. I really acknowledge the trust he put into me and the responsibilities he offered me. I wish that Jürgen will ever be the first to understand how planets form.

I'm grateful to Carsten Dominik for refereeing my thesis. I hope he liked it and that he maybe got some ideas for his own work during reading it.

I want to thank my collaborators who worked with me on the papers on which this thesis is based. The intense and productive work with Andras Zsom and Chris Ormel was a wonderful symbiosis between experiments and theory, which I hope will be continued in a similar way for the next years. Thanks to Ralf Geretshauser, we learned so much about our 'dust cakes', and I personally got an impression for the modeling of those in so many long and inspiring phone calls. René Weidling worked with me for his Bachelor's thesis and he really did a great job. Owing to his motivation it was possible to put our ideas for the compaction experiment into effect and we never would have thought this to result in a paper that became so important for us. Many thanks to Frithjof Brauer, who helped us with the collision timescales in the same paper, which was too theoretic for me at that time – but I'm happy that I learned it. With Maya Krause I could discuss all the material property stuff we needed for the SPH paper, e.g. on long train rides with red wine which did not feel so long in the end. My thanks also go to Roland Speith and Kees Dullemond for the direct and indirect collaboration through Ralf and Andras.

I also enjoyed the work with my colleagues at the offices next door and acknowledge their contribution to this work. I thank Christopher Lammel, Daniel Heißelmann, Stefan Kothe, Rainer Schräpler, and Stephan Olliges to give me access to their unpublished experiment data, such I was able to include up-to-date results into our model. During his Diploma thesis – and actually not next door anymore – Jens Teiser started the calibration of the SPH code with his first deceleration curves and XRT measurements.

This thesis was accomplished within the frame of the Forschergruppe 759 'The Formation of Planets: The Critial First Growth Phase', which is granted by the Deutsche Forschungsgemeinschaft. This research unit is a great and inspiring environment for young PhD students and I really enjoyed this. I want to thank the speakers and all the people who had their work with it for initiating and organizing this group and all the events and

workshops. Moreover, such a group is also carried by the people, and after our very nice Bad Honnef winter school I really felt a warm team spirit.

I want to thank my colleagues at my home institute Institut für Geophysik und extraterrestrische Physik for the great atmosphere and working environment. Whenever I needed help, I knew someone to ask and found a helpful expert for every problem. Moreover, I was happy for the discreet distraction that was always possible, i.e. the training runs, the weekly volleyball, table soccer games, the coffee break or barbecues. These interpersonal events helped me to relax and to be fresh for the next steps.

Of course, the most important people for me are my family and my friends and I want to thank those for always keeping me down to earth. It's the simple things in life that really count but it's easy to forget this when being absorbed by a fascinating problem like the formation of planets.